FLOW OF BUBBLES AND FOAMS IN NARROW MICROFLUIDIC GEOMETRIES

by

Michal Marek Solarski

A thesis submitted to

the University of Birmingham

for the degree of

DOCTOR OF PHILOSOPHY

UNIVERSITY OF BIRMINGHAM

University of Birmingham Research Archive

e-theses repository

ABSTRACT

The movement of gas-liquid foams through narrow channels of various complex geometries is commercially challenging and technically important. This thesis investigates the dynamics of bubbles and foams in microfluidic channels with constrictions, expansions and obstacles.

The flow of single bubbles in a sudden contraction, followed by a sudden expansion was studied. Effect of the capillary number was investigated, showing that bubbles deformation increased with it. Larger bubbles were also investigated in different constrictions with the emphasis on the snap-off break-up. Effect of thin liquid films is shown experimentally to be the main contribution. Furthermore, inertial effects are found to be influential during the final neck collapse.

Foams in microfluidic channels with constrictions were investigated with regards to topological changes, including bubble re-arrangements and various break-ups caused by higher shear stresses. Effects of the geometry, including, constriction width and length, are highlighted. The neck collapse also gives different scalings for various break-ups, suggesting different dynamics and forces driving the break-ups. Furthermore, foams in suddenly and gradually expanding channels were analysed with regards to velocity, elasticity and plasticity.

Foams flowing in channels with spherical obstacles were studied. Dynamics of different foam regimes are presented as they flow around centrally located obstacle. The bamboo foam was found to generate two bubbles via lamella division mechanism. The sizes of the daughter bubbles are correlated with the capillary number, liquid fraction and initial bubble size. Additionally, shifting the location induced only size dependence. A more complicated structure consisting of four obstacles was studied experimentally and analysed with regards to the new number of bubbles generated. All the data is shown to collapse on a single line and to be in agreement with the numerical results.

ACKNOWLEDGEMENTS

This was one of the most challenging times I have experienced in my entire life. I have learned to be independent, patient and not to give up even when things do not go your way. Many mixed feelings went through my head during the three years, making me question many aspects of my life. The non-scientific lessons that I have learned during those years are as much if not more important as all of the scientific ones and will stay with me forever to guide me through the rest of my life.

CONTENTS

LIST OF TABLES

LIST OF FIGURES

27

NOMENCLATURE

A_b	bubble area
A_{box}	area investigated
A_{Hpb}	area of the horizontal plateau border
A_{Vpb}	area of the vertical plateau border
A^*	dimensionless bubble area
d	diameter
d	distance from a point on the interface in the direction of the outward normal to the point of the nearest interface
d_b	bubble diameter
d_{crit}	distance of two interfaces coming close to each other
d_o	obstacle diameter
f_{T1}	frequency of the T1 events
H	channel height
h_t	liquid film thickness
H_{pb}	height of the plateau border
k	flow consistency index
l	average of the lengths and edges adjacent to a point on the interface
$\vec{l} = (l_x, l_y)$	links of the neighbouring bubble centres
l_b	perimeter of the bubble
l_c	constriction length
l_{min}, l_{max}	segment lengths range of the interface
L	channel length
L_{pb}	length of the plateau border

L_0	initial bubble length
L_x	axial bubble length
L_x^*	dimensionless axial bubble length
L_0^*	dimensionless initial bubble length
$\mathcal{L}$	length scale
$\bar{\bar{M}}$	texture tensor
n	flow behaviour index
$\underline{n}$	unit normal vector
N	number of bubbles contained in the channel
N_{T1}	number of T1 events found
p_b	bubble pressure
P_C	capillary pressure
P_G	gas pressure
P_L	liquid pressure
P_{MIN}	minimum gas pressure to enter the flow-focusing orifice
Q_G	gas flow-rate
Q_L	liquid flow-rate
r_0	circumferential radius of curvature
r_1, r_2	principle radii of curvature
$\overrightarrow{r_{s2}}, \overrightarrow{r_{s1}}$	position vectors of linked bubble centres
r_b	bubble radius
r_c	radius of curvature
r_c	axial radius of curvature
r_c^*	dimensionless radius of curvature

R_O	obstacle radius
$\vec{R}$	position of the box investigated
s_1, s_2	pairs of neighbouring centres
t	time
t_b	time bubble breaks
t_c	time bubble reaches constriction centre
t_{movie}	length of the video
U_f	foam velocity
U_L	average liquid velocity
U_x	axial bubble velocity
U_y	transversial bubble velocity
U_{fr}	bubble front velocity
U_{ta}	bubble tail velocity
v_d	driving velocity
V_G	gas volume
V_L	liquid volume
V_b	bubble volume
V_{Hpb}	horizontal plateau border volume
V_{Vpb}	vertical plateau border volume
$V(R)$	volume of box investigated at position R
w_c	constriction width
w_n	bubble neck width
w_{or}	orifice width
W	channel width

W_b	bubble width
W_i	bubble initial width
W_{pb}	plateau border width
x_f	bubble front tip position
x_f^*	dimensionless bubble front tip position

Greek symbols

α	power-law coefficient
β	power-law exponent
γ	shear rate
η	disjoining pressure
$\hat{\eta}$	dimensionless disjoining pressure
θ	angle between adjacent edges
θ_c	constriction angle
λ	friction coefficient
λ_1, λ_2	eigenvalues
μ	liquid viscosity
μ_P	plastic viscosity
ρ	liquid density
σ	surface tension
τ_0	apparent yield stress
τ_s	shear stress
τ	time to break
τ_b	break-up time
τ_b^*	dimensionless break-up time

τ_o break-up time scale

ϕ_{ch} foam channel liquid volume fraction

ϕ_L/ε_L foam liquid volume fraction

ϕ_{or} foam inlet liquid volume fraction

ΔA_b change in the bubble area

ΔP pressure difference

Λ_t aspect ratio of channel width to flow-focusing orifice

Λ_A ratio of the daughter bubbles

F_κ curvature force

F_λ friction force

T_λ time-scale

Abbreviations

cmc   critical micelle concentration

fps   frames per second

EOR   enhanced oil recovery

LMW   low molecular weight

NaDBS   sodium dodecylbenzene sulfonate

PAH   polyaromatic hydrocarbons

PDMS   poly(dimethylsiloxane)

rpm   revolutions per minute

UV   ultra-violet

Dimensionless numbers

Bo   Bond number

Ca   Capillary number

Re   Reynolds number

We   Weber number

1 INTRODUCTION

1.1 INTRODUCTION

Foams are colloidal systems that are composed of gas bubbles separated from each other by interconnected thin liquid films. They can be classified into two different regimes, based on the volume fraction of the continuous phase. If the liquid fraction is very low, the foam is said to be dry, and if it is substantial, the foam is said to be wet. The volume liquid fraction also affects the structure of the foam; thus, the two regimes may significantly differ (Stevenson, 2012).

Foams have found many applications over the last century, including cosmetics, pharmaceuticals, food, fire-fighting, enhanced oil recovery and froth flotation, to name a few. However, due to their complex structure such as viscoelasticity, metastability and finite yield stress (Weaire and Hutzler, 1999), they are challenging to model and predict which motivated many researchers to undertake studies of them.

Flowing foams are used in applications such as enhanced oil recovery or fire-fighting, which picked up interest in studying their dynamics in narrow passages, such as cracks, valves and porous media (Calvert, 1988; Wong *et al.*, 1995a; Singh *et al.*, 1997; Conn *et al.*, 2014; Wu *et al.*, 2017). They often flow on a micro-scale which used to be difficult to study and observe. However, with the improving technologies of micro-visualisations, this has become a reality.

In this work, a study of the flow of gas-liquid bubbles and foams in microfluidic channels with narrow passages will be presented. The main aim is to improve the fundamental understanding of single bubbles and foams in channels with constrictions and obstacles. Varying the cross-sections of the channels can have a profound effect on the dynamics of foams, such as topological changes which include bubble fragmentation or change of

structure. Foam encounter similar dynamics and geometries in many of the applications by flowing through for example a valve (fire-fighting), a nozzle (ice-cream) and porous media in order to efficiently displace oil (enhanced oil recovery application) or deliver surfactant to contaminated soil (soil remediation). The work presented here should therefore, improve understanding of foams and how they behave in narrow passages by answering some fundamental questions: how bubbles and foams are affected by the capillary number; how they break; what capillary number or foam structure is required for particular topological change; which forces contribute to the break-ups; which parameters will allow the calculation of the final number of bubbles in the channel, or the bubble size distribution after passing through a channel variation; and, how the bubbles and foams are affected when the dimensions of the constrictions or obstacles are changed. Answering all of the above questions should give new insights into understanding bubble dynamics and helping predicting the bubble size distribution for the above-mentioned applications. Furthermore, the results presented here should also improve understanding of bubbles and foams for the lab on a chip which heavily relies on the transportation of bubbles and drops.

Single bubbles in the presence of surfactant were studied through various constrictions in order to shed light on the complex behaviour of flowing foams. Bubble profile will be presented with regards to elongation and compression and velocities between the front and the rear of a bubble in liquid solutions of different viscosity values. Furthermore, gas slugs undergoing separation through constrictions were investigated. The thin liquid films surrounding bubbles and channel dimensions were found to play a significant role in the fragmentation. Furthermore, the bubble neck variation just before the break-up was studied, which allowed understanding forces that drive such break-up.

A similar investigation was carried out for foams through constrictions, explaining different instabilities that they underwent and how they were affected by various constrictions. Many findings apply to the foams of higher liquid fractions far from the usual dry limit studied in two-dimensional channels. Moreover, foams in expanding channels are analysed in terms of their velocity, elasticity and plasticity.

Apart from constrictions, foams often have to flow around obstacles which may have a different effect on their dynamics. Bubbles were observed to undergo division when flowing around spherical obstacles. The division was not observed in the constricted flows. The way the bubbles were divided and, therefore, how the new bubbles were generated by flowing around obstacles of different sizes is presented. The study should improve understanding of foam generation through bubble division in porous media.

1.2 OUTLINE OF THE DISSERTATION

This dissertation presents various features of bubbles and foams observed in narrow microfluidics passages. The literature relevant to each particular results chapter is reviewed separately. It is structured as follows:

Chapter 2 deals with a general background of foams, which include discussion of surfactants, foam structure, various ways of foam generations, factors affecting the foam stability and their applications.

Chapter 3 presents the materials and methods used in this dissertation.

Chapter 4 describes the study of single bubbles flowing through constrictions in microfluidic channels. At first, bubbles of sizes comparable to the constriction width are investigated in terms of elongation, compression, and velocities between particular parts of a bubble. The influence of bubble velocity and viscosity of the liquid are also considered. Furthermore, larger bubbles are studied in the constricted flow. Bubble fragmentation is

analysed, including time required for the break-up, the effect of the shape of the constriction, bubble neck collapse and the generation of the daughter bubbles.

Chapter 5 undertakes the study of foams in constricted microfluidic channels. Various foam regimes are investigated at different velocities in the sudden and gradual constrictions. Topological changes are explained with their occurrence presented for different foam types. A comparison between the sudden and gradual constriction is presented. Additionally, larger foam structures are studied in the gradual constrictions, describing the effects of constriction width and length. The influence of channel expansion on foam is analysed with regards to velocity, elasticity and plasticity. Results are compared for suddenly and gradually expanding channels.

Chapter 6 considers foams flowing around circular obstacles. Observations of structural and topological changes are described for different foam regimes. Trains of bubbles that their lamella spans the width of the channel are investigated further. Explanation of how they are divided around obstacles of different sizes and positions is presented. A more complex channel consisting of four obstacles is also studied. The aspect of foam formation through the four-obstacle structure is investigated and compared with the numerical results.

Chapter 7 outlines the general conclusions of this dissertation and suggestions for future research in this area.

2 GENERAL BACKGROUND

2.1 FOAMS

Foam is defined as a dispersion of gas bubbles in a liquid, with the gas phase being a discontinuous phase within a continuous liquid phase. The two-phase fluid is a colloidal system that can be thought of as gas bubbles being enclosed by interconnected thin liquid films. The volume liquid fraction of the foam is directly related to the foam quality. This fraction can either be small (liquid fraction ≤ 5%) and composed of polyhedral bubbles, or higher (liquid fraction ≥10%) and composed of spherical bubbles (Weaire and Hutzler, 1999). The two regimes are known as dry foam or high quality, and wet foam or low quality, respectively.

Foams have had a number of household applications for a long period of time. For example, in applications such as cleaning and cosmetic, products with higher foaming ability are often considered as being of better quality. Their applications are also numerous in the food industry, pharmaceuticals, cutting transport, enhanced oil recovery, fire-fighting, froth-flotation, and biotechnology (Bikerman, 1973; Prud'homme and Khan, 1996; Stevenson, 2012; Cooke and Hirt, 2017).

2.2 SURFACTANTS

One can attempt to produce foam from pure water; however, this will never work. If a gas is injected below the surface of the water, gas bubbles will rise to the surface because of the buoyancy force. The bubbles then escape the surface and coalesce or burst immediately once in contact with each other. This is due to the system restoring a state of equilibrium with minimum energy. In order to generate actual gas-liquid foams, an agent is needed to adsorb at the gas/liquid interface (e.g. a thin film) and stabilise it by lowering the surface interfacial free

energy (Aubert *et al.*, 1986). This prevents the bubbles from rupturing. The surface-active agents, also known as surfactants, allow foaming by reducing the surface tension of the fluid. Lower surface tension, in turn, means less energy is required for bubbles to be created and rise to the surface of the liquid. The surface-active agents can be categorised into two classes due to their molecular characteristic properties, namely low molecular weight (LMW) surfactants and complex surfactants such as proteins. In the past few decades, particle-based foams have been increasing in popularity, where only particles (no surfactants) are used to produce and stabilise foams (Binks, 2002; Hunter *et al.*, 2008).

Since the focus of this thesis is on the dynamics of bubbles and foams due to the variation in the geometry of the channel, only one type of surfactant was chosen so that the foaming characteristics remained uniform for different channels.

2.2.1 LOW MOLECULAR WEIGHT SURFACTANTS

The use of surfactants for foams is due to their amphiphilic molecular structure; meaning one of their parts is hydrophobic (has low water attraction; non-polar group), and one is hydrophilic (high water attraction; polar group). Once a surfactant is added to a fluid such as water, its molecules will tend to adsorb at the air/water interface where they will position themselves in such a manner that the hydrophobic part is oriented away from the bulk liquid, i.e. exposed to the air, while the hydrophilic part is in direct contact with the solution (Aubert *et al.*, 1986). Such order of the molecules reduces the free energy of the system by changing the original arrangement of the liquid molecules (Pugh, 2016). This means that the surface tension is now lowered and therefore, less energy is required to produce foam, making the liquid more foam-favourable.

The surface tension of a surfactant-based solution will decrease together with the increase of surfactant concentration caused by a greater number of monomers adsorbed at the

gas/liquid interface. Beyond a certain value of surfactant concentration, when the solution is oversaturated with surfactant molecules, these molecules start to associate with each other and form micelles in the bulk (Aubert *et al.*, 1986). Once the molecules create micelles, the concentration of the surfactant has reached what is known as the critical micelle concentration (cmc). In this case, even if more surfactant is added, the surface tension will not decrease. The critical micelle concentration means that the liquid has reached a constant minimum surface tension value because the monomers at the interface are so tightly packed that there is no room for other molecules and that they have to stay in the bulk of the liquid (Pugh, 2016). A representation of the surfactant molecules at different concentrations can be seen in Figure 2.1. Because of Brownian thermal motion, there is a migration of molecules from the surface to the bulk. This generates fewer monomers at the actual surface; however, any space left behind at the surface is quickly filled with other monomers caused by diffusion so that a dynamic equilibrium is established.

Low molecular surfactants are classified into four further groups based on the nature of the polar part (Pugh, 2016); they are categorised as follows :

1. Anionic: the polar group contains a negative charge.
2. Cationic: the polar group contains a positive charge.
3. Zwitterionic: the polar group contains both positive and negative charge.
4. Non-ionic: the polar group contains no apparent charge.

Depending on the foam properties that are required (e.g. bubble size, half-life-time or low wall friction); it is essential that one knows which surfactant to choose from depending on their purpose. Anionic surfactants are the oldest and most popular type. They have a good detergency which makes them widely used as cleaning products (Yuan *et al.*, 2014). The negatively charged ions bind to positively charged particles, such as clays, which give them

the ability to effectively remove soils (Williams, 2007). Cationic surfactants as mentioned above are positively charged, and since the surface of the hair and skin is negatively charged (Rhein, 2007), they can bind together very strongly. Consequently, the process of removing the surfactant from the hair or skin becomes difficult and it may also cause skin irritation. Thus, they are commonly used for other applications, such as corrosion and mineral flotation (Yuan *et al.*, 2014). Zwitteronic surfactants on the other hand, have low toxicity and are biodegradable (Van Ginkel, 2007) which makes them predominantly used as shampoos, shower gels and other cosmetics (Yuan *et al.*, 2014). Non-ionic surfactants do not form ions in aqueous solutions and are used in the food industry (Yuan *et al.*, 2014). Examples of each surfactant type are listed in Table 2.1.

The non-polar part of the molecules can also differ; however, they are in general long-chain hydrocarbon radicals.
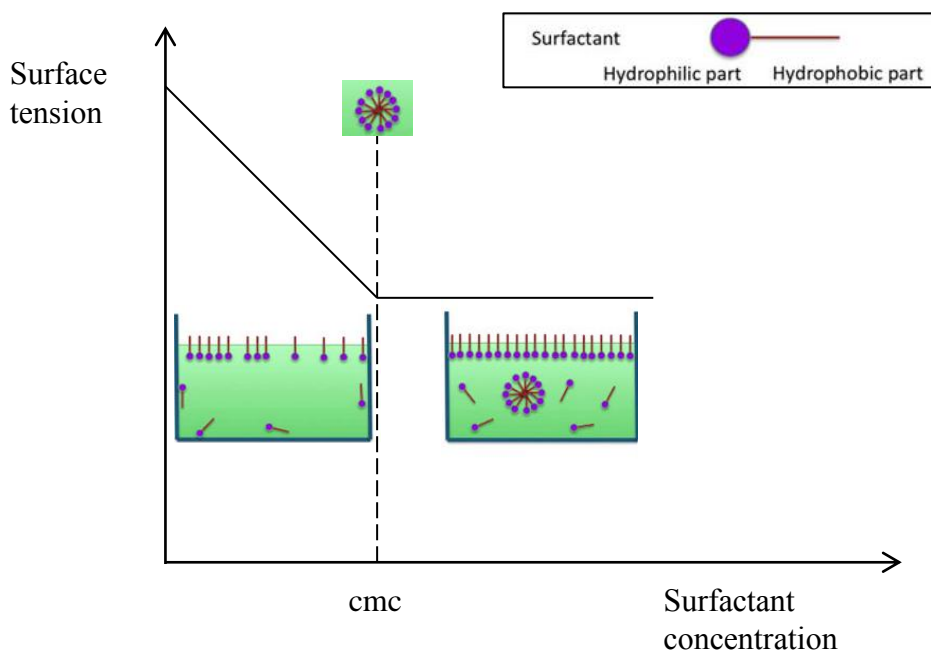
Figure 2.1 Representation of the surfactant molecules and the relation of the surface tension with the increase of the surfactant concentration. Three types of monomers behaviour are illustrated: (i) free monomers in the bulk, (ii) adsorbed monolayer at the surface of the liquid and (iii) formed micelles (Pugh, 2016).

Class	Example	Molecular formula
Anionic	Sodium dodecylbenzenesulfonate	$CH_3(CH_2)_{11}C_6H_4SO_3Na$
Cationic	Dodecyltrimethylammonium chloride	$CH_3(CH_2)_{11}N(CH_3)_3Cl$
Zwitterionic	Lauramidopropyl betaine	$C_{11}H_{23}CONH(CH_2)_3N^+(CH_3)_2CH_2COO^-$
Non-ionic	Triton X-100	$C_{14}H_{29}(OCH_2CH_2)_2OH$

Table 2.1 Examples of four surfactants and their related classes as well as their structures

2.3 FOAM STRUCTURE

Foams, as previously mentioned, are gaseous bubbles surrounded by interconnected liquid films. Depending on the liquid fraction of the foam, whether high or low, they can have different shapes. High liquid foam is referred to as wet foam and can be identified by having spherical bubble shapes that are separated by very thick liquid films known as lamellae (Weaire and Hutzler, 1999). This can often be observed in newly made foam that is still fresh such as the head of a beer after pouring it into a glass. The low liquid content foam, however, is referred to as dry foam. The dry foam structure consists of polyhedral bubbles rather than spherical and very thin liquid films in between the gas bubbles (Weaire and Hutzler, 1999). The films are almost flat, with a thickness often under 100 nm. Dry foam can be generated by injecting gas at small flow-rate or through a larger orifice into surfactant solution. It is also observed at the top of the static foam in a column after the liquid has drained down, so essentially the older foam will transform into the dry limit structure. Both of the foam types can be seen in Figure 2.2. The foam liquid volume fraction also known as liquid hold-up is directly related to the foam quality which is determined by the following equation

$$\phi_L = \frac{V_L}{V_G + V_L} \tag{2.1}$$

where ϕ_L is the liquid hold-up and V_G and V_L are the volume of the gas and the volume of the liquid in the foam, respectively.

a)	b)
Dry foam	Wet foam
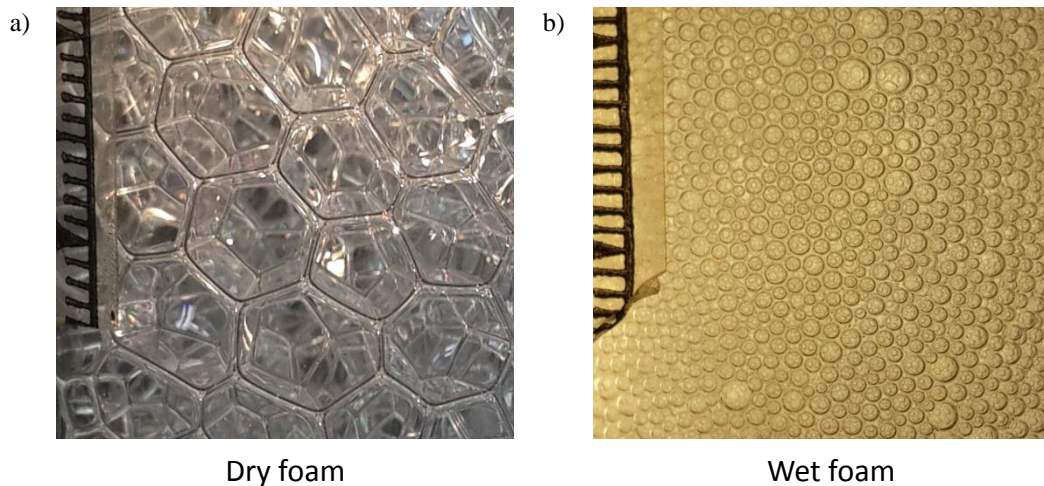
Figure 2.2 Images of a) dry and b) wet foam in a glass column. Notice the polyhedral bubbles of the dry foam and spherical bubbles surrounded by thick fractions of liquid in the wet foam.

   In the dry foam structure, each of the thin films or lamellae meets at what is known as the plateau border. The name of this region is named after Joseph Plateau, who experimentally studied such junctions in his paper (Plateau, 1873). Plateau observed soap bubbles and soap films suspended on wireframes and noticed that three lamellae always meet at exactly 120°. Each of the plateau borders allows identifying the edges of the bubbles. Four of these edges must always join at angles of $\cos^{-1}(-1/3) = 109.5°$ at what is often referred to as nodes. These structure regions can be determined in the three-dimensional foam; however, they are difficult to observe in foam images simply because the images are two-dimensional and can often be deceiving. The Plateau laws can be observed in Figure 2.3 of a simulated foam in Surface Evolver (Brakke, 1992) thanks to the courtesy of Simon Cox. This illustration allows seeing through the three-dimensional foam. In the two dimensional foam, such as in a Hele-Shaw cell or a microfluidic channel, the plateau borders often look like the nodes and the nodes can be hard to determine. The pressure inside the bubble is larger than the pressure outside the bubble, including the pressure inside the plateau border. This is

because of the curvature of the interface that can be expressed using the Laplace-Young equation

$$\Delta P = \sigma \left(\frac{1}{r_1} + \frac{1}{r_2} \right) \qquad (2.2)$$

where ΔP is the pressure difference across the interface, σ is the interfacial or surface tension and r_1, r_2 are the two principal radii of the curvature. Naturally for spherical bubbles $r_1 = r_2 = r$ and therefore equation (2.2) becomes

$$\Delta P = \frac{2\sigma}{r}. \qquad (2.3)$$
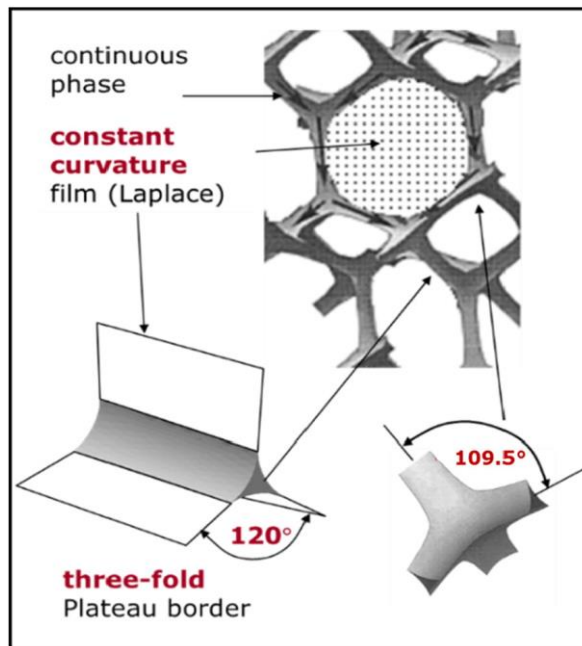
Figure 2.3 Illustration of three films meeting at the plateau border and four edges at the nodes (image from Simon Cox).

Depending on the bubble generation, as well as the channel that the bubbles are confined by, the structure can be polydisperse meaning heterogeneous with respect to the bubble size, as in the previous example of wet foam in Figure 2.2. It can be clearly observed (even by eye) that the bubble size distribution is quite broad. Another structure such as

45

honeycomb has fully monodisperse bubbles usually with a dispersity index being significantly low meaning all bubble areas are uniform (Figure 2.4). The bubble size, as well as the bubble size distribution, is responsible for the foam texture. Apart from bubble size variation, the actual size of the bubbles is also crucial. The foam can have a fine texture, meaning small bubbles like the wet foam in Figure 2.2 or coarse texture which is related to large bubbles such as the one in the dry foam in the figure mentioned above. Bubble size and their distribution are predominant foam characteristics that enable comparison between different foam experiments.
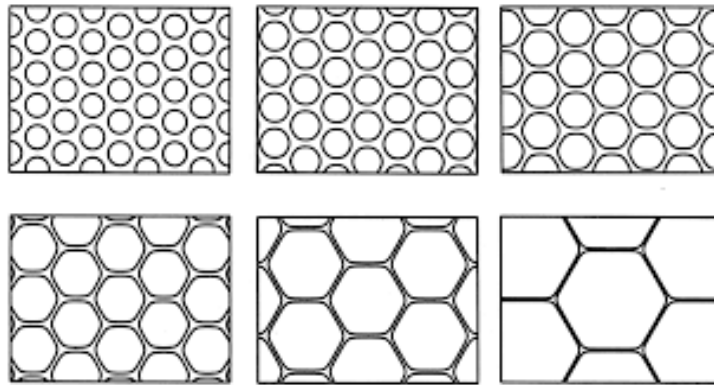
Figure 2.4 Illustration of honeycomb foam structures for various liquid fractions, starting from top left ϕ_L =0.5, 0.4, 0.3, 0.2, 0.1, 0.05 (Image from Kraynik and Reinelt (1999)).

2.4 FOAM GENERATION

Foam can be generated in a variety of ways, depending on the properties that are required of it. Generations include whipping, shaking or injecting a gas into a surfactant solution. All of these examples fall into two methods of foam formation, namely condensation and dispersion (Bikerman, 1973). The condensation method includes opening a bottle of beer or champagne. In this case, the gas is released at different pressure (usually lower) than it was originally saturated in the liquid. Another example involves the chemical generation of gas in the liquid, such as fermentation. The dispersion method, on the other hand, includes more

straightforward ways of foam formation, such as whipping eggs or other food products. Shaking the solution and therefore, directly introducing air to the liquid is another way. In the industrial processes such as froth flotation, gas is injected directly through an orifice or through a porous plate. This form of foam generation leads to obtaining much more desirable foams, formed of either coarse or fine bubbles depending on the size of the orifice and the flow-rate of gas. It has been shown in the literature (Deshpande and Barigou, 2000) that gas flow-rate through a sintered glass has an impact on the bubble size. Usually, low flow-rates generate larger bubble sizes since only gas passes through the larger pores. Increase in the flow-rate results in the gas passing through smaller pores and therefore reducing the bubble size. The single orifice can be used to generate relatively monodisperse three-dimensional foams but only at low flow-rates. Using single orifice in two-dimensional channels such as in microfluidics or Hele-Shaw cells will produce monodisperse foam; examples can be seen in Figure 2.5.
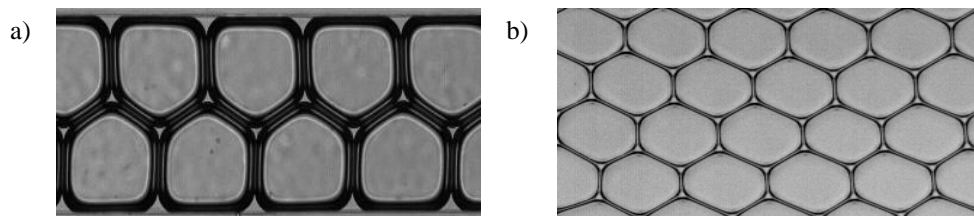
Figure 2.5 An example of a fully monodisperse staircase structure generated using a single orifice: a) in a microfluidic channel (dispersity index < 1%), b) in a Hele-Shaw cell (dispersity index < 3%).

2.5 FOAM STABILITY

As previously mentioned, a foam system is generally thermodynamically unstable, and it is of utmost importance to be able to generate stable foam systems for the applications. This is because a single bubble can burst as soon as the foam is formed, therefore, highlighting that stability is a crucial component. The stability of the foam is affected by many parameters

including, surfactant type, liquid viscosity, liquid surface tension, surrounding temperature or foam morphology, to name a few (Weaire and Hutzler, 1999). The main processes that disintegrate the bubbles and cause the foam to collapse or to cease are

- Drainage

- Coalescence

- Coarsening

Drainage, as the name itself suggests, involves the drainage of the liquid from the foam. Since the liquid films are all interconnected in the foam system, the liquid can drain from the top of the foam column to the very bottom resulting in only a liquid layer at the bottom of the foam. This effect of gravity is mainly caused because of the gradient of gas and liquid density. Additionally, the pressure difference between films and plateau borders causes the capillary suction, so that liquid drains from the lamella to the plateau borders (Weaire and Hutzler, 1999). When the liquid drains through the foam, the film starts thinning and eventually reaches a thickness that can suddenly rupture and start foam collapse. During this process, the bubbles burst, and because of the film thinning, they also start coalescing with their adjacent cells resulting in larger bubbles.

Coalescence, as mentioned above, can be caused by drainage or, for example, gentle heating of the foam. It involves film thinning and rupture between adjacent bubbles, which can be better understood by understanding the Gibbs-Marangoni effect. This process is the mass transfer across the interface between two fluids due to the gradient of surface tension. During drainage, the liquid drains away from the bubble surface area towards the plateau borders, carrying surfactant molecules along with it. This reduces the surfactant concentration at the upper interface, which causes the surface tension gradient of the thin liquid film (Pugh, 1996). Similarly, the expanding film can have its surface area increased, causing a local

change in the surface tension. The surfactant monomers from the bulk and other parts of lamella with lower surface tension, quickly move to the areas with higher surface tension and re-establish an equilibrium state (Aubert *et al.*, 1986). This mechanism is dependent on the rate of diffusion and adsorption of the surfactant molecules to the interface. Thus, surfactants with higher rates of both diffusion and adsorption can produce a stronger Gibbs-Marangoni effect which can effectively reduce the rate of film thinning and therefore slow down the rate of drainage (Pugh, 1996). Surfactant concentration can also influence the Gibbs-Marangoni effect since more molecules will be packed tighter at the interface and therefore react better to the areas with fewer molecules. However, foams with an oversaturated amount of surfactant can cause the molecules from the bulk liquid to react faster than the ones at the interface which might not prevent the film thinning and cause rupture of the lamella.

Even when the drainage is slowed down and the foam system can resist coalescence, a coarsening may occur. This process involves inter-bubble gas diffusion through foam films. According to the Young-Laplace equation (Eq. (2.2)), smaller bubbles have smaller radii than larger bubbles resulting in greater pressures. This can be observed in the example below (Figure 2.6), where the larger bubble has a concave shape because of the pressure difference. The pressure in the smaller bubbles causes the gas to dissolve into the liquid film and then into the larger bubble. This process causes the larger bubble to grow at the expense of the small one. This effect is also known as disproportionation or Ostwald ripening (Pugh, 2016). Coarsening strongly depends on the surfactant molecules on the films of the foam since the gas molecules have to penetrate the surfactant monolayers in order to diffuse to other bubbles (Pugh, 2016).
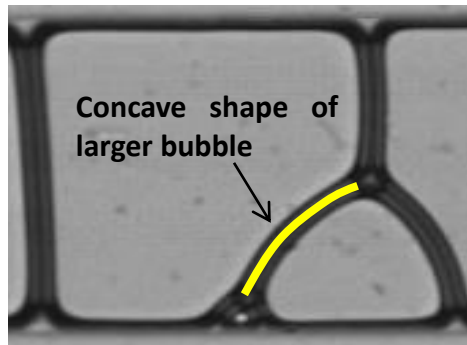
Figure 2.6 Illustration of the pressure difference between two adjacent bubbles. From a larger bubble perspective, the edge has a concave shape indicating smaller pressure inside, whereas, from a small bubble perspective, the edge has convex shape suggesting higher pressure inside.

It should also be noted that evaporation of the liquid from the foam can also boost the foam collapse, especially if the temperature of the system is increased or the foam is left open to the air. Naturally, keeping the foam in the closed vessel can prevent evaporation. Using compact monolayers, such as the ones obtained from fatty alcohols (Langevin, 2000) can also decrease the rate of the evaporation.

In order to obtain foam with a long-life, the processes above need to be specifically addressed and slowed down. Changing the rheology of the bulk solution could affect the stability of the foam e.g. increasing bulk liquid viscosity by adding for instance glycerol, guar gum or carboxymethyl cellulose, and, therefore, increasing the viscosity in the foam films and plateau borders, can slow down the rate of the drainage process and therefore, the rate of the foam collapse. Using non-ionic surfactants with long-chain carbons as the monomers can help to slow down the thinning of the films and thus prevent bubble coalescence (Pugh, 2016).

Choice of the dispersed phase can also enhance the stability of the foam. Using nitrogen instead of carbon dioxide can reduce coarsening. This is because nitrogen is less water-soluble and it will take longer for the gas to diffuse from smaller bubbles. Ideally, producing a fully monodisperse foam with all of the bubbles being of uniform size, and therefore of

relatively identical inner pressures, can stop inter-bubble gas migration and eliminate coarsening completely. Particle-based foam, whether produced solely by particles or combined with a surfactant, can also be the key to producing ultra-stable foams (Alargova *et al.*, 2004) that could possibly withstand high temperatures as well as high pressures for applications under harsh conditions.

It is also important to understand that in micro-flows such as the ones studied here, the dimensions of the channels are below 1 mm which means that the effect of gravity can be neglected (see 2.6.2). Thus, the drainage in the foams is almost totally absent, resulting in the absence of thinning of the films and therefore, coalescence. Moreover, the foams studied in this thesis were also very monodisperse which eliminated the possibility of coarsening. Such experimental conditions allowed the extraction of foam behaviour caused by different channel geometries and flow conditions, rather than other disintegrating processes.

2.6 FOAM TRANSPORT

Flowing gas-liquid foam has been used for decades across many applications. Industries such as petroleum are pioneers of using foams, more specifically in oil recoveries, froth flotation or separation of minerals. The usefulness of flowing foams caused researchers from all over the globe to undertake studies of them. Many first experimentalists focused on understanding flows in capillaries (Blauer *et al.*, 1974; Raza and Marsden, 2007) and porous media (Roof, 1970; Burley *et al.*, 1984; Khatib *et al.*, 1988; Kovscek and Radke, 1994; Cohen *et al.*, 1996) because of their applications. Pipe flow has also been intensively studied including various pipe lengths, diameters, inclinations, bends and fittings (Okpobiri and Ikoku, 1983; Thondavadi and Lemlich, 1985; Calvert, 1990; Valkó and Economides, 1992; Deshpande and Barigou, 2000, 2001a, 2001b). In the past two decades, foam flows in microfluidics have also gained significant attention due to excellent control of flow parameters such as liquid fraction,

bubble size and velocity and channel properties. A detailed literature review can be found in more detail in each of the results chapter (Chapter 4, 5 and 6).

In porous media, the flow of foam is often related to microchannel flow involving foams and single bubbles (gas slugs). The slugs were observed to undergo separation upon flowing through the smaller cross-sectional area (Kovscek and Radke, 1994). Instabilities which generate new foam include processes such as snap-off, lamella division and leave-behind. Each of these mechanisms ensures that the bubble lamella is regenerated so that the foam is not ceased due to, for example, rupture. Depending on the pore or obstacle that the foam or bubble must flow through as well as the system conditions, often one of the three mechanisms will occur. Illustrations and more detailed explanations can be seen below.

2.6.1 TOPOLOGICAL CHANGES

2.6.1.1 Instabilities in porous media

Snap-off

The snap-off break-up is a mechanical operation which involves the gas bubble such as slug to form a liquid collar around its neck as it passes through an orifice or a throat. This collar then increases in size and snaps the neck of the bubble at the throat, which results in the production of a new bubble. This mechanism is driven by the pressure difference when the gas enters the pore. At first, the front of the bubble enters the pore throat (Figure 2.7 (a)), as it passes through it, the front then expands (Figure 2.7 (b)). Because of the curvature difference between the gas part already in the throat and the rest of the bubble, there is a capillary pressure difference. This creates a pressure gradient of the continuous phase which pushes the liquid from the pore body into the throat and forces the collar to grow and snap as it can be seen in Figure 2.7 (c). The mechanism has been studied in constricted glass capillaries (Gauglitz *et al.*, 1988; Rossen, 2000; Roman *et al.*, 2017) as well as non-circular capillaries

(Ransohoff *et al.*, 1987). In more recent years, snap-off has also been introduced in microfluidics, in geometries such as three-dimensional step constriction (Wu *et al.*, 2017). However, the problem has been frequently studied in perfectly shaped constrictions, such as between two circles or through a gradual contraction. More geometries involving angled constrictions or longer throats could shed more light on fundamental understandings. Also, few studies have focused on bubble dynamics, such as neck variation and daughter bubbles which are addressed in this thesis. Snap-off, as well as the literature review, is discussed in more details in Chapter 4.
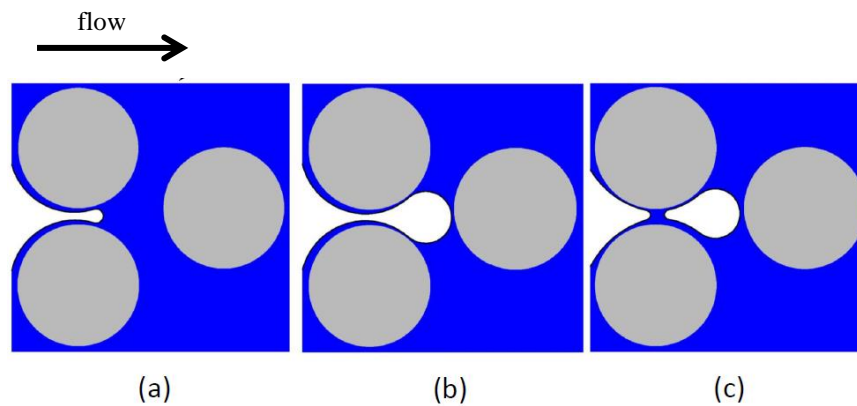
Figure 2.7   Illustration of the snap-off mechanism: a) gas invades the pore body, b) gas enters the pore body and c) wetting fluid moves back to snap-off the gas thread. Blue colour represents the continuous phase, white colour represents the dispersed phase, and grey colour represents the solid grains (from Almajid and Kovscek (2016)).

<u>Lamella division</u>

Lamella division may occur when foam consisting of bubbles larger than the size of the pore flows through a "branching point". This mechanism, in contrast to snap-off, cannot be regarded as a foam generation mechanism since the lamella must already exist in order to be divided, i.e. it has to flow as a single bubble or foam. A schematic of the lamella division can be observed in Figure 2.8. This instability has few requirements for it to occur, such as larger bubble size comparing to the pore volume, as well as other pores being free of other bubbles

so that gas can enter them. This type of break-up has been studied in foam-flooding experiments by Kovscek and Radke (2009), Ma *et al.* (2012) and Almajid and Kovscek (2016). Cox (2015) also studied a bamboo flow around single obstacles using Surface Evolver. He showed that even with the obstacle in the centre, the symmetry of the bubble is broken, thus, creating a non-symmetrical staircase that follows a structure based on how the very first bubble has been broken. However, the problem has not been thoroughly investigated in microfluidic channels for different foam regimes as well as various sizes of pores (obstacles). Lamella division through a single round obstacle in the centre and off-centre could better improve porous foam flow understanding, with regards to the sizes of the daughter bubbles. More complex channel involving few obstacles could also give information about foam formation in porous media. Chapter 6 will shed more light on this particular problem.
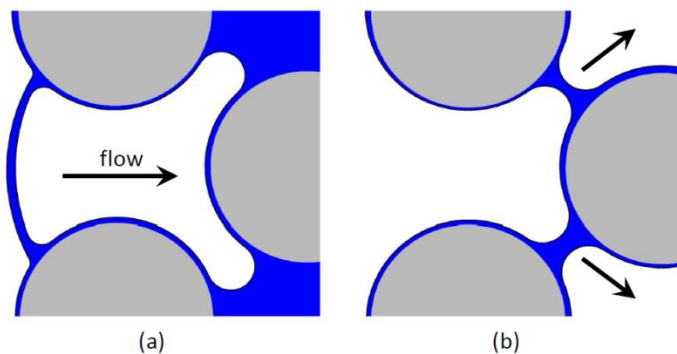
Figure 2.8 Illustration of lamella division mechanism: a) gas enters the "branching point", b) lamella is divided into two parts. Blue colour represents the continuous phase, white colour represents the dispersed phase, and grey colour represents the solid grains (from Almajid and Kovscek (2016)).

Leave-behind

The mechanism of leave-behind, as described by Ransohoff and Radke (1988), occurs when two bubbles flow through a pore, and then both of them coalesce to form one bubble and

leave behind a lens as it can be seen in Figure 2.9. This mechanism can also occur with a single gas slug wrapping around the obstacle or pore and squeezing the liquid into the lamella which is left behind. The left-behind lamella or lens is parallel to the direction of flow and because of that generates a "weak" foam according to Ransohoff and Radke (1988).
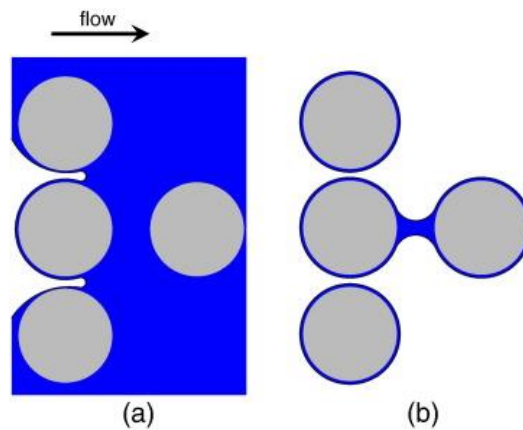
Figure 2.9 Illustration of leave-behind mechanism a) gas enters the body of the pore b) a stable left-behind lamella is formed. Blue colour represents the continuous phase, white colour represents the dispersed phase, and grey colour represents the solid grains (from Almajid and Kovscek (2016)).

2.6.1.2 T1 events

In flowing foams, one of the topological changes involves bubble rearrangement such as in two-dimensional shear flow presented below (Figure 2.10).
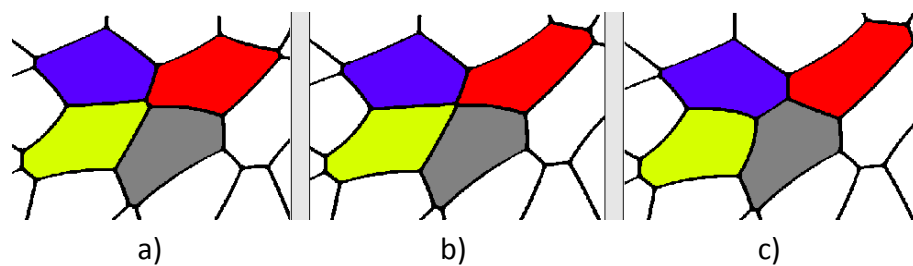
Figure 2.10 An illustration of a T1 event in a two-dimensional foam; a) at first red and yellow bubbles are in contact just before the T1; b) exact moment of the T1 occurrence (the edge disappears) c) blue and grey become adjacent bubbles after the T1 event (original images were taken from Dollet and Raufaste (2014) and modified).

Each bubble has a surface energy that can be found by adding its total interface area. Due to the elasticity of the foams, they store some elastic energy which is proportional to their surface. The so-called T1 event leads to saturation of the stored energy, which involves four bubbles interchanging their neighbours. In this process, one of the edges shrinks until it disappears and a new one is formed so that two bubbles which initially did not share an edge become neighbours (Figure 2.10). The expense of this process forces the other two neighbours to lose an edge and become more distant. Once the new configuration is established, the foam reaches its equilibrium state. This operation is another example of foams possessing a yield stress. The process of topological changes such as T1 events will be shown to occur in some examples and explained in more details in Chapters 5 and 6.

2.6.2 DIMENSIONLESS NUMBERS

In fluid dynamics, whether in Newtonian fluids such as water or complex such as foams, it is important to understand different forces acting on a fluid in the given system. Examples of the forces include viscous forces, surface tension forces, inertial forces and gravitational forces. Depending on the scale that is used in the experiments, some forces may be neglected such as gravitational forces on a micro-scale. However, in order to understand why gravitational forces can be neglected, it is crucial to calculate dimensionless numbers. These are the numbers that calculate ratios between different forces. Thus, applying dimensionless analysis to the flow problem that one is investigating, can suggest for instance, which forces can be neglected and which forces are dominant. Moreover, they can be used to scale up a system. The major dimensionless numbers related to this work are presented below:

Bond number

The Bond number (Bo) also known as the Eötvös number (Eo) is the ratio of the surface tension forces (capillary forces) to gravitational forces and is calculated as follows (Günther and Jensen, 2006)

$$Bo = \frac{\Delta \rho g L^2}{\sigma},$$

where $\Delta \rho$ is the density difference between the two phases, g is the gravitational acceleration, L is the characteristic length and σ is the surface tension. Large Bond number indicates that gravitational forces are dominant and thus, the surface tension has little to almost no effect on the system. On the other hand if the value of the Bond number is below 1, it indicates that the gravitational forces are negligible compared to the surface tension forces. Thus, in the micro-systems (such as the ones studied here), the typical characteristic length is below 1 mm. Since the dimensionless numbers are calculated using standard SI units, this produces a very low numerator (since the characteristic length needs to be multiplied by 10^{-6} to get metres and then squared) and therefore, a very small Bond number ($\ll 1$). In consequence, the gravitational forces are negligible when compared to the capillary forces.

Reynolds number

The Reynolds number is one of the most important dimensionless numbers in fluid mechanics since it indicates the type of flow in the system such as laminar (Re < 2100, flow is relatively ordered) or turbulent (Re > 4000, flow is more random or chaotic). The values of Re between 2100 and 4000 are considered a transition flow and can be a mixture of both flows. The Reynolds number is defined as the ratio of inertial forces to viscous forces and is calculated as follows (Reynolds, 1883)

$$Re = \frac{\rho U L}{\mu},$$

where ρ is the density of the fluid, U is the velocity of the flow, L is the characteristic length of the system and μ is the dynamic viscosity of the fluid. Since the characteristic length in the micro-flows is very small, similarly to the Bond number, the Reynolds number is often quite small. The typical Reynolds number in the experiments studied in this thesis was below 30, which suggest that the inertial forces are small and in some cases even negligible compared to the viscous forces. However, a localised Reynolds number based on for example the velocity of the flow in a small throat of the channel can be much larger and indicate that the inertial forces are important or even dominant over the viscous forces (van Hoeve *et al.*, 2011).

Weber number

The Weber number is another dimensionless quantity that can be found in fluid mechanics especially in multiphase flows where an interface between two fluids is present. It is the measure of the importance of the inertial forces to the surface tension forces and it is calculated as follows (Günther and Jensen, 2006)

$$We = \frac{\rho U^2 L}{\sigma},$$

where ρ is the density of the fluid, U is the velocity of the flow, L is the characteristic length of the system and σ is the surface tension of the fluid.

Capillary number

The capillary number is the most important dimensionless quantity in micro-flows such as in microfluidics or porous media. It compares the effects of the viscous forces (due to drag) and the surface tensions forces that act on the interface between two fluids. It is defined as follows (Shi *et al.*, 2018)

$$Ca = \frac{\mu U}{\sigma}.$$

Small capillary numbers indicate the importance and the dominance of the capillary forces ($<$ 10^{-5}), whereas at high capillary numbers the surface tension forces become negligible compared to the viscous forces. In the microfluidic flows, there is usually a competition between the two above-mentioned forces which makes the capillary number a crucial quantity. For example, the surface tension tends to minimise the surface area of a bubble inside a microfluidic channel. However, as the velocity is increased, the capillary number and therefore, the viscous forces, become important. In consequence, the shape of the bubble gets deformed by the friction of the liquid flow. In all of the experiments in this thesis, the capillary number is used to characterise different flows and behaviours of bubbles and foams and is therefore, the most import dimensionless number.

2.7 FOAM APPLICATIONS

As already mentioned in 2.1, applications of gas-liquid foams are numerous; they can be found in every household in cleaning and cosmetics products, or food and beverage products. Moreover, they are applied in many industries such as oil recovery (Rossen, 2000; Farajzadeh *et al.*, 2012), soil remediation (Kilbane *et al.*, 1997; Wang and Mulligan, 2004; Jones *et al.*, 2013), froth flotation (Hubbard, 2004; Pugh, 2005) or fire-fighting (Calvert, 1988; Gardiner *et al.*, 1998). It is also understood that gas-liquid foams are precursors for solid foams such as food, polymer, ceramic, metallic and concrete. The unique properties that put them ahead of other single-phase systems (e.g. water) or two-phase systems (e.g. emulsions) are listed below.

Expansion ratio

Since foams may have a small liquid fraction of the total volume, the expansion ratio can be substantial. This means that the total volume of the liquid of the foam is small compared to the total volume of the foam. It also means that gravity does not affect it as significantly as it

would a typical liquid of substantial density such as water. This characteristic is generally applied in the materials for fire-fighting technology and efficiently displacing oil from oil contained reservoirs (Stevenson, 2012).

Specific surface area

Specific surface area is defined as the total surface area of the total mass or volume. Foams possess relatively large specific surface area (Stevenson, 2012). This foam characteristic provides faster absorption and purification of gases and oils, which makes them a leading system in froth flotation such as separation of particles based on hydrophobicity (e.g. mineral processing or coal).

Yield stress

Foams possess finite yield stress, i.e. a stress has to be applied before they exhibit deformation. This makes foams useful in delivering drug agents or household cosmetic products, including shaving foam.

Foams are consistently found to have new industrial applications. More recently, foams have been found not only to work as a displacement fluid-like in the case of oil recovery but also as a carrier fluid that can deliver chemicals to unsaturated zones such as soils which motivated researchers to carry out more studies (Kilbane *et al.*, 1997; Chowdiah *et al.*, 1998; Wang and Mulligan, 2004; Zhang *et al.*, 2014; Géraud *et al.*, 2016). Foams can be used to extract polyaromatic hydrocarbons (PAHs) from the soil and/or to stimulate the biodegradation of PAHs. Moreover, the application of air injection and vacuum in conjunction with the use of foams provides mobility control/containment of the treatment zone which is not possible with surfactant flooding and, therefore, poses a reduced risk to groundwater contamination (Kilbane *et al.*, 1997).

In pharmaceuticals, foams have been used to deliver drugs and more recently to reduce and treat varicose veins by injecting foams into the veins. This treatment, also known as sclerotherapy allows efficient removal of varicose veins. This application motivated new studies (Tessari *et al.*, 2001; Ceulen *et al.*, 2010; Morrison *et al.*, 2010; Bai *et al.*, 2018) mainly due to the risk of side effects such as deep-vein thrombosis or phlebitis.

It has been highlighted that foams possess advantages over other systems such as their large expansion ratio and large specific surface area. They are, therefore, an interest in many applications. Interestingly, even though they are made out of gas and liquid, they behave as neither, which makes them a very unique and fascinating system. Their complexity, including their structure and metastability, brings together researchers from many branches of science, including chemistry, engineering and mathematics. Because of many foam applications and their complex dynamics, process improvement arising from experiments has the potential to generate savings, thus making foams still a popular research topic that is prominent in industry and academia.

3 EXPERIMENTAL MATERIALS AND METHODS

3.1 INTRODUCTION

This chapter presents the materials and methods used in this study. Explanation of how microfluidic channels were fabricated is explained, followed by illustrations of flow visualisation. Channel properties are described, explaining how bubbles/foams are generated in the flow-focusing junction. Various foam regimes that can be generated are also presented. The methods used for measuring foam properties, including liquid volume fraction and velocity, are illustrated.

3.2 MATERIALS AND METHODS

3.2.1 MATERIALS

The materials used in the experiments included: (i) an anionic surfactant Sodium dodecylbenzene sulfonate (NaDBS) supplied by Sigma Aldrich (98% purity), (ii) glycerol supplied by BDH (98.5% purity), (iii) compressed nitrogen gas oxygen-free supplied by BOC gasses.

Each surfactant solution in this study was prepared by dissolving NaDBS in distilled water or a mixture of water and glycerol, and was always used within two days. In between the experiments, the solutions were kept in closed containers in order to avoid surface tension increase due to evaporation. This allowed a comparison of the same liquid properties in various experiments. The concentrations of the surfactant were calculated based on their molecular weight with the critical micelle concentration of NaDBS in pure water being 0.44 g/L. Different concentrations of glycerol were added in order to vary the viscosity. Adding glycerol to the solution changed the amount of the surfactant that was required to reach the critical micelle concentration i.e. the amount of surfactant required increased with the increase

of the glycerol concentration. Tables with the corresponding liquid properties will be shown in each particular chapter.

3.2.2 SURFACE TENSION MEASUREMENTS

Every liquid solution in this work had its equilibrium surface tension (σ) measured via the du Noüy ring method technique using a tensiometer (Attension Sigma 701). In this technique, a platinum ring was submerged in the liquid and then very slowly lifted from the surface using an electro-balance. A force had to be applied to raise the ring from a liquid surface. The surface tension that was related to the required force was displayed on the computer software of the instrument. Each measurement was repeated 10 times and averaged with a measurement error of 3%. The measurements were carried out at room temperature (25°C). The corresponding surface tension values used throughout the experiments will be presented in each chapter.

3.2.3 LIQUID VISCOSITY MEASUREMENTS

The viscosity (μ) of the solutions was measured using a rotational rheometer (TA instruments HR2) with parallel plates (40 mm). This measurement was performed by measuring the viscosity of the solution at various shear rates (0-1000 s^{-1}). The required shear rates were obtained by changing the rotational speed of the top plate. Each shear rate had a 30 s equilibrium time before the measurement was taken. This allowed the shear stress to be constant at every measurement step. All the solutions used in this work were Newtonian. The viscosity was measured at 25°C with each test being repeated ten times. The error range was ±5%. The corresponding viscosity values used throughout the experiments are presented in each chapter.

3.2.4 FABRICATION OF MICROFLUIDIC CIRCUITS

The circuits studied in this chapter were firstly designed on AutoCAD, consisting of various channel lengths, widths and constrictions, ranging from the narrowest parts of 20 μm up to the widest of 840 μm. Once the designs were finished, they were then imprinted on a chrome transparent mask via Micro Lithography Services Ltd, UK.

The circuits were fabricated using standard soft lithography techniques (Duffy *et al.*, 1998). At first, 5 grams of SU8-2035 (MicroChem, Westborough, USA), a negative photoresist, was added onto a silicon wafer (d = 100 mm, Si-Mat, Germany) (Figure 3.1 (a-b)) and spin-coated at 3000 revolutions per minute (rpm). Negative photoresist means that the parts exposed to ultra-violet (UV) become cross-linked. In order to ensure the reproducibility of the channel depth, the moulds were fabricated in a clean room with controlled temperature and humidity. Unfortunately, the SU8-2035 degrades over time, which means that even though the surrounding environment was well controlled, there was a slight variance in channel depth over time. Once an even spread of photo-resist across the silicon wafer was achieved, it was soft baked for 5 minutes at 65°C followed immediately after by 35 minutes at 95°C. The photomask was then aligned with the silicon wafer (Figure 3.1 (b-c)) using a mask aligner and exposed to UV light for 2 x 40 seconds (Figure 3.1 (c-d)). There was a break between each 40-second exposure in order to prevent cracking of the photoresist. The silicon wafer then underwent further baking; 3 minutes at 65°C and 12 minutes at 95°C. Lastly, the channels were developed using SU8 developer (MicroChem, Westborough, USA) and cleaned with isopropanol (Sigma Aldrich, UK). A master mould was created using the above procedure, which could be reused for microfluidic channels (Figure 3.1 (d)).
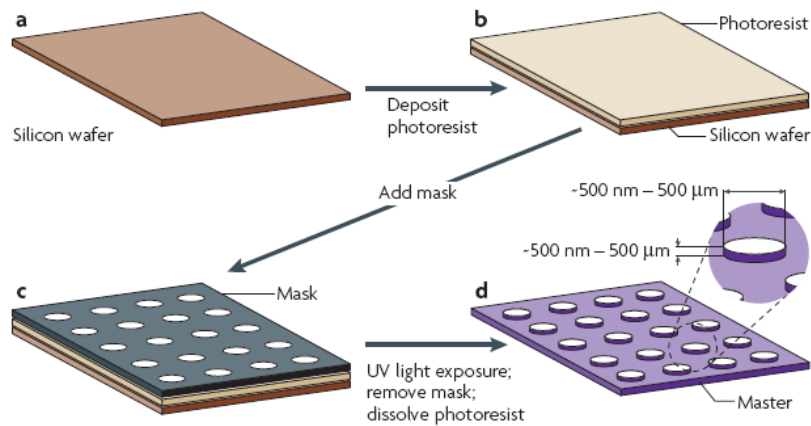
Figure 3.1 A diagram explaining the main steps of fabricating microfluidic channels (image taken from http://www.elveflow.com/wp-content/uploads/).

Once the master was produced on the silicon wafer, as described above, it was then glued to a petri dish so that it could serve as a mould for poly(dimethylsiloxane) (PDMS). An elastomer kit (Sylgard 184; Dow Corning Corp) was used to fabricate the final channels. The kit mentioned above included a liquid silicone elastomer base (vinyl-terminated PDMS) and a curing agent (a mixture of a platinum complex and copolymers of methylhydrosiloxane and dimethylsiloxane). The two liquids were mixed (10:1 ratio) and poured over the master mould. The petri dish full of PDMS mixture was then degassed under vacuum until there were no visible bubbles on it. The wafer was then cured in the oven at 70°C for approximately 90 minutes in order to harden the PDMS and left overnight at room temperature to be used the following day. The PDMS channel was then carefully cut with a knife so that the mould would not get damaged. Each channel was then peeled from the master serving as the top layer of the microfluidic device. Inlet and outlet holes were punched using a biopsy punch (1.5 mm, Miltex by Kai). The PDMS, together with a glass slide, was then oxidised (plasma-treated) using a corona discharge (BD20ACV, Lab Treater, Electro-Technic Products, USA) for about 40 seconds each. This ensured irreversible bonding once the two were brought in contact which each other resulting in the glass slide sealing the channels. PDMS is well

known as being hydrophobic, and even though oxidising can change its wettability characteristic, it is only a temporary solution. The PDMS retrieves its characteristics within 5 min of the treatment. It was, therefore, necessary to inject a surfactant solution within 2 min of bonding so that the liquid could absorb onto the PDMS surface while it was hydrophilic. Leaving the microfluidic device immersed in water overnight ensured correct wettability for the gas-liquid flow, which lasted approximately for 8-10 hours.
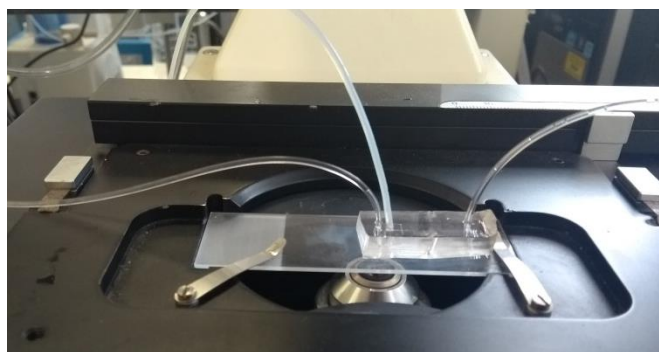
Figure 3.2 Image of a microfluidic device placed on a microscope. On the left a silicone tube connected to a liquid inlet and a Teflon tube connected to a gas inlet. On the right, a tube connected to the outlet.

3.2.5 FLOW VISUALISATION

The microfluidic device (Figure 3.2) investigated was placed on a Zeiss Axiovert 200m inverted microscope in order to visualise the flow and adjust the light intensity (Halogen light Zeiss) that was necessary for observation. The microscope had a high-speed camera (Photron Mini AX100) mounted on the side of it, capable of achieving 514000 frames per second (fps) at its smallest resolution (128 pixels × 16 pixels). The camera shutter, as well as the frame rate (4000 – 60000 fps), were chosen according to the desired flow-rate. Bubble break-up time, as well as the neck decline, was captured at a much higher frame-rate (30000 fps – 170000 fps), also chosen according to the desired flow-rate. The light from the microscope shines on the channel vertically, so it is bright (grey in here) at the centre of each bubble. However, the rest of the bubble is dark because the light is radiated to the outside of the

microchannel through refraction and total reflection. The curved interface of each of the bubbles is, therefore seen as black, as shown in Figure 3.3.
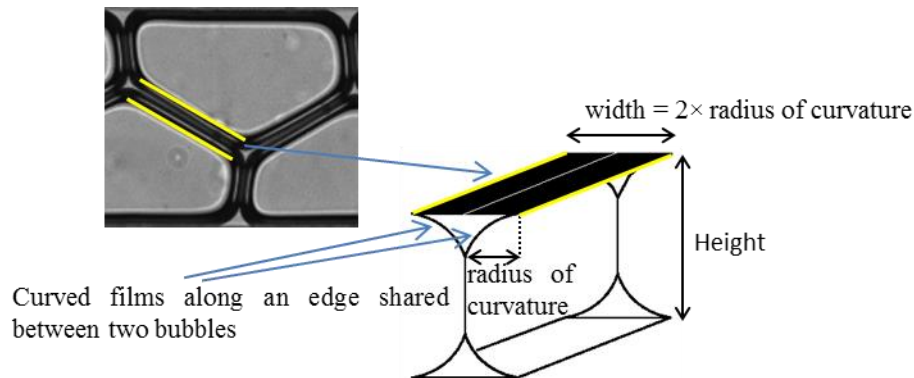
Figure 3.3 A schematic of the edge shared by two bubbles. The width between two bubbles, which is seen as black from above (between the yellow lines) corresponds to two curved interfaces, one from each bubble.

3.2.6 CHANNEL PROPERTIES

Each microfluidic device used in this study was composed of two main parts: (i) the left part of the device responsible for generating the foam which included gas and liquid inlets as well as branches which meet at the flow-focusing junction, (ii) the right part of the device was the part that was experimentally studied, consisting of either a constriction or expansion (Chapters 4 and 5) or obstacles (Chapter 6) located between 5 to 8 mm downstream of the flow-focusing junction. The distance between the flow-focusing junction and the area of interest (constriction/obstacle) was chosen to be relatively long so that the pressure drop across the constriction or obstacle would not affect the bubble generation. The dimensions of the flow-focusing channels were kept constant for each chapter (unless stated otherwise) in order to study the same foam or bubble type. Schematic of the channel is shown in Figure 3.4. The dimensions of the flow-focusing part and constriction (or obstacle) are specified in each corresponding results chapter.
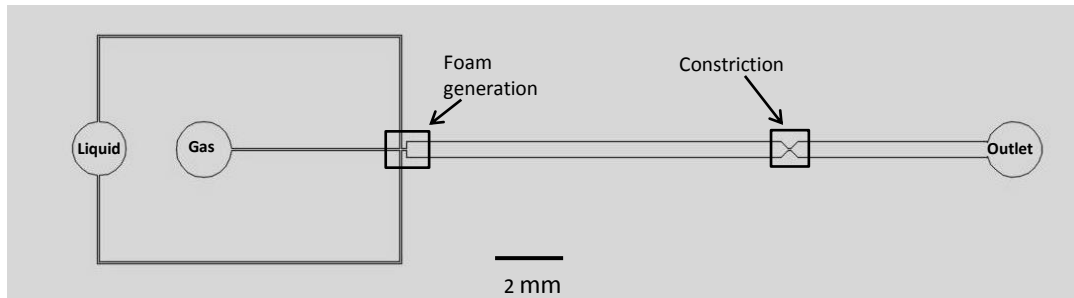
Figure 3.4 The schematic of the circuit (from Chapter 5). The liquid and gas inlets are located on the left-hand side, as well as the highlighted flow-focusing part (Figure 3.5 (a)). While on the right-hand side, the main channel with the highlighted constriction (Figure 3.5 (b)) are located, followed by the outlet.
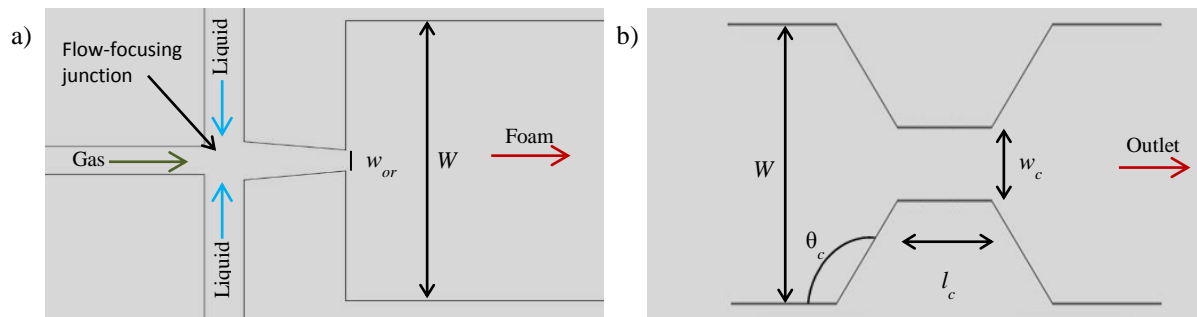
Figure 3.5 The highlighted sections of Figure 3.4: a) the flow-focusing part, b) the constriction. In (a) gas is injected through the centre channel whereas the liquid through the outer channels. Both of the phases meet at the flow-focusing junction where they generate a bubble through the orifice and displace it into the main channel downstream of the flow-focusing junction. In (b) an example of a gradual constriction is presented showing the relevant constriction dimensions: width (w_c), length (l_c) and angle (θ_c).

3.2.7 FLOW-FOCUSING

The flow focusing device can be seen in Figure 3.5 (a). This technique has been widely used in microfluidic systems (Garstecki *et al.*, 2004; Raven *et al.*, 2006; Raven and P. Marmottant, 2007). The method can generate various bubbles as well as foams by simultaneously injecting gas and liquid phases and manipulating their pressures or flow-rates. In this study, the liquid phase was injected through the outer channels as indicated by the blue arrows in Figure 3.5 (a). The dispersed phase was Nitrogen gas injected through the inner channel (green arrow in

Figure 3.5 (a)). Both of the phases were controlled through a pressure controller (Elveflow OB1 0-2000 mbar) with the liquid phase being passed and measured through a flow-meter (Elveflow 1 -1000 μl/min) and gas phase through a volumetric gas-flow meter (Bronkhorst). The flow diagram of the experimental setup is seen in Figure 3.6. The two phases met at the junction near an orifice just before the main channel. By adjusting both of the pressures accordingly, various foam regimes were obtained, including a wide range of bubble volumes (V_b) and liquid volume fractions (ϕ_L). The aspect ratio (Λ_t) of the orifice width (w_{or}) to the width of the channel (*W*) was kept constant ($\Lambda_t = 13.5 \pm 0.5$) for most of the channels except for the channels that generated slug bubbles ($\Lambda_t = 1$).
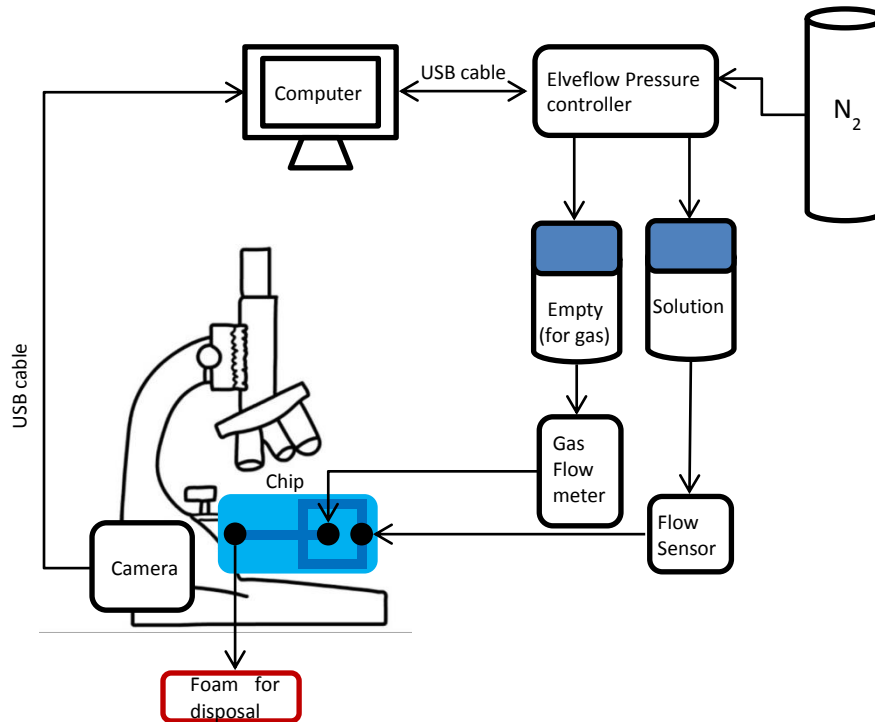
Figure 3.6 Flow diagram of the experimental setup used in this thesis.

3.2.7.1 Bubble generation

The liquid injected through the outer channel at a desired flow-rate (Q_L) generates a pressure drop that forces the liquid to flow through the orifice into the main channel. By then introducing the gas at constant pressure (P_G), the gas stream pushes the liquid through the

orifice into the main channel creating a cavity which is simply a bubble. This cavity then expands until a neck in the throat is formed, which is pushed by the surrounding liquid. The liquid forces the neck to narrow so much that a bubble is pinched-off and released into the main channel downstream of the throat. Consequently, the tip of the gas stream retracts due to surface tension forces and repeats the process, generating either dripping bubbles or foam structures. This method allows producing monodisperse bubbles (dispersity index < 10%), which significantly reduces coarsening as there is minimal gas diffusion in between the neighbouring bubbles based on the Laplace pressure. The resulting images of the bubble generated via pinch-off can be seen in Figure 3.7.

The bubble pinch-off in microfluidic systems has been studied before by Garstecki *et al.* (2006), Dollet *et al.* (2008), van Hoeve *et al.* (2011) and Lu *et al.* (2014). Dollet *et al.* (2008) have shown that the neck (w_n) of the bubble collapses in two stages; both being related to the channel dimensions. Depending on the aspect ratio of the throat to the channel height (*H*), the neck could either narrow linearly with time or non-linearly. The linear collapse occurs in cases when the neck is larger than one of the orifice dimensions. For instance, if the orifice is 40 μm wide with a height of 20 μm, the neck will decrease from 40 μm to 20 μm linearly with respect to time, because it is only pushed by liquid from its sides as shown in Figure 3.7. This is called a 2D collapse (Dollet *et al.*, 2008) as the neck is pushed only from the transversal direction. Once the neck reaches a width of 20 μm, it can now be pushed from all directions since its width is equal to or smaller than both the width and the height of the throat. This 3D collapse is non-linear, collapsing much faster in the very final stage, as shown by van Hoeve *et al.* (2011). At first, it was assumed that the fast diminishing of the neck could be due to Bernoulli suction (Dollet *et al.*, 2008). However, investigations made by van Hoeve *et al.* (2011) highlighted that the fastest collapse is exclusively due to liquid inertia and the neck

becoming less slender, which means that the axial radius of curvature decreases faster than the circumferential radius of curvature.

t = 0.00	t = 0.16	t = 0.24	t = 0.40
t = 0.56	t = 0.76	t = 0.89	t = 0.94
t = 0.97	t = 0.98	t = 0.99	t = 1.03
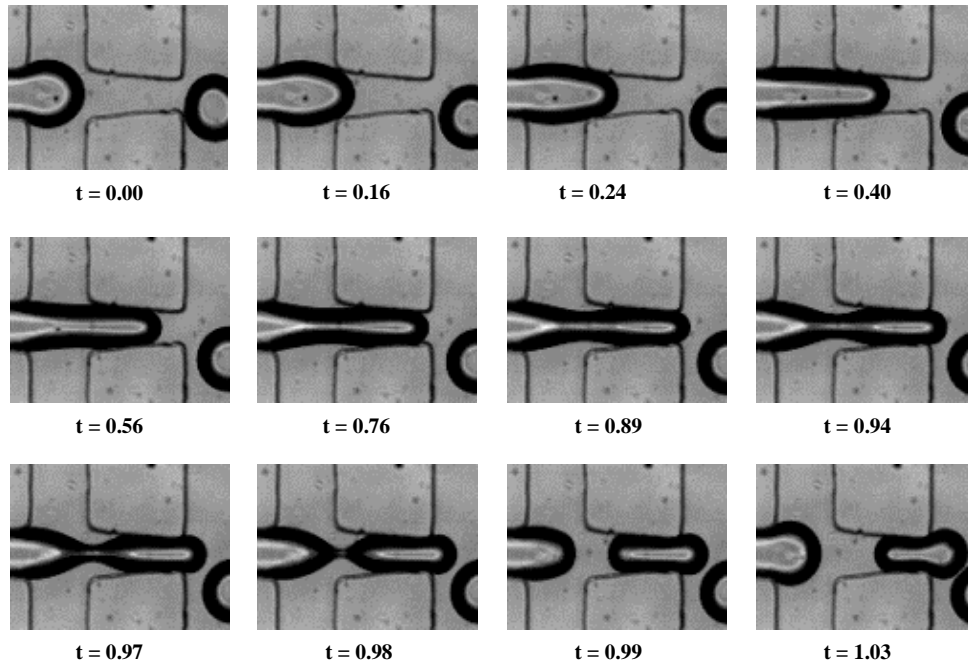
Figure 3.7 Consecutive sequence of images of bubble pinch-off in the flow-focusing junction used in Chapter 5, *t* is in milliseconds.

The throat used in Chapter 5 (w_{or} = 30 μm) was always smaller than the channel height (H = 45 μm). Hence, only a 3D non-linear collapse was expected in the study. However, at low gas pressures bubbles were pinched upstream of the actual throat which produced a linear decrease. A graph showing the neck decrease with time is presented in Figure 3.8. It can be noticed that the fast neck decrease occurs at 45 μm which is the depth of the channel. The corresponding dimensions of the flow-focusing devices that were used throughout the experiments are shown in each chapter.
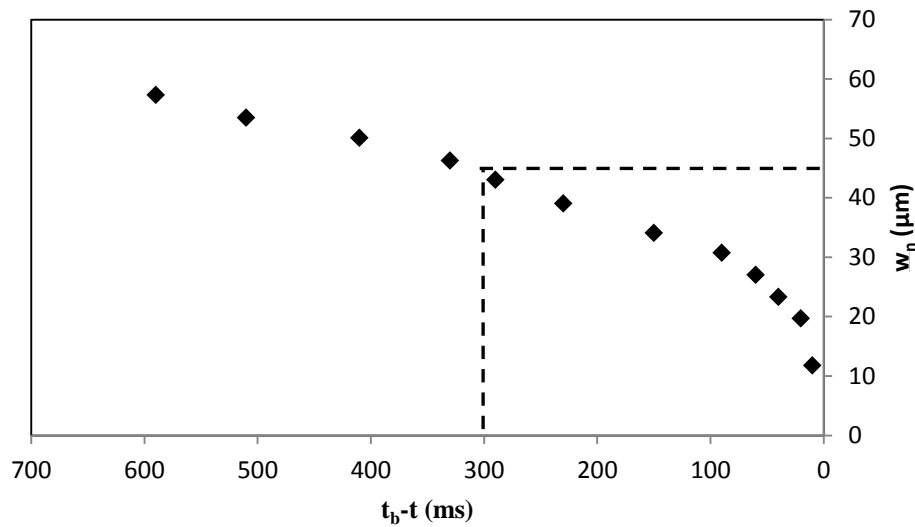
Figure 3.8 Plot of the neck decrease with time. Notice two different stages of the collapsing neck, with the change at 45 μm which is the depth of the channel.

3.2.7.2 Foam regimes and bubble size

The channel dimensions are the most crucial parameters in the microfluidic system responsible for bubble pinch-off, as explained above. Moreover, the aspect ratio of the width orifice to the channel width is also responsible for the bubble volume achieved. Bubbles generated in the microfluidic devices have been well researched by Raven and P. Marmottant (2007) and later by Vuong and Anna (2012), who identified various structures such as dripping, alternating, slugs and bamboo foams.

For each liquid pressure (P_L), there is a minimum gas pressure (P_{MIN}) that is required for the gas stream to penetrate the orifice. This is most likely due to capillary effects, as reported previously by Raven, Marmottant and Graner (2006). By keeping the liquid pressure constant, a full range of bubbles and foam structures can be visualised.

Slug bubbles

Single slug bubbles were generated in the same way as the foams. However, the dimensions of the flow-focusing throat were the same as the main channel, i.e. all the channels were of the same size (200 μm) with an aspect ratio of 1 ($\Lambda_t = 1$). At higher ratios of the liquid

pressure to gas pressure ($P_L/P_G > 1.20$), almost spherical bubbles were obtained (Figure 3.9 top). By keeping the liquid pressure constant and increasing the gas pressure, the size of the bubble increased as well as the frequency. Examples of slug bubbles generated can be seen in Figure 3.9 below.
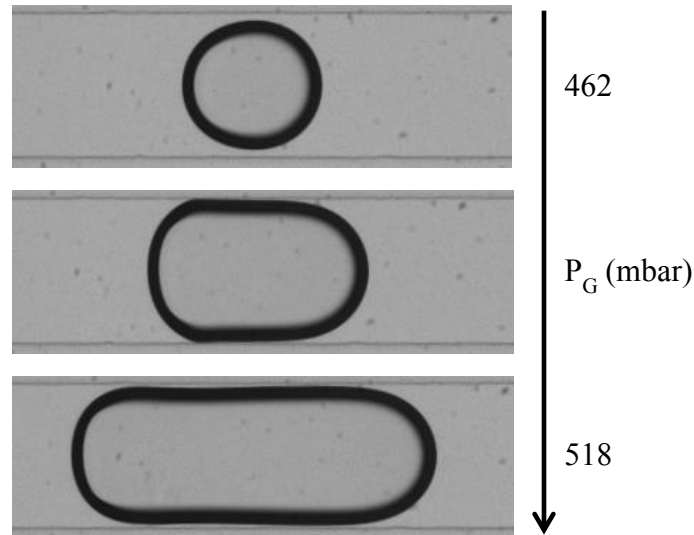
Figure 3.9 Examples of three slug bubbles generated at constant liquid pressure (575 mbar).

The bubble size was calculated based on the videos captured in the upstream section of the constriction using ImageJ (Schneider *et al.*, 2012). From each video, 5 to 10 bubbles were analysed in terms of the bubble size. The bubbles had a very monodisperse distribution (dispersity index < 5%). The images were converted to black and white so that the gas part was displayed as white, while the curved interfaces appeared black. The white gas part was then filled using "fill holes" plugin so that the total bubble appeared black. The size of each bubble was recorded and then averaged out to give an average size of the condition investigated. Using "analyse particle" tool in ImageJ, full data sets (bubble area, bubble position and bubble length) were obtained for different conditions investigated.

Foams

At first, when P_G has reached P_{MIN}, small dripping bubbles at low frequency are observed (Figure 3.10 (a)). Increasing P_G further, results in the increase of the frequency of the bubbles generated as well as their size (Figure 3.10 (b-d)). The bubbles eventually start being closely packed and produce foam structures, as shown in Figure 3.10 (e-h). Depending on the initial bubble size, the foam structures can span the width of the channel either having more than three bubble rows, three bubble rows, two bubble rows or a single bubble row also known as bamboo. Throughout the rest of this study, each foam regime will be referred to either as >3-row, 3-row, 2-row (or staircase) or 1-row (or bamboo).
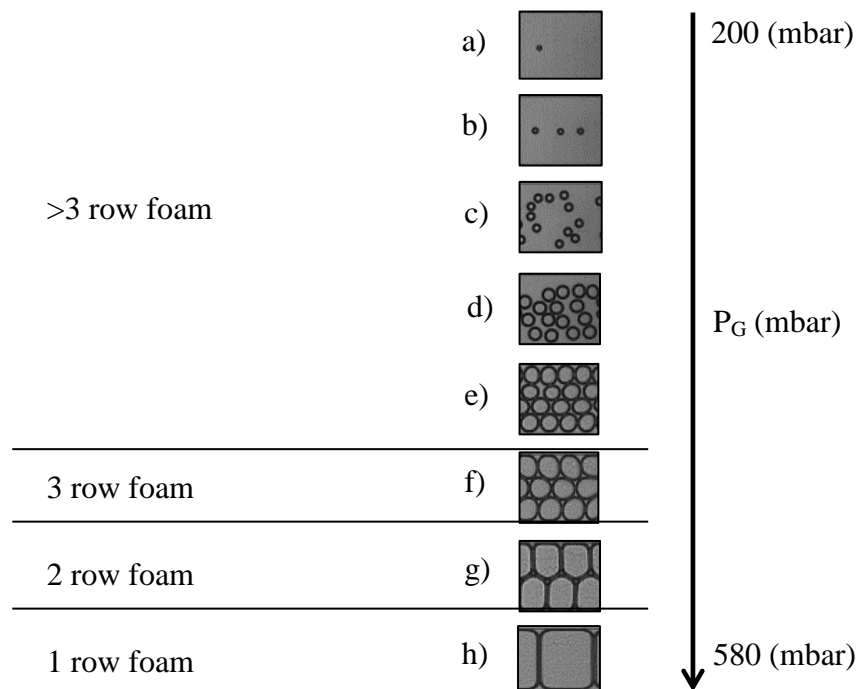
Figure 3.10 Schematics of foam regimes and bubble sizes at constant liquid pressure (550 mbar) in this example. Images (a-e) refer to > 3-row foam, (f) to 3-row foam, (g) to 2-row foam and (h) to 1-row foam.

The average bubble size downstream of the flow-focusing throat was obtained using ImageJ by analysing between 500-1000 frames. A portion of an image was taken upstream of the constriction/obstacle, and the images were converted into black and white using the auto-

threshold function. The error was found to be ≤ ±1 pixel (i.e. ±2 μm). The gas area was visualised as white. The images were then tracked using a morphology plugin that calculated the white round area of the gas part of each bubble. Sometimes minimum and maximum limits had to be manually inserted in order to avoid including liquid areas in between the bubbles. The average size was calculated only from images that did not overlap so that the same bubble was not considered more than once.

3.2.8 FOAM LIQUID FRACTION

One of the most crucial parameters in foam systems and applications is the liquid volume fraction, also called liquid hold-up. It is defined as the ratio of the liquid volume to the total foam volume, including gas and liquid. In microfluidics, there are two different foam liquid fractions. The inlet liquid fraction (ϕ_{or}) based on the two flow-rates and defined as

$$\phi_{or} = \frac{Q_L}{Q_G + Q_L}, \tag{3.1}$$

where Q_L is the liquid flow-rate, and Q_G is the gas flow-rate. Foam liquid hold-up can also be calculated from the images by analysing the area occupied by the plateau borders and the liquid films between bubbles. This is defined as the volume of a bubble as follows

$$\phi_{ch} = \frac{V_L}{V_G + V_L}, \tag{3.2}$$

where V_L is the volume of the liquid and V_G is the volume of the gas. Notice that $\phi_{or} \neq \phi_{ch}$ because the two injected phases (liquid and gas) can have different velocities. The volume of the liquid of each bubble consists of the horizontal plateau borders (V_{Hpb}) (liquid fraction along the curved perimeter of the bubble) and the vertical plateau border (V_{Vpb}) (liquid fraction shared between three or two bubbles along the height of the bubbles).

The liquid fraction between two neighbouring bubbles is the area (A_{Hpb}) contained by the curved interfaces denoted as horizontal plateau border (green in Figure 3.11) and can be

calculated as follows $A_{Hpb} = \frac{1}{2}(4 - \pi)\left(\frac{W_{pb}}{2}\right)^2$ (Vitasari and Cox, 2017) where W_{pb} is the width of the discussed plateau border. Now each such edge is shared between two bubbles. Thus, half of it belongs to one bubble. The total volume of the horizontal plateau border of one bubble is; therefore, half of the area (A_{Hpb}) multiplied by the perimeter of the bubble (l_b) and then multiplied by two since each bubble has horizontal liquid fraction at the top plate as well as the bottom plate, hence

$$V_{Hpb} = \frac{1}{2} \times A_{Hpb} \times l_b \times 2 = A_{Hpb}l_b. \tag{3.3}$$
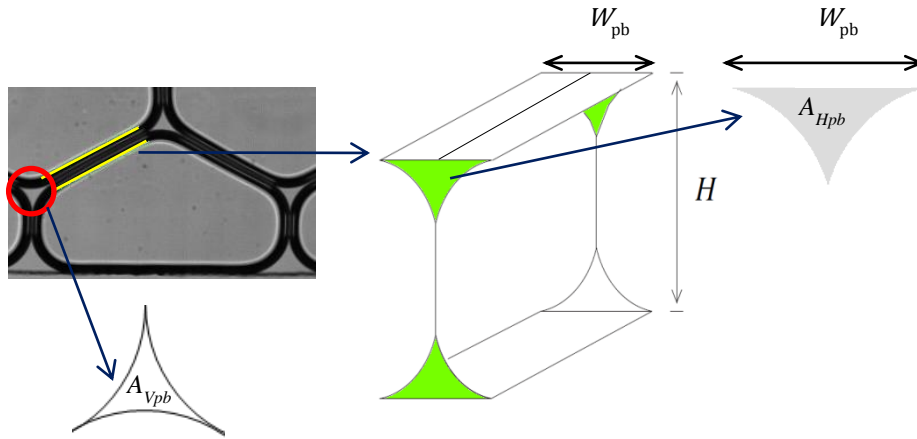
Figure 3.11 Schematic of plateau borders of a bubble in a microfluidic channel: the horizontal plateau border is the area confined by two curved interfaces along the edge, whereas the vertical plateau border is the vortex where three bubbles meet.

The vertical plateau border, however, is shared between three bubbles if in bulk or two if near the wall. Thus, it varies between different foam regimes. Small bulk bubbles may have six of the vertical plateau borders, whereas larger bubbles can have three bulk plateau borders and two at the wall as seen in the example of staircase foam in Figure 3.11. The volume of one such plateau border is evaluated by multiplying the area of it A_{Vpb} (which can be calculated as follows $A_{Vpb} = \left(\sqrt{3} - \frac{\pi}{2}\right)\left(\frac{W_{pb}}{2}\right)^2$ (Vitasari and Cox, 2017)) by the height of the

channel. Assuming a bulk bubble with six vertical plateau borders, the total volume has, therefore, six such volumes, each shared by three bubbles, thus

$$V_{Vpb} = \frac{1}{3} \times 6 \times H \times A_{Vpb} = 2HA_{Vpb}. \qquad (3.4)$$

The liquid volume fraction based on the images, however, often underestimates the actual value. As mentioned earlier, the two phases can have different velocities, and it is not visible to the eye of the camera how much liquid is flowing above/below the bubbles as well as around them. It is, therefore, more accurate to use the initial liquid hold-up based on the two flow-rates. However, the channel liquid fraction was used in most of the analysis in Chapter 6 due to small liquid flow-rates injected that were difficult to measure.

Since the single bubbles investigated in this work (Chapter 4) were flowing as single cells surrounded by large proportions of liquid, the liquid volume fraction was relatively large. Moreover, because the frequency of the bubbles generated was relatively small, the measured gas flow-rate fluctuated a lot, making it very difficult to measure it. The volume liquid fraction is, therefore, not taken into account in Chapter 4.

3.2.9 VELOCITY MEASUREMENTS

In two-phase foam systems in microfluidics, two different velocities can be used. Since the channels are rectangular, and bubbles follow the law of minimising the surface energy and therefore, taking the smallest shape they can, liquid fractions are flowing in the corners of the channels at their own velocity. The average liquid velocity (U_L) can be calculated as a superficial velocity based on the two flow-rates as well as the cross-section of the channel as follows

$$U_L = \frac{Q_L + Q_G}{W \times H}, \qquad (3.5)$$

where Q_L, Q_G, W and H are the liquid flow-rate, gas flow-rate, channel width and channel height, respectively.

Another velocity that can be measured and was used in the analysis of all of the experiments is the bubble or foam velocity extracted directly from the sequence of images. Details are presented below.

Slug Bubbles

Since the focus in Chapter 4 is on a single cell rather than bulk foam, using ImageJ the position of a centre of a bubble was recorded at two different locations in the upstream channel. This allowed a simple calculation of a distance travelled between the two images in pixels and then converted to microns using a scale bar from an image. Subsequently, time was calculated between the two images, based on a frame rate the video was recorded. The distance the bubble travelled was then divided by the time calculated to give the velocity of a bubble. The velocity of five bubbles was measured for each video and then averaged out with an error of less than 3%.

Foams

The average foam velocity was calculated based on the movement of bubbles between two consecutive frames. Matlab software was used to calculate the average foam velocity, more specifically, PIVLab. This software tracks the movement of edges and vortices between two consecutive images and then averages them out. The calculation is based on the interrogation windows chosen by the user, which analyses the movement of the edges/vortices in that particular window (Figure 3.12). The size is chosen depending on the size of the edges as well as the frame rate. A few interrogation regions can be chosen at the same time so that the largest window can capture the highest velocity, while the smallest region can capture the smallest movement and therefore, lowest velocities. The software also enables plotting

contour plots of velocity fields, vectors as well as streamlines. For the majority of time, only the foam velocity (U_f) upstream of the constriction/obstacle was recorded since the software often underestimated velocities in the centre of the constriction, especially at the highest flow-rates. The number of films and vertices in the constriction was too small and flowing too fast to obtain precise values of the velocity. Additionally, bubble break-up also affected those calculations.
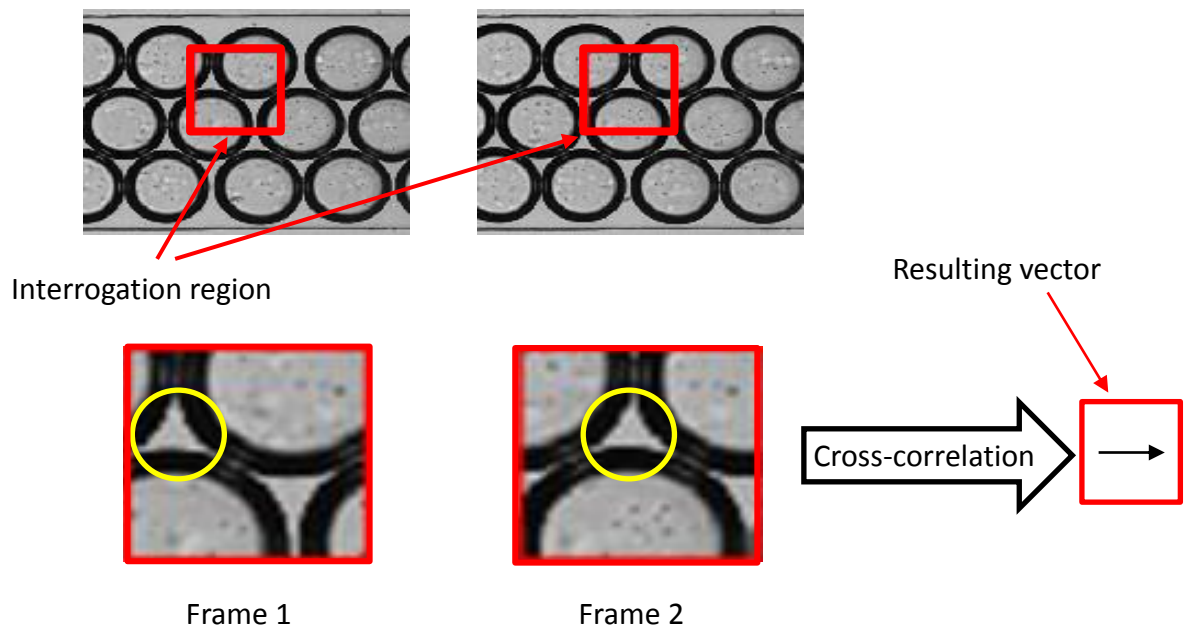
Figure 3.12 Illustration of how PIVLab calculates the resulting velocity vector between two consecutive frames. Curved interfaces that confine the highlighted plateau border move horizontally between the two frames, which produce a horizontal vector.

4 SINGLE BUBBLE FLOW IN MICROFLUIDIC CHANNELS WITH CONSTRICTIONS

In this chapter flow of *in situ* generated single bubble through microfluidic channels with constrictions is presented. Microfluidics was chosen due to possessing many advantages over large laboratory equipment and allowing good visualisation. Local deformation of small bubbles is analysed with regards to velocities between the front tip and the rear tail, as well as, compression and elongation of a bubble at a particular position along the constriction. The problem of a single bubble through a sudden or a gradual contraction/expansion is studied in order to shed some insightful light on snap-off with regards to break-up time, neck variation and daughter bubbles. Additionally, the effect of the shape of the constriction on snap-off is also highlighted. Wide range of capillary number is used for most of the problems by varying the liquid viscosity and velocity.

4.1 INTRODUCTION

Gas slugs, as well as single bubbles, can be precursory to studies of flowing foams. Single bubbles can improve understandings of foam dynamics including instabilities and behaviour of particular bubble parts in a similar way to studying single soap film (Barigou and Davidson, 1993) which shed some insightful light on the disjoining pressure of thin films as well as the behaviour of plateau border and capillary suction.

The bubbles have been studied in tubes and capillaries by researchers as early as 1961 (Bretherton, 1961; Taylor, 1961). Bretherton studied two cases of a long bubble in capillaries with a zero contact angle at a wall. One of the problems undertaken by him was the flow of long bubbles in a tube of small radius pre-filled with a viscous fluid. The diameter of the tube was small so that the gravity effects were negligible, a bubble propagating through such

capillary deposits a thin film of the fluid on the wall. Based on his lubrication theory he found that some of the parameters (e.g. pressure drop along the bubble) were dependent on the capillary number (Ca) which is the ratio of viscous to surface tension forces. Most importantly, he calculated that the thickness of the wetting fluid was proportional to $Ca^{2/3}$ in the limit of small capillary number (Ca → 0). Those results were found to be in agreement with the computer simulations (Singh *et al.*, 1997) and experiments of bubbles in microfluidic channels (Chen *et al.*, 2015). The results were later extended to rectangular axisymmetric channels in the range of small capillary numbers (Wong *et al.*, 1995a) and numerically (Hazel and Heil, 2002). Hazel and Heil (2002) showed that as the cross-section changes from a square to a rectangular (Width/Height > 1) the thickness of the film is not uniform along both of the axes of the channel. Along the longer semi-axis, the thickness is greater, and the difference of the film thickness increases with the capillary number as well as the ratio of the channel width to height.

The problems of gas slugs through constricted capillaries found more interest due to enhanced oil recovery application and, therefore, larger interest in understanding the mechanism that drives the foam generation/regeneration in porous media. Since foams can flow as single lamella in porous media, studying long slugs of bubbles in constricted capillaries could give insights to break-ups and criterions for them. This reason alone picked up interest from Roof (1970) who investigated trapping oil drops in porous media and identified snap-off as the primary mechanism in the break-up process of droplets and bubbles. He showed that as the droplet travels through a constricted capillary, the curvature of the bubble is larger at the throat of the constricted tube when compared to the unconstricted sections. Hence, the capillary pressure (defined as the difference between gas and liquid pressure i.e. $P_c = P_G - P_L = \frac{2\sigma}{r_b}$ where r_b denotes a bubble radius at any given point) is greater

at the throat than anywhere else along the droplet or bubble. This pressure difference along the interface allows the liquid to invade the throat of the constriction and snap the non-wetting fluid into smaller daughter droplets (or bubbles).

Subsequently, gas slugs and snap-off gained more attention as a porous media foam generation mechanism with studies carried out in square capillaries with constrictions (Gauglitz *et al.*, 1987), smoothly constricted non-circular capillaries (Ransohoff *et al.*, 1987) and constricted cylindrical capillaries (Gauglitz *et al.*, 1988). Gauglitz *et al.* (1988) correlated many parameters, including liquid rheological characteristics, constriction shape and break-up time. According to their mathematical model, the break-up time should decrease with the capillary number to the power of -2. Experiments in a wider throat confirmed those results, whereas in a narrow throat the results applied to bubbles above the critical capillary number. Below the critical capillary number, the bubbles were dependent on the Ohnesorge number, which relates the importance of viscous forces to inertial and surface tension forces. In the square capillary (Gauglitz *et al.*, 1987), the results varied from those obtained in the cylindrical capillary, since the thickness of the thin liquid films is smaller than the liquid in the corners of the channel. The break-up time was therefore found to be weakly dependent on the capillary number; instead, it was the constriction geometry that was crucial.

In general, snap-off was found to occur when capillary pressure was large enough so that the gas would invade the constriction but then decrease so that the liquid could re-enter the throat. In the cylindrical constriction (Roof, 1970) as well as beadpacks (Falls *et al.*, 1988) it was shown that the capillary pressure at the throat has to drop by 50% to initiate snap-off. Rossen (2000) explained different mechanisms when the capillary pressure could fall so that snap-off may occur including liquid saturation, pressure fluctuations in between trains of bubbles, or in a narrow constriction when liquid drains back into the constriction.

More recently snap-off was also studied (Wu *et al.*, 2017) in the microfluidic channel through a sudden constriction involving a step (Figure 4.1) so that a single bubble had to flow through a constriction with a narrow width, length as well as height. They found that the bubble size distribution was decreasing with the increase of the capillary number, with the newly formed bubbles being often smaller than the previously formed bubbles.
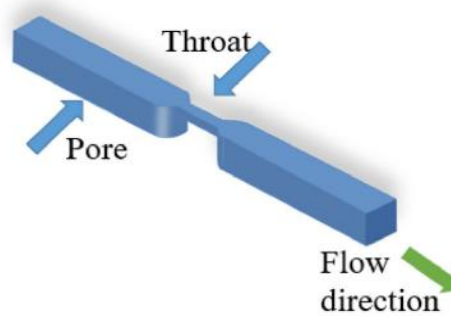
Figure 4.1 Illustration of the 3D constriction studied by Wu *et al.* (2017).

There is still a lack of fundamental understanding of bubbles and their dynamics near the constriction and the effect of the capillary number on the elastic strain (i.e. elongation/compression) and velocities of particular bubble parts. By understanding bubble deformation of a single bubble and the effect of the capillary number on it, those results can be incorporated into various models of bulk foams in porous media where the foam can flow as single bubbles or gas slugs (Falls *et al.*, 1988).

This chapter will also shed light on the break-up time of bubbles in rectangular channels with constrictions. In the literature the focus was always on the square and cylindrical capillaries which do not represent well the porous media, i.e. they are often irregular thus; rectangular channels should give better insights to snap-off in porous media. In addition, dimensionless analysis is applied to the neck collapse before snap-off and suggests that inertial forces are crucial in the final stages of snap-off. Such results have not been previously reported in the literature for snap-off, thus this is the first study that reports this novel finding.

4.2   CHANNEL AND SOLUTIONS PROPERTIES

Two different channel dimensions were used in this chapter: (i) the first one was used for the generation of small bubbles that did not undergo any break-up (Figure 4.2 (a)), the flow-focusing dimensions can be seen in the highlighted part, (ii) the second one was used for the slug bubbles, a much wider flow-focusing channel was used (Figure 4.2 (b)) with the flow-focusing part of the same width as the primary channel (200 μm in this case). This was necessary to generate large gas bubbles. The former channel had a depth of 40 μm which was the same as the constriction width so that bubbles would flow through a constriction with a square cross-section. The latter channels had a depth of 60 μm. The dimensions of the flow-focusing channels were kept constant in order to study the same type of slug/bubble. Each constriction investigated is shown in the relevant results/discussion section.

Liquid solutions used in this chapter are shown in Table 4.1 and Table 4.2 for the first part (4.3.1) and for the second part (4.3.2), respectively. The viscosity was modified by adding glycerol at different concentrations in order to increase the initial value of the capillary number ($Ca = \frac{U_f \mu}{\sigma}$ where U_f, μ, σ are the foam velocity, solution viscosity and surface tension, respectively). The capillary number was also varied for each of the solutions by changing gas/liquid pressures and, therefore, the velocity of the flow. In addition, adding glycerol to the solution increased the surface tension value by up to 3 mNm[-1], however, as mentioned above the majority of the analysis was carried out with regards to the capillary number and, hence, any variations in the value of the surface tension were already considered.
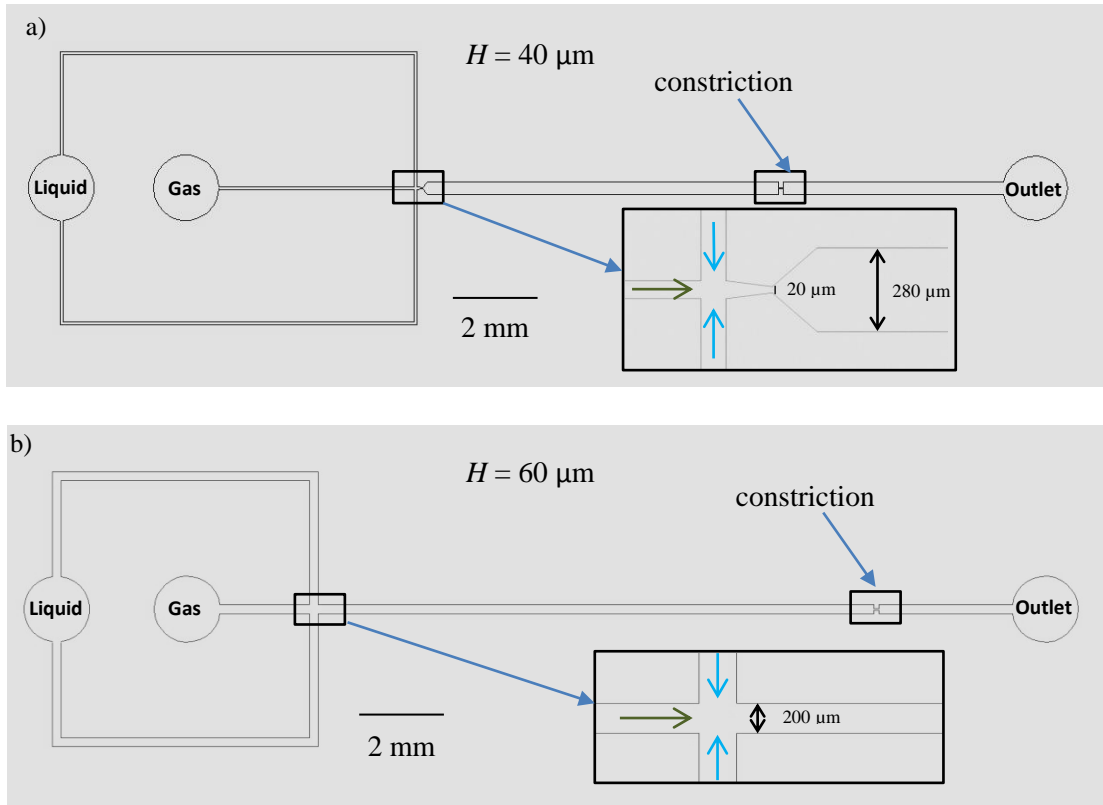
Figure 4.2 Schematics of the two channels used in this chapter: a) dimensions of the channel used for small bubbles that did not undergo break-ups, b) dimensions of the channels used for slug bubbles (green arrows indicate gas phase whereas blue arrows indicate the liquid phase).

NaDBS (cmc)	Glycerol (w/w)%	Viscosity (μ) mPa.s	Surface tension (σ) mNm^{-1}
3	55	10.0	35.1
3	66	21.1	36.4
3	75	46.3	37.6

Table 4.1 Liquid parameters used in the small bubble flow experiments (4.3.1).

NaDBS (cmc)	Glycerol (w/w)%	Viscosity (μ) mPa.s	Surface tension (σ) mNm^{-1}
3	33	3.7	34.2
3	50	7.4	35.1
3	66	21.1	36.4

Table 4.2 Liquid parameters used in the snap-off experiments (4.3.2).

4.3 RESULTS AND DISCUSSION

4.3.1 LOCAL DEFORMATION OF SMALL BUBBLES THROUGH A CONSTRICTION

Small bubbles undergoing local deformations in a sudden contraction followed by an expansion were studied. The bubble size was similar to the constriction width so that snap-off was not favoured (reducing the constriction width by a half caused snap-off above Ca = 1.20 $\times$ 10^{-2}). The goal of this study was to improve understanding of bubble dynamics with regards to their local deformation (elongation/compression) as well as the velocity between the front tip and the rear tail. The main focus is on the constriction shown in Figure 4.3 that had a length (l_c) of 100 μm. However, another shorter constriction (l_c = 40 μm) was also studied and is compared in the major subsections. Any results that refer to the short constriction will be specified as the "sharp" (due to shorter length). Otherwise, the results refer only to the longer constriction.

The average bubble diameter (d_b) was of the similar size as the constriction width or slightly larger (42 μm < d_b < 58 μm), hence, only results for the sudden constrictions are presented since there were no profound differences between the sudden and the gradual constriction.
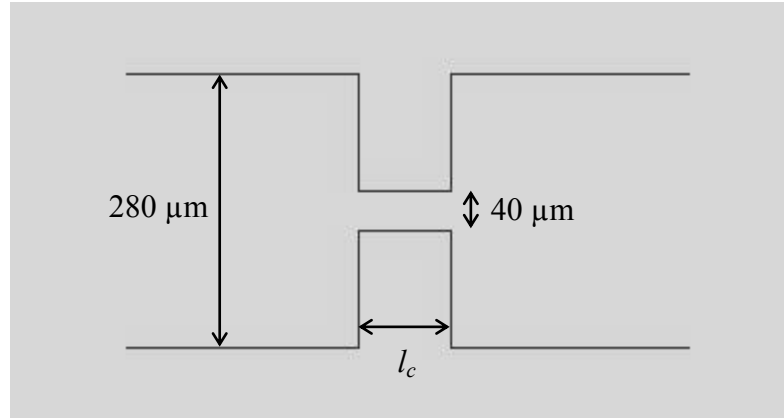
Figure 4.3 Dimensions of the constriction studied (not to scale). The length of the constriction (l_c) of the main channel investigated was 100 µm. A shorter length of approximately 40 µm was also considered.

4.3.1.1 Local deformation

Local deformation as the bubble flowed over the sudden contraction/expansion is presented. The following description refers to the sequence of images below (Figure 4.4) at particular times. At first, the bubble has a spherical shape ($t = 0.00$ ms) and its movement experiences friction with the top and bottom parts of the channel. As it approaches the constriction ($t = 1.73$ ms $- t = 2.10$ ms), the viscous shear forces cause the front tip to accelerate due to the sudden reduction of the channel width so that the curvature of the tip is increased. At the same time, the tail of the bubble is still in the upstream section of the constriction flowing at a lower velocity, thus generating a velocity gradient. The outcome is an elongated shape of a bubble that keeps increasing until it reaches its maximum strain ($t = 2.27$ ms). The maximum value occurs just as the front tip has passed the centre of the constriction while the tail is located just before the suddenly narrowed part. Subsequently, its tail reaches the constriction and, therefore, starts accelerating, flowing faster than the front ($t = 2.37$ ms). This produces a bullet-like shape inside the constriction with the curvature of tail getting smaller ($t = 2.47$ ms). Furthermore, as the front exits the constriction it decelerates due to the sudden increase in the channel width while the tail starts reaching its maximum velocity ($t = 2.57$ ms). Subsequently,

the bubble changes its elastic strain to compression and, therefore, obtains its minimum length just as the tail exits the constriction ($t = 2.73$ ms). The curvature of the tail is almost zero (or negative at higher capillary numbers) causing a croissant shape. The curvature then slowly increases as the surface tension restores the initial spherical shape ($t = 2.97$ ms $- t = 3.67$ ms).
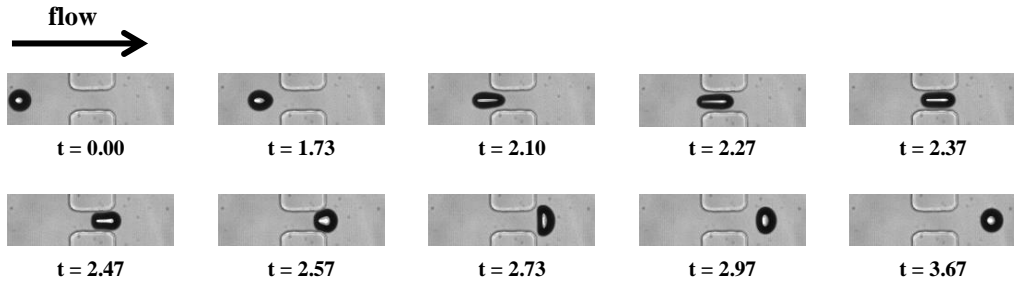
Figure 4.4 Consecutive sequence of images of a bubble going through a sudden contraction/expansion, t is in milliseconds (Ca $= 2.23 \times 10^{-2}$, $\mu = 10.0$ mPa.s).

From the images like the example shown above, axial bubble length (L_x) was extracted as the bubbles passed through the constriction (scaled with the initial bubble diameter, i.e. $L_x^* = L_x/d_b$). The length was then plotted as a function of the position of the front tip (x_f) that was scaled with the constriction length (l_c), i.e. $x_f^* = x_f/l_c$. Thus, the zero value corresponds to the centre of the constriction, while -0.5 and 0.5 represent the start and end of the constriction, respectively. From the plot below (Figure 4.5), it can be seen that the length of the bubble increases gradually as the front of the bubble reaches the constriction due to the sudden reduction in the width of the channel. The maximum length of the bubble as it elongates inside the constriction is reached between x_f^* values of 0 and 0.5, which means when the front tip is located between the centre and the end of the constriction. The length then declines at a faster gradient when compared to the bubble expansion. This is because the rear tail of the bubble reaches a higher maximum velocity inside the constriction than the front tip, caused by a bubble contraction. Explanation of the velocities between the particular bubble parts is

presented in the next section. As the length now decreases, the bubble gets compressed and reaches its smallest length right after the constriction before gradually restoring its shape.

Both of the extreme values vary with the change in the capillary number. As the capillary value increases, the maximum length also increases. This is due to viscous forces becoming more dominant and thus, allowing bubbles to stretch to greater lengths. In all of the examples studied here, the maximum L_x^* value was reached whenever the rear tail was between $x^* = $ -0.65 and -0.55. This means that the front tip had to shift its location to the right as the bubble was able to elongate more due to the higher capillary number. Thus, the position of the front tip varied slightly between 0.13 and 0.41 for the range of the capillary numbers studied here. Similarly, the minimum value also decreased with the increase in the capillary number. The position of the front tip varied between 0.93 and 0.99, usually moving away from the constriction with the increase in the capillary number. The maximum elongation was also found to be affected by the size of the bubble. Larger bubbles were found to reach greater maximum lengths. Assuming a two-dimensional flow without the loss of generality so that variations in the direction normal to the observation plane are omitted, the bubble can be represented by a circle in the upstream section and roughly an ellipse inside the constriction (Figure 4.6). Now, since the bubble inside the constriction was confined by the walls, its minor axis is approximately the width of the constriction (w_c). The conservation of mass (or area in this case) suggests that

$$d_b^2 = w_c \times L_{x\,max}. \tag{4.1}$$

Thus, increasing the initial diameter of the bubble enforces greater elongation. The maximum elongation was, therefore, found to increase linearly with the product of the capillary number and the initial diameter of the bubble (scaled with the constriction width) (Figure 4.7 (a)). The minimum length, on the other hand, decreased as a function of the capillary number (Figure

4.7 (b)) only, since the bubbles were free to elongate vertically in the downstream channel. Similar results were found for the sharp constriction, although the maximum elongations reached by bubbles were significantly smaller due to the shorter constriction and smaller velocities inside the constriction (showed later). The smallest length, on the other hand, was not significantly smaller when compared to the longer constriction. This is because the bubbles were not confined by the walls once flowing in the downstream section; thus, being weakly dependent on the constriction length. However, the rear tails of bubbles reached smaller velocities in the sharp constriction, which in turn, produced slightly smaller minimum lengths (Figure 4.7 (b)).
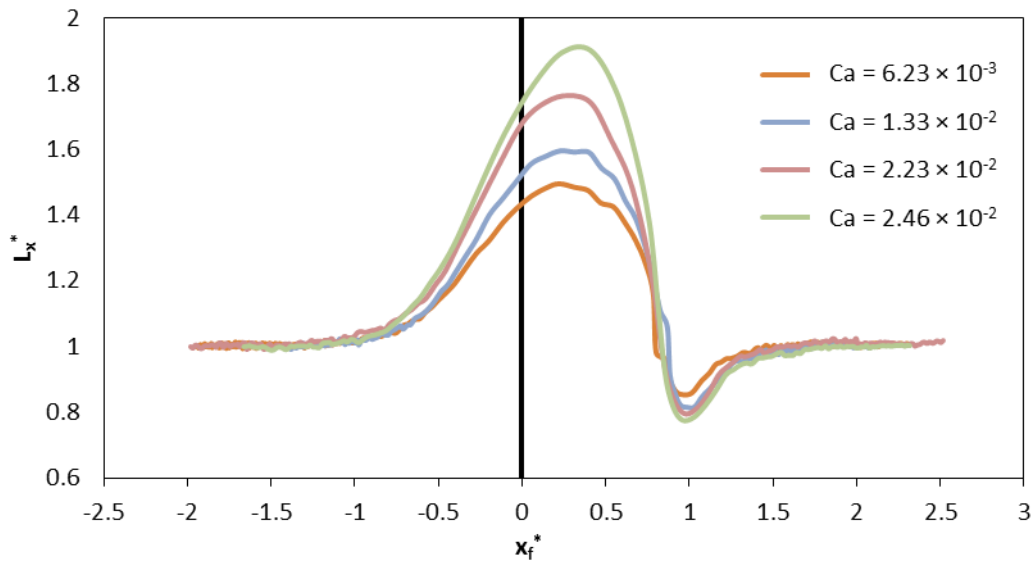
Figure 4.5 Plot of the dimensionless length of a bubble (L_x^*) as a function of the dimensionless position of the front tip (x_f^*) at four different capillary numbers.
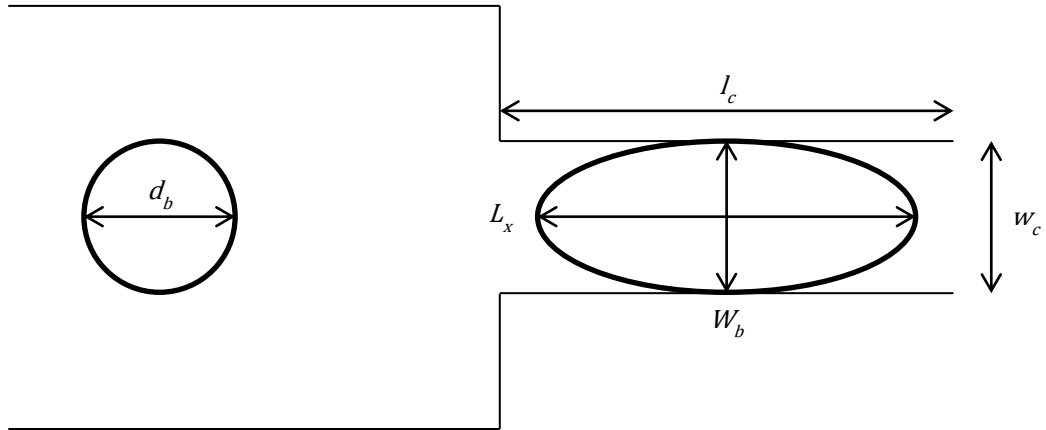
Figure 4.6 Illustration of a bubble at two different positions in the channel: upstream of the constriction, where the bubble is undeformed, and its size is represented by the diameter; inside the constriction where the bubble is elongated, and its size is represented by its length (L_x) and its width (W_b). The shape of the bubble as an ellipse is far from true, especially at higher capillary numbers where bubbles can elongate beyond the length of the constriction or have their axial interface deformed (negative curvature) by the liquid inside the constriction. Nonetheless, the approximation is valid for the capillary number range used.
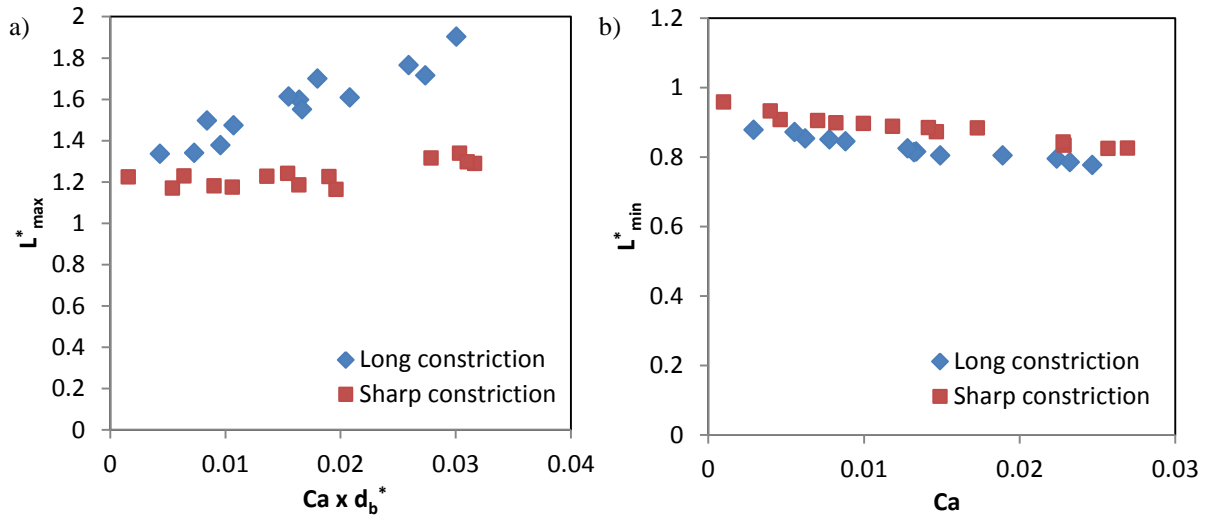
Figure 4.7 Plot of a) the maximum bubble length as a function of the capillary number and initial bubble diameter, b) the minimum bubble length as a function of the capillary number.

4.3.1.2 Local dynamics

A plot (Figure 4.8) is presented for the example at Ca = 2.46 × 10^{-2} showing velocities of the bubble front (U_{fr}) and its rear tail (U_{ta}) scaled with the average bubble velocity in the

91

upstream channel (U_b). Naturally, when a bubble is flowing in the upstream channel that has a uniform cross-section; both of the parts have the same constant velocity. As now the bubble front is approaching the constriction, it gradually accelerates due to channel width getting narrower and, therefore, undergoing strong viscous shear forces that impose deformation on the front tip. The maximum velocity of the front is reached inside the constriction as suggested by the mass conservation and it is almost constant for the time the front is inside the constriction. It reaches a value almost twelve times greater than the bubble velocity in the upstream section. As the bubble front leaves the constriction, its velocity is gradually decreasing due to the increase in the channel width. At first, the decline of the velocity seems to be symmetric with the incline before the constriction, however, around $x^* = 1$, there is a small jump in the velocity which breaks the symmetry. This velocity jump can be related to Figure 4.5 in the previous section. Around $x^* = 1$, the bubble reaches its maximum compression as the rear tail contracts after leaving the constriction. In consequence, the bubble front also temporarily accelerates. The surface tension then tries to restore the circular shape (curvature increases) of the bubble in order to minimise the surface energy, causing the front tip to have its velocity briefly increased. The rear tail of the bubble in a similar way to the front is accelerating when it approaches the constriction. The maximum velocity is reached inside the constriction ($0.2 \leq x^* \leq 1.2$ on Figure 4.8) but just before the centre of the constriction. Furthermore, the rear tail reaches a higher maximum value when compared to the front almost fifteen times greater than the initial velocity. The reason could be that once the bubble is inside the constriction, it can create an additional obstruction of the constriction, thus, affecting the local mean flow. Hence, it can generate a higher pressure drop of the carrier fluid which can increase the speed of the rear tail. Moreover, as the bubble exits the constriction, it contracts. Thus, the surface tension forces contribute to the velocity of the tail.

As expected, both of the velocities increased with the increase in the initial velocity of the bubble (Figure 4.9). It has to be noted that in this work, the velocity of the tail did not diverge at higher initial velocities. Such results were reported by Dawson, Häner and Juel (2015) due to tail thinning caused by thicker films at the constriction. However, the size of the bubble used in their paper was significantly larger than the constriction width, which allowed liquid to grow as the bubble passed through the constriction.

The sharp constriction produced similar results, although the velocities reached inside the constriction were lower. Since the constriction length is shorter, the bubble front tip and rear tail had a shorter residual time inside the constriction. Thus they were forced to slow down almost immediately because of the sudden channel expansion. In consequence, they did not reach as high velocities as the bubbles in the longer constriction. It is worth noting that in both of the constrictions; the front tips had second maxima of very similar velocities during bubble expansion in the downstream channel. Such results were not reported for larger bubbles in the absence of surfactant (Dawson *et al.*, 2015).
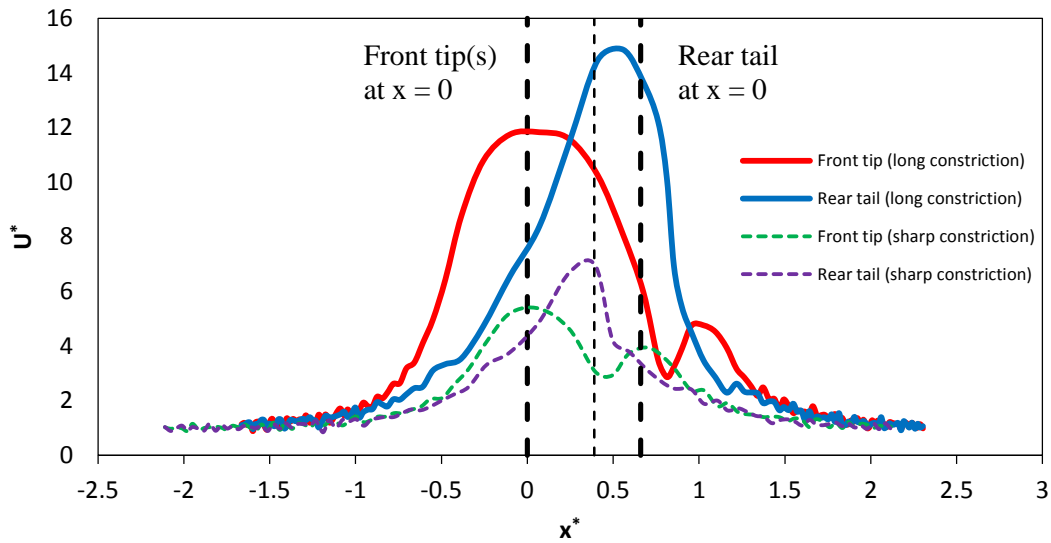
Figure 4.8 Plot of velocities of the front tip (red) and the rear tail (blue) of a bubble flowing at $Ca = 2.46 \times 10^{-2}$ in the main constriction. The dotted green and purple lines correspond to the front tip and the rear tail (respectively) of the sharp constriction flowing at $Ca = 2.57 \times 10^{-2}$. The origin corresponds to both of the front tips at the centre of the constriction, whereas the thick dashed line corresponds to the rear tail of the long constriction and the thin dashed line corresponds to the rear tail of the sharp constriction at the centre of the constriction. Notice the second maxima of the front tips.
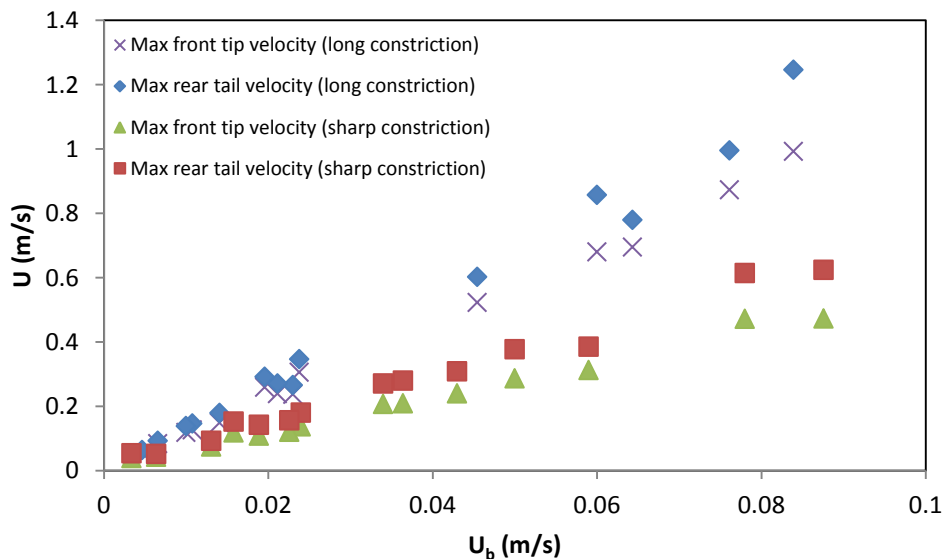
Figure 4.9 Plot of the velocities of the front tip and rear tail as a function of the initial bubble velocity for the long and sharp constriction.

Although, a simple study, it serves as the basis for understanding bubble behaviour and dynamics in constricted channels. The above results suggest that the bubble deformation increases linearly with the capillary number and that another two parameters namely, initial bubble size and the shape of the constriction are also important. The same dynamics are shown to occur in bulk foams (Chapter 5) where the tips of a bubble can flow at different velocities, causing a velocity gradient and, therefore, induce bubble elongation. Once in such a system and confined by other bubbles, even small stress may produce bubble break-up (Golemanov *et al.*, 2008; Denkov *et al.*, 2009).

4.3.2 SNAP-OFF IN CONSTRICTIONS

In all of the experiments in this section of this work, including various glycerol concentrations and different constrictions, only one type of instability was observed, namely snap-off. Snap-off was illustrated in Chapter 2 (2.6.1.1) as the foam (or lamella) generation (or regeneration) in porous media. The example shows a gas slur flowing between two rocks. In this work, however, a single bubble/slug of various sizes (horizontal length between 180 μm and 650 μm) was studied as it flowed through a constriction. Most of the work that has been done in the past has focused on gradually constricted throats and often in square capillaries so that the liquid films deposited by the bubble were uniform and, therefore, the axial radius of curvature was neglected (Ransohoff and Radke, 1986; Gauglitz *et al.*, 1987, 1988; Ransohoff *et al.*, 1987; Gauglitz and Radke, 1990; Tsai and Miksis, 1994). Moreover, the bubbles studied were of similar size and often very long, so there was enough time for the liquid to accumulate in the throat and initiate snap-off. In the study here, however, the bubble flows through a rectangular cross-section (200 μm × 60 μm) and then through one of the constrictions such as a sudden (or a gradual) contraction followed by a sudden (or a gradual) expansion. Thin liquid films, as well as liquid in the corners, should be the main contributors

to snap-off. According to Bretherton (1961), thin liquid film (h_t) has a size of the order of $Ca^{2/3}$. Hammond (1983) has shown that the response time (here, the break-up time) in thin films is proportional to $(h_t)^{-3}$, suggesting that the break-up time should be proportional to Ca^{-2}. However, in a square capillary or rectangular capillary, the liquid in the corners can be more substantial than in the thin liquid films as shown by Gauglitz, St. Laurent and Radke (1987). Based on those results, the break-up time may be dependent on the geometry of the constriction rather than Ca^{-2} until the thin liquid films become of the order of the corner regions. The schematics of the cross-sections of geometries used by Gauglitz, St. Laurent and Radke (1987) are seen in Figure 4.10. Furthermore, the liquid in the corners experiences lower resistance when compared to the thin films surrounding the bubbles in the limit of $Ca \rightarrow 0$ as shown by Wong, Radke and Morris (1995a, 1995b) and so it can travel even an order of magnitude faster. Fuerstman *et al.* (2007) showed experimentally that the velocity in the corners (or gutters) can be twice as large as the velocity of the bubble in a microfluidic channel in the presence of surfactant. However, the solution was not oversaturated with the concentration of surfactant. They suggested that the flow in the corners caused a sweep of surfactant molecules at the interface from one end to another and in turn, generated a gradient of surface tension. This produced a pressure drop across the surface of the bubble that allowed liquid to flow through the corners. At first, the focus is on the gas bubbles in solutions of different viscosities through various constrictions, followed by a neck collapse analysis as well as the number of the daughter bubbles generated.
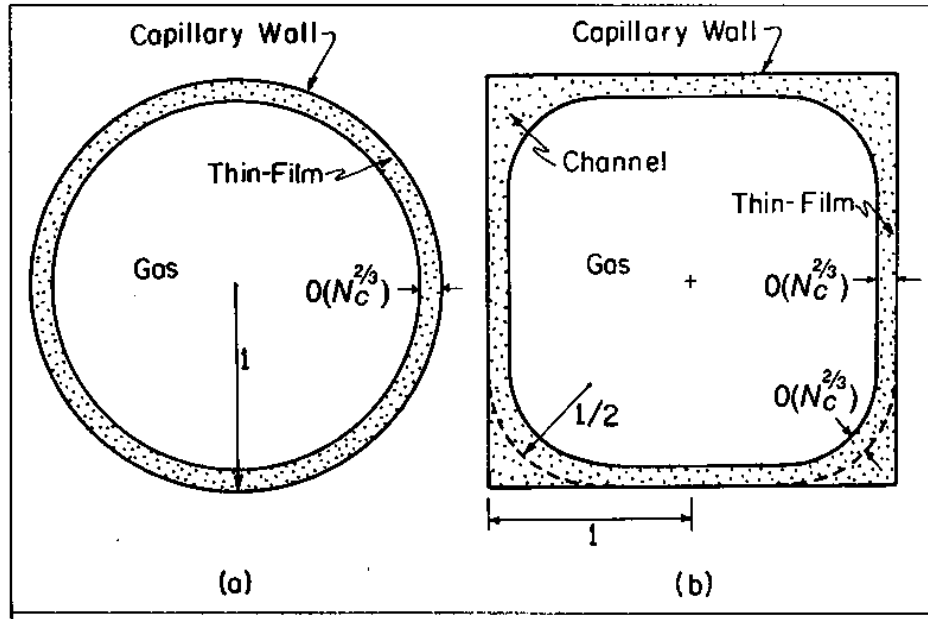
Figure 4.10 Illustrations of the cross-sections of a) a cylindrical capillary and b) a square capillary studied by Gauglitz, St. Laurent and Radkle (1987). N_c refers to the capillary number.

4.3.2.1 Theory

Snap-off occurs if the pressure difference across the bubble interface in the throat temporarily drops by a factor of 2 so that enough liquid can invade it. This pressure difference which is the capillary pressure (P_C) is governed by the surface tension as well as the curvature of the gas/liquid interface and is given by the Laplace-Young equation as follows

$$P_C = P_G - P_L = \sigma \left(\frac{1}{r_1} + \frac{1}{r_2} \right), \tag{4.2}$$

where r_1 and r_2 are the principal radii of curvature. Assuming that the bubble has a uniform gas pressure, it means that in Figure 4.11 the capillary pressure at point 1 is given by

$$P_C = P_G - P_{L1}, \tag{4.3}$$

where P_{L1} refers to the liquid pressure at a point 1. Similarly, the capillary pressure at a point 2 in Figure 4.11 is given by

$$P_C = P_G - P_{L2}, \tag{4.4}$$

where P_{L2} is the liquid pressure at a point 2. The liquid pressure at point 2 must be smaller than the liquid pressure at point 1 so that the gradient in the pressure can force liquid to invade the throat. The calculations would be simple if the channel was cylindrical or square and converge very gradually, meaning that liquid thin films around a bubble would be uniform at each axial position and of the order of $Ca^{2/3}$. In the square gradually constricted channel, this would allow calculating the radius of curvature of the corner and neglect any variation in the axial radius. However, the evolution of the axial radius, especially near constriction walls, may change the way bubbles snap. According to Legait (1983), a large axial radius of curvature should stabilise the interface from snap-off. Legait conducted experiments in square constrictions with sharp sudden walls and did not observe snap-off. When a bubble approaches a constriction, its front tip curvature increases due to viscous shear forces in the same way as the small bubbles in 4.3.1. However, because the initial size of the bubble fills the total width of the upstream channel, the interface from the walls of the upstream channel to the constriction throat has a shape as if it travelled along the gradually narrowing walls. Thus, the bubble occupies a much smaller section of the cross-section just before the constriction so that the corners and films merge (the liquid area between 1 and 2 in Figure 4.11). As such, the liquid in the upstream corners of the channel does not necessarily flow into the corners of the constriction. Hence, the liquid that flows through the corners of the constriction might be from liquid films, thus, flowing at the order of $Ca^{2/3}$. In addition, at higher capillary numbers and because of $W/H > 3$, the liquid in the corners and the thin films merge together as soon as the bubble is formed in the unconstricted section of the channel as shown numerically by De Lózar, Juel and Hazel (2008).
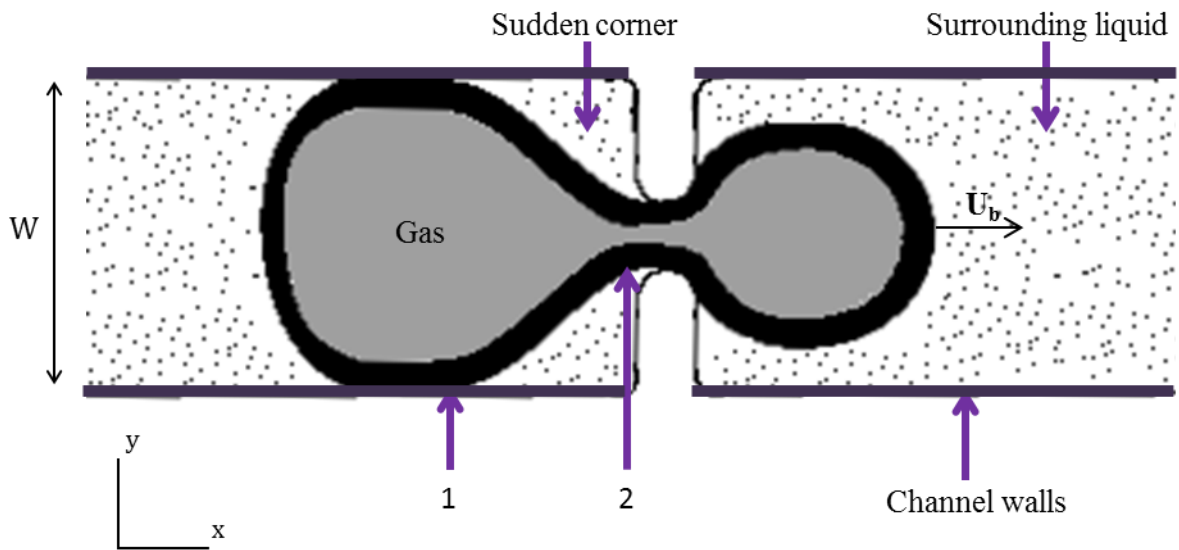
Figure 4.11 Illustration of a bubble inside the constriction, prior to snap-off. The numbers 1 and 2 refer to the positions of the capillary pressure. Notice the liquid area before the constriction called "sudden corner". Throughout this chapter, any reference made to "sudden corner" refers to that area.
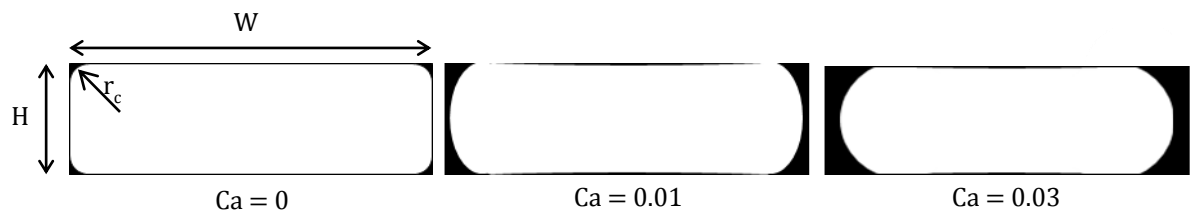
Figure 4.12 Illustration of the cross-section of a bubble profile in the straight section of the channel at three different capillary number Ca = 0, Ca = 0.01, Ca = 0.03. First, as Ca is in the very small limit, the thin liquid films are almost negligible, and liquid can only flow through the corners with a radius of curvature $r_c \sim H/4$. At larger capillary number (Ca = 0.01) the liquid films along the width of the channel increase substantially, the corners and the thin films merge producing the radius of curvature of the bubble that is greater than $H/2$. At the largest capillary number showed (Ca = 0.03), the radius of curvature of the bubble becomes approximately $H/2$ and is constant for all bubbles at higher capillary numbers. As the capillary number increases the liquid film increases between the shorter wall (H) and the bubble as if the bubble was getting axisymmetric, however, this never occurs even at Ca >1 (De Lózar *et al.*, 2008).

Looking at the cross-section of the straight channel (Figure 4.12 (Ca = 0)), the deposited liquid corners have a radius of curvature r_c. In a square capillary (Legait, 1983; Ransohoff *et al.*, 1987), it has been approximated to be a quarter-length of the capillary face. In the study here, r_c can be approximated to be a quarter of the height of the channel. Scaling r_c with $H/2$ (which corresponds to the radius of a cylindrical capillary since $H < W$)

$$r_c^* = \frac{r_c}{H/2} = \frac{1}{2} + O\left(Ca^{\frac{2}{3}}\right). \tag{4.5}$$

However, this radius of curvature is only valid at low capillary numbers ($< 10^{-3}$), thus as the thickness of the liquid increases the corners will merge, and the radius of curvature becomes half of the height of the constriction (Figure 4.12 (Ca = 3.00×10^{-2})).

The break-up time (τ_b) is a residual time between the times when the front of the bubble arrives at the centre of constriction (t_c) and the time it breaks/snaps (t_b). It estimates how long it takes for the liquid to invade the constriction and generate a new bubble. Moreover, faster break-up time results in a generation of a smaller bubble since the new bubble is directly proportional to the bubble velocity and the break-up time. Smaller bubbles are favoured in applications such as enhanced oil recovery since they can reduce gas mobility (Prud'homme and Khan, 1996). The break-up time is calculated in the following manner

$$\tau_b = t_b - t_c. \tag{4.6}$$

The break-up time was extracted by recording frames when the bubble front reached the centre of the constriction and the time it snapped (Figure 4.13). The two frames were subtracted from each other to give the total number of the frames it took to snap and then divided by the frame rate the movie was recorded to give an accurate time.
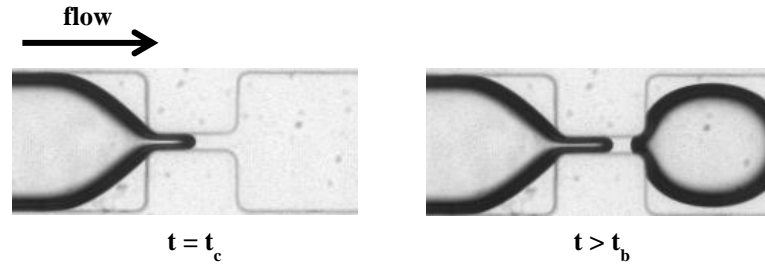
Figure 4.13 Illustration of the two frames used for calculating the break-up time. Top image: bubble front arrives at the centre of the constriction ($t = t_c$), bottom image: the bubble is already snapped ($t > t_b$).

From equation (4.6), dimensionless break-up time (τ^*_b) is scaled as follows

$$\tau^*_b = \frac{\sigma\tau_b}{\mu H}.$$
(4.7)

Variation of the bubble size is higher in the horizontal direction than in any other direction since the bubbles are constrained by the channel walls. Therefore, the initial horizontal bubble length (L_0) is assumed to represent the size of a bubble and is scaled as follows

$$L_0^* = \frac{L_0}{H}.$$
(4.8)

4.3.2.2 Three-dimensional view of the neck

Since in all of the experiments studied here the height of the channel was always larger than the width of the constriction ($H > w_c$), it was essential to understand the shape of the neck of the bubble inside the constriction. An experiment was carried in order to observe the evolution of the neck in the normal direction to the observation plane.

The microfluidic device was bonded with another PDMS slab and cut in such a way that it could be placed on the microscope glass so that a view from the height of the channel could be obtained. It is relatively difficult to see clearly through a cut PDMS, so the image is not very sharp. However, the contour of the bubble is quite visible (Figure 4.14 top row). This proved that once the bubble entered the constriction, its neck occupied almost the total height

of the channel even though the constriction was only 20 μm wide. This means that the neck was not circular since its height was just under 60 μm whereas the width was that of the constriction (20 μm in this example). Thus, at first, the neck was reduced by the liquid until it had a radius of curvature half of the constriction width (Figure 4.14 t = 0.30 ms) and then became circular. Images showing the example in one of the sudden constrictions (l_c = 30 μm, w_c = 20 μm) as well as illustrations of the neck in other planes are presented in Figure 4.14.

t = 0.00 ms **t = 0.30 ms** **t = 0.62 ms**
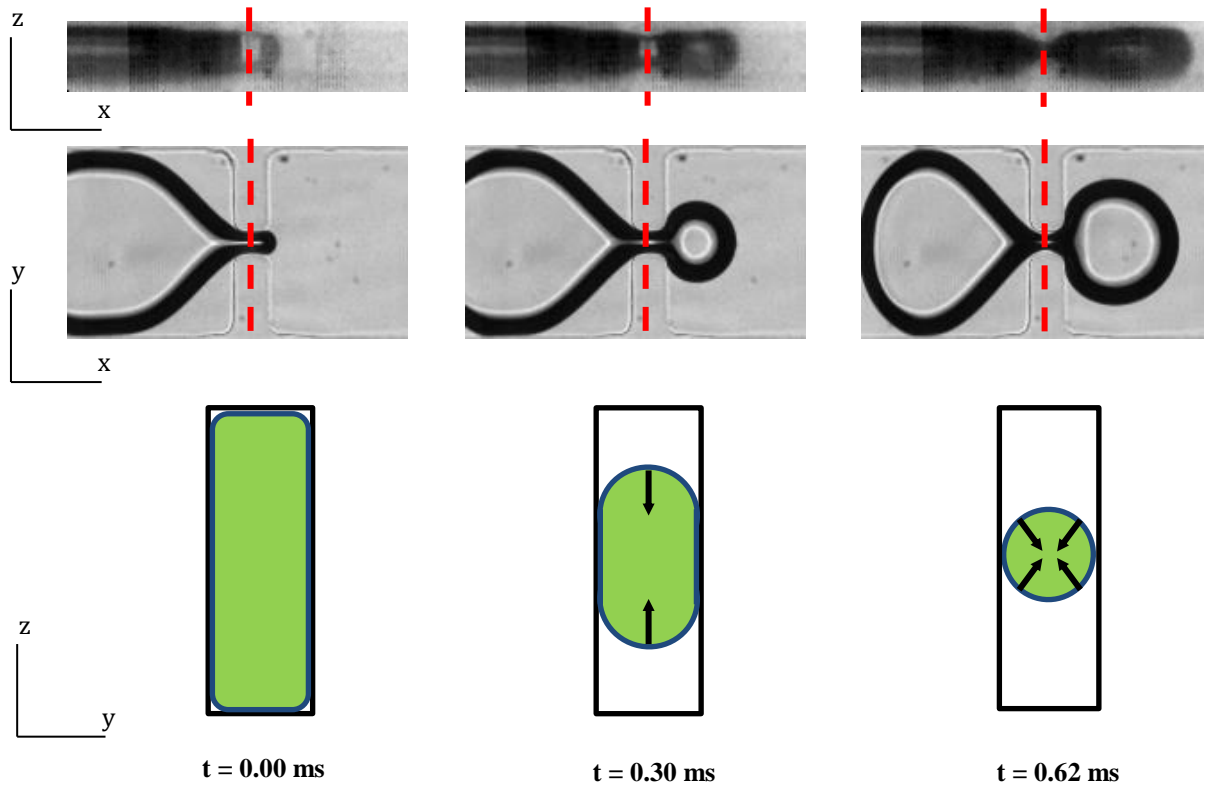
Figure 4.14 Illustration of the neck of the bubble at Ca = 1.80×10^{-2} in three different planes as it enters the constriction (t = 0.00 ms), is reduced vertically (t = 0.30 ms), becomes circular as it reaches the width of the constriction (t = 0.62 ms).

The above study shows that the neck of the bubble had to be first reduced vertically (from the z-direction) before it was also reduced in the transversal direction (final decrease that is seen in the (xy) observation plane). This means that not all of the bubbles studied were expected to snap as the break-up time varies for different constrictions and is dependent on

the liquid films and, therefore, the capillary number. Thus, at some of the flow conditions (initial bubble size, liquid viscosity and velocity), the bubbles might pass through one of the constrictions before being thinned to the circular shape.

4.3.2.3 Break-up time

Results of the break-up time as a function of the capillary number and/or bubble length are now presented for various constrictions.

4.3.2.3.1 Sudden constrictions

Illustrations of the four sudden constrictions studied in this section are seen in Figure 4.15. Two of the constriction studied will be called sharp (l_c = 30 μm Figure 4.15 (a) and (c)) and from here on they are referred to as sharp 20 μm (w_c = 20 μm) and sharp 40 μm (w_c = 40 μm). The other two constrictions will be called long (l_c = 120 μm Figure 4.15 (b) and (d)) and referred to as long 20 μm and long 40 μm. Initially, all of the four constrictions were supposed to have very sharp corners, however, after the fabrication, all of them turned out slightly rounded especially the sharp 40 μm constriction (Figure 4.15 (c)). Although the fabrication was repeated, it did not improve the sharpness of the corners. Because of the access and time constraint in the fabrication room, the constriction was used as it was fabricated. Since the constriction width produces the same radius of curvature inside the constriction, the focus is first on the two narrow constrictions (sharp 20 μm and long 20 μm) and then on the two wide constrictions (sharp 40 μm and long 40 μm).
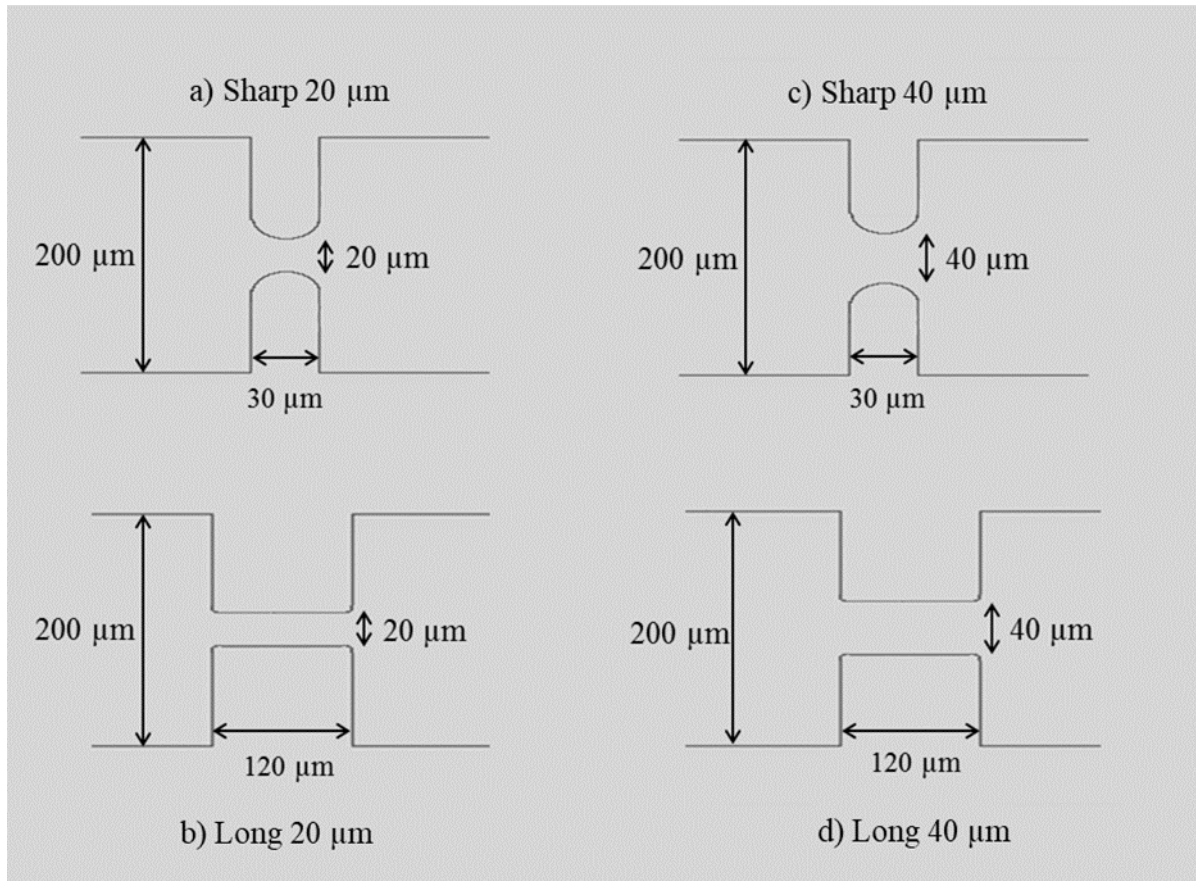
Figure 4.15 Schematics of the four sudden constrictions studied; a) Sharp 20 μm, b) Long 20 μm, c) Sharp 40 μm, d) Long 40 μm (not to scale).

4.3.2.3.1.1 Narrow constrictions

In the narrow constrictions, when bubble approaches the constriction, the tip of the bubble is reduced due to the viscous shear forces, and thus, it is narrow enough to enter the constriction. As the bubble flows along the constriction walls, it causes a capillary pressure gradient as already explained in the theory section because of the larger curvature in the corners of the constriction. However, depending on the velocity of the bubble as well as the surface tension, the liquid in the upstream might not reduce the neck vertically to the circular shape (Figure 4.14 (c)) before the bubble has fully passed the constriction as it is shown for the two examples in Figure 4.16. Thus, there are minimum capillary numbers above which bubbles always exhibit snap-off.
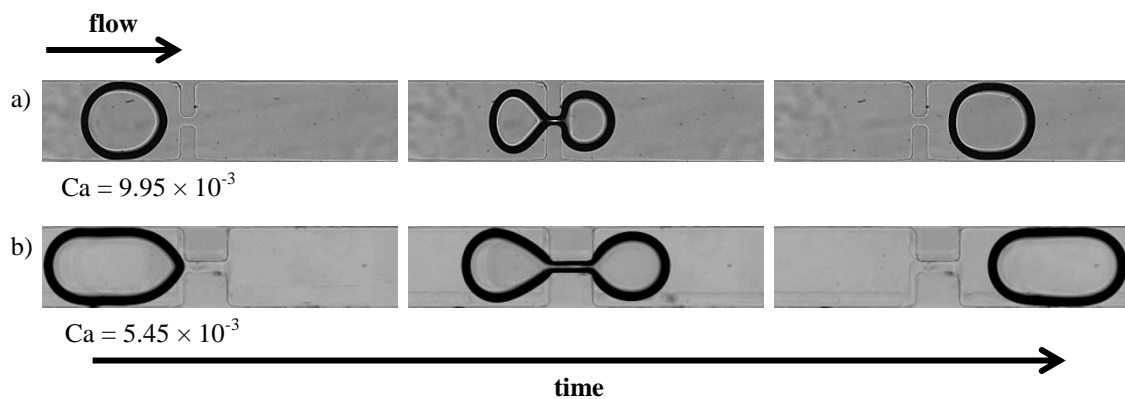
Figure 4.16 Example of bubbles flowing at insufficient capillary numbers to cause snap-off in a) sharp 20 μm constriction, b) long 20 μm constriction.

As mentioned above, once the critical capillary numbers are reached (Ca_{cr} ~1.16×10^{-2} and Ca_{cr} ~7.48×10^{-3} for the sharp 20 μm and long 20 μm respectively) bubbles start snapping inside the constriction, thus generating new bubble or bubbles. Both constrictions produced similar results. At lower capillary numbers the neck was reduced downstream of the middle point of the constriction. However, as the capillary number increased, the snap-off position moved towards the upstream part of the channel, most likely due to thicker films. Thus, above the certain capillary number in the sharp 20 μm constriction, the neck of the bubble was reduced at the entrance of the constriction. Consequently, the liquid was visually contributing to the neck thinning from the sides near the constriction. In the long 20 μm constriction, the neck was almost always snapped inside the actual throat while the bubble was still occupying the early part of the constriction. Around $Ca = 3.00 \times 10^{-2}$ the bubbles were observed to snap closer to the constriction entrance, but the constriction was still too long to visually observe liquid contribution from the upstream channel. Examples of bubbles snapped at different capillary numbers are shown in Figure 4.17.

105
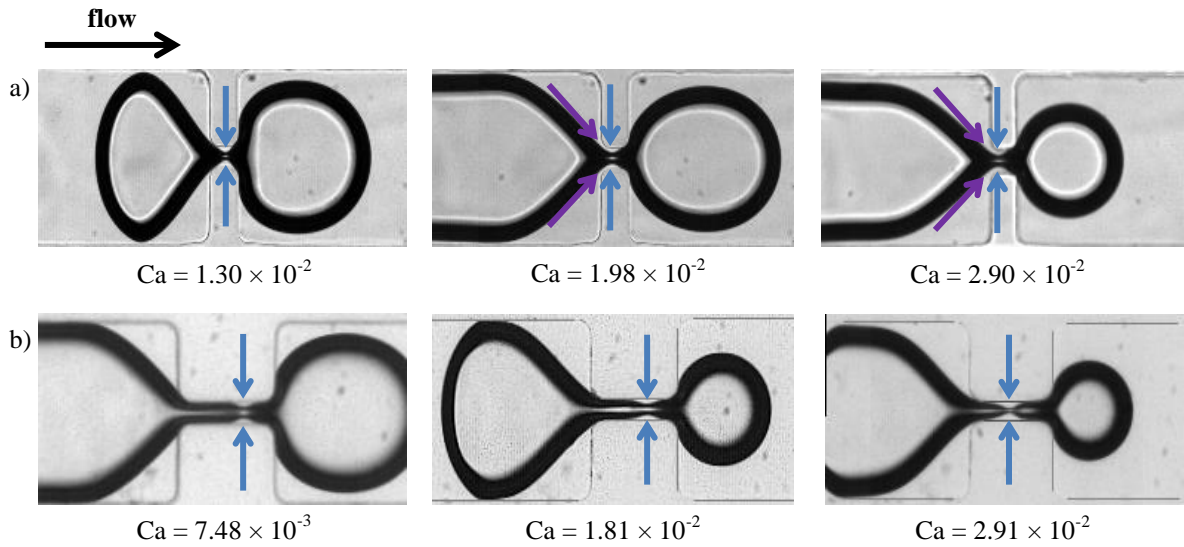
Figure 4.17 Examples of bubbles snapping at different capillary numbers in a) sharp 20 μm constriction, b) long 20 μm constriction. The blue vertical arrows point where the snap-off location is occurring. Notice no neck thinning earlier in the constriction in (b) and how the location moves towards the upstream part in (a) and (b) especially in the last picture at the highest capillary numbers shown. In (a) the snap-off location moves towards the left, where liquid visually contributes from the sides (purple arrows). However, this s shown to

The neck of the bubble has to be reduced to 20 μm in order to form a full liquid collar so that it can be reduced from all directions. However, as soon as the bubble enters the constriction, its corner curvature increases approximately to a quarter of the constriction width ($r_c = w_c/4$) which allows the liquid to enter the constriction through both the corners and the thin liquid films above and below the bubble. Because the constriction is very narrow, the corners and flat section near the shorter length (i.e. top and bottom plate) merge almost instantly, and so the radius of curvature becomes $w_c/2$ which means that the neck is stable to snap (Gauglitz *et al.*, 1987). The bubble size was not found to affect the break-up time in both of the constrictions. Mostly because of the fast merging of the corners inside the constriction, which quickly allowed the liquid to invade the constriction and reduce the neck.

Since the liquid in the corners of the upstream channel merges with the thin films just before the actual constriction, they both should be of the order of the thin films and, therefore,

strongly dependent on the capillary number. This is best understood by the fact that the break-up time was found to decrease with the capillary number to the power of 2.11 and 1.99 (Figure 4.18) for the sharp 20 μm and long 20 μm constrictions respectively. This agrees well with the theoretical predictions in the cylindrical capillary (Gauglitz *et al.*, 1988) where the break-up time decreased with the capillary number to the power of -2, exclusively due to the liquid in the thin films ($h_t = O(Ca^{2/3})$). Moreover, the bubbles in the longer constriction required slightly shorter time at approximately the same capillary number. Since the break-up time is measured whenever the tip of the bubble reached the centre of the constriction, the bubble in the longer constriction has already a longer residual time inside the constriction. Consequently, the change in the capillary pressure may already allow the liquid to invade the throat and start reducing the neck, which in turn, results in a faster break-up time. In addition, longer bubble necks are less stable since they are more susceptible to Plateau-Rayleigh instability (Ohta *et al.*, 2011).
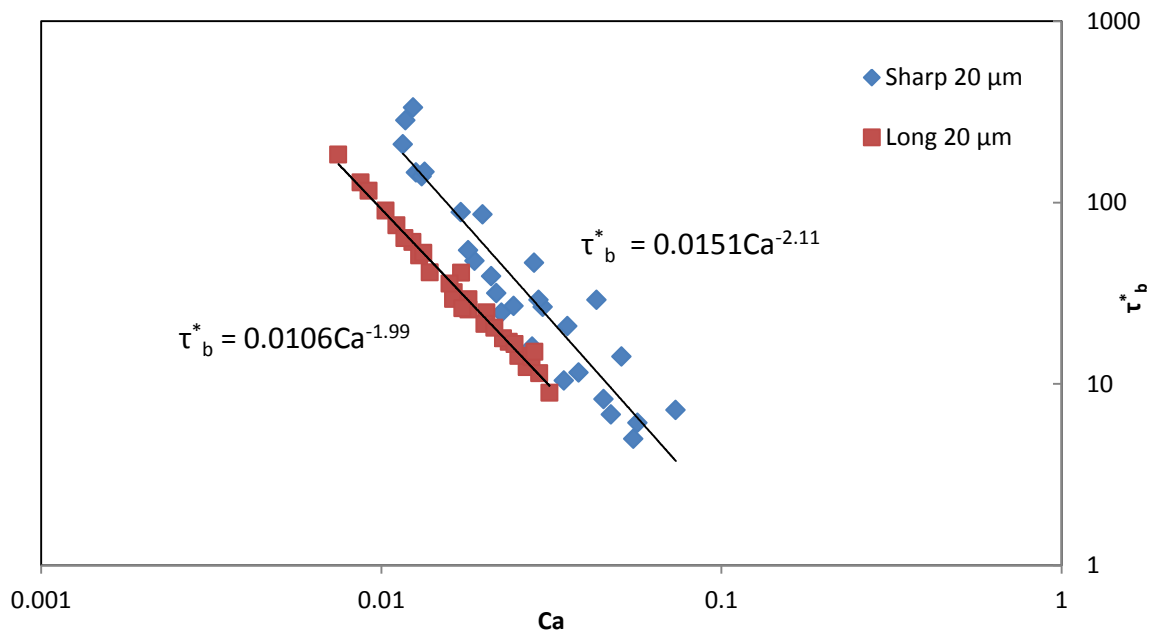
Figure 4.18 Plot of the capillary number against the dimensionless break-up time for the two narrow constrictions: sharp 20 μm and long 20 μm.

4.3.2.3.1.2 Wide constrictions

Similarly to the narrower constrictions, the two wider constrictions, sharp 40 μm and long 40 μm, required a minimum capillary number for bubbles to undergo snap-off. However, since the constriction width is two times larger than previously, the initial radius of curvature ($r_c = w_c/4$) in the corner of the constriction must also be two times greater than before. Hence, the capillary pressure is two times smaller when compared to the narrow constrictions, and, therefore, the liquid does not enter the constriction as fast. Thus, some bubbles did not exhibit snap-off in a capillary range Ca = 1.60×10^{-2} to Ca = 2.00×10^{-2} (Figure 4.19), which is approximately two times larger than the critical capillary numbers required for the narrow constrictions. Hence, although the liquid films are quite thick, they are not always sufficient to cause snap-off in the wider constrictions (Figure 4.19).
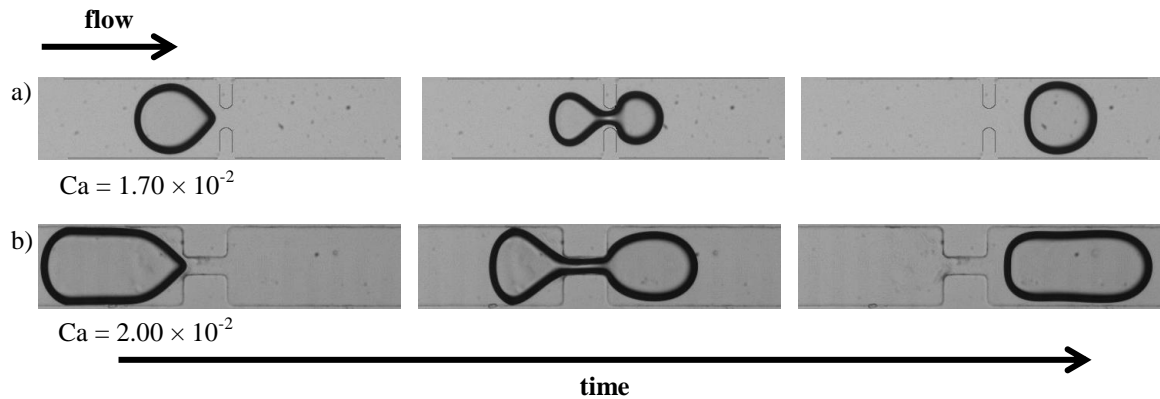
Figure 4.19 Example of bubbles flowing at insufficient capillary numbers to cause snap-off in a) sharp 40 μm constriction, b) long 40 μm constriction.

One of the key differences between the narrow and wide constrictions observed was the bubble size dependence for snap-off. It was observed that in the wide constrictions, large bubbles took a much longer time before having their neck reduced and snapped when compared to the small bubbles. The dependence was strong for the sharp 40 μm constriction and slightly weaker for the long 40 μm constriction. In addition, because higher capillary numbers were required to observe snap-off than for the narrow constrictions, the bubbles were

often snapped close to the upstream channel, especially in the sharp 40 μm constriction (Figure 4.20 (a)). Thus, there was a visible contribution from the liquid approaching from the sides or even sudden corners just before the constriction.
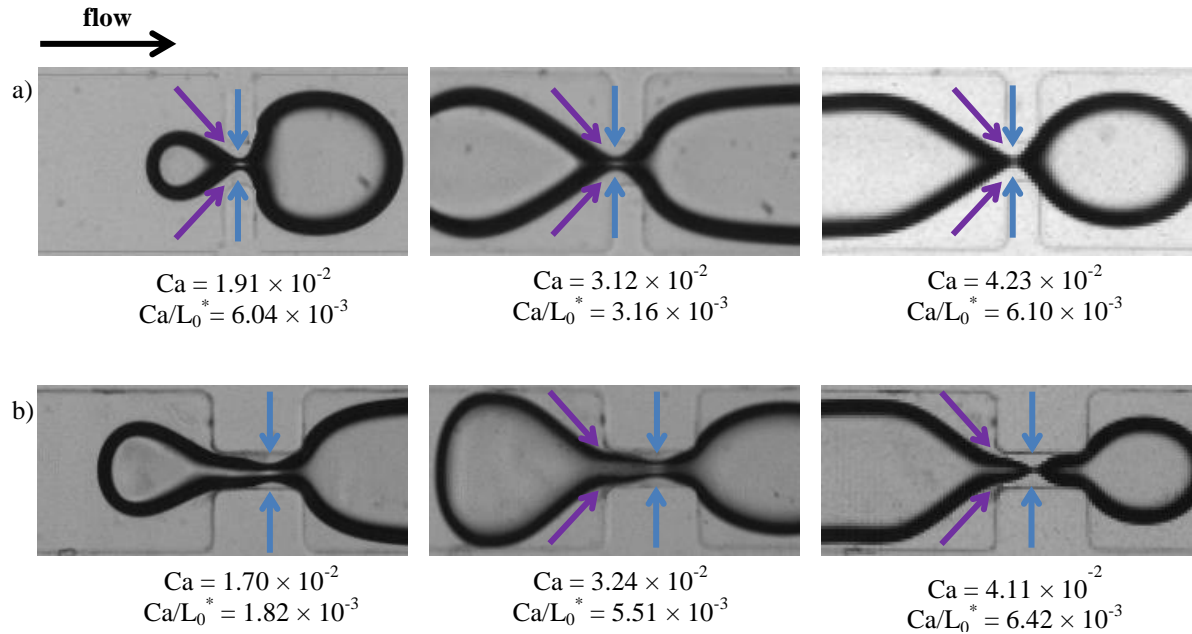
Figure 4.20 Examples of bubbles snapping at different capillary numbers in a) sharp 40 μm constriction, b) long 40 μm constriction. The blue vertical arrows point where the snap-off location is occurring, and purple arrows show from where the liquid can also contribute. Notice how the snap-off location moves towards the upstream part in (a) and (b). In (a) the liquid in upstream of the constriction visually contributes to the narrowing across all of the constrictions. In (b) this occurs later around $Ca = 3.00 \times 10^{-2}$, however, the second image in (b) is not that clear, although small cavities in that image were observed.

The break-up time was again expected to be strongly dependent on the thin films due to large capillary numbers. However, since the constriction was not reduced by more than 50% ($w_c > H/2$), the liquid that flowed through the corners of the constriction could reach a static shape so that the radius of curvature inside the constriction remained uniform (Gauglitz *et al.*, 1987). Thus, significantly thicker films were required in order to reduce the neck vertically from 60 μm to 40 μm and in consequence be pushed by the liquid from all directions. In the

sharp 40 μm constriction, it seems that the circumferential radius of curvature of the neck just upstream of the constriction varied faster than the one inside the actual constriction due to the liquid contribution from the sides and possibly sudden corners (i.e. from viscous normal stresses). Indeed, the break-up time for the sharp 40 μm constriction was found to have an exponent of -1.4, which is different from the usual -2 and indicates a contribution of liquid at different order. Moreover, as mentioned earlier, bubble length was found to be crucial for the sharp 40 μm constriction and was included in the plot. Larger bubbles occupy a larger volume of the channel so that the liquid fraction surrounding the bubble is smaller. In addition, the resistance to the flow is higher in the corners and films deposited by longer bubbles (Wong *et al.*, 1995a) which could also explain why smaller bubbles snap faster in the wider throats. By taking the bubble size into consideration, the exponent was again altered. The value of α for $(Ca/L_0^*)^\alpha$ found experimentally was -1.25 (Figure 4.21).

The break-up time of the long 40 μm constriction was also found to be strongly dependent on the thin films, decreasing with the capillary number to the power of -2.31 which is yet again relatively close to -2 (shown in the next section). However, there was a slight dependence on the bubble size (especially for long bubbles), most likely due to the liquid contribution from films (experiencing higher resistance due to bubble size) at the walls. Nevertheless, it allowed plotting break-up times for both of the constriction on the same graph (Figure 4.21) and directly comparing the results. As before, the break-up time calculated was lower for the longer constriction agreeing with the results in the narrower constrictions.
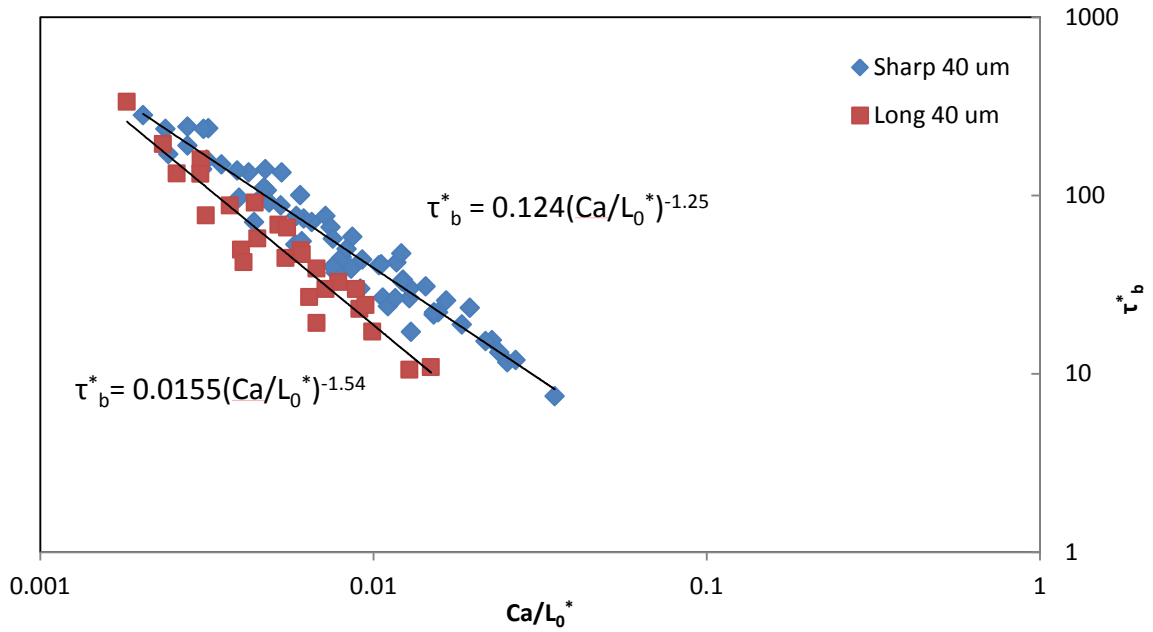
Figure 4.21 Plot of the capillary number over the dimensionless bubble length (eq. 4.8) against the dimensionless break-up time for the two narrow constrictions: sharp 40 μm and long 40 μm.

4.3.2.3.2 Gradual constrictions

Gradual constrictions with the walls inclined at a 45° angle were investigated. Such constrictions allow bubbles to travel along the solid walls, thus, reducing the amount of liquid that was held in the sudden corners in the sudden constrictions. Moreover, since the liquid surrounding the bubble flows more like a plug flow, a bubble is depositing a more uniform liquid film when close to the constriction. In addition, the axial curvature of the interface is smaller inside the constriction, which should make the neck more stable to snap (Legait, 1983). Hence, a slightly faster break-up time is expected. The focus is on the wider constrictions since the narrower ones were found to have almost identical results as the sudden constrictions (presented later). Additionally, results of the break-up time are compared with the results obtained for the sudden constrictions.

4.3.2.3.2.1 Wide constrictions

Two wider gradual constrictions are presented in Figure 4.22. They slightly differ from the sudden constrictions as the lengths have turned out to be shorter by 15 μm and 20 μm for the sharp and long constriction respectively. However, this is assumed to have a small effect on the break-up time since the radius of curvature of the neck of the bubble that drives the capillary pressure is dependent on the width and the height of the constriction. Besides, the length will be shown to have a small effect on the foam dynamics in wider constrictions in Chapter 5 (5.3.1.4.2).
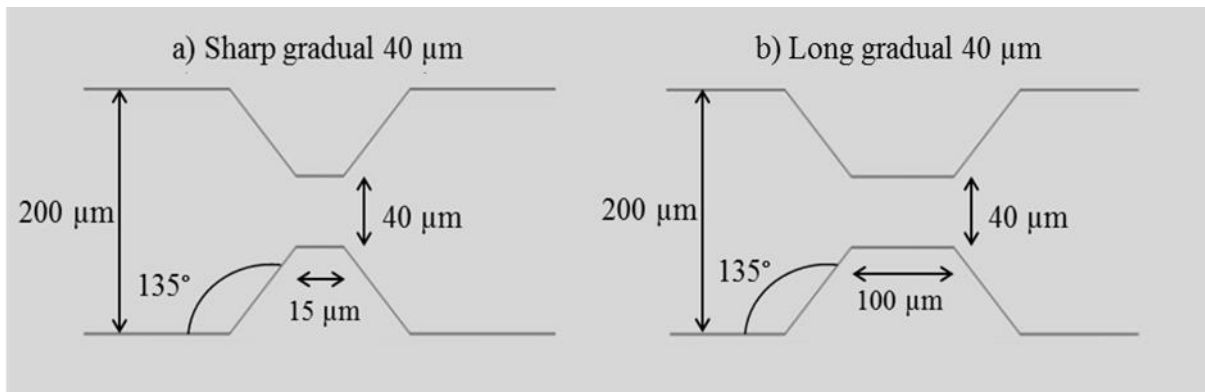
Figure 4.22 Schematics of the two gradual constrictions studied: a) sharp 40 μm, b) long 40 μm (not to scale).

As earlier, at capillary numbers of insufficient liquid thickness, the bubbles managed to pass through the constrictions without experiencing snap-off. Bubbles flowed through the constriction slow enough so that the liquid in the constriction corners and the films remained in the equilibrium or they had a small length so that the liquid did not reduce the neck enough to cause snap-off. Examples are shown in Figure 4.23 below.
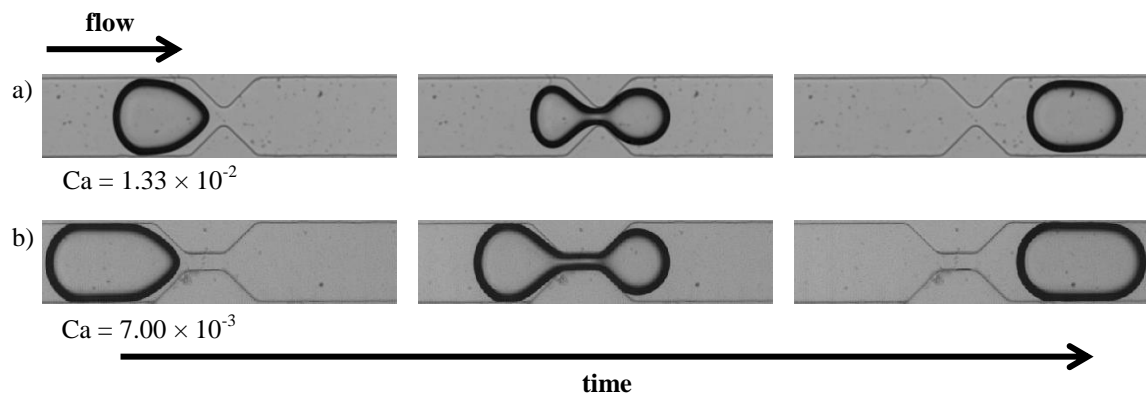
Figure 4.23 Example of bubbles flowing at insufficient capillary numbers to cause snap-off in a) sharp gradual 40 μm constriction, b) long gradual 40 μm constriction.

The two wide gradual constrictions had a very strong resemblance to the sudden constrictions. The bubbles in the sharp gradual 40 μm constriction were again observed to snap slightly upstream of the constriction, and in consequence, the liquid was able to visually contribute to the narrowing (Figure 4.24 (a)). In the longer constriction, this started occurring later, once the narrowest point of the neck was closer to the centre of the location (Figure 4.24 (b)).
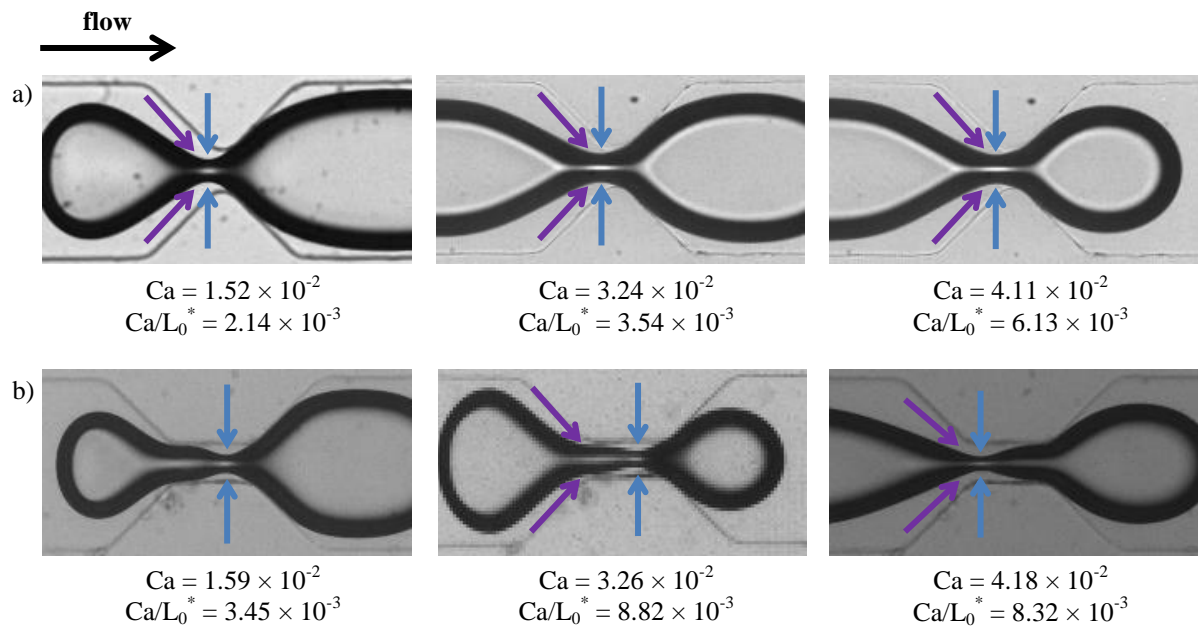
Figure 4.24 Examples of bubbles snapping at different capillary numbers in a) sharp gradual 40 μm constriction, b) long gradual 40 μm constriction. The blue vertical arrows point where the snap-off location is occurring, and purple arrows show where the liquid may also contribute from. Similar to the sudden constriction, the snap-off location moves towards the upstream part in (a) and (b) and in (a) the liquid in upstream of the constriction visually contributes to the narrowing across all of the constrictions. In (b), similar to the sudden constriction, this occurs later around $Ca = 3.00 \times 10^{-2}$.

The sharp gradual 40 μm constriction had its break-up time dependent on the capillary number as well as the length of a bubble in a similar way to the sudden constriction. Thus, the liquid films are responsible for thinning of the bubble neck and generating a new bubble. However, due to the large width of the constriction, the radius of curvature inside the constriction could again reach a static shape. Thus, thicker liquids were required (such as the ones surrounding a small bubble with less flow resistance), or longer residual time so that enough liquid could accumulate and snap the neck (e.g. longer bubbles). The break-up time found experimentally is proportional to the capillary number over the scaled bubble length to the power exponent of -1.61 (Figure 4.25). The power exponent is larger than in the case of the sharp sudden 40 μm constriction (-1.25) which suggests that the liquid at an order closer

to $Ca^{2/3}$ was contributing towards snap-off. Since the constriction does not contain sudden corners, there is less liquid approaching the neck of the bubble from those regions. Furthermore, the break-up time for the sharp gradual 40 μm was slightly faster. As mentioned earlier, the liquid along the gradual walls does not flow towards the sudden corners, (it is more uniform) and the axial radius of curvature stabilising the neck from snap-off is also smaller.
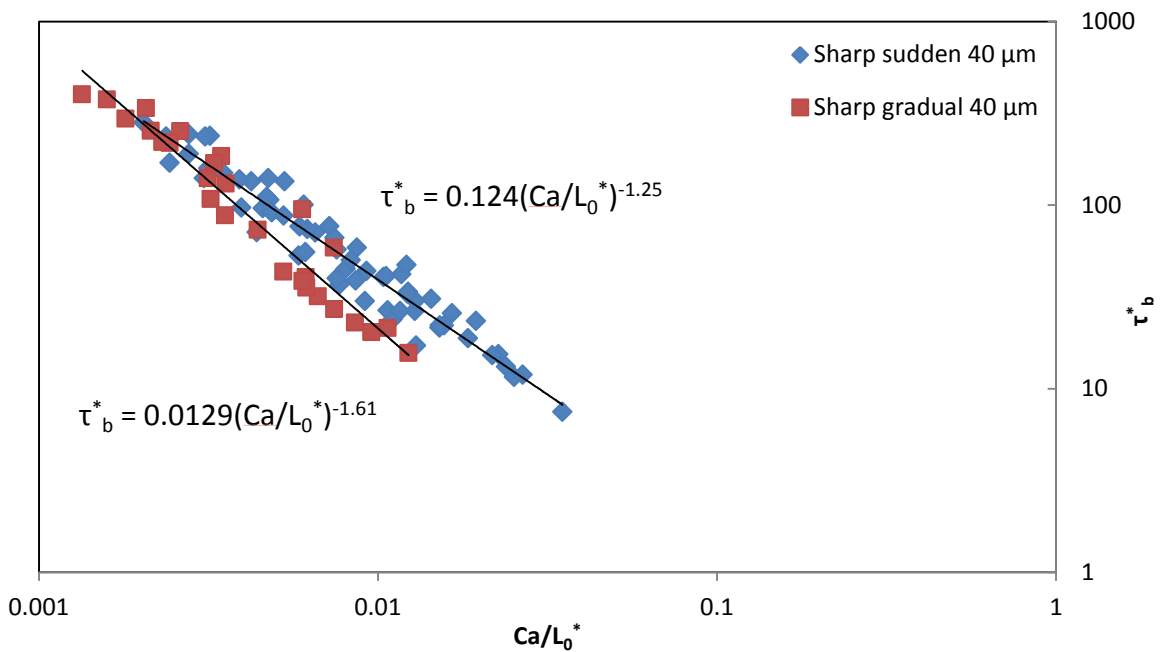
Figure 4.25 Plot of the capillary number over the dimensionless bubble length against the dimensionless break-up time for the sharp sudden 40 μm and sharp gradual 40 μm constrictions.

The break-up time for the long gradual 40 μm constriction was proportional to the capillary number to the power of -2.15 (Figure 4.26) which is remarkably close to the power of -2 and suggests a contribution from films at $O(Ca^{2/3})$. In addition, bubbles experience larger deformations (by having a longer neck) due to the longer constriction. Subsequently, bubbles require a longer time to pass the constriction when compared to the sharp constrictions. Thus, the liquid has more time to accumulate inside the constriction, which reduces the bubble size dependence. Comparing the break-up time with the sudden constriction of the same

dimensions yet again proves that on average, the liquid accumulated faster inside the gradual constriction.
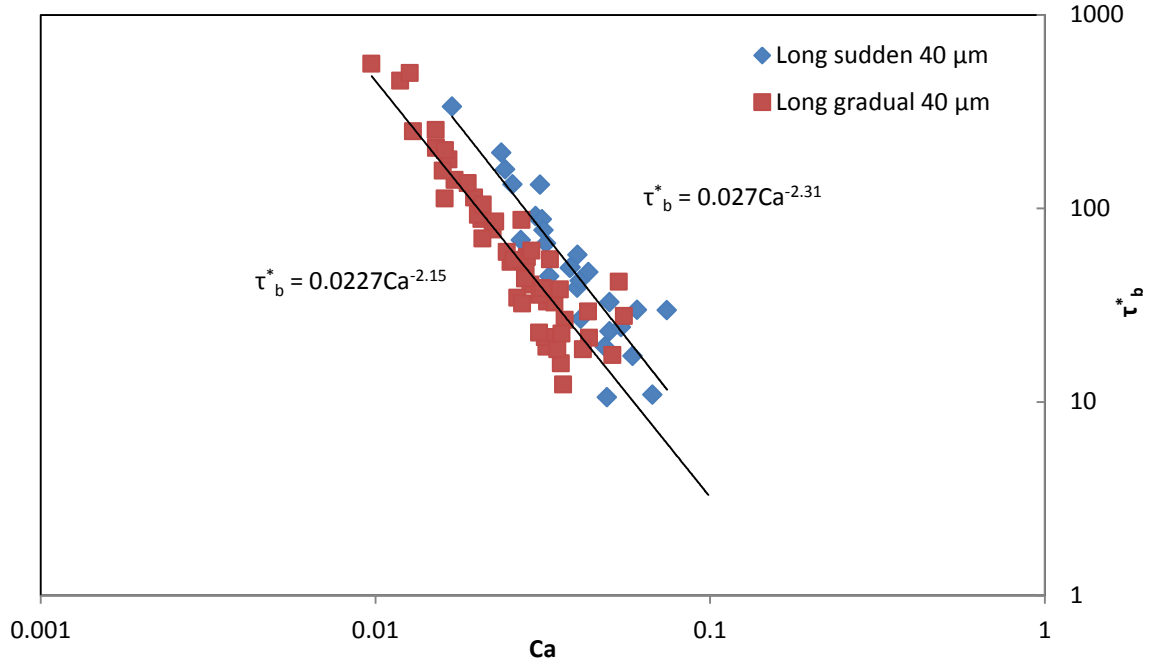
Figure 4.26 Plot of the capillary number against the dimensionless break-up time for the long gradual 40 μm constriction.

4.3.2.3.2.2 Narrow constrictions – a remark

The break-up time in the sudden narrow constrictions was occurring relatively fast due to the flow of thin films close to the constriction (mostly above and below the bubble). The corners inside the constriction merged almost instantly, and the narrowing of the neck became very sudden. Moreover, there was no dependence on the bubble size or any contribution from the sudden corners, although in the sharp 20 μm constriction the majority of the bubbles was snapped upstream of the narrowest points. Those results are confirmed by the gradual constriction (gradual sharp 20 μm in Figure 4.27 (a)) where the break-up time obtained from the least square method was almost identical as the one for the sudden sharp 20 μm (Figure 4.27 (b)). Hence, it can be concluded that in the narrow constrictions, the walls of the constriction have a negligible effect on the break-up time.
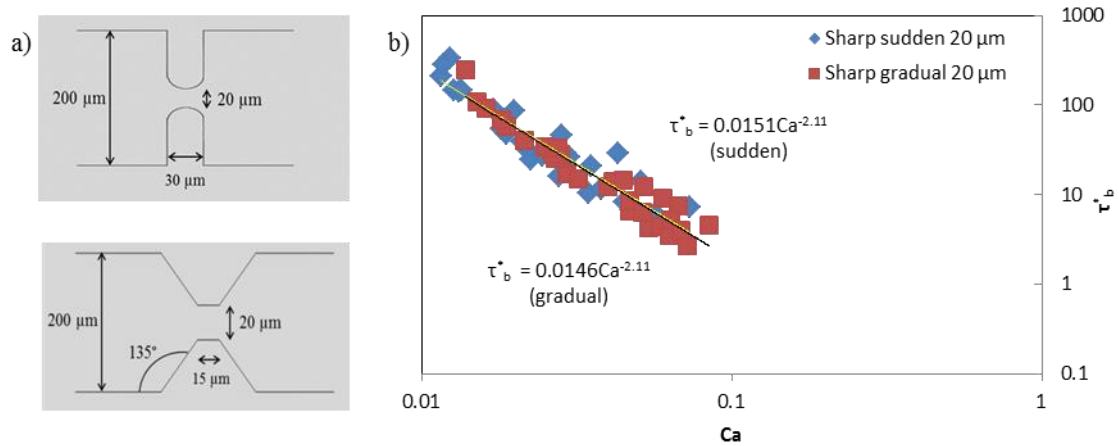
Figure 4.27 Comparison of the two narrow, sharp constrictions a) schematics of the sharp sudden 20 μm constriction (top) and sharp gradual 20 μm constriction (bottom), b) direct comparison of the break-up time functions. Notice the two lines for sudden (orange) and gradual (black) are almost the same. The power-law exponent is the same (2.11) whereas the coefficient differs by 5×10^{-4}.

4.3.2.4 Dynamics of bubble thinning

The bubble neck at the constriction before snap-off and how fast it decreases can shed light on the importance of particular parameters that directly affect it. The width of the neck (w_n) seen in Figure 4.28 was measured once it underwent a negative curvature until the time it snapped ($\tau = t_b - t$). This allowed obtaining a profile for the neck collapse as a function of time. Each neck collapse was then fitted with a power-law equation (using the least square method) $w_n = \alpha \tau^{\beta}$. The graphs (Figure 4.29) are plotted for various sudden constrictions (gradual constrictions produced similar results, so they are omitted here) as well as viscosities.
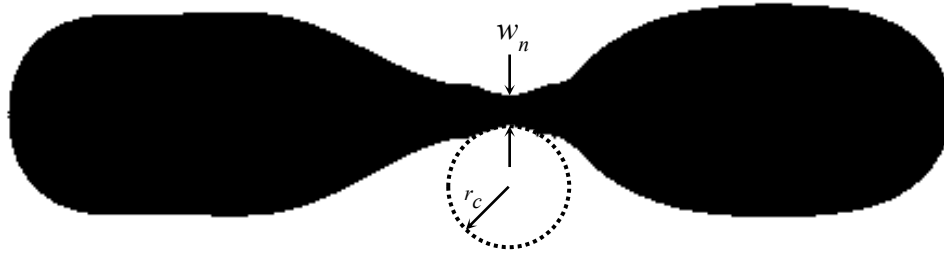
Figure 4.28 Contour of a bubble inside the constriction showing the neck measured (w_n) as two times the circumferential radius (r_0) and the axial radius of curvature (r_c).

From all the experiments carried out, the power-law exponent β was found to be 0.33±0.06. Thus, the exponent value is close to a 1/3 which is a value previously reported in the flow-focusing junctions in microfluidic channels (Dollet *et al.*, 2008; Fu *et al.*, 2010; van Hoeve *et al.*, 2011; Lu *et al.*, 2014) and vertical axisymmetric pinch-off (Gordillo *et al.*, 2005). The exponent value is independent of the constriction shape, including angle, width or length. Moreover, the exponent value is independent of the liquid viscosity range used in this work which is contrary to the vertical bubble pinch-off in a tank (Burton *et al.*, 2005), where the exponent increased from 0.5 to 0.66 and 1 for the liquid viscosity values of 1-10 mPa.s, 10-100 mPa.s and > 100 mPa.s respectively. The coefficient α was found to be 4.27±1.28. The standard deviation of α is much greater than the standard deviation of β since its value depends on all the other flow parameters including flow-rate, liquid viscosity and constriction shape.
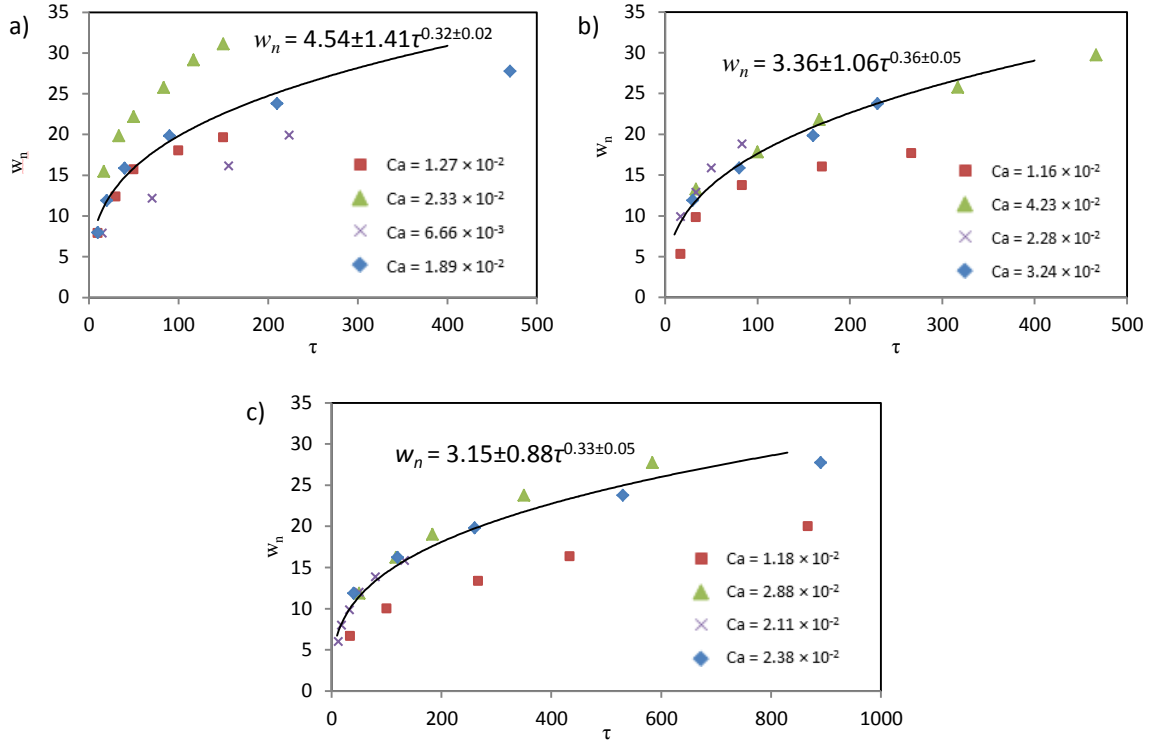
Figure 4.29 Plot of the neck collapse during snap-off for all of the four sudden constrictions (square -sharp 20 μm, triangle - sharp 40 μm, cross - long 20 μm, rhombus - long 40 μm) and three viscosities: a) 3.3 mPa.s, b) 7.4 mPa.s, c) 21.0 mPa.s.

Although it is the surface tension and the bubble curvature that initiates snap-off as indicated by the necessary change in the capillary pressure at the constriction, the analysis of all the forces acting on the neck might suggest otherwise. By comparing the three dimensionless values, i.e. the capillary number (Ca), Reynolds number (Re) and Weber number (We), which relate the importance between the surface tension forces, viscosity forces and inertial forces, one can find the most dominant forces based on the exponent. As τ is approaching 0, the circumferential radius ($r_0 = w_n/2$) can be taken as the characteristic length, and the radial velocity of the neck decrease can be taken as the characteristic velocity ($\frac{\partial r_0}{\partial t}$). Hence, the Reynolds number (relates inertial to viscous forces) is given by

$$\text{Re} = \frac{\rho r_0 \frac{\partial r_0}{\partial t}}{\mu}, \tag{4.9}$$

119

where ρ is the density of the liquid. The Webber number (relates inertial forces to surface tension forces) is given by

$$We = \frac{\rho r_0 \left(\frac{\partial r_0}{\partial t}\right)^2}{\sigma}.$$ (4.10)

Accordingly, the capillary number is given by

$$Ca = \frac{\mu \frac{\partial r_0}{\partial t}}{\sigma}.$$ (4.11)

It can now be assumed that $r_0 \propto \tau^{0.33}$ (Figure 4.29). The three numbers will, therefore, diverge as they approach the singularity, i.e. $Re \propto \tau^{-0.33}$, $We \propto \tau^{-1}$ and $Ca \propto \tau^{-0.66}$. Consequently, the inertial forces dominate over the surface tension and viscous forces as the neck is approaching its collapse. Similar results have been found by van Hoeve *et al.* (2011) at the flow-focusing junction in the microfluidic channel with a square cross-section. The exponents they have found were 0.33 for the first stage and 0.41 for the very final stage just before the collapse. It is difficult to measure precisely the very final stage of the collapse as the neck thinning is very fast, van Hoeve *et al.* (2011) used a frame-rate of 1 million frames per second. However, it seems the values of the power-law exponent found here (0.33±0.06) are in agreement with the pinch-off values at the flow-focusing junction. Additionally, they showed that the neck collapse is due to liquid inertia only and not gas/liquid inertia as in the case of the axisymmetric pinch-off by Gordillo *et al.* (2005) who showed that Bernoulli suction (gas inertia) also contributes to the final collapse of the neck. In this work, however, the axial radius of curvature scales with a power-law exponent 0.55±0.03 which is larger than 0.33±0.06 obtained for the circumferential radius of curvature. This indicates that there is a difference in the neck decrease between the two radii. Thus, this analysis highlights the importance of understanding the neck collapse from a three-dimensional point of view, as

suggested by Eggers *et al.* (2007) and van Hoeve *et al.* (2011). Hence, by calculating the slenderness ratio (Eggers *et al.*, 2007) given by $r_c / r_0 \propto \tau^{0.55}/\tau^{0.33}$, the slenderness approaches 0 as the neck is thinning and so the neck becomes less slender. Therefore, the liquid that reduced the neck in its final moments must be flowing spherically inward. This is again a similar result that was found by van Hoeve *et al.* (2011), and hence, it can be concluded that the neck collapse is driven by the liquid inertia and the decrease in the slenderness ratio in the final collapse of snap-off.

4.3.2.5 Daughter bubbles

As the bubble passes through one of the constrictions, it may break once as suggested by the break-up time or more to generate more than one daughter bubble. Again, whether the bubble will snap more than once depends on the temporary capillary pressure drop and, hence, the curvature of the bubble. More snap-off means smaller bubble size distribution and, therefore, the desired reduction of gas mobility in applications such as enhanced oil recovery. In this section, the number of new bubbles produced is correlated with the flow parameters (bubble size and capillary number).

Since the break-up time for the constrictions was dependent on the thin films and, therefore, the capillary number, the number of new bubbles generated must also be strongly dependent on it. Increasing the capillary number produces thicker liquid films in the channel, which snaps bubbles much quicker. In addition, thicker films may snap bubbles more than once, since after snapping off the first bubble, the tip of the remaining bubble is much smaller, i.e. has a large curvature. Consequently, the capillary pressure forces liquid to invade the throat again and because of the narrow tip/neck of the bubble (often smaller than the height and the width of the constriction) the liquid generates many new bubbles in the channel. Examples are presented in Figure 4.30.
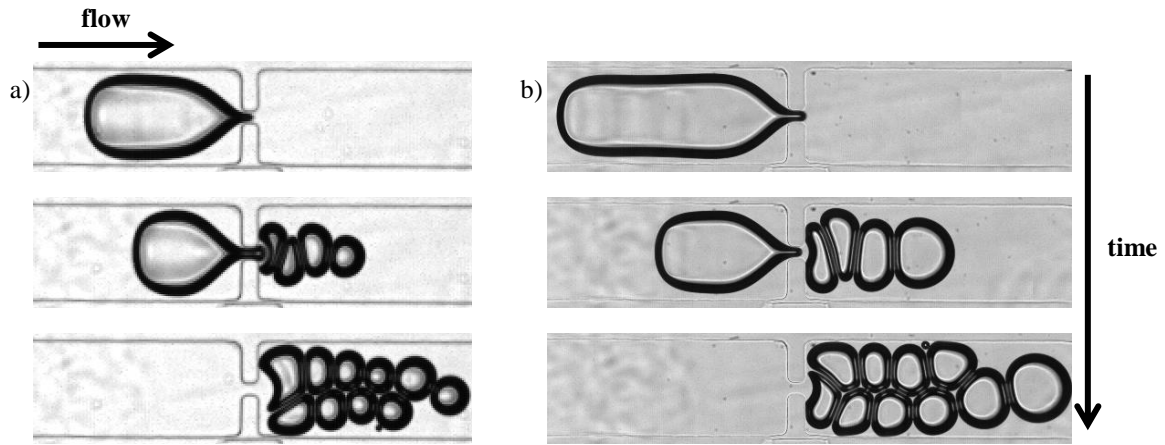
Figure 4.30 Illustration of a repeated snap-off in the sharp sudden 20 μm constriction: a) Ca = 5.51×10^{-2}, $L_0^* = 5.27$, b) Ca = 3.53×10^{-2}, $L_0^* = 8.20$. In both of the examples, the number of bubbles generated via snap-off is the same (10), however, in (a) the bubble is shorter but moving at a higher capillary number, thus generating the same number of bubbles as the longer bubble in (b). Notice that the final number of bubbles generated in both of the cases is 11. However, one of the bubbles which was vertically elongated in the downstream channel was divided by the newly generated bubble (this is about to happen in the second picture in (a)) into two smaller bubbles. The bubbles that were not generated via snap-off are omitted from the daughter bubbles analysis.

Naturally, longer bubbles can be snapped more frequently, since they take a longer time to pass through the constriction during which the capillary pressure might drop again and, therefore, produce more bubbles. Thus, the number of new daughters generated (n_d) should be directly proportional to the product of the initial bubble size as well as the capillary number, i.e. Ca $\times$ L_0^*. However, in the 40 μm constriction, especially the sharper ones, the break-up time was also dependent on the initial bubble size. It was found that the size of the first bubble must be subtracted from the initial size. Thus the number of new daughters generated was calculated from the remaining part of the mother bubble and the capillary number. For simplicity, the same calculation was done for all of the constrictions. The total number of new bubbles generated is, therefore, plotted as a function of Ca $\times$ L_r^*, where $L_r^* = (L - U_b \tau_b)/H$.

The total number of new bubbles generated was found to increase with the product of the capillary number and the remaining bubble length. As expected, narrower constrictions generated more bubbles at relatively similar capillary numbers. The liquid can invade the narrow constrictions more easily due to the larger curvature of the bubble inside the constriction, and, therefore, lower pressure. This generated a repeated snap-off that based on the experimental results produced almost twice as many new daughters. Moreover, there was almost no significant difference between the two constrictions of the same width. The break-up time was slightly shorter for the longer constriction, which resulted in smaller bubbles generated. However, when the width of the constriction is the same, so is the curvature of the remaining mother bubble inside the constriction once the first bubble is snapped, which gives the same capillary pressure.

Since the number of new bubbles generated for the wider constrictions was almost two times lower and the length of the constriction had no significant influence, results from all of the constrictions are plotted on the same graph (Figure 4.31) where $Ca \times L^*_r$ is also scaled by 0.5 for all of the wider constrictions. All of the data points fall on the same line, suggesting that the total number of new bubbles generated for the range of the capillary numbers and bubble sizes used increases almost linearly with both of the parameters. More bubbles generated should be inversely proportional to the bubble size distribution which was also found to decrease with the capillary number (Wu *et al.*, 2017) in a 3D constriction (see Figure 4.1). The number of bubbles generated here was not sufficient to analyse the actual bubble size distribution.

It has to be noted that there is quite a bit of a scatter in Figure 4.31 due to the fact that the same bubble lengths do not always represent the same bubble volumes. As the capillary number increases, bubble deposits thicker films which reduce the width of the bubble in the

channel and so a bubble of the same length as the one at lower capillary number occupies less volume. In addition, the films also re-arrange at different location of the bubble (Wong *et al.*, 1995a), thus changing the shape and, therefore, the curvature of the bubble in the straight channel. It would be interesting to study snap-off numerically so that the evolution of bubble shape (with regards to volume) and the velocity field of the liquid surrounding the bubble could be well investigated in all three dimensions.
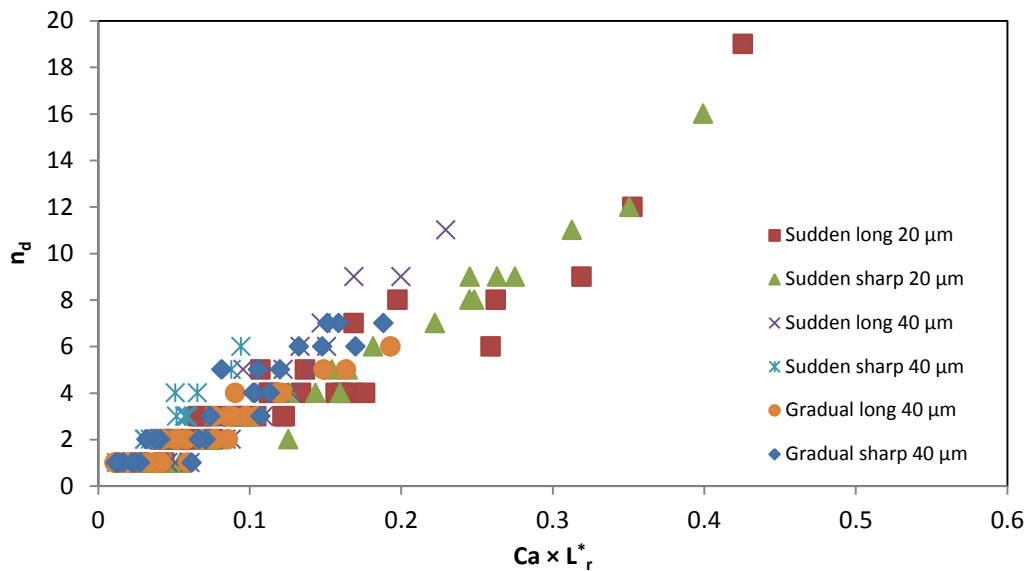
Figure 4.31 Plot of the new daughters generated as a function of the capillary number and initial bubble length.

4.4 CONCLUSIONS

Single bubbles at various capillary numbers were investigated in shear flow in sudden constrictions. The elastic strain of the bubble was described well by the capillary number, thus suggesting that the deformation is dependent on the surface tension and viscous forces. The bubble length increased with the product of the capillary number (due to larger viscous shear forces) and the initial bubble length (due to the bubble being confined by the walls of the constriction in the transversal direction). The bubbles were boundary-free in the transversal

direction upon exiting the constriction, thus, generating only a capillary number dependence. The velocities of the front tip and the rear tail increased inside the constriction, as suggested by the mass conservation. Moreover, the velocity of the rear tail was found to be greater across different capillary numbers due to bubble contraction caused by surface tension. The sharper constriction generated similar results, although all the extremities were smaller.

Snap-off was also investigated through channels with variable cross-sections. The break-up time in the sudden narrow constrictions was found to be proportional to the capillary number to the power relatively close to -2, which corresponds to the contribution from liquid films. In addition, the neck decrease was fast and primarily due to thin liquid films surrounding the bubble near the front. Break-up time calculated in the gradual constriction of almost the same dimensions confirmed those results. In wider constrictions, where the bubble curvature was two times smaller, the break-up time was also found to be dependent on the bubble size, although, weakly for the long constrictions and strongly for the sharp constrictions. Gradual wide constrictions were found to have similar effects to the sudden constrictions. However, bubble break-up time was slightly faster, due to the contribution from more uniform films and smaller axial radius of curvature.

The analysis of the neck collapse produced interesting results. The neck scaled with a power exponent close to 1/3 across different constrictions, liquid viscosities, bubble velocities and bubble sizes. Such results were found to be totally different from vertical bubble pinch-offs where the scaling exponent varied with the liquid viscosity. The exponent value found corresponds to the effect of inertia, even though inertial forces are often negligible on a microscopic scale. Thus, this novelty finding of inertia contribution during the neck collapse in snap-off should be incorporated into future models of bubbles flowing in porous media for both oil recovery and soil remediation. Moreover, the three-dimensional analysis of the neck

was found to be essential. The axial radius of curvature was found to have a larger power-law exponent than the circumferential radius during the final thinning of the neck. Such results correspond to the neck of the bubble becoming less slender as it approaches its collapse, primarily caused by the liquid flowing spherically inward.

The number of bubbles generated due to snap-off was found to be dependent on the capillary number and bubble size. However, because of the break-up time dependence on the bubble size in some of the wider constrictions, the size of the first bubble generated (governed by the break-up time and initial velocity) was subtracted from the initial size. The number of new daughter bubbles was, therefore, found to increase with the product of the capillary number and the remaining bubble length. In addition, the data from all of the constrictions fell on to the same line, with the number of bubbles generated in the wider constriction to be almost twice as small. These results suggest that the bubble size, the capillary number and the shape of the pore are not always sufficient to calculate the number of bubbles generated in the porous media where the bubble dynamics are mostly dominated by snap-off. The break-up time for a particular constriction geometry (or general channel shape) may also be required in order to obtain the true number of bubbles generated. Thus, the above results suggest that for applications such as oil recovery and soil remediation, the control parameters for predicting bubble size distribution after passing through various pores include, the capillary number and the remaining bubble length which is also dependent on the break-up time.

5 FLOW OF GAS-LIQUID FOAMS IN MICROFLUIDIC CHANNELS WITH CONSTRICTIONS

In this chapter, flow of *in situ* generated foam through microfluidic channels with constrictions is studied. Microfluidics allows good visualisation of two-dimensional foam flow. Because of well-controlled and stable foams, microfluidics enables the study of their mechanical properties. In addition, gravity effects are negligible in a microfluidic system which reduces vertical drainage and, therefore, coalescence. The bubbles have almost complete monodisperse size distribution, and thus there is no difference in the Laplace pressure between the neighbouring bubbles, which means no gas diffusion. Coarsening is, therefore, absent during the experiments. This chapter presents various foam regimes generated in the flow-focusing device (Garstecki *et al.*, 2004) that are forced to flow through different constrictions, such as a sudden (or a gradual) contraction followed by a sudden (or a gradual) expansion. Foam structures undergoing deformations, topological changes and bubble break-up are investigated as they pass through different constrictions.

5.1 INTRODUCTION

One of the first papers on foam flow through channels with variable cross-sections was published by Calvert (1988). His work was primarily motivated by fire-fighting applications where the foam is required to pass through valves. He studied flow through four two-dimensional models of the following types of valve: diaphragm; gate; globe; and, ball (Figure 5.1). Each model was designed in such a way that it was possible to adjust the opening to fully open as well as 50% open by area. He observed that stagnation points might be found in areas of low shear rates, generally where the velocity is lower compared to other parts of the channel. Moreover, the more complex design of a globe valve can cause high shear rates,

which can almost completely degrade the foam to an air/water slug. He, therefore, concluded that it is crucial to use valves such as diaphragm or gate since foam is able to expand through wider angles without undergoing significant degradation.
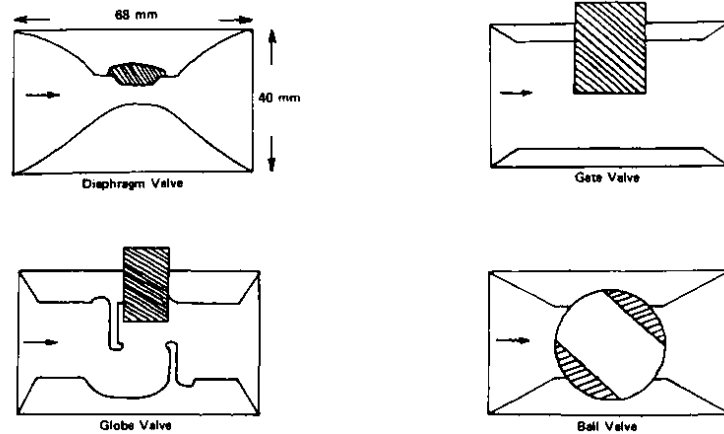
Figure 5.1 Original illustration of the four valves studied by Calvert (1988).

A study that investigated a two-dimensional flow of foam through a contraction was carried out by Dollet (2010) with regards to velocity, elasticity and plasticity. He analysed foam flow in a Hele-Shaw cell with a gap of 2 mm through a sudden contraction followed by a sudden expansion. Dollet showed that the foam in his case did not exhibit any dead zone or vortices in the corners of the channels, contrary to other viscoplastic (viscous fluid that has a yield stress) fluids such as gels (Jay *et al.*, 2002). Moreover, the flow downstream of the constriction was purely convergent meaning the velocity along the transversal axis above the central line ($y = 0$) was negative while below it was positive. However, at the exit, the velocity vectors diverge from the central line before reaching a maximum value and start converging towards the centre (Figure 5.2 (a)). Dollet also showed that the principal stress occurs towards the contraction were bubbles tend to be deformed the most by the converging channel, showing that they elongate as they approach the constriction. He observed that just before exiting the constriction, bubbles slightly relax before changing their elastic stress and becoming compressed. As they flow further away from the constriction their elastic stress

changes towards equilibrium, however, final equilibrium is not reached as the foam gets out of the field of view (Figure 5.2 (b)). With regards to plasticity, Dollet showed a map of the frequency of T1 events. The topological re-arrangement mostly occurred near the contraction, more specifically within a radius of 7 cm from the central point of it (Figure 5.2 (c)). This showed that foam behaves as a viscoelastic fluid in regions relatively further away from the constriction which can be attributed to the elastic nature of the foam and explain the reason for the streamlines going back towards the central axis. Dollet also showed that other parameters, such as the bubble area, contraction length and width, as well as flow-rate, did not have a qualitative effect on the foam flow. More specifically, the behaviour of foam did not differ significantly when varying those parameters. Similar analysis techniques are applied in this thesis to foams flowing through expanding microfluidics channels. Moreover, the foam investigated is of a much higher liquid fraction (~13%) compared to Dollet's (0.2-0.4 %).

Simulations of convergent flows have also been carried out in order to compare the results with the experiments and to find out if they can be used to predict the foam flow (Jones *et al.*, 2011; Jones and Cox, 2012). Jones and Cox showed that simulations, using Surface Evolver (Brakke, 1992) with a quasi-static model (quasi-static refers to a slow-velocity flow, where the inertial forces are low and can be neglected), generally agree with the experiments with regards to velocity fields, profiles, strain and stress. Some variations did occur since not all the experiments were carried out in the quasi-static regime; however, they fell within the range of the error bars. Moreover, they showed that the results agreed best when the experiments were very close to a two-dimensional system, meaning higher channel depth or higher free-stream velocity reduced the agreement.
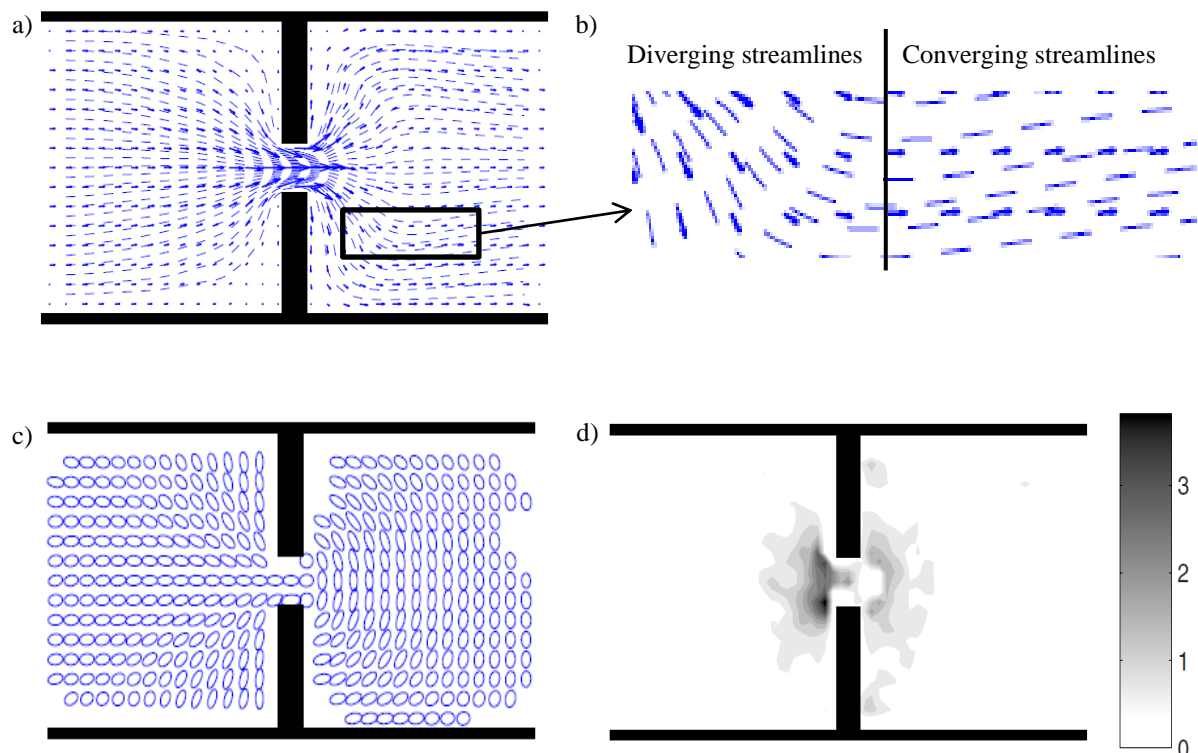
Figure 5.2 Images representing the contraction flow investigated by Dollet (2010): a) velocity profile b) enlarged area of (a) that shows diverging and then converging streamlines in the downstream section, c) elongation stress, d) T1 distribution.

Another problem was studied by Dollet and Bocher (2015) in a gradually converging channel using two different solutions, namely, SDS (sodium dodecyl sulphate) with negligible surface viscoelasticity and, hence, low wall friction, and a mixture with a fatty acid that has large surface viscoelasticity and, thus, large wall friction. Negligible friction at the side walls makes the foam to follow a self-similar profile which is comparable to a Newtonian profile since the foam is quasi-incompressible. However, introducing higher friction at the walls is responsible for losing the self-similarity and also shows that the velocity at the side walls is lower compared to the centre of the channel. They also observed that bubbles elongate more at the walls in the convergent section of the channel.

On the capillary scale, most of the conducted research focused on fundamental studies of bubble pinch-offs in microfluidic channels at the flow-focusing junction (Garstecki *et al.*,

2006; Dollet *et al.*, 2008; van Hoeve *et al.*, 2011; Lu *et al.*, 2014), as well as single bubbles through glass capillaries or a microfluidic constriction already presented in Chapter 4.

A more relevant study was conducted by Liontas *et al.* (2013), who studied foam flow in a microfluidic channel with a constriction representing a gap between two rocks. In their investigation, they showed that bubbles could break via different mechanisms which can involve interaction between bubbles and walls of the constriction, as well as break-ups only through bubble-bubble interaction. They referred to these mechanisms as neighbour-wall and neighbour-neighbour pinch-off, respectively. Moreover, by plotting a graph of bubble volume against a capillary number, they obtained a map with particular regions of each break-up for different foam types. Therefore, for their particular constriction, one could use their study to predict the given topological change based on bubble size and velocity. A study carried out by Liontas *et al.* (2013) is further investigated in this thesis by varying constriction shapes for a similar system. The study here presents that foams can break through more than just the three usual mechanisms associated with the oil recovery (2.6.1.1). In addition, the conditions that each of the break-up favours are described, which should improve understanding of the topological changes in porous media for both oil recovery and soil remediation applications. Furthermore, these geometries could also be employed in other microfluidics systems to increase the total number of bubbles in the channel. This in turn would increase the polydispersity of the studied foams and therefore, be more applicable to real life foams which are rarely monodisperse. Polydisperse foams would allow studies of coarsening caused by the gas diffusion only since the liquid drainage and therefore, coalescence are absent in the micro-flows (see 2.5).

5.2 CHANNEL AND SOLUTION PROPERTIES

Two different channel dimensions were used in this chapter: (i) the first one was used for the generation of foams flowing through a constriction (Figure 5.3 (a)); (ii) the second one was used for the generation of foams flowing through an expansion (Figure 5.3 (b)). The dimensions of the flow-focusing junctions (highlighted in Figure 5.3) and the depth of the channels were kept constant in their corresponding subsections. Each constriction or expansion investigated is shown in their relevant results/discussion sections.

Only one liquid solution was used throughout this chapter; NaDBS in the water at a concentration of 3 cmc ($\sigma = 32.2$ mNm^{-1}, $\mu = 0.93$ mPa.s).
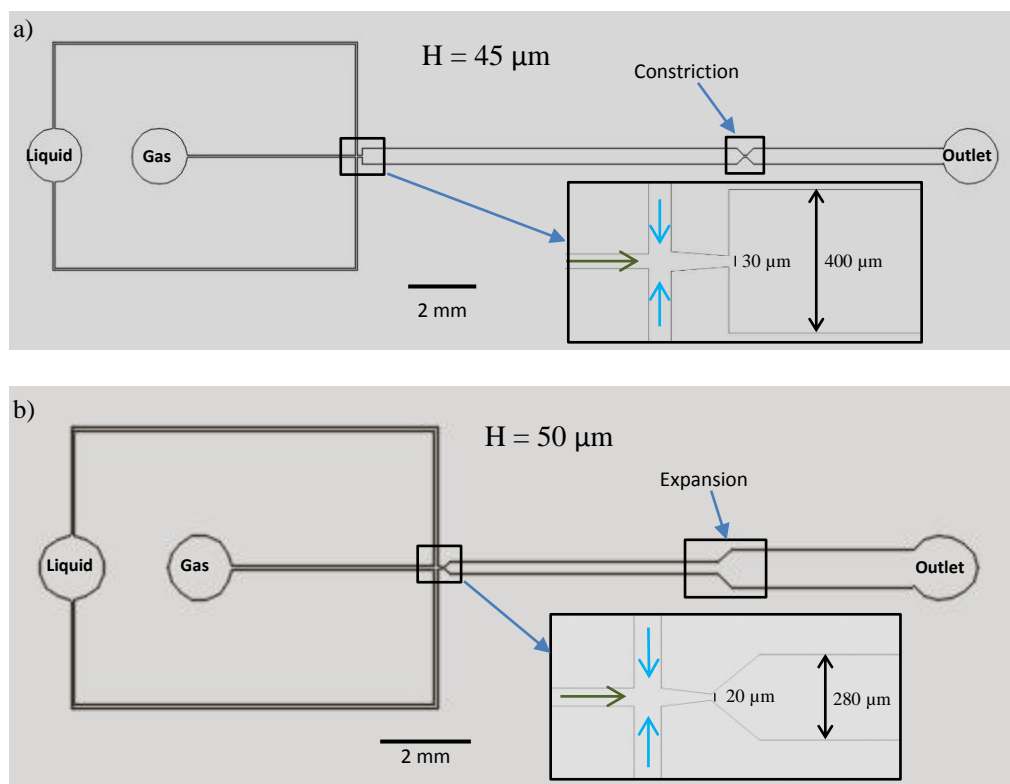
Figure 5.3 Schematics of the two channels used in this chapter: a) dimensions of the channels used for constrictions, b) dimensions of the channels used for expansions (green arrows indicate gas phase whereas blue arrows indicate the liquid phase). The dimensions of a constriction (or expansion) are shown in the relevant results section.

5.3 RESULTS AND DISCUSSION

5.3.1 CONSTRICTIONS

5.3.1.1 Sudden contraction followed by expansion

The first constriction studied in this chapter was a sudden contraction followed by sudden expansion. The circuit was fabricated as explained in Chapter 3 and included the flow-focusing part from Figure 5.3 (a) as well as the constriction. The dimensions of the constriction can be seen below (Figure 5.4) with the width (w_c) 35 μm and the length (l_c) 75 μm.
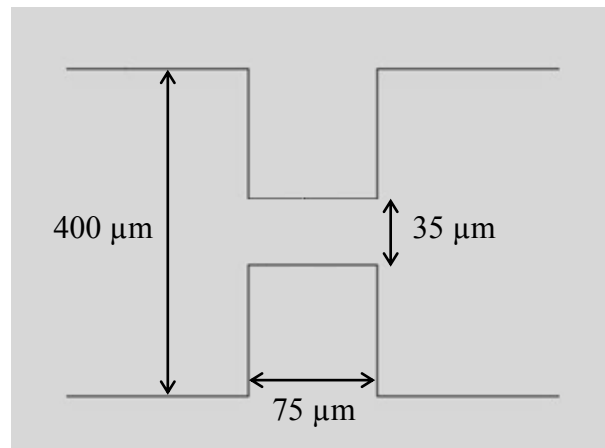
Figure 5.4 A schematic of the sudden contraction/expansion and its dimensions (not to scale).

A foam regime map (Figure 5.5) was drawn for the sudden expansion as a function of gas and liquid pressure imposed (controlled through a pressure controller see 3.2.7). As mentioned in Chapter 3, minimum gas pressure was required at each of the liquid pressures for the gas to enter the orifice and generate the bubbles. Before that, there is only liquid flow in the channel. Once the dripping bubbles were generated, they then increased in size and frequency. Above certain gas pressures at each liquid pressure, the foam ceased to exist, and only annular flow was observed which was identified by long perturbed slug, this was not assumed to be foam and therefore not taken into account in the analysis. Downstream of the

constriction the bubble size distribution was increasing for the larger bubbles (except for the

bamboo) as the liquid pressure increased due to the higher number of topological changes.
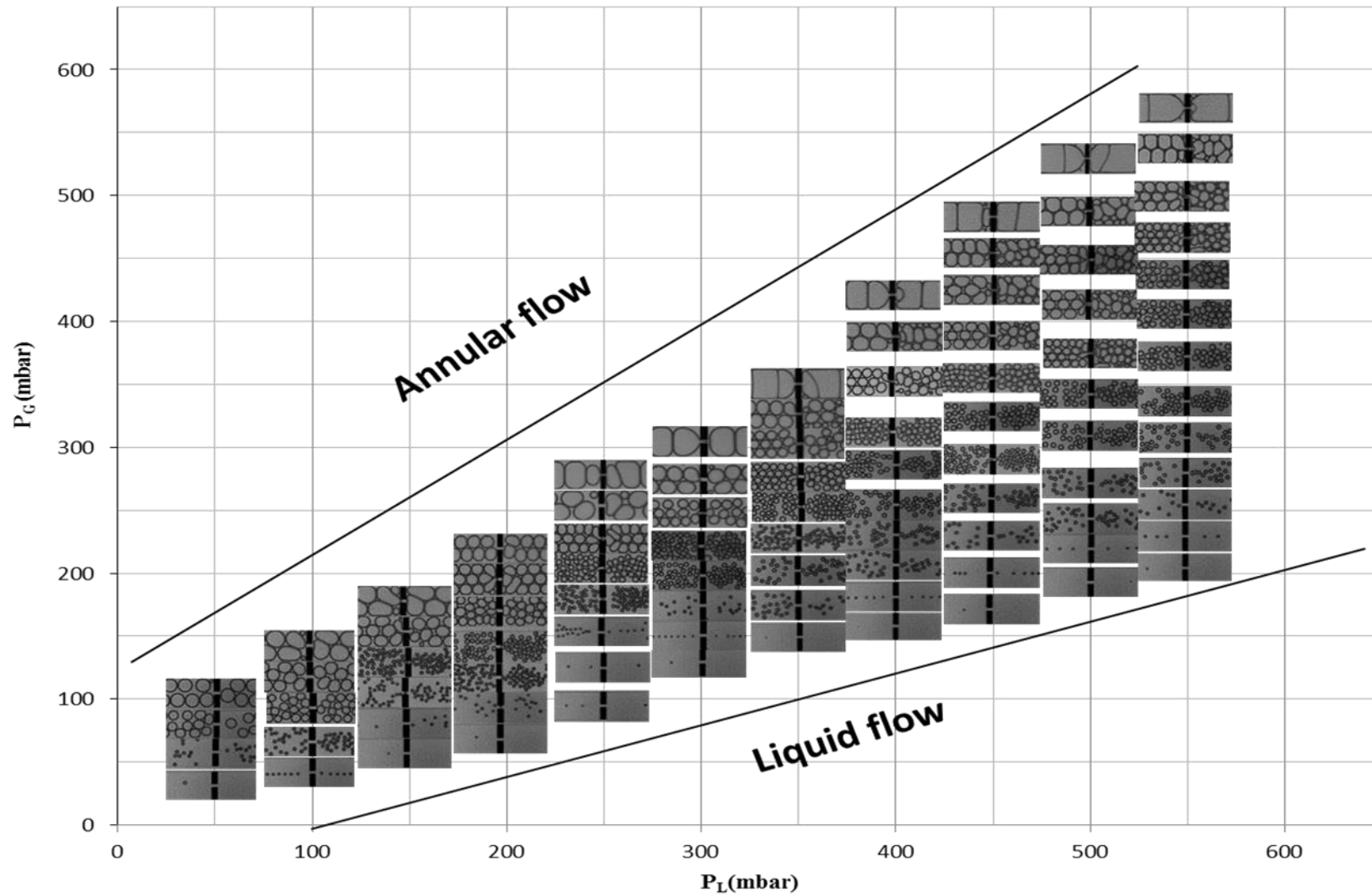
Figure 5.5 A foam regime map of the sudden constriction as a function of liquid and gas pressure.

5.3.1.1.1 Phenomena observed

Foam dynamics as they pass through the constriction were studied for all four foam types (>3-row, 3-row, 2-row, 1-row, see 3.2.7.2) and analysed in terms of their size. The size of the bubble in the microfluidic channels is related to the foam liquid fraction or quality (Raven *et al.*, 2006). No effect, as well as three types of break-ups, were observed as bubbles pass through the constricted throat, namely snap-off and two different types of pinch-offs; neighbour-wall and neighbour-neighbour.

5.3.1.1.1.1 No effect

Each of the four foam regimes at a specific condition (presented later) underwent "no effect". This means that the foam entering the constriction as well as exiting was not significantly affected. The bubbles could slightly increase in size through expansion due to the pressure drop ($P_1V_1 = P_2V_2$) or even re-arranged themselves so that bubbles at the bottom wall upstream would end up at the top downstream of the constriction (Figure 5.6(c)). However, the structure exhibited no visible difference, and the bubble size distribution remained unchanged. Foams that were composed of small bubbles or under low shear rates often managed to pass through the constriction without any effect. At low velocities, the surface tension at the interface allows the bubbles to deform elastically so that each bubble first elongates horizontally as it enters the constriction and then vertically (compresses) as it exits the constriction. This phenomenon is due to each bubble having its parts flowing at different velocities, in the same way as the single small bubbles in Chapter 4 (4.3.1.2). As the bubble approaches the constriction, its front tip accelerates due to the convergent flow through a smaller cross-section while the tail is still in the upstream section. This forces the bubble to elongate inside the constriction. Once the front fully passes through the orifice, it slows down

as the downstream cross-section is wider. However, at the same time, the rear of the bubble is accelerating through the constriction and, when exiting, forces the bubble to change its elastic stress so that the bubble elongates vertically.
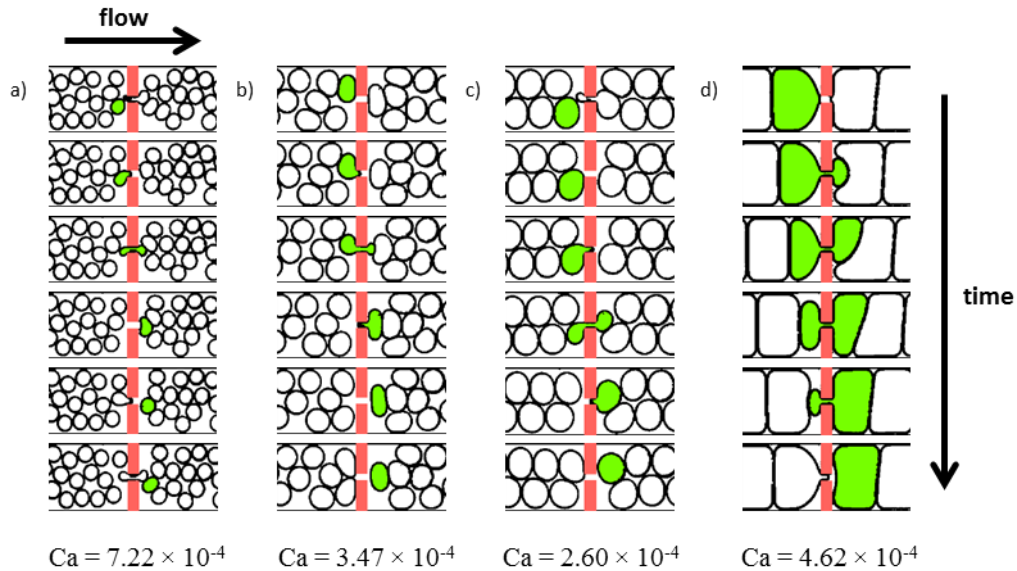
Figure 5.6 Consecutive sequence of images of foams that exhibit no effect: a) >3-row, b) 3-row, c) 2-row, d) 1-row. Notice how the green bubble stretches when inside the constriction and then gets compressed for a), b) and c). Bamboo, not that clear since it is almost wetting the channel's walls because of its size and hence, has no space to elongate vertically. In c), the bubbles alternate, notice how the green bubble changes its position from bottom to top upon passing the constriction.

It was observed, across many conditions, that bamboo foam did not break or change its structure at all. As the bubbles always flow one after another and almost wet the channel walls, the foam always passed through the constriction in a systematic manner. Because of its initial structure, the bubbles cannot approach the constriction together and, therefore, break through contact with its neighbouring bubbles. This foam also required much larger gas pressures as can be seen in the flow regime map (Figure 5.5), which produced slightly drier foams and therefore, snap-off was not observed. The bamboo foam is, thus, not included in the break-up analysis through sudden contraction/expansion. It is worth noting that in porous

media where bubbles can flow as a train of bubbles just like the bamboo foam snap-off is not very likely when flowing through variable cross-section similar to a constriction. Thus, snap-off is favoured more near the in-flow end where bubbles are still relatively wet and flow as slugs rather than as trains of bubbles.

5.3.1.1.1.2 Snap-off

One type of mechanical break-up that bubbles can undergo in constricted flows is snap-off. This type of break-up does not involve an interaction of a bubble with its adjacent bubbles but instead is caused by the change in capillary pressure, as shown in Chapter 4. For this break-up to occur, the bubbles must be wet so that sufficient liquid can flow around them and accumulate in the throat before the snap-off. The constriction does favour snap-off since it is narrow and longer than a sharp constriction which allows the liquid to accumulate faster in the constriction throat. In the system here, snap-off mainly occurred when the bubble approached the constriction from one of the sides (Figure 5.7) with liquid flowing from the other. This caused thinning of the bubble neck from one side (where the liquid could accumulate) as can be seen in all three foam regimes in the figure mentioned above. The blue arrows highlight where the liquid pushes on the neck prior to snap-off. For all three foam regimes, snap-off was observed on its own for a relatively small number of conditions, with the exception of the staircase foam, and often accompanied by the neighbour-wall pinch-off. Since a thorough study of snap-off was presented in Chapter 4, and this chapter considers foams and a closer look at the interaction between the bubbles, snap-off will only be briefly mentioned throughout this chapter.
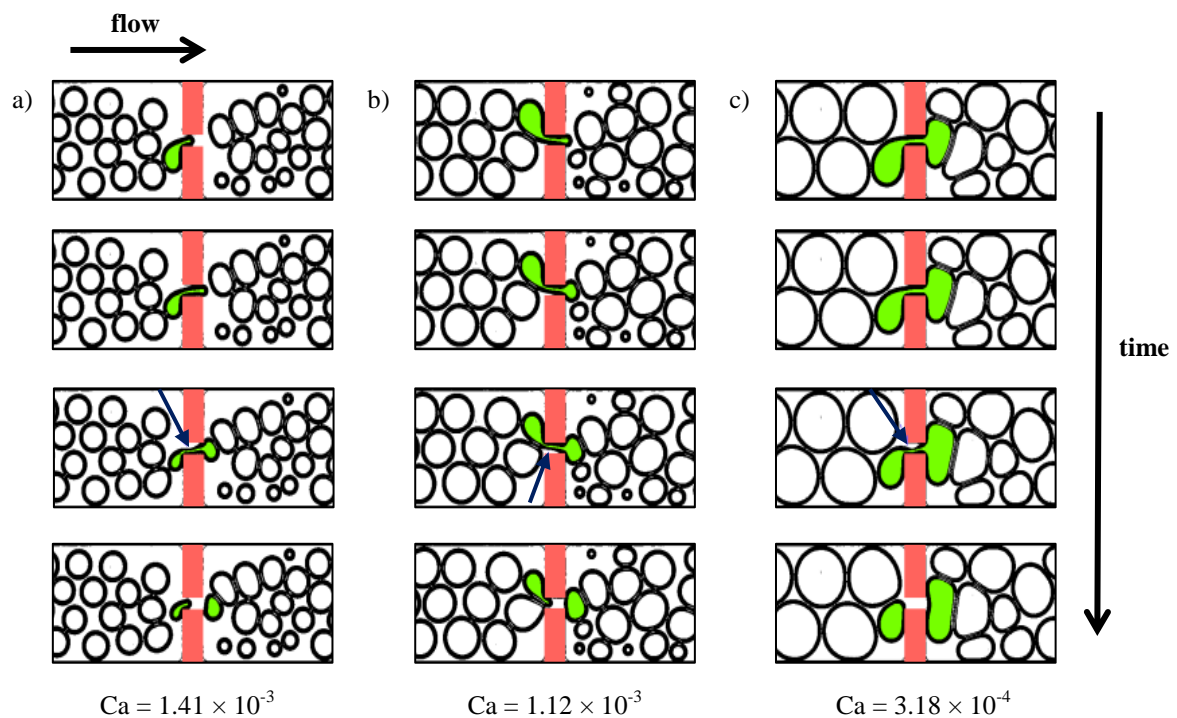
Figure 5.7 Consecutive sequence of images of foams undergoing snap-off: a) >3-row, b) 3-row, c) 2-row. The blue arrows (in all the third pictures from top) indicate where the liquid pushes on the bubble neck to initiate snap-off.

5.3.1.1.1.3 Neighbour-wall pinch-off

The first type of break-up that was observed for all three foam regimes was a type of break-up previously described in the literature as the neighbour-wall pinch-off (Liontas *et al.*, 2013). This type of break-up, as the name suggests, involves interaction between the main bubble, its neighbouring bubble and the wall of the constriction. The bubble approaching the constriction stretches as it enters the constriction. However, as bubbles are now moving at faster velocities and flowing closer to each other, another bubble tries to enter the constriction simultaneously. It results (Figure 5.8) in the bubble pressing on the tail of the bubble already in the constriction against the wall of the constriction. As it continuously pushes against the wall, the lamella of the bubble narrows until it breaks and ends up dividing the bubble into two pieces. For this type of pinch-off to occur, two bubbles must always approach the constriction

relatively close to each other so that two of them try to pass through the constriction together. Depending on the initial size of the bubble, as well as arrangement, each bubble can be divided once or more times. Some larger bubbles were observed to be pinched up to four times, thus increasing the number of bubbles in the channel by a factor of 4. However, the frequency of the break-up also increases with velocity. If the velocity is not fast enough, only some bubbles may undergo pinch-off while others manage to pass through the throat unaffected. In Figure 5.8 (a) for >3-row foam, the green bubble is divided into two smaller pieces, while the blue bubble is unchanged, resulting in three bubbles downstream of the constriction. In the example given in Figure 5.8 (b) for 3-row foam, bubbles are relatively large and tightly packed. As the green bubble elongates across the constriction, its blue neighbour breaks it via the neighbour-wall pinch-off. Now, the left-behind tail of the green bubble ends up splitting the blue bubble through the same mechanism. However, the central red bubble is also close to the constriction and ends up dividing the small green tail again. This means that the green bubble was divided twice resulting in three smaller bubbles downstream of the constriction. For the 2-row foam, the break-up is very systematic. In the example given in Figure 5.8 (c), the green bubble once again is divided twice; first by the blue bubble and then by the red one. The break-up alternates in this case so that the total number of bubbles is three times larger downstream of the constriction. It has to be noted that the neighbour-wall pinch-off is closely related to the lamella division since the lamella of the bubble is thinned against a wall. However, a large bubble arriving at the branching point may have its interface wrapped around a rock and as it continues to be displaced by, for example, a liquid, its lamella thins and breaks independently of other bubbles. Thus, both break-ups possess similar features and can be considered as part of the same family of break-up.

140
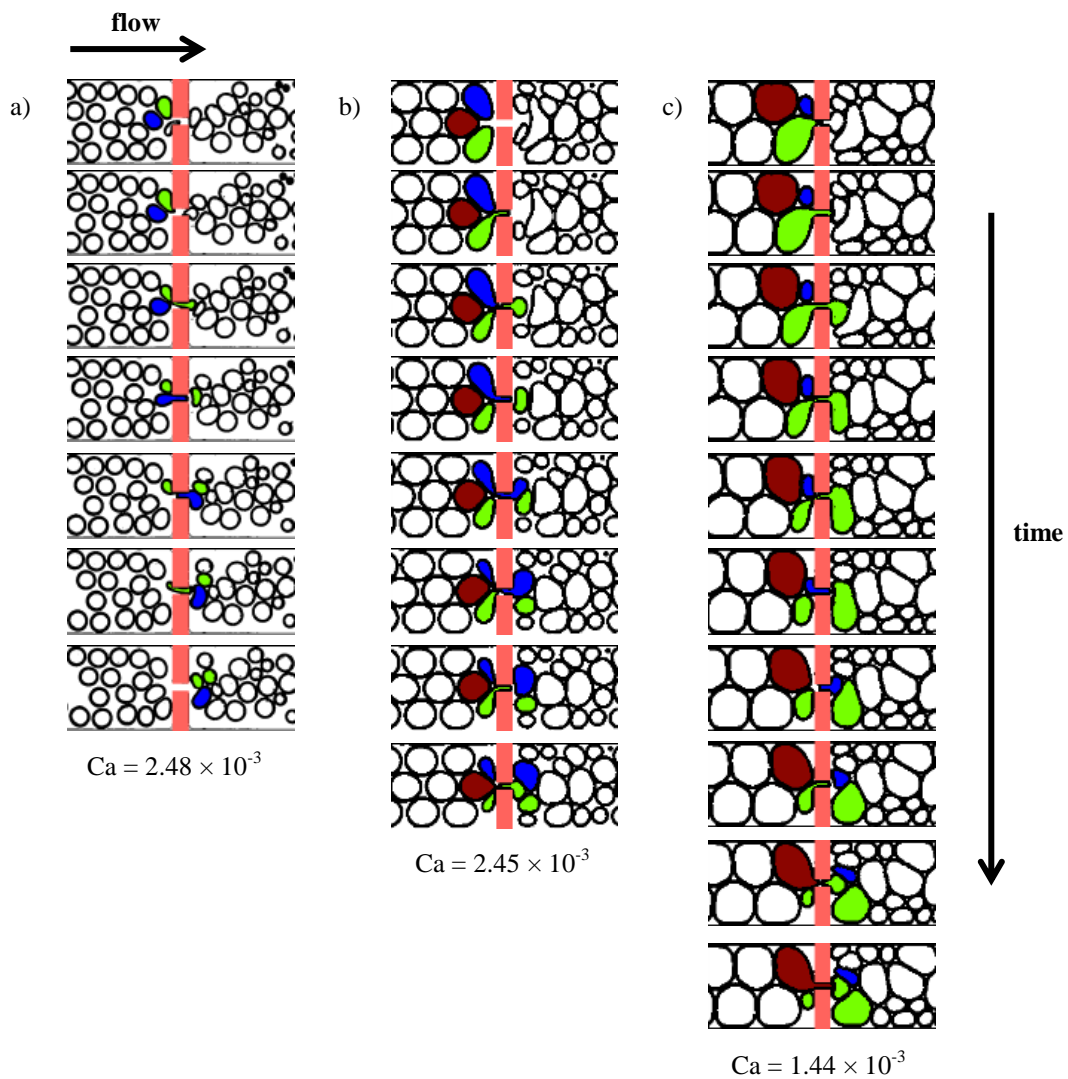
Figure 5.8 Consecutive sequence of images of foams that exhibit neighbour-wall pinch-off mechanism; a) >3-row, b) 3-row, c) 2-row. The green bubble in each sequence is the bubble that gets pinched into smaller bubbles. Notice in (b) the green bubble is divided twice, generating three bubbles. Moreover, its tail pinches the blue bubble resulting in only two bubbles. Thus, the pinch-off in the 3-row foam is not always uniform. In (c) the green bubble is divided twice and so are the rest of the bubbles when they flow through the constriction, generating three times more bubbles in the downstream section.

5.3.1.1.1.4 Neighbour-neighbour pinch-off

The second type of pinch-off observed in the constriction for $\geq$ 3-row foam was neighbour-neighbour pinch-off, also known as "structure induced capillary instability" (Golemanov *et*

al., 2008). This break-up as the name again suggests, involved a three-bubble interaction and the bubble being broken up along with its two neighbours. From Figure 5.9, it can be seen that the central bubble approaches the constriction first, and as the front flows faster than the tail, the velocity gradient along the interface causes the bubble to elongate. Its two neighbouring bubbles are so close to each other that they confine the central bubble, and because of the high shear rates, they also try to enter the constriction. By pressing on the tail against each other, they pinch off the tail of the central bubble, breaking it up into two pieces. This break-up is similar to the neighbour-wall pinch-off, differing only by how the bubble edge replaced the hard wall of the constriction. For this mechanism to occur, the shear stress must be sufficient so that the soft edges of the bubbles can break another bubble. Surfactant interfaces can support mechanical stress (Sadhal and Johnson, 1983); thus, they are rigid to some extent (actual rigidity depends on the surfactant type). Increasing the capillary number and therefore, the flow velocity can increase the rigidity, thus explaining the necessity for high capillary numbers for this pinch-off to occur. Additionally, the bubbles must flow very closely packed so that 3 bubbles always try to approach the constriction together. Therefore, strong interactions between the adjacent bubbles as well as viscous forces (due to high capillary number) contribute towards the elastic stress of the bubble and result in a capillary instability of the central bubble. In such confinement and arrangement, the stress exerted on the bubble in order to break does not have to be significant (Denkov *et al.*, 2009), which could explain why bubbles are able to break the lamella of the central bubble. If the arrangement of bubbles is such that the central bubble is not flowing first, the neighbour-neighbour pinch-off might not be triggered. This type of pinch-off occurred only for >3-row and 3-row foam. Naturally, the staircase foam structure does not allow three bubbles to approach the constriction together, so the pinch-off is absent for this foam regime. It has to be noted that whenever

neighbour-neighbour pinch-off occurs, the neighbour-wall pinch-off conditions are satisfied and thus, the neighbouring bubbles always break through the latter pinch-off, as can be seen in Figure 5.9. This means that neighbour-neighbour pinch-off is always accompanied by the neighbour-wall, as previously seen, the reverse is not true.
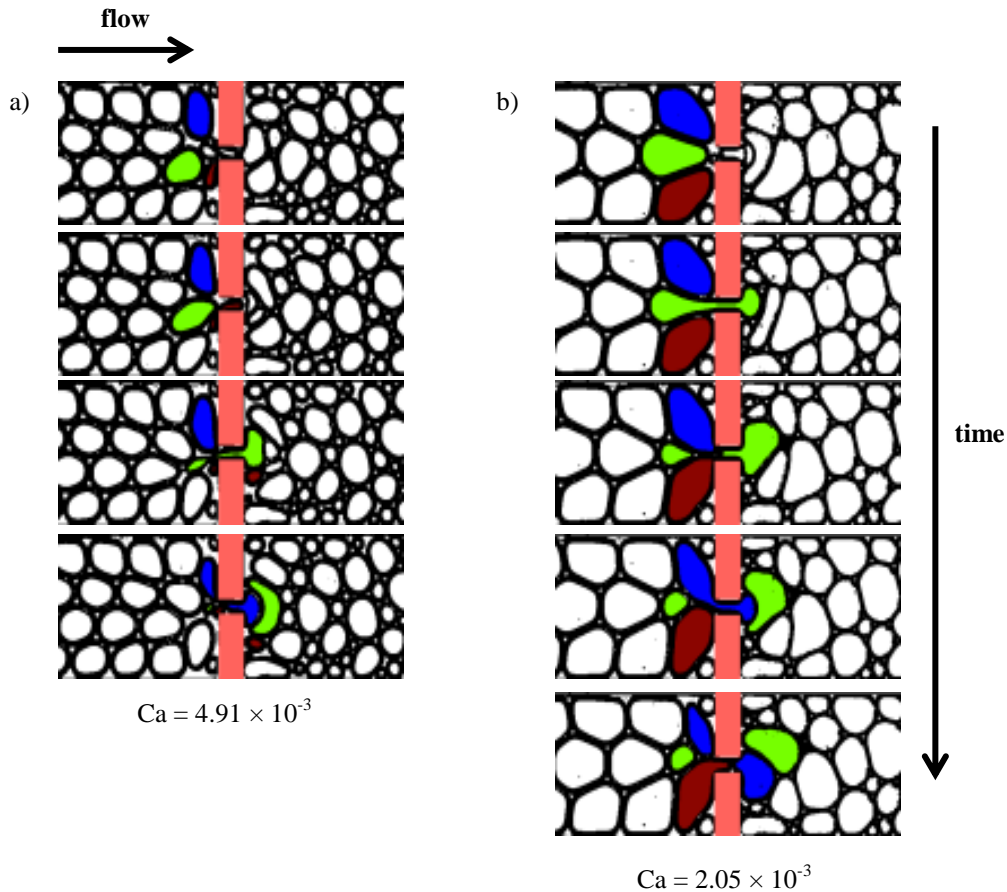
Figure 5.9 Consecutive sequence of images of foams that exhibit neighbour-neighbour pinch-off mechanism: a) >3-row, b) 3-row. The green bubble is the one that gets pinched by the adjacent bubbles. Notice how the blue bubbles in the last images are broken-up through the neighbour-wall mechanism.

5.3.1.1.2 Foam behaviour with regards to flow conditions

For each of the three foam types, a graph has been plotted of the capillary number ($Ca = \frac{U_f \mu}{\sigma}$) against the dimensionless bubble area ($A^* = \frac{A_b}{W^2}$). Since the bubble size is often related to the liquid fraction and therefore, foam quality, it should be a valid choice. The capillary number

was driven by the liquid flow-rate and gas pressure since all the other parameters in this section (viscosity and surface tension) were kept constant. Each of the different observed phenomena was plotted separately in order to identify regions of their occurrence. This means that knowing bubble size and velocity, which is related to the inlet pressure, enables prediction of bubble dynamics via one of the mechanisms explained above.

5.3.1.1.2.1 >3-row and 3-row foam

A graph (Figure 5.10) of the capillary number against the dimensionless bubble area has been plotted for two foam regimes, namely >3-row and 3-row foam. As both underwent identical phenomena, regions of each of them can be clearly distinguished, and both regimes can be plotted together. By looking at the graph, it can be seen that the three regions can be identified. At first, there is no effect region for small capillary numbers ($Ca < 1.85 \times 10^{-3}$) and almost all bubble sizes. This means that at low gas and liquid pressures, bubbles can flow through the sudden constriction without undergoing any changes i.e. the shear stress is not sufficient to force bubbles to enter the constriction simultaneously. Similarly, the liquid flowing around the bubbles is not sufficient to reduce the neck and initiate snap-off. Increasing the pressure further, and hence increasing the capillary number, bubbles start undergoing snap-off and neighbour-wall pinch-off. Since the two regimes often required that the gas pressure was lower than the liquid pressure in order to be generated, the foam was usually wetter, and snap-off often occurred together with the neighbour-wall pinch-off. This region has a minimum capillary number ($Ca = 1.15 \times 10^{-3}$ for $A^* = 0.133$ & $Ca = 1.78 \times 10^{-3}$ for $A^* = 0.056$) that can be seen on the plot. It has a slightly curved line between itself and the no effect region due to the fact that smaller bubbles require larger minimum capillary numbers for the same effect. This is because smaller bubbles can squeeze through the contraction significantly easier and they are often wetter with many bubbles not flowing

closely packed so that two bubbles are not always approaching the constriction together. In >3-row foam, bubbles often flow surrounded by a large fraction of liquid rather than many gas bubbles (Figure 5.8 (a)). Thus, for the neighbour-wall pinch-off to happen, they must always flow in a manner so that two bubbles approach the constriction together. Otherwise, they will flow through it one by one without break-up (or undergo snap-off). The tails of broken bubbles are usually too small to undergo additional pinch-offs. This is contradictory to 3-row foam. At larger sizes, bubbles are packed similarly to sphere packing with either central or wall bubbles being axially further ahead in the channel (Figure 5.8 (b)). This means that even when a central bubble spans the constriction width itself so that no other bubble can flow in, its significant portion, i.e. tail is still left behind and will be pinched by one of the neighbouring bubbles against the constriction wall. Depending on the initial bubble size, the tails may or may not undergo additional pinch-offs resulting in a greater total number of bubbles downstream of the constriction.

By increasing the capillary number again, the bubbles start undergoing the second instability, i.e. neighbour-neighbour pinch-off. The trend is very similar to the first pinch-off (Figure 5.10). This means that there is a critical capillary number that has to be met in order for bubbles to start breaking through that mechanism. Smaller bubbles will require larger shear-rates to undergo neighbour-neighbour because of their sizes and the local liquid fractions, similarly as is in the case of neighbour-wall pinch-off. Because now for >3-row foam, three bubbles must always approach the constriction together, the wet foam will very rarely break through the given mechanism. Well packed foam that has four bubbles spanning the channel width (as shown in Figure 5.9 (a)) may break through neighbour-neighbour pinch-off. For 3-row foam, the arrangement plays a crucial role. Since bubbles span channel width in threes, only the central bubble undergoes neighbour-neighbour pinch-off. The central

bubble, however, has to always flow ahead of its two neighbours so that when it stretches across the constriction, the two neighbours pinch its tail against each other. This break-up is quite regular, with the central bubble being broken-up almost identically at constant flowrates.

It can be deduced that by knowing the capillary number and foam properties, one can predict when bubbles will start breaking and through which type of break-up. Using this graph, a break-up can also be avoided. By taking the constriction dimension into the analysis, foam generation through an orifice like a valve or a nozzle can also be predicted rather well. More specifically, foam pushed out through a valve will not break if the shear rates applied are in agreement with the required plot region.

Figure 5.10 Plot of the capillary number against the dimensionless bubble area for >3-row and 3-row foams. Lines indicating regions are arbitrary.

5.3.1.1.2.2 2-row foam

An identical graph has been plotted for the staircase foam in Figure 5.11. Now, snap-off has its own region due to the fact that larger bubbles obstruct the constriction for much longer,

allowing enough liquid to accumulate at the constriction. At very low capillary numbers ($Ca < 1.57 \times 10^{-4}$), bubbles will flow through the constriction unchanged for a small number of conditions. Once the velocity is increased, bubbles start undergoing snap-off, especially at smaller sizes when the liquid fraction is relatively high so that the foam is wetter than in any other regime. There is then a minimum capillary number around 5.60×10^{-4} and 1.50×10^{-3} for larger and smaller bubbles to exhibit neighbour-wall. However, the smallest (and therefore wettest) bubbles which are in the neighbour-wall region also break via snap-off. This means that once a minimum capillary number for pinch-off has been reached, bubbles size and therefore, foam quality plays a crucial role in whether snap-off does or does not occur. The results differ from the findings made by Liontas *et al.* (2013) in a circular constriction of width 20 μm, where the same foam regime was independent of capillary number; the bubble size was the sole factor responsible for each different phenomenon. The no-effect region was present across many capillary numbers usually for smaller bubble sizes. The constriction used in their study, however, had curved walls which did not allow enough liquid to accumulate at the constriction and cause snap-off. Additionally, the depth of the channel was greater (by 10 μm); thus, it was possible that the liquid did not always reduce the neck in the normal direction to the observation plane before the bubble passed the constriction. Moreover, based on the observations, the 2-row foam generated in their channel looked wetter, which could also explain the reason why in their work bubbles at higher capillary number managed to flow through the constriction without exhibiting pinch-off.
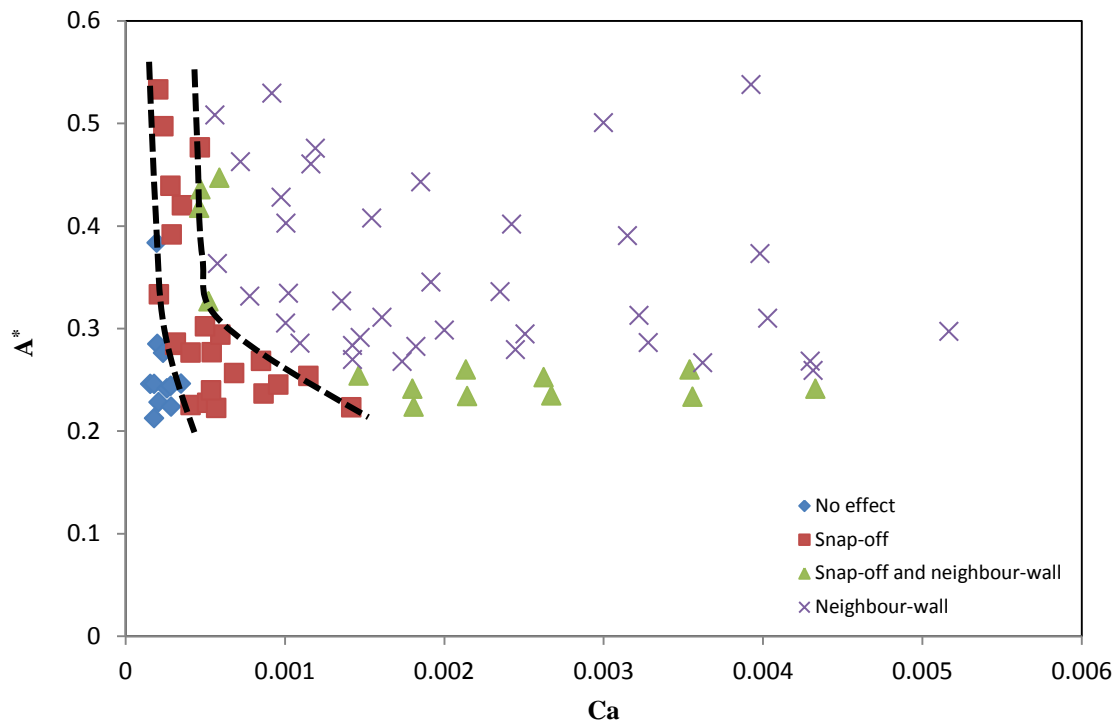
Figure 5.11 Plot of the capillary number against the dimensionless bubble area for 2-row foam.

5.3.1.2 Gradual contraction followed by expansion

Different constrictions with gradually contracting and then gradually expanding walls were also studied. A constriction with almost the same dimensions as the sudden constriction was also studied and is compared later on. For better visualisation of the phenomena observed in a gradual constriction, a wider and sharper constriction was chosen with walls at 45° that had an orifice width of 70 µm and a small length of around 8 µm (Figure 5.12). The same constriction was supposed to be studied initially as a sharp sudden orifice. However, many attempts were made in order to fabricate the constriction which had failed. Because of the small surface of the constriction walls and a small aspect ratio (one wall width = 8 µm, length = 165 µm), the walls would simply collapse. This resulted in foam flowing over the top of the constriction, as it would be in a straight channel. In a gradual constriction, this was not a problem since the constriction walls were at an angle which produced a much larger surface

148

area of the constriction walls. A study of the constriction shown below was therefore carried out using the same flow-focusing device as before. Because of the larger constriction width, snap-off was also rare.
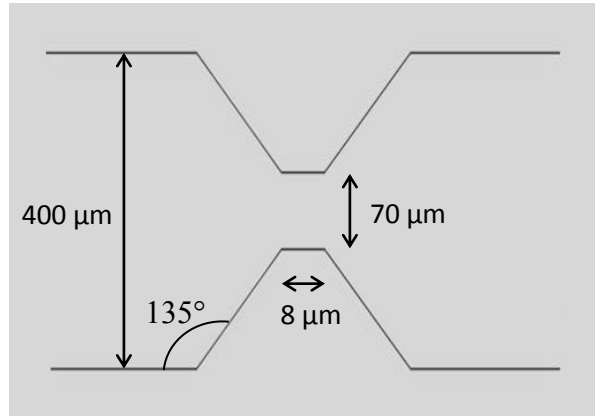
Figure 5.12 A schematic of the gradual contraction/expansion and its dimensions (not to scale).

5.3.1.2.1 Phenomena observed

The same types of dynamics were observed in gradual constriction as in sudden constriction, including no effect and two types of pinch-off. Additionally, particular foams underwent different behaviours such as re-orientation and re-orientation with pinch-off that are now going to be explained in more detail.

5.3.1.2.1.1 Re-orientation

This phenomenon was strictly observed in gradual constrictions alone. As bubbles flow through the gradual orifice, they simply re-orient their direction from horizontal to vertical upon passing through it. This was observed for two types of foams, 3-row and 2-row. At first, bubbles upstream of the constriction flow in a way so that 3 or 2 bubbles span the channel width. As described for the sudden constriction, bubbles at first elongate when they approach the constriction, and then they get compressed. However, because of the gradual constriction, the bubbles slide along the gradual edge and elongate diagonally across the constriction

(Figure 5.13), changing their initial position. As the bubbles now exit the constriction, they are large enough to span the width of the channel vertically (compressed), either in pairs or on their own, and because they are well confined between the surrounding bubbles and channel walls, they do not restore their initial shape but maintain the new one, changing the structure of the foam downstream of the constriction. This results in bubbles spanning the width of the constriction having 2-row and 1-row from the 3 and 2-row foams, respectively. In order for this change to happen, the initial bubble size must be large enough to span the width of the channel having either two bubbles or one bubble. Based on the experimental results, for the 2-row foam, the projected bubble diameter had to be larger than 240 μm, which is equivalent to > 0.6W. For the 3-row foam, the projected diameter had to be in between 170 μm and 180 μm which is less than 0.5W. One could expect a diameter of 0.5W; however, bubbles are generally compressed meaning their vertical length (must be 200 μm for re-orientation) is longer than their horizontal length and therefore the projected diameter is less than 0.5W. Even if the bubble size is correct, but the flow is too fast, the bubbles might undergo one of the break-ups instead. Similarly, if bubbles are not tightly packed or relatively wet (spherical shape), they have sufficient time and space to restore their original shape once they pass the constriction. In >3-row foam the bubble size was not large enough to undergo re-orientation since two or three small bubbles are not large enough to fill the total width of the channel.

The re-orientation is technically a topological change; a well-known T1 event in foaming systems. The T1 event is a topological deformation often occurring in shear flows (see 2.7.1.2), which results in the re-arrangement of adjacent bubbles due to saturation of the elastic energy at the surfaces of the bubbles. It should also be noted, that some bubbles will attempt the "re-orientation", but because they are not large enough to span the width of the channel, they will go back to their initial structure (Figure 5.13 (c)). This shows that bubbles

prefer the vertical direction upon exiting the constriction which can be attributed to bubble compression during the contraction of a bubble as it was shown for the single small bubbles (4.3.1.1). Furthermore, by choosing particular channel confinements, the bubbles can be forced to acquire particular shapes. This phenomenon has been observed in a similar foam system (Liontas *et al.*, 2013) as well as in emulsions (Surenjav *et al.*, 2009).

$$Ca = 6.35 \times 10^{-4} \qquad Ca = 4.04 \times 10^{-4} \qquad Ca = 2.97 \times 10^{-3}$$
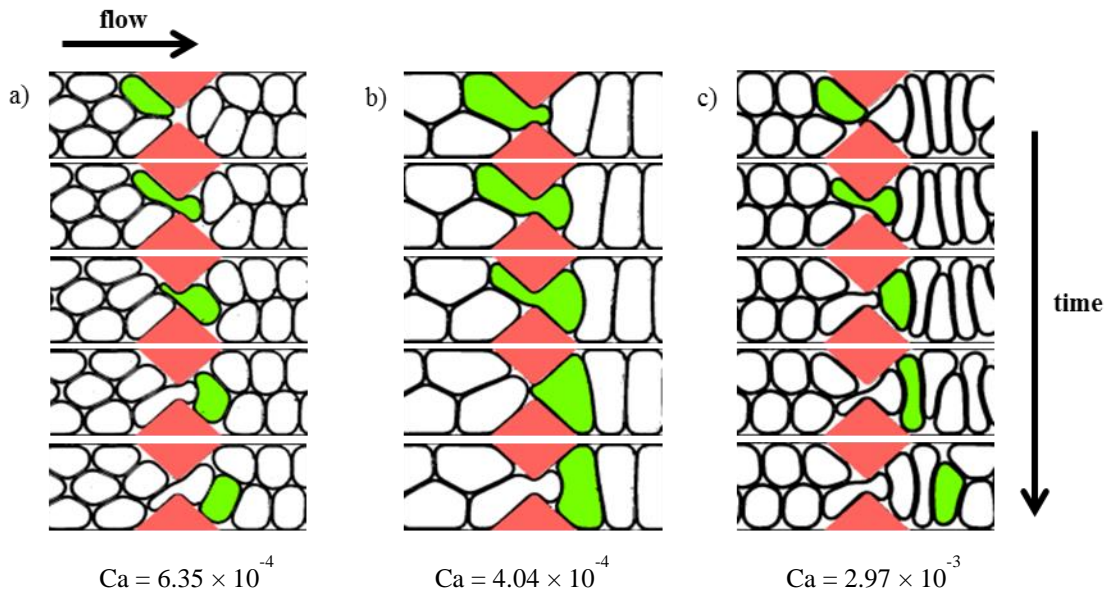
Figure 5.13 Consecutive sequence of images of foams that undergo the re-orientation: a) 3-row foam to 2-row foam, b) 2-row foam to 1-row foam, c) 2-row foam that initially tries to re-orient but goes back to its upstream structure because of the bubble size being not sufficiently large enough.

5.3.1.2.1.2 Re-orientation with pinch-off

Another bubble behaviour observed in a gradual constriction, which is essentially a neighbour-wall pinch-off, is re-orientation with pinch-off. As the name itself suggests, this phenomenon involves bubbles undergoing re-orientation as well as pinch-off. Similar to re-orientation, this type of dynamic only occurs for 3-row and 2-row foams, so only when bubbles can be re-oriented. However, because bubbles are either too large or flowing too fast, some of them are being pinched against the wall of the constriction resulting in interesting

patterns. Very few conditions for 3-row foam triggered this behaviour, usually somewhere between re-orientation and neighbour-wall regions. This means that for 3-row foam, these points can be identified as transition points from re-orientation to pinch-off.

On the other hand, for the 2-row foam, the behaviour occurs across a wide range of the capillary numbers. The main idea in order to observe re-orientation with pinch-off is an enormous bubble size so that one of the bubbles is axially much closer to the constriction than its neighbour behind it. The first portion of the already pinched bubble that passes through the throat is large enough to span the total channel width. Its pinched tail, however, is usually stuck between two large bubbles because of its small size, as shown in Figure 5.14. Which position the initial bubble will take is crucial for the remaining bubbles. If the first bubble is pushed towards the top edge, the rest will try to follow, so when steady state is achieved, the downstream structure is relatively uniform and ordered. However, pressure fluctuations associated with lower velocities may cause a change in the location of the small bubbles. This pattern is described in more detail in the staircase section through gradual constrictions (5.3.1.4).
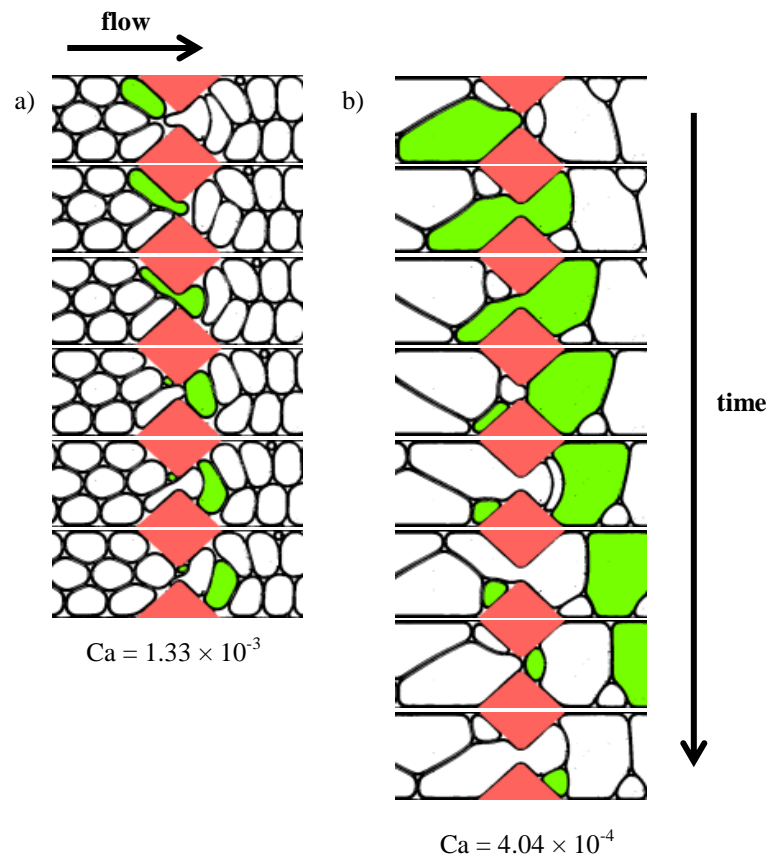
Figure 5.14 Consecutive sequence of images of foams that undergo the topological change and bubble break-up in the way of re-orientation with pinch-off; a) 3 to 2, b) 2 to 1. Notice that in (b) the small pinched bubble is at the top wall (first two images) whereas the next small bubble goes to the bottom wall.

5.3.1.2.2 Foam behaviour with regards to flow conditions

Same plots to those for the sudden constriction have been plotted (Figure 5.15, Figure 5.16 and Figure 5.17). More specifically, the capillary number against the dimensionless bubble area for the three foam structures (>3-row, 3-row and 2-row) were plotted.

5.3.1.2.2.1 >3-row foam

No effect, as well as two pinch-off instabilities, were observed for >3-row foam. Since now the bubbles pass through a much wider orifice (70 μm) and do so gradually, the minimum capillary number required was higher (2.50×10^{-3}) compared to the sudden constriction in order to observe the neighbour-wall pinch-off (Figure 5.15). Also, bubble size played a more

vital role in this case since most of the bubble diameters were smaller than the throat. This allowed small bubbles at higher capillary numbers (from Ca = 6.00×10^{-3} to Ca = 8.00×10^{-3}) to pass through the constriction without any break-up. Snap-off was not favoured because of the wider and shorter constriction, especially in this regime where bubble diameter was close to the constriction width. Snap-off was therefore not observed in >3-row foam. The no-effect region is dominant at capillary numbers up to 2.40×10^{-3} independent of bubble size and then at moderate capillary number values (Ca = 2.50×10^{-3} to Ca = 6.00×10^{-3}) for bubble sizes A^* < 0.07. At the highest capillary numbers (Ca = 6.00×10^{-3} to Ca = 8.00×10^{-3}), when bubbles experience high shear stress, only smaller bubbles (A^* < 0.04) managed to pass the constriction without any structural change. This is primarily due to bubbles not flowing closely packed, and even if two bubbles approach the constriction together, they are too small to pinch each other. The neighbour-wall pinch-off is dominant at moderate capillary numbers whenever A^* is above 0.06, thus when the average diameter is already larger than the width of the constriction (A^* = 0.06 corresponds to d_b = 110 μm). At the highest capillary numbers, where bubbles experience more substantial shear stress (conditions that favour pinch-offs), only larger bubbles (A^* > 0.06) break via the neighbour-neighbour pinch-off. As a result, there is a critical capillary number (Ca = 6.00×10^{-3}) as well as critical bubble size (A^* = 0.06) for this pinch-off to occur. The values are not much larger than the critical capillary numbers necessary for the pinch-offs in the sudden constriction. This shows that the pinch-offs are indeed favoured in similar conditions. However, the dimensions of the constriction, especially its width, can have a profound effect on which bubble size exhibit the pinch-offs.
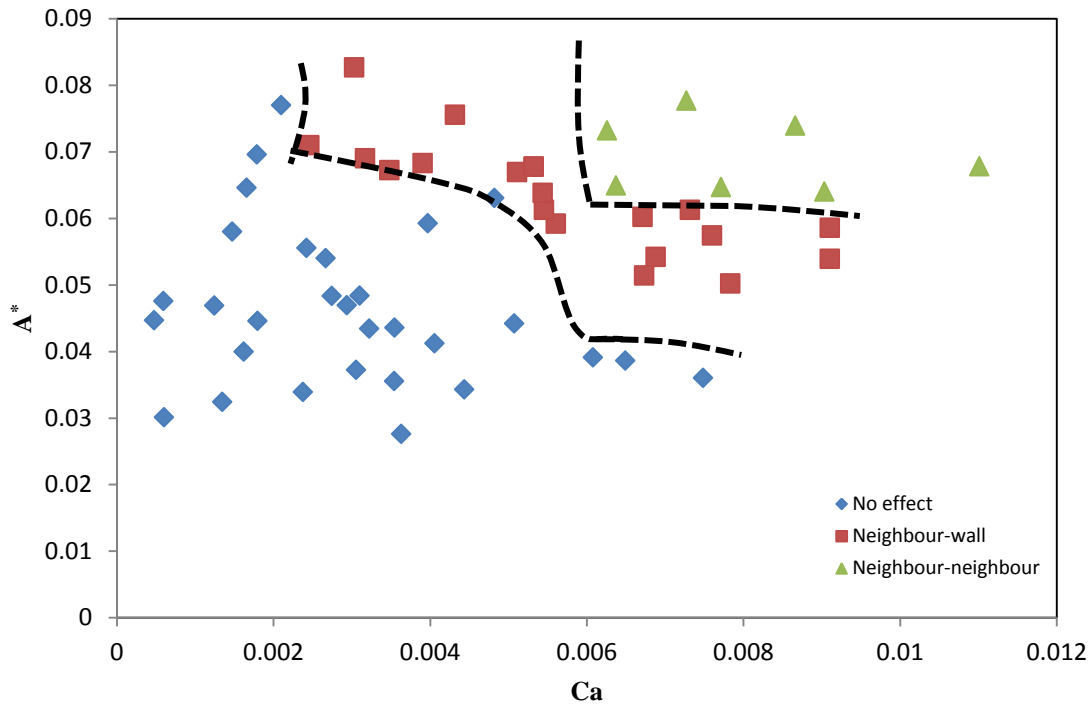
Figure 5.15 Plot of the capillary number against the dimensionless bubble area for >3-row. Lines indicating regions are arbitrary.

5.3.1.2.2.2 3-row foam

For the 3-row foam, exactly the same behaviours were observed as for the >3-row foam, along with the newly observed re-orientation and re-orientation with pinch-off. From Figure 5.16, it can be noted that no effect is dominant in the low capillary regime ($Ca < 2.00 \times 10^{-3}$), where the shear stress is not large enough for any of the pinch-offs to occur. Increasing the size of the bubbles to the projected diameter greater than $0.4W$ (i.e. $A^* > 0.14$), allows two bubbles to span the width of the channel. Hence, bubbles start re-orienting. This region is the smallest out of all of them (excluding re-orientation with pinch-off) since only a small percentage of bubbles will undergo this topological change. As mentioned before, as soon as bubbles reach the minimum capillary number for pinch-off ($> 1.00 \times 10^{-3}$) and maintain the size that allows the re-orientation, they start re-orienting with a pinch-off. Re-orientation with a pinch-off occurred infrequently, but these points are crucial since they indicate where the

155

transition begins between no effect and pinch-off. As earlier, both of the pinch-off mechanisms required minimum capillary numbers, since bubbles must experience sufficient shear stress. Neighbour-wall has a minimum capillary number (1.85×10^{-3}) that needs to be met in order to undergo this instability. A slightly smaller capillary number (3.72×10^{-3}) is required for the larger bubble size ($A^* = 0.16$), showing again that the volume is crucial as in the case for the sudden constriction. As already mentioned, the neighbour-neighbour pinch-off requires high shear stress so that the deformed outer bubbles can break the central bubble. Such shear stress was observed above $Ca = 4.00 \times 10^{-3}$, but only above $A^* = 0.10$, since smaller bubbles were not close enough to break via the neighbour-neighbour pinch-off through a 70 μm wide constriction. Thus, bubbles only underwent the neighbour-wall pinch-off.
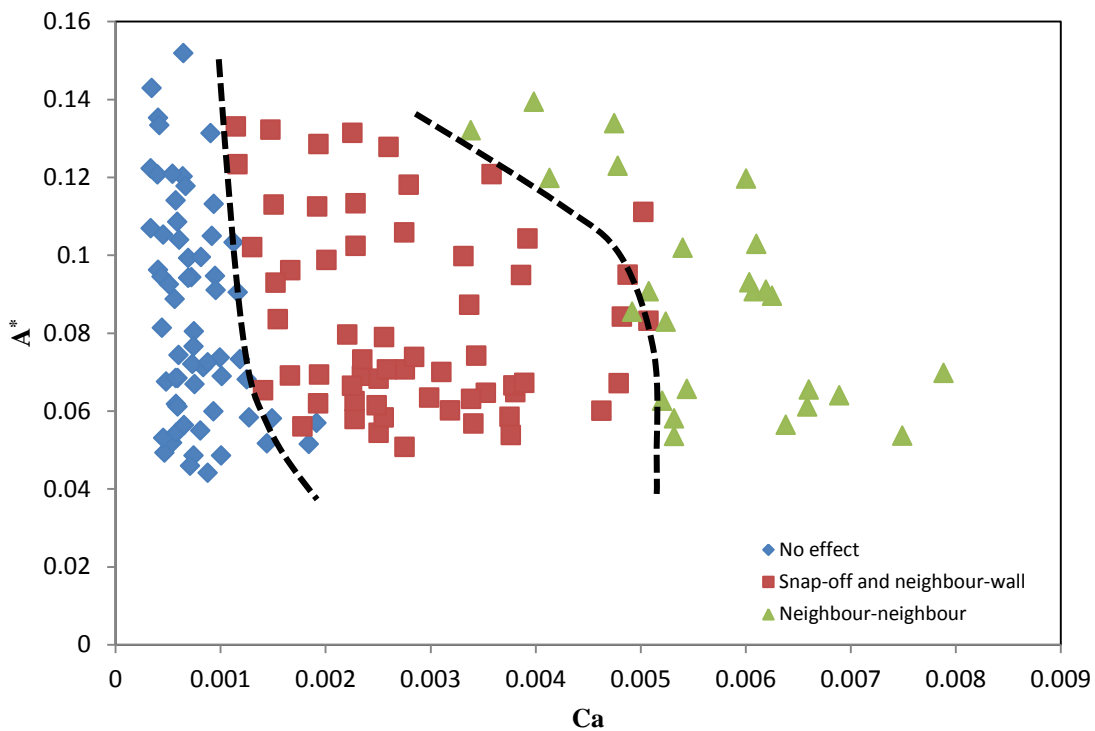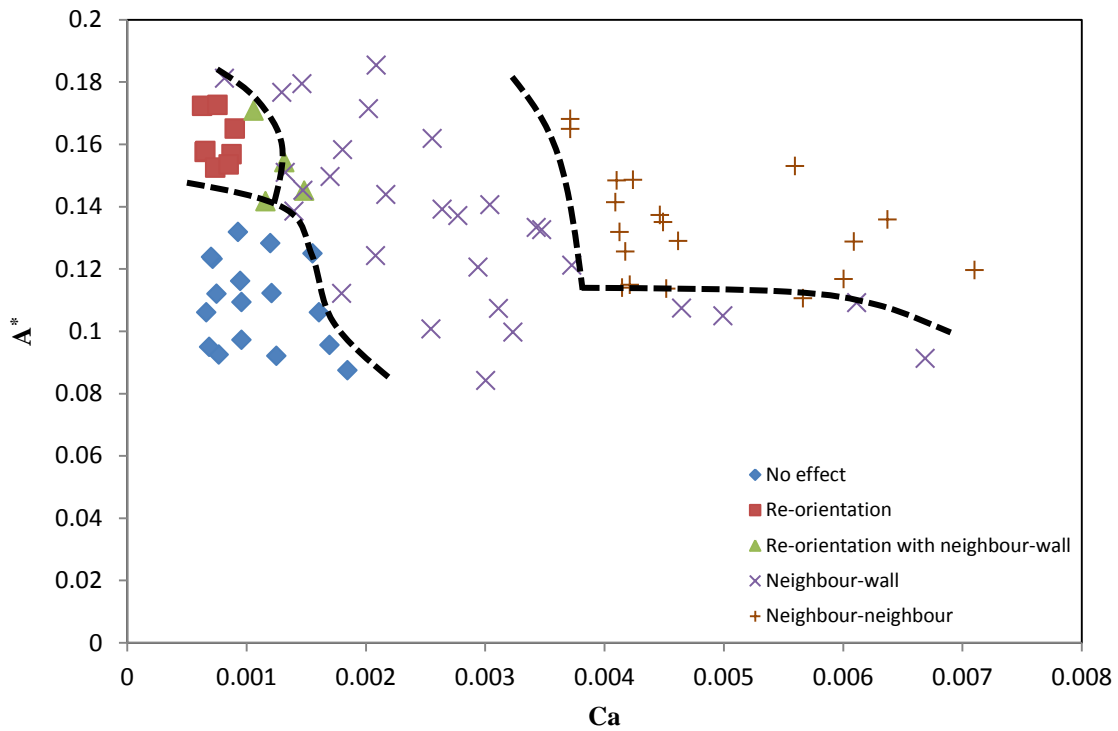

Figure 5.16 Plot of the capillary number against the dimensionless bubble area for the 3-row foam. Lines indicating regions are arbitrary.

5.3.1.2.2.3 2-row foam

The 2-row foam now has five phenomena including no effect; re-orientation; re-orientation with pinch-off; snap off together with a pinch-off; and, pinch-off on its own. However, it is challenging to distinguish snap-off together with a pinch-off from pinch-off since it only occurs in very few cases (Figure 5.17). It is, therefore, classified in the same category as pinch-off, so the 2-row foam structure is now divided into four regions. The no-effect regime occurs for relatively small bubbles. The gradual walls of the constriction make it easier for the bubbles to flow along the angled walls before being pinched, contradictory to the sudden constriction. Since bubbles flow in an alternating manner without hitting the constriction walls at a 90° angle, they can easily pass unbroken at much higher velocities. In fact, a critical capillary number can be identified around 3.00×10^{-3} above which bubbles always break, independently of the bubble size. The re-orientation region from 2 to 1 is very similar to the 3-row foam, meaning bubble size has to be large enough to span the width (this time on its own), but it cannot be too large or flow too fast. Thus, the size of the bubble must be above A^{*} = 0.30, with the capillary number below 7.84×10^{-4}. However, if the bubble size is greater than A^{*} = 0.55, the bubbles are so large and dry (compact) that even when a substantial portion of the bubble passed through the constriction (large enough to span the width of the channel), its tail is still in the upstream section and is pinched by the upcoming bubble. The outcome of such flow results in the re-orientation with pinch-off. If the bubbles are of appropriate size for the re-orientation but flow too fast (Ca $> 7.84 \times 10^{-4}$), the shear stress is sufficient for them to break via the usual neighbour-wall pinch-off. The pinch-off region can be identified from the plot across a wide range of the capillary numbers, with the critical capillary number increasing for smaller bubble areas, again showing the importance of the bubble size. The re-orientation with pinch-off is almost independent of the capillary number,

157

occurring for all capillary numbers, as long as A^* is around 0.5 or more and above Ca > $5.00 \times$ 10^{-4}. As mentioned earlier, at such large bubble sizes, one of the bubbles in the staircase structure is further ahead from its adjacent bubble by usually a half of its size ($A^* = 0.25$). Hence, that portion of the bubble passes through the constriction unaffected before the upcoming bubble. In addition, the angled walls of the constriction allow the bubble to slide along the walls in such a way, that more than half of the bubble can pass through it before the pinch-off. Hence, the large portion is approximately $A^* \geq 0.3$, which is always large enough to span the width of the channel and therefore, ends up being re-orientated. Since there is another smaller pinched bubble (or two), the structure takes a form of re-orientation with pinch-off. It is also essential to remember that the downstream section and where the small bubble is placed is dependent on the very first bubble location, which dictates the direction for the rest of the bubbles. However, even though the bubbles are almost entirely monodisperse, a small difference in bubble size or a pressure fluctuation can change the direction of the small pinched bubble as can be seen in Figure 5.14 (b), where bubbles start going to the bottom wall rather than the top as the earlier ones do in the first image of the sequence. Moreover, in the re-orientation with pinch-off, the bubble is always split exactly the same, either once or twice. This means that the number of bubbles downstream of the constriction is either two or three times the total number of bubbles upstream of the constriction. Due to the larger constriction width, snap-off occurred only for a small number of conditions mostly for smallest (wettest) size and fast velocity. Moreover, such conditions satisfied the neighbour-wall pinch-off; thus, snap-off was always accompanied by the mentioned pinch-off.
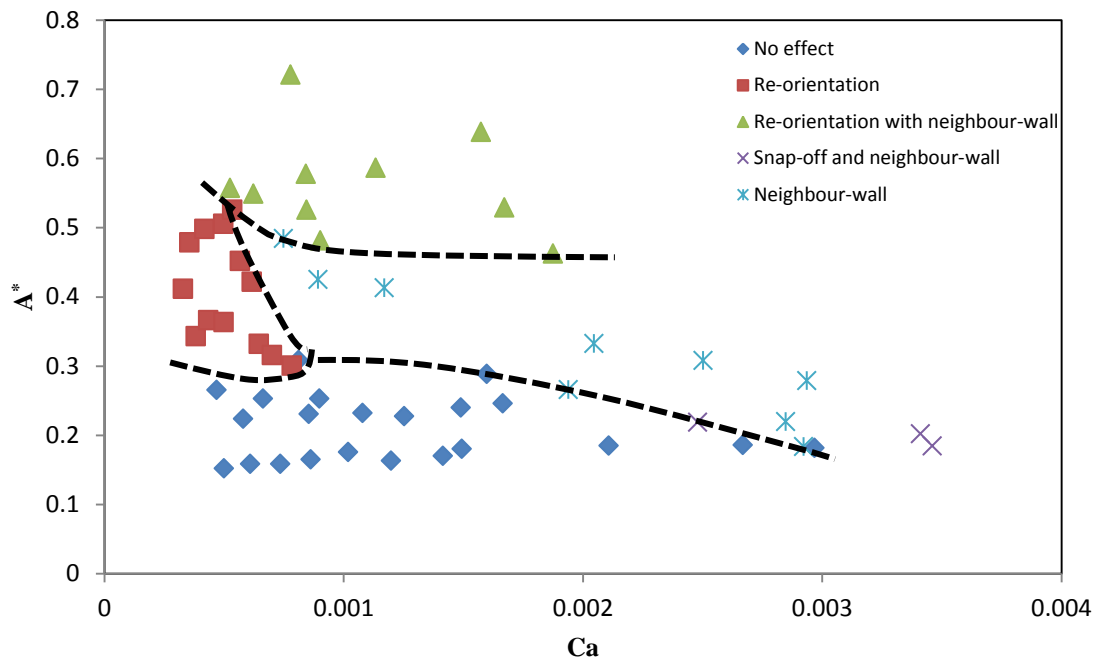
Figure 5.17 Plot of the capillary number against the dimensionless bubble area for the 2-row foam. Lines indicating regions are arbitrary.

5.3.1.3 Direct comparison of sudden and gradual constrictions

Ca vs A^* results have been plotted for a sudden and gradual constriction of the same width (Figure 5.18). The fabricated length was slightly different (+15 µm for gradual); however, it should not cause significant effect since the width of the constriction is more important as is shown later.
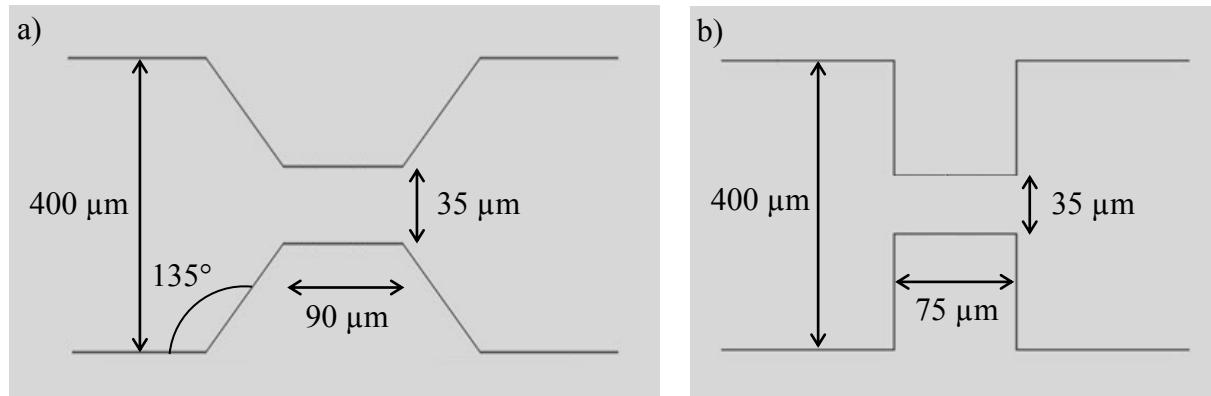
Figure 5.18 Dimensions of the two constrictions compared: a) the gradual and b) the sudden constriction (not to scale).

5.3.1.3.1.1 Differences and similarities found

Naturally, the main difference between the two constrictions is the appearance of an extra structure in the gradual constriction, namely re-orientation for the 3 and 2-row foam. The follow up is then the re-orientation with pinch-off, which was also absent in the sudden constriction. Plots of Ca vs A^* have been obtained for the sudden and gradual constrictions for the three foam regimes and are presented in Figure 5.19.

Looking at all the graphs below (Figure 5.19 (a-f)), it can be noted that the regions of the break-ups have similar shapes, with smaller bubbles often requiring a greater capillary number, i.e. more substantial shear stress to undergo the same dynamics when compared to large bubbles. As already mentioned throughout this chapter, smaller bubbles can flow through the constriction without being pinched since they do not need to elongate as much (hence not leaving the substantial part in the upstream section) and they do not flow as closely packed (higher liquid fractions). Moreover, gradual constriction often required larger capillary numbers when compared to the sudden constriction for both of the pinch-off mechanisms for >3-row and 3-row foam (Figure 5.19 (a-d)). The start of the snap-off/neighbour-wall regime was not that much different for >3-row foam, although higher capillary numbers were

observed for the gradual throat (2.50×10^{-3} compared to the sudden constriction 1.80×10^{-3}). In sudden constriction, the outer bubbles often arrive at the sudden constriction walls and then approach the constriction throat at the $90°$ angle. Thus, once the bubble enters the constriction, its front tip is already in the constriction, whereas the rear tail flows along the wall in the upstream part. The middle bubble (or even two) flows directly into the constriction, which makes it easier for that bubble to pinch the bubble already in the constriction. In the gradual constriction, the outer bubbles approach the constriction at a $45°$ angle, which often results in the central bubble flowing through the constriction after the adjacent outer bubbles have already passed the constriction.

Similar reasoning applies to the neighbour-neighbour pinch-off in both of the regimes observed (>3 & 3-row). In the gradually constricted channel, the outer bubbles near the walls very often approach the constriction first. This means that the central bubble reaches the constriction later and thus is less likely to be pinched by the two neighbouring bubbles. In the sudden constriction, the bubbles near the side walls would flow to the corners of the channel just before the constriction, thus allowing the central bubble to flow first and then get squeezed by the two outer bubbles. This resulted in observing the neighbour-neighbour pinch-off at lower flow-rates in the sudden constriction.

In the case of the 2-row foam, apart from the obvious distinct features (re-orientation and re-orientation with pinch-off), gradual constriction has a broader snap-off region, especially for small bubbles (Figure 5.19 (e & f)). As already explained for the two smaller regimes, bubbles get pinched more easily in the sudden constriction. Thus, snap-off with neighbour-wall was observed at the same velocities that caused only snap-off in the gradual constriction.

In general, gradual walls of the constriction allow the bubbles to approach and exit the constriction at angles which enables them to stay more compact (flowing consistently along the walls) and hence, maintain their vertical direction. This causes re-orientation of bubbles and therefore, reduces the number of bubbles per row downstream of the constriction. Furthermore, the gradual constriction requires more substantial shear stress for most of the pinch-off mechanisms. These results can be used to determine which break-ups will occur in porous media if the conditions and geometries are known, and therefore, improve calculating and understanding the bubble size distubution, which would subsequently allow predicting foam properties in the subsurface reservouirs. In addition, since the sudden walls of the constriction favour break-ups and reduce the chances of re-orientation, they can also be added to similar microfluidic systems in order to increase the total number of bubbles in the channels.
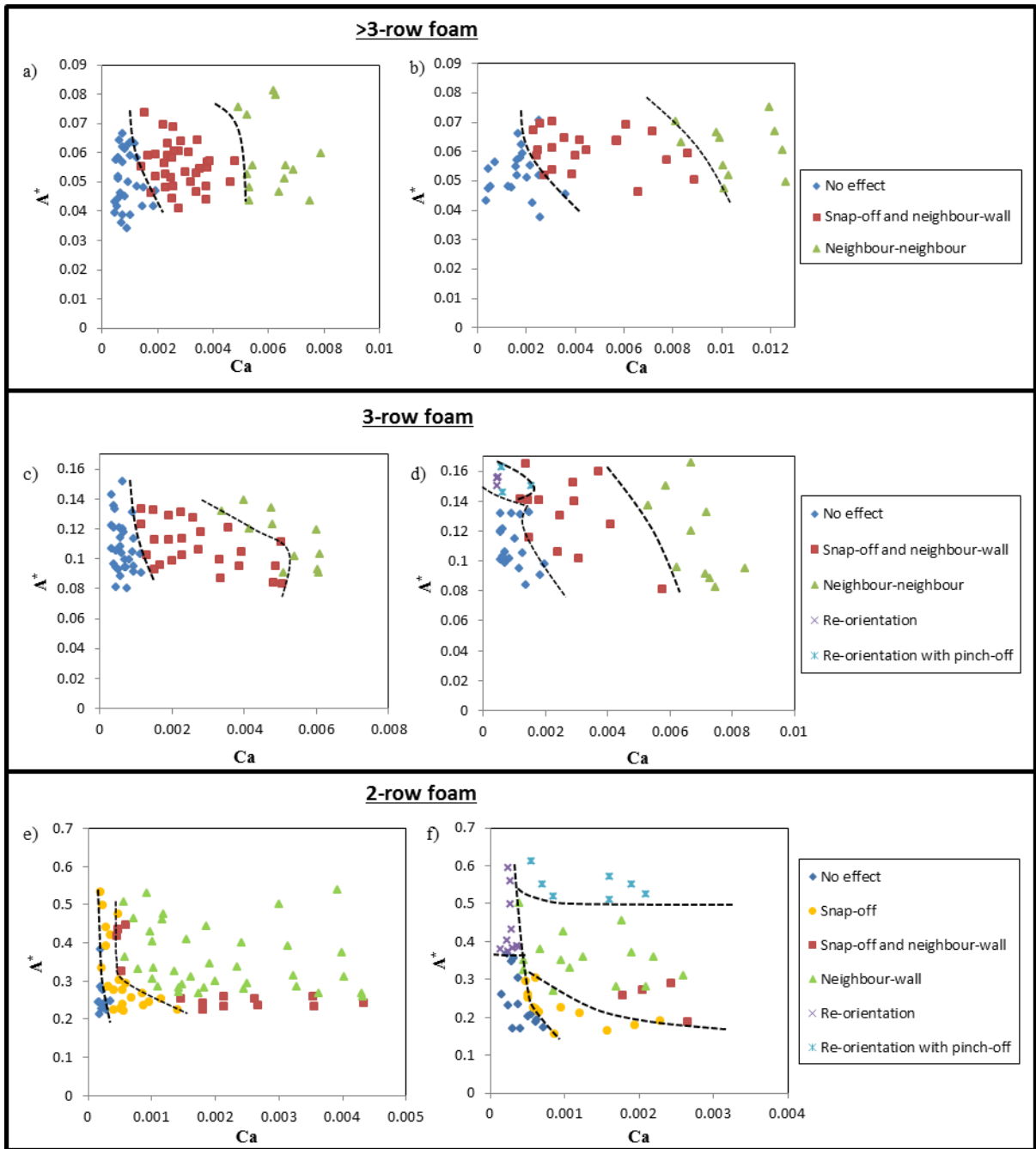
Figure 5.19 Plot of the capillary number against the dimensionless bubble area for all of the regimes in sudden and gradual constriction: >3-row foam a) sudden, b) gradual; 3-row foam c) sudden, d) gradual; 2-row foam e) sudden, f) gradual. Lines indicating regions are arbitrary.

5.3.1.4 Staircase foam flow through gradual constrictions

The flow of 2-row foam through four different gradual constrictions has been studied. The 2-row foam has been chosen out of all regimes since the structure, in general, resembles slightly drier (low liquid content) foam throughout the wide range of flow-rates. It has also been reported in the literature that the typical bubble size in porous media is two times the pore dimension based on the analysis of bubble size distribution through actual sandstone (Ettinger and Radke, 1992; Chen *et al.*, 2008). It has to be remembered that in porous media, the porosity is often very small and so studying dry foam with bubbles larger than the constriction seems more relevant to foam applications, such as enhanced oil recovery or soil remediation. Another reason for choosing this particular structure was the ability to simulate it using Surface Evolver (Brakke, 1992) by mathematicians from Aberystwyth University (on-going work). Initially, four constriction results are compared in terms of Ca vs A^{*}.

5.3.1.4.1 Constriction dimensions and phenomena observed

The four channels studied consisted of precisely the same flow-focusing device as described before. The four devices differed only in terms of constriction dimensions which are given in Figure 5.20 below. Two constrictions were sharp (length 8 µm) with two different widths (35 µm and 70 µm) and two long constrictions (length 90 µm) with two different widths (35 µm and 55 µm). The same behaviours were observed as explained before for the gradual contraction followed by expansion, namely, no-effect, re-orientation, snap-off, pinch-off and re-orientation with pinch-off.
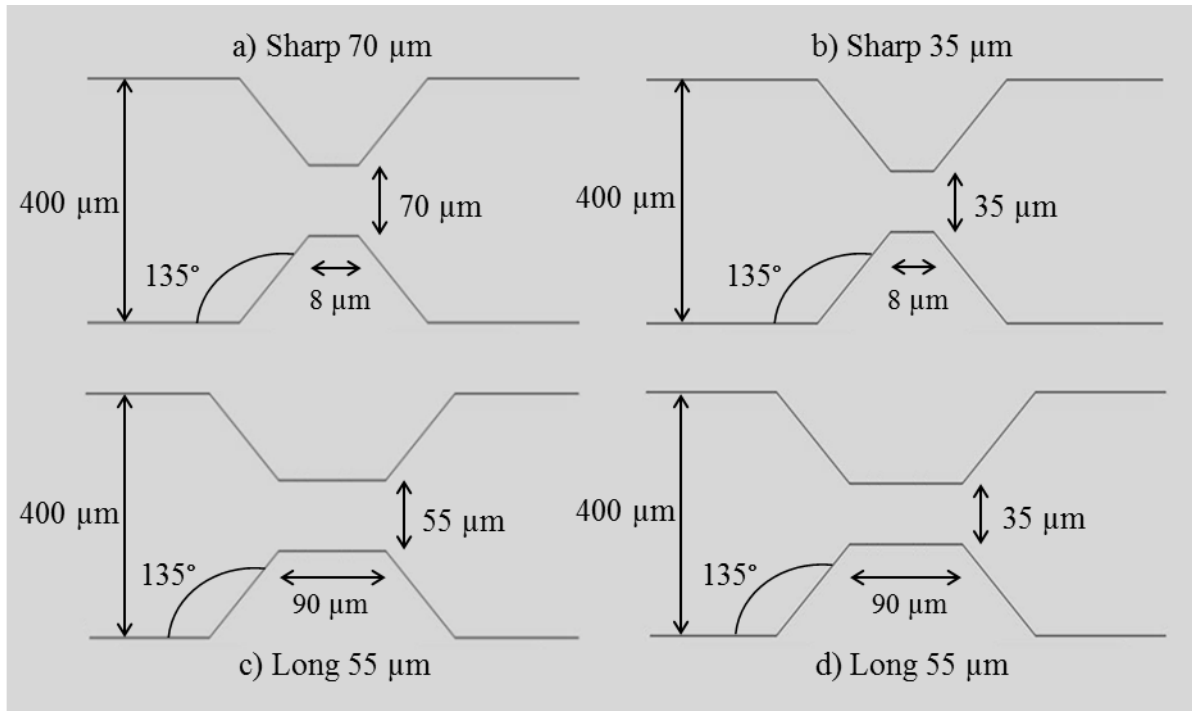
Figure 5.20 The schematic of the four constrictions studied; a) sharp 70 μm, b) sharp 35 μm, c) long 55 μm, d) long 35 μm (not to scale).

Images of the four behaviours observed in the gradual constrictions can be seen below (Figure 5.21). Snap-off is omitted in the mentioned figure since it mostly occurred in the two narrower constrictions (sharp 35 μm and long 35 μm) and very rarely in the wider constrictions (observed only three times in the sharp 70 μm). Naturally, through each of the constrictions foam underwent no effect at particular conditions, including low velocities where shear stress was not large enough to cause any of the topological changes. Larger bubbles at low flowrates exhibited re-orientation as expected since their sizes allow them to span the width of the channel. Largest bubbles almost independently of the capillary number underwent re-orientation with pinch-off. Different images of re-orientation with pinch-off can be seen in Figure 5.21, showing the variations of this phenomenon. As stated before, depending on the initial bubble size, velocity and constriction, the bubbles were pinched once or twice in this structure. The small pinched bubbles could end up in various locations generating interesting patterns (Figure 5.21 bottom images). The same pinched bubbles would

often be relatively monodisperse (calculated dispersity index <10%) and located either at the top or bottom wall or even in the middle as can be seen in Figure 5.21 (Long 55 μm constriction picture (a)) in re-orientation with pinch-off. Since bubbles follow the law of minimising the surface energy, the foam would end up having almost an ordered structure in the downstream section.
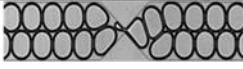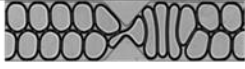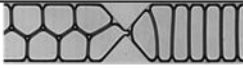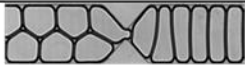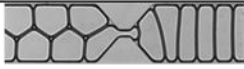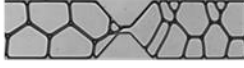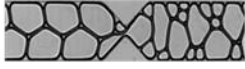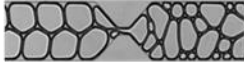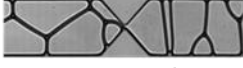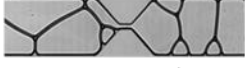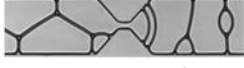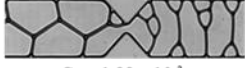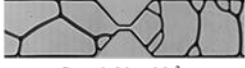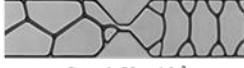
flow →	Sharp 35 μm	Sharp 70 μm	Long 35 μm	Long 55 μm
No effect	$Ca = 1.33 \times 10^{-3}$	$Ca = 2.94 \times 10^{-3}$	$Ca = 7.22 \times 10^{-4}$	$Ca = 2.40 \times 10^{-3}$
Re-orientation	$Ca = 3.75 \times 10^{-4}$	$Ca = 7.80 \times 10^{-4}$	$Ca = 3.75 \times 10^{-4}$	$Ca = 4.91 \times 10^{-4}$
Pinch-off a)	$Ca = 8.66 \times 10^{-4}$	$Ca = 7.51 \times 10^{-4}$	$Ca = 4.04 \times 10^{-4}$	$Ca = 6.35 \times 10^{-3}$
Pinch-off b)	$Ca = 2.05 \times 10^{-3}$	$Ca = 2.51 \times 10^{-3}$	$Ca = 1.56 \times 10^{-3}$	$Ca = 2.77 \times 10^{-3}$
Re-orientation with pinch-off a)	$Ca = 4.04 \times 10^{-4}$	$Ca = 5.20 \times 10^{-4}$	$Ca = 4.33 \times 10^{-4}$	$Ca = 3.18 \times 10^{-4}$
Re-orientation with pinch-off b)	$Ca = 1.62 \times 10^{-3}$	$Ca = 1.88 \times 10^{-3}$	$Ca = 1.01 \times 10^{-3}$	$Ca = 1.53 \times 10^{-3}$

Figure 5.21 Various phenomena observed in the four constrictions. Pinch-off and re-orientation with pinch-off included two images per constriction in order to show the variations of break-ups observed.

5.3.1.4.2 Comparisons and similarities

By collecting many data points for each of the constrictions, different foam dynamics have been identified for each constriction on Ca vs A^* graphs (Figure 5.22). Effects of the constriction width and length are presented below.
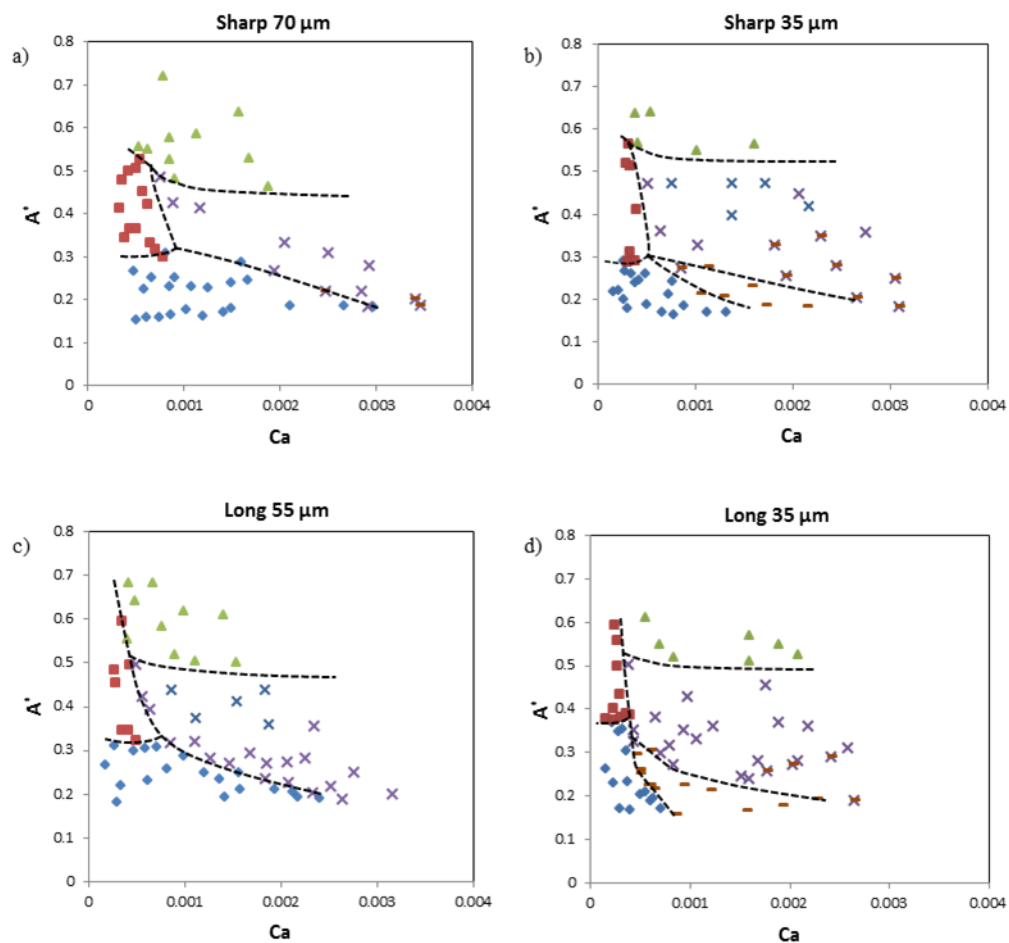
Figure 5.22 Plot of the capillary number against the dimensionless bubble area for the 2-row foam for all of the four constrictions: a) sharp 70 μm, b) sharp 35 μm, c) long 55 μm, long 35 μm. Symbols are as follows: ◆ no effect, ◼ re-orientation, ▲ re-orientation with pinch-off, ✕ pinch-off and ▬ snap-off. Whenever pinch-off and snap-off symbols overlap each other, they are indicative of an occurrence of both at the same condition. Lines indicating regions are arbitrary.

Constriction width

The first two plots (Figure 5.22 top row) are for the two sharp constrictions. This allows direct comparison of the constriction width and its effect on the staircase foam. The main difference between the two graphs is the snap-off region. In the 70 μm throat, snap-off was only observed accompanied by the neighbour-wall and above $Ca = 2.48 \times 10^{-3}$, whereas in the 35 μm constriction snap-off was observed on its own at various sizes ($A^* < 0.35$) and capillaries

as small as 8.65×10^{-4}. As already mentioned in Chapter 4, snap-off in microfluidic channels is driven by the thin liquid films surrounding the bubbles. The films are directly proportional to the capillary number; thus bubbles at higher capillary numbers deposit thicker film which can snap more quickly. Moreover, a narrower neck is snapped more easily since the radius of curvature that drives snap-off is smaller, hence allowing faster liquid invasion. In addition, the neck must only be reduced from 35 μm (and not 70 μm), thus explaining the reason of more frequent occurrence of snap-off at lower capillary numbers in the 35 μm constriction. In Figure 5.23, bubbles flow at similar conditions through the sharp 35 μm (a) and the sharp 70 μm (b). In the narrower constriction, the neck is simply snapped by the liquid. In the wider constriction, the neck does exhibit negative curvature which suggests that liquid has reduced the neck in the direction normal to the observation plane; however, the bubble passes through the constriction before it can be snapped. Moreover, by looking at Figure 5.23 (c), which is a magnified view of (b), it can be seen that liquid starts flowing past the bubble (just after the narrowest part). The small cavity indicated by the blue arrow shows where the liquid passes through so that snap-off is not triggered. This indicates that pressure at that location must be lower than the pressure in the throat, therefore, allowing the liquid to flow downstream rather than accumulate at the throat of the constriction. Indeed, it can be seen in the consecutive images (Figure 5.23 (c)), that this region becomes larger, implying continuous flow of liquid into the downstream section.

The re-orientation was observed at similar conditions, although faster bubbles managed to re-orient in the wider constriction, simply because in the narrower constriction the bubbles had to undergo more considerable deformation, leaving a substantial portion downstream that was pinched by the upcoming bubble.

The minimum critical capillary number for pinch-off for both of the sharp constrictions was almost independent of the constriction width. Naturally, the actual critical capillary number varied with the size of the bubble. However, approximately above Ca = 2.50×10^{-3}, all bubbles were getting pinched independently of the size since the velocities and, therefore, shear stress was large enough for the pinch-off to occur. In the narrower throat, the no-effect region was much smaller compared to the wider throat because of the snap-off occurrence. It can also be speculated that the pinch-off in the narrower constriction could occur at lower capillary numbers but was prevented by snap-off. This suggests that in a similar system but in drier conditions, the bubbles could undergo pinch-off and therefore, have a different minimum critical capillary number from the sharp 70 μm. The evidence supporting this statement is shown in the next section (5.3.1.5.1).

Re-orientation with pinch-off occurred for the largest bubbles, although slightly larger bubbles ($A^* > 0.55$) were necessary for the narrower throat since bubbles around $A^* = 0.50$ were getting pinched more frequently, causing generation of bubbles that had an insufficient area to span the total width of the channel.
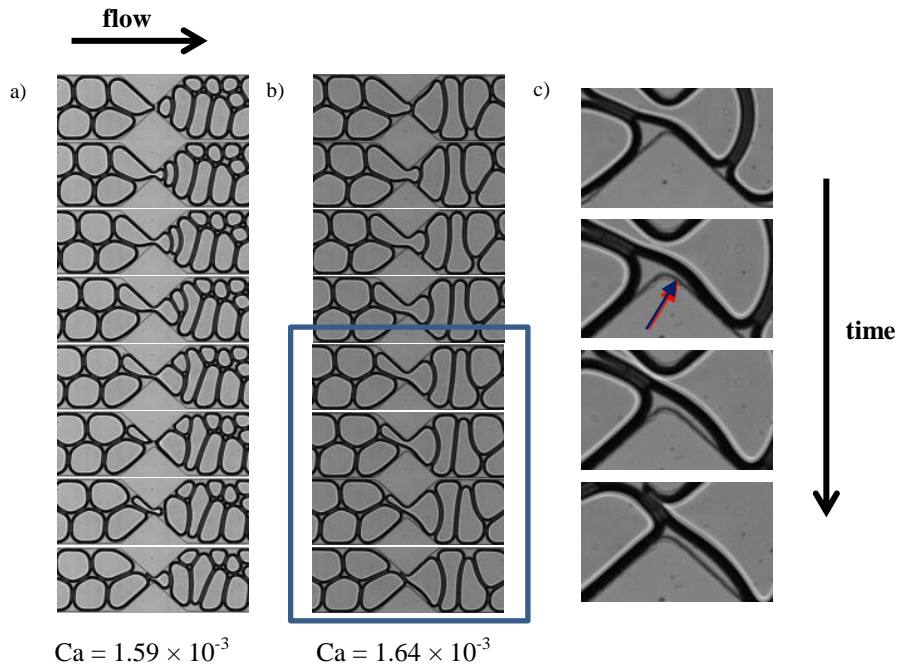
Figure 5.23 Consecutive sequence of images of foam through two constrictions of two different widths: a) snap-off in the 35 μm throat, $\phi_{or} = 0.23$, b) no effect in the 70 μm throat at snap-off conditions in the 35 μm throat $\phi_{or} = 0.21$, c) close up on the last four images of (b) showing where the liquid bypasses the bubble instead of accumulating in the constriction.

A similar conclusion can be made for the bottom row of Figure 5.22, where the two constrictions have the same length (90 μm) and differ only in width (55 μm vs. 35 μm). Qualitatively, the differences between the two constrictions are almost the same as the differences already explained for the sharp constrictions. It can be noted once again that much faster bubbles can pass through the wider constriction without being broken up, confirming that the width of the geometry is a crucial factor to avoid or impose break-up. The most apparent difference is once again the region of snap-off, as well as, snap-off together with pinch-off, which shows that it is favoured by the narrower throats. In the 55 μm constriction, snap-off was not observed. Although negative curvature was observed, (which generally occurs prior to snap-off) the liquid instead passed around the bubble exactly the same as in the case of the sharp 70 μm constriction that was shown in Figure 5.23. Perhaps larger bubbles

could allow a sufficient amount of liquid to form a collar and snap a neck inside the long 55 µm constriction. However, this was not observed in the system used. Re-orientation with pinch-off was again found to be in agreement with other two constrictions, i.e. $A^* \geq 0.50$.

<u>Constriction length</u>

By looking at the two graphs on the right-hand side of Figure 5.22 (short 35 µm and long 35 µm), the length of the constriction could be directly compared (8 µm vs. 90 µm). Smallest bubbles had a slightly larger capillary number for the bubbles to start pinching-off or snapping in the shorter throat. Since bubbles had to elongate more through the constriction and, therefore, require more time to pass through it, this allowed enough liquid accumulation in the constriction at lower velocities (when compared to the short throat) causing snap-off. It has been shown in Chapter 4 that longer constrictions require less time for the liquid to invade the throat in order to snap slug bubbles. Thus, the results found here are in agreement with the slug bubbles and, therefore, also apply to foams. A similar argument can be used for the pinch-off. Although the critical points are not significantly different (Ca = 5.30×10^{-4} vs. Ca = 3.90×10^{-4} for $A^* \sim 0.50$ and Ca = 3.11×10^{-3} vs. Ca = 2.67×10^{-3} for $A^* \sim 0.20$), bubbles almost immediately pass the narrowest part of the constriction in the sharp 35 µm and start expanding. This is not the case in the long 35 µm constriction where the bubble has to deform more substantially before expanding in the downstream channel. At the same time, it leaves a significant portion in the upstream section, which is easily pinched by the upcoming adjacent bubble.

The effect on the dynamics of the bubble caused by the length was not as significant as in the case of the width, even though the length difference was over nine times larger and the width only twice as large. Moreover, by looking at the left-hand side of Figure 5.22, where the two widths and lengths are different, it seems that they have similar regions with some

small variations. It seems that the longer constriction requires a lower maximum capillary number for the no-effect to occur when compared to the 70 μm throat, Ca = 2.30 × 10^{-3} and Ca = 2.90 × 10^{-3} respectively. Above those values, the shear stress is sufficient for bubbles to undergo the pinch-off mechanism. Based on the results presented in this work, this value should increase with the increase of the constriction width. Thus, it can be argued that if the width was changed from 55 μm to 70 μm, the throat would require a larger capillary number, possibly larger than the one observed in the sharp 70 μm constriction. This shows that with the increase of the width of the constriction, the length becomes less significant as bubble size is more comparable to the width of the constriction and, therefore, not as strongly deformed.

5.3.1.5 Dynamics of bubble thinning

Studying bubble neck and its decrease as it approaches the pinch-off or snap-off can shed light on the bubble dynamics and the forces that contribute to those instabilities. As it was explained in Chapter 4, the bubble neck during snap-off collapsed non-linearly and due to liquid inertia. The data from all the constrictions did not vary that much, and thus, the graph of each break-up consists of the lines obtained from various channels and conditions. The time to break (τ) is plotted as a function of the width of the neck (w_n). τ is calculated as follows

$$\tau = t_b - t, \tag{5.1}$$

where t refers to the time at which the width measurement is taken and t_b the time the bubble breaks. Once the neck exhibited a negative curvature, it was measured at different frames until the final pinch-off or snap-off. A power-law equation (using the least square method) was then tried to fit for all the data points for each of the three instabilities which produced different coefficients and exponents. Results are discussed below.

5.3.1.5.1 Snap-off

In all of the examples studied, the neck decreased non-linearly across different conditions due to the fact that it was pushed from all directions since the constriction width was smaller than the channel height (snap-off observed very rarely in 70 μm and 55 μm). It can be deduced that liquid flow from the normal direction to the observation plane contributed to the unstable neck in Figure 5.24. Although it looks like the neck is only pushed by the liquid from one side of the constriction, it is later observed that the neck is eventually pushed from the other side as well. This means that the liquid is flowing spherically inward around the neck in the constriction. Once this occurs, the neck becomes very unstable and decreases at a faster rate. This can be identified in Figure 5.25 once the break-up time is below 100 μs. The power-law ($w_n = \alpha \tau^\beta$) exponent was very consistent throughout different conditions, with $\beta = 0.3 \pm 0.03$. This value corresponds to the exponent of $\beta = 1/3$, which confirms the results of snap-off in a single bubble flow. The value obtained experimentally is due to liquid inertia and the neck becoming less slender as it was explained in Chapter 4. A similar coefficient was found in the flow-focusing channels (Dollet *et al.*, 2008; Fu *et al.*, 2010; van Hoeve *et al.*, 2011; Lu *et al.*, 2014) and vertical axisymmetric pinch-off (Gordillo *et al.*, 2005) as already reported in Chapter 4. Also, the pinch-off of shaving foam (Huisman *et al.*, 2012) was found to have a similar exponent.

flow →

a)

b)

time ↓

$Ca = 2.11 \times 10^{-4}$
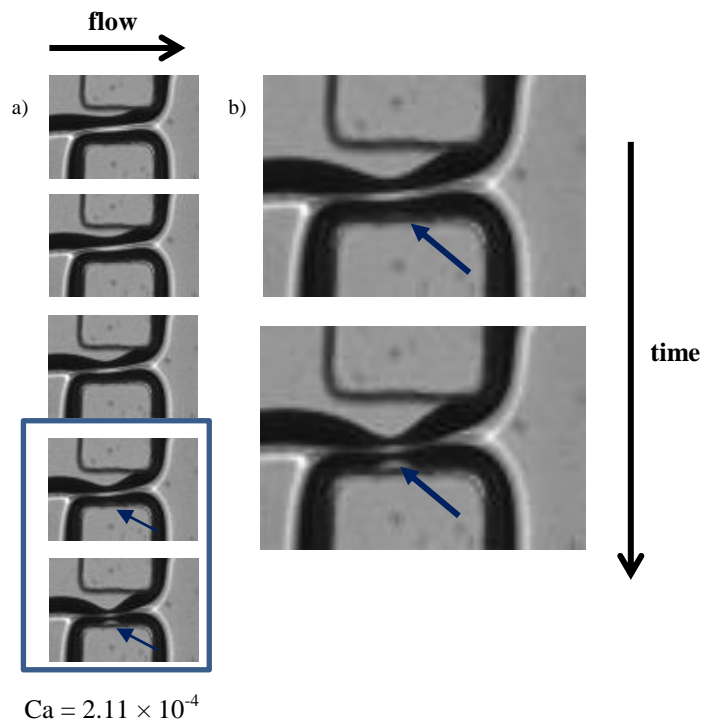
Figure 5.24 Consecutive sequence of images of foam exhibiting snap-off in the sudden constriction; a) asymmetric snap-off b) close up on the last two images of (a) where the blue arrow indicates radial liquid flow.

$$w_n = 5.14 \pm 0.31\tau^{0.30\pm0.03}$$

Legend:
- $Ca = 2.06 \times 10^{-4}$
- $Ca = 2.11 \times 10^{-4}$
- $Ca = 3.16 \times 10^{-4}$
- $Ca = 3.54 \times 10^{-4}$
- $Ca = 4.63 \times 10^{-4}$
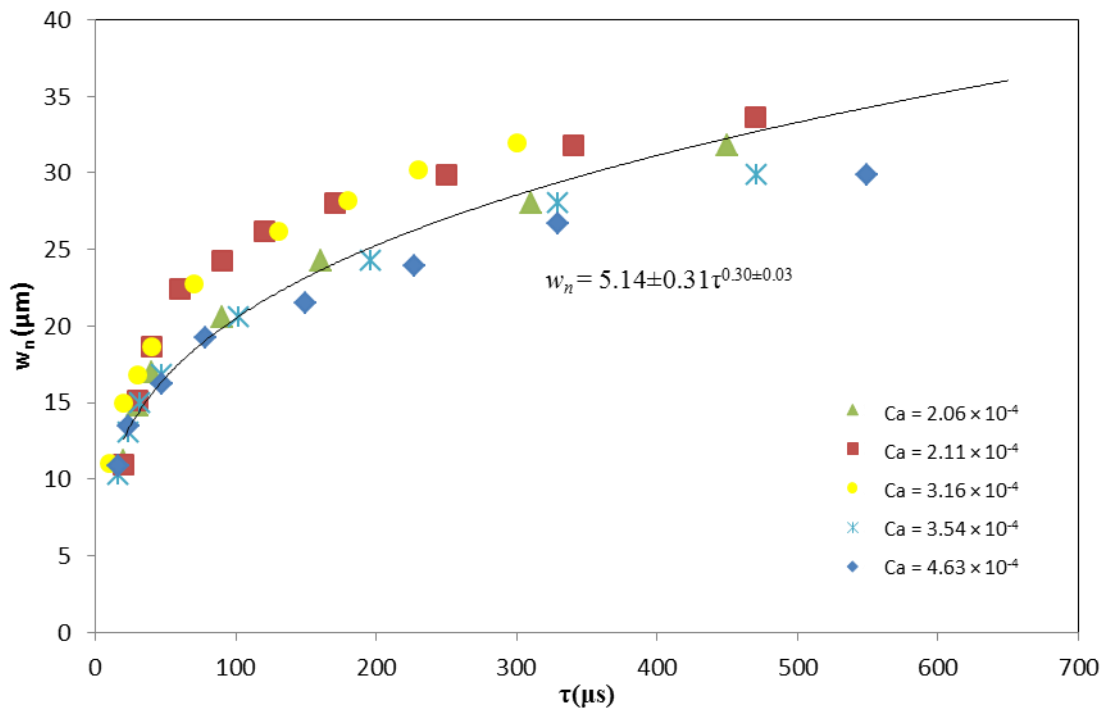
Figure 5.25 Plot of the neck collapse during snap-off at different velocities in the sudden constriction for the 2-row foam. Gradual constrictions produced same exponents.

174

A careful observation was required during the experiments, especially when foam underwent snap-off and neighbour-wall. Some results that looked (at low frame-rate) as if the bubbles underwent neighbour-wall could deceive the observer. A snap-off that was initiated by neighbour-wall was observed under some conditions, noticeable only at a high frame rate ($\geq$ 100000 fps). As the neighbouring bubble approaching the constriction was pressing on the bubble lamella against the constriction wall, the liquid accumulated in the throat would snap the lamella just before pinch-off occurred (Figure 5.26). How the neck was decreasing at two different positions is also shown in Figure 5.27. The two widths vary in a relatively similar way in the first stage (100 μs $< \tau <$ 600 μs) with the pressed width (red) being smaller. Once
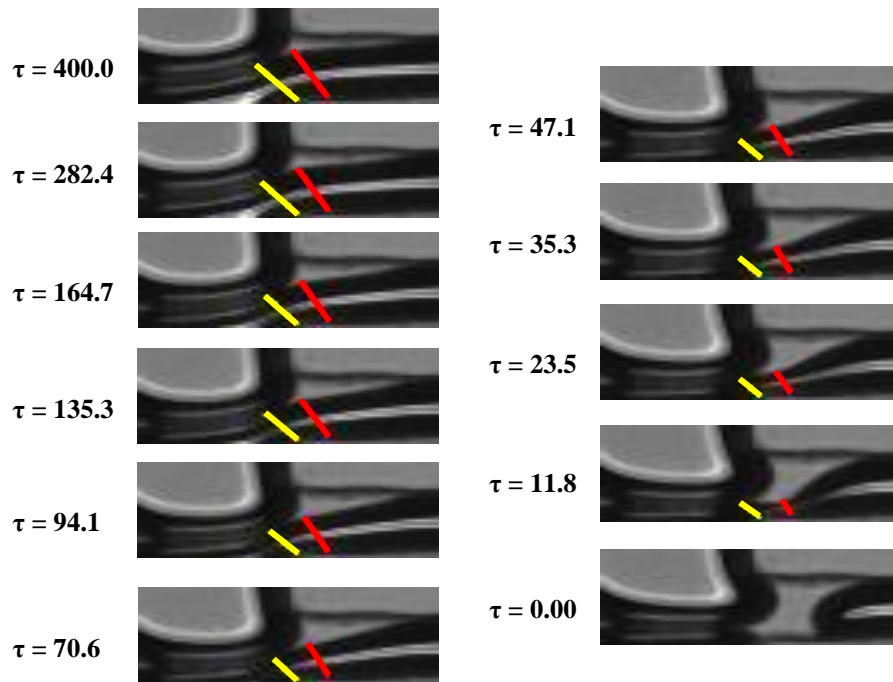
Figure 5.26 Bubble neck collapse at two positions, yellow line due to the bubble pressing against the wall and red line that was triggered by the same bubble but then proceeded to snap (τ is in ms). Ca $= 5.90 \times 10^{-4}$, $\phi_{or} = 26\%$.

 the neck that is eventually snapped (yellow line in Figure 5.26 and yellow points Figure 5.27) gets to around 25 μm, it becomes unstable and thins independently of the other bubble but only due to the liquid flow in the constriction. The red line still continues to thin, but once the

negative curvature of the snapped neck becomes visible, the thinning becomes much faster and surpasses the pinch-off, resulting in only snap-off. This shows the importance of snap-off in a constricted flow; especially in wetter foams, where the liquid can strongly contribute to foam break-up even when the lamella reduction is initiated by bubble-bubble interaction. It also has to be noted that this snap-off was observed in some cases where it prevented the neighbour-wall pinch-off every single time as the foam passed through the constricted throat, indicating that the same but drier conditions could result in bubbles undergoing neighbour-wall rather than snap-off.
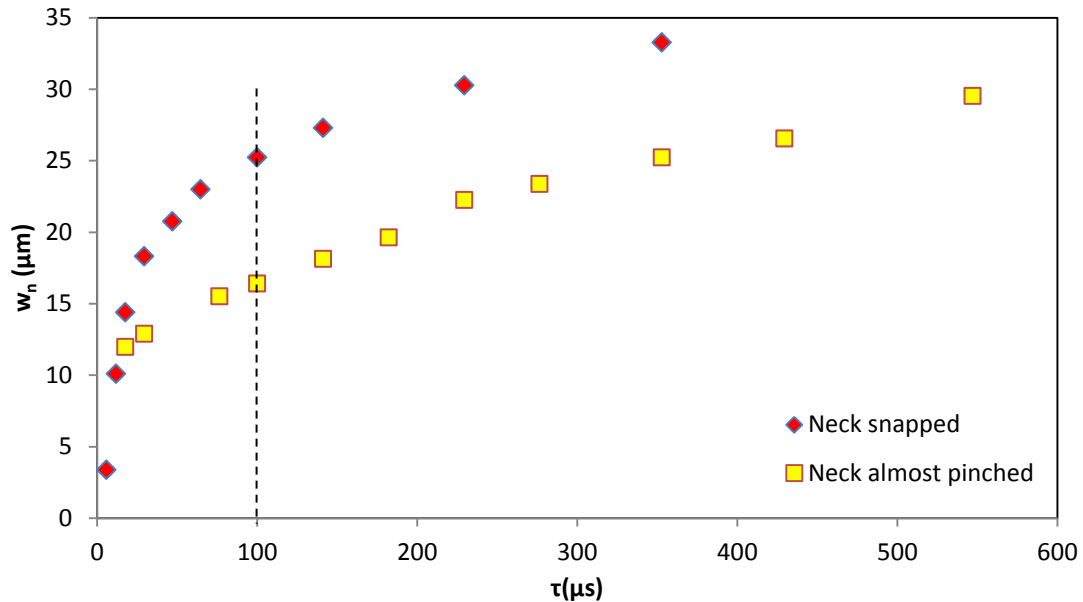
Figure 5.27 Plot of the neck decrease due to the bubble pressing against the constriction wall and the neck collapse caused by the snap-off.

5.3.1.5.2 Neighbour-wall pinch-off

The neighbour-wall pinch-off produced a power law equation with the coefficient of $\alpha = 2.17 \pm 0.3$ and the exponent of $\beta = 0.49 \pm 0.03$ (Figure 5.28). The coefficient of the power-law equation has a broader standard deviation due to the fact that it is dependent on the liquid flow-rate, gas pressure, bubble regime/arrangement, pinching bubble and constriction type.

The exponent, on the other hand, has a small variation (SD = 0.03) and was also found in a similar microfluidics system (Liontas *et al.*, 2013). Moreover, it corresponds to the bubble pinch-off in a low viscosity solution (<10 mPa.s) that was reported by Burton, Waldrep and Taborek (2005). During the neighbour-wall pinch-off, the bubble that pushes on the pinched lamella flows freely at a velocity similar to the liquid velocity while the pinched bubble is quite stationary until the final pinch-off. The pinching bubble together with the surrounding liquid can be thought of as the external phase and since the viscosity of the solution is low (0.93 mPa.s), it produces a low viscosity like collapse. Moreover, the bubble breaks at the exact time when the pinching bubble touches the constriction wall, meaning the pinching bubble and its stress is the main driving force of the break-up. Hence, the neck does not become as unstable as in the case of snap-off.
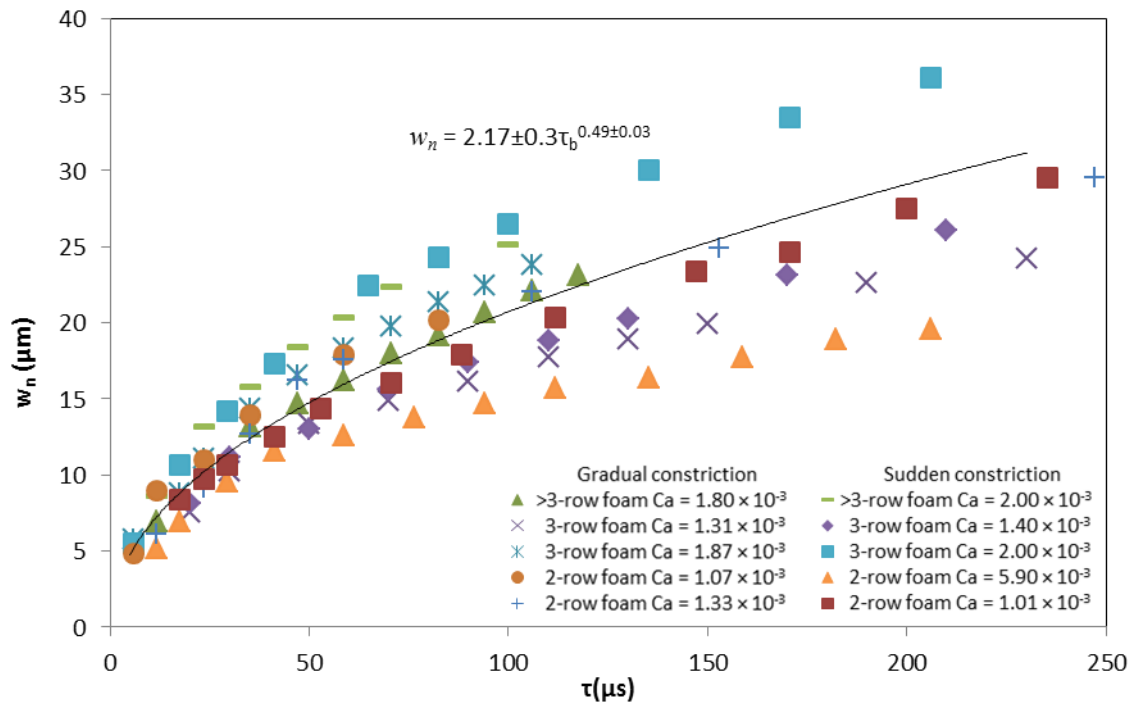
Figure 5.28 Plot of the neck collapse due to the neighbour-wall pinch-off. The data shown is from various experiments from the gradual and sudden 35 μm throat constrictions.

5.3.1.5.3 Neighbour-neighbour pinch-off

The neighbour-neighbour pinch-off generated a different power-law equation compared to the neighbour-wall pinch off. The coefficient found was $\alpha = 0.58\pm0.1$ with the exponent $\beta = 0.99\pm0.03$ (Figure 5.29). The exponent corresponds to the bubble pinch-off in the fluid of very high viscosity (>100 mPa.s) (Burton *et al.*, 2005). The similar exponent was found in the studies by Liontas *et al.* (2013) with a different constriction which again indicates that the coefficient is independent of the channel geometry and is most likely universal. Since the driving forces in this break-up are the two neighbouring bubbles (more precisely, the normal stresses of the two bubbles exhorting on the pinched bubble), their dynamics mimic the highly viscous fluid. This is probably caused by the quasi-stationary movement of the two outer bubbles along the horizontal direction just before the constriction. Since for this regime the bubbles must be close together and confined, they do not move as freely near the constriction as in the case of the neighbour wall pinch-off (where a bubble moved at the same velocity as the liquid) and thus produce a high flow resistance-like external surrounding. Such results show that it might be appropriate to model foam and its apparent viscosity even two orders of magnitude higher than the actual viscosity of the liquid.
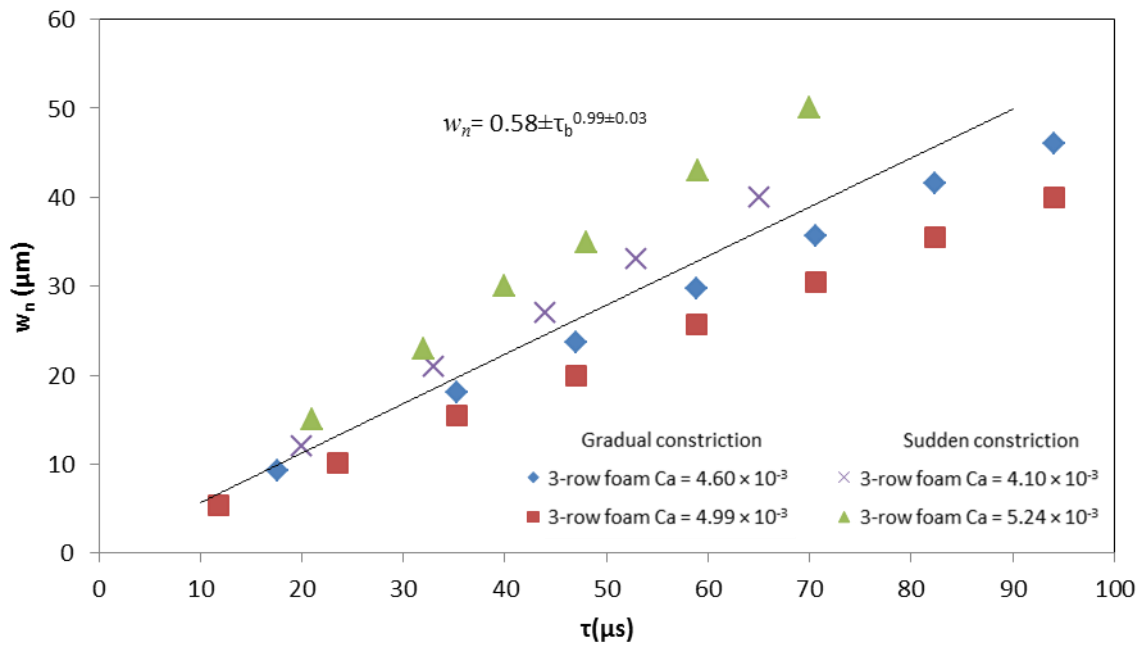
Figure 5.29 Plot of the neck collapse due to the neighbour-neighbour pinch-off. The data shown is from various experiments from the gradual and sudden 35 μm constrictions. The data shown is quite limited because at higher velocities it was difficult to capture and measure precisely the final collapse.

5.3.2 SUDDEN AND GRADUAL EXPANSIONS

So far, the focus has been mainly on the bubble dynamics as they approach or just inside the constriction, including different types of break-ups. However, as the bubbles leave the constriction, they undergo bubble rearrangement due to channel expansion which can impose both elastic and plastic deformations. A study involving a flow of foam in a diverging channel was carried out in a channel larger than before so that standard image analysis techniques could be applied. The channel downstream of the flow-focusing device was 280 μm wide while the expansion had an aspect ratio of three (channel width 840 μm). The expansion channel was not very long (~3 mm see Figure 5.3 (b)) so that it would not cause the device to collapse. Since PDMS is elastic, the channel walls can collapse if the device is very long and wide. The dimensions of the main parts of the channels studied are shown in Figure 5.30.
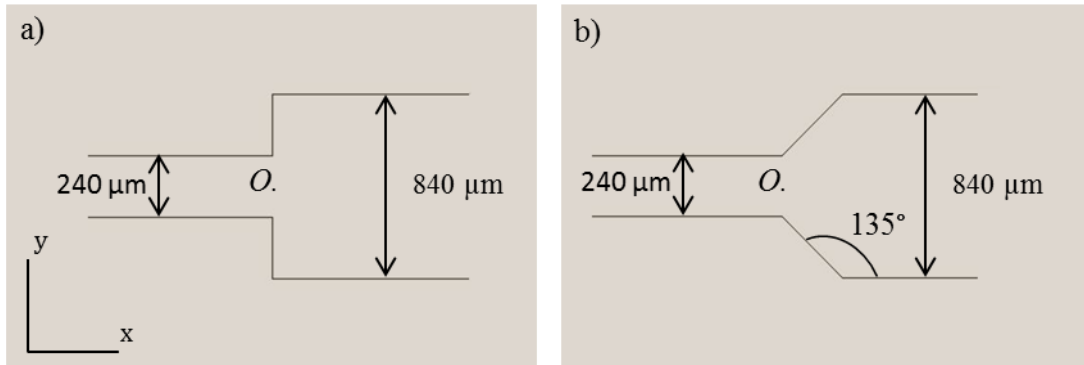
Figure 5.30 A schematic of the expansion channels (not to scale) studied: a) the sudden expansion and b) the gradual expansion. In both of the geometries the origin is taken to be in the middle of the start of the expansion.

Bamboo foam, as well as staircase foam, were studied in the expanding channels and are presented below.

5.3.2.1 Bubble rearrangement

Bamboo and 2-row foam through the diverging channel underwent similar bubble rearrangements, whether gradual or sudden. One could manipulate the arrangement of the bubbles in the expanded channel by varying the initial bubble size and velocity. Such processes generated bubbles to go from bamboo to 4, 3, 2, 1-row foam and staircase to go to 7, 6, 5, 4, and 2-row foam (Figure 5.31). It should be noted that the 2-row foam did not re-arrange to the 3-row foam structure. This was due to the fact that the natural state of the staircase would be to arrange into the 2-row vertical foam upon passing over the expansion (Figure 5.31 (b)) the last image), however, if the size was not large enough (as in the same figure but previous image), the bubbles would start changing their elastic stress towards equilibrium (i.e. adapting the hexagonal shape). The bubbles would, therefore, not be large enough to span the total width in threes and thus would not produce the 3-row stable structure. The bubble size was, therefore, crucial in order to obtain the correct arrangements, however, for 1 to 1 as well as 2 to 2 arrangements, flow velocity was also crucial so that the

bubbles would not have time to relax and restore their shape. At low velocities, energy input from the flow-rates is small, and so bubbles are not experiencing high shear stress which allows them to simply relax and restore their shape to hexagonal (in a planar view) unless the bubble size is relatively large. For the 1 to 1 arrangement at low velocities, bubbles had to be as large as $A^* > 4.11$ (Figure 5.32) to maintain the expanded shape. More energy is applied at higher velocities, which allows smaller bubbles to sustain the same film expansion as larger bubbles at lower velocities. In addition, viscous forces become more dominant, allowing larger elongations. Since the bubbles are flowing faster and they are more compact, the same behaviour (1 to 1) was observed at values as low as $A^* = 1.94$.
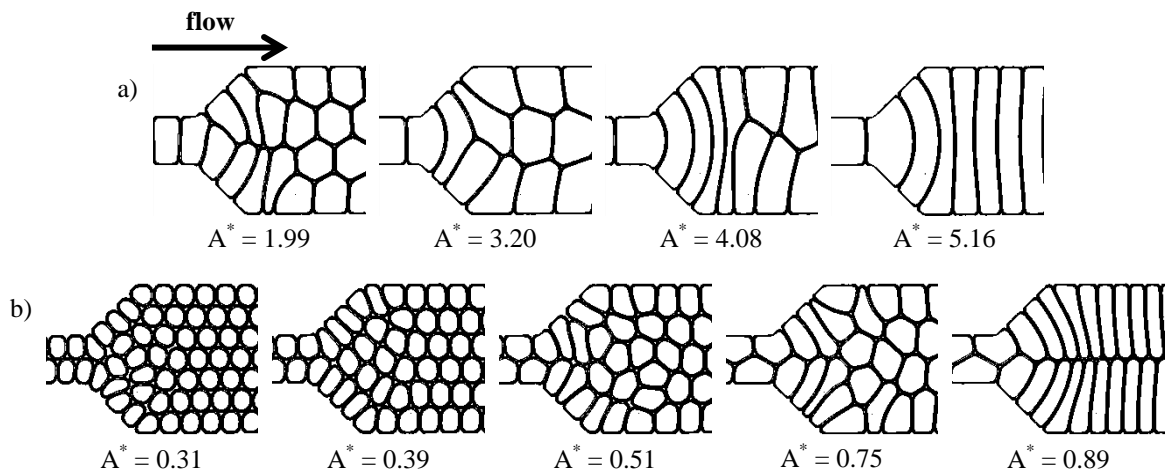
Figure 5.31 Images showing different re-arrangements in the gradually expanding channel at similar velocities: a) from bamboo starting from left to 4-row, 3-row, 2-row and 1-row, (b) from staircase starting from left: 7-row, 6-row, 5-row, 4-row, 2-row. Identical arrangements were observed in the sudden expansion.
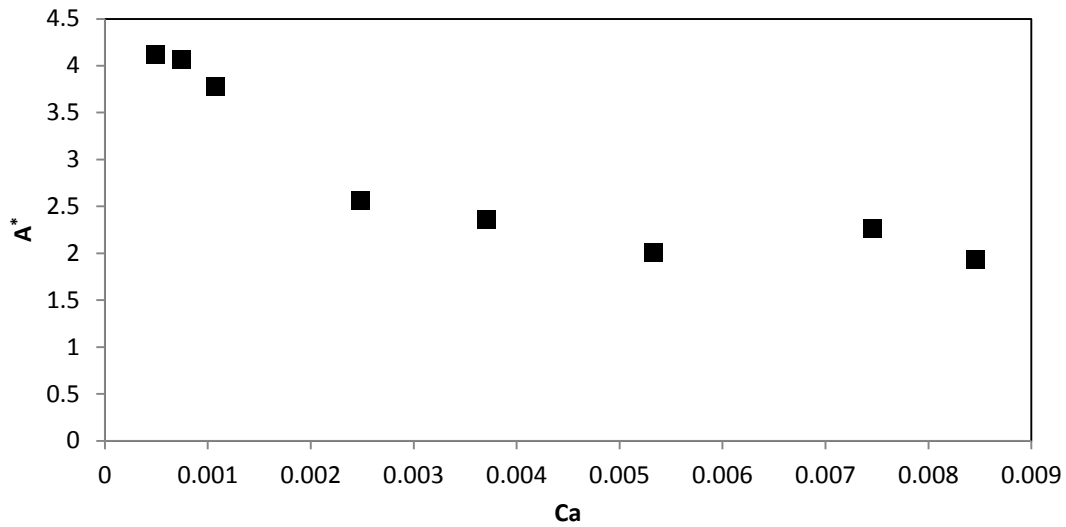
Figure 5.32 Plot of the capillary number against the smallest bubble size that was observed in both of the expansions for the bamboo to 1-row foam.

5.3.2.2 Staircase foam case study

A comparison of two similar cases was studied in a sudden and gradual expansion. The investigated foam originally had a staircase structure in the upstream channel, which then translated to the 7-row structure in the downstream channel. The two cases studied were relatively similar in terms of the initial foam velocity, liquid volume fraction and bubble size (Table 5.1).

Expansion type	U_f (m/s)	ϕ_{or}	A^*
Sudden	0.27	0.15	0.18
Gradual	0.26	0.16	0.17

Table 5.1Table showing parameters of the two cases studied in the suddenly and gradually expanding channels.

Images of the two cases investigated are shown below (Figure 5.33). The volume liquid fractions calculated from the flow-rates were 0.15 and 0.16 for the sudden and gradual expansion, respectively. Therefore, the foam was in a slightly wetter regime which generated relatively wet corners with low velocities in the sudden expansion. Some bubbles that managed to flow into the corners ended up being overflown by other bubbles, thus creating

182

temporary recirculating zones. On average, each bubble in the corner was surpassed by four bubbles. Thus, the initial positions were significantly changed. The same behaviour was not observed in the gradual constriction where bubbles would always flow towards the exit.
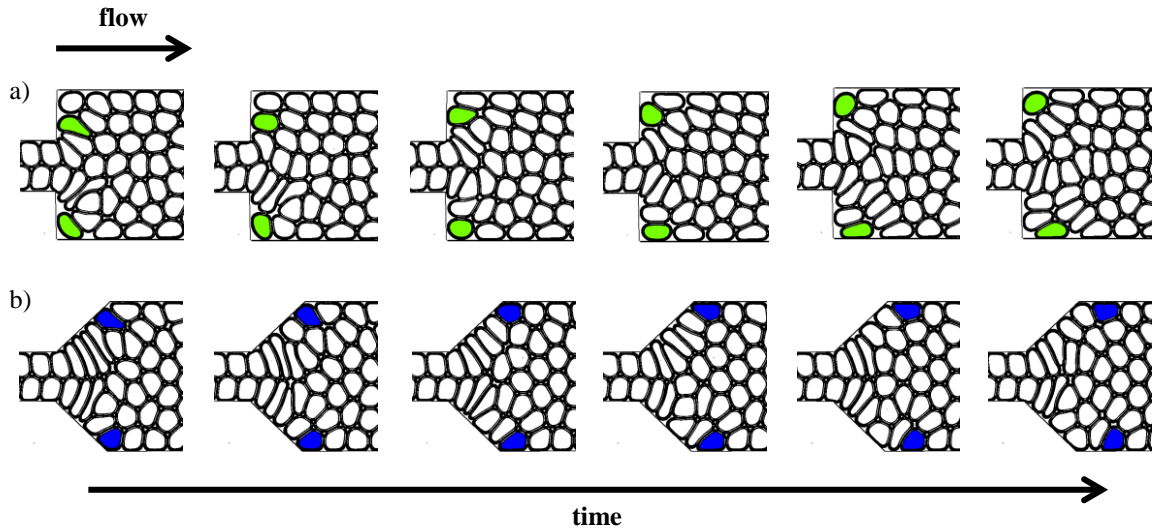
Figure 5.33 Consecutive sequence of images of foam flowing through a diverging channel: a) sudden expansion, notice how the green bubbles get stuck in the corners while other bubbles flow over them, eventually the bottom green bubble is pushed away; b) gradual expansion, the blue corner bubbles simply diverge along the walls as in a plug flow.

5.3.2.2.1 Velocity profile

Velocity profiles were obtained as described in 3.2.9 for the two cases studied and are shown below in terms of velocity vectors and magnitude (Figure 5.34). As expected, the highest velocities were observed in the upstream section of the channels, where the channel width is smallest. In the sudden expansion as mentioned before, lowest velocities were observed in the corners of the constrictions where some bubbles ended up getting stuck in there, allowing other bubbles to flow over them. This created temporary recirculating zones, as indicated by the lowest velocity magnitude (Figure 5.34). Such features were not observed in the dry foam (Dollet, 2010), where during a steady-state, the foam exiting contraction flowed towards the very corners and then carried on towards the exit. Moreover, bubbles in those corners created

additional structure confinement that gave a similar velocity profile to the gradual constriction. This can be identified on the velocity values along the central line (Figure 5.35), where both horizontal velocities (U_x) have similar gradients once they reach the expanding zone. Although one should expect a faster drop in the sudden expansion, the wet corners as well as the "recirculating bubbles" produced a much smoother profile. In addition, the gradual expansion had the second change of the channel's width which generated a variation in the transversal velocity (U_y) from the zero value and a slight variation in the gradient of U_x. Once the bubbles reach their near-equilibrium state, they start flowing as in the plug flow as indicated by the zero value of U_y.
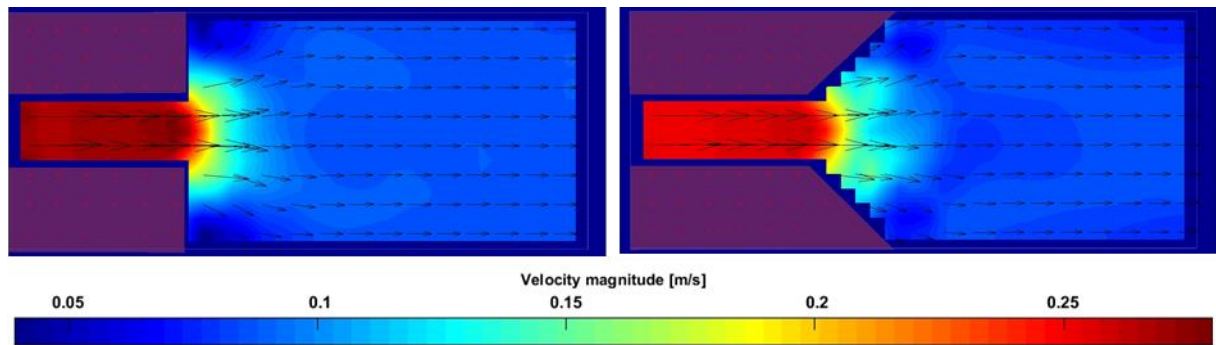
Figure 5.34 Velocity field for the two expansions, left sudden and right gradual. Notice lowest velocity magnitude in the corners of the sudden expansion.

184
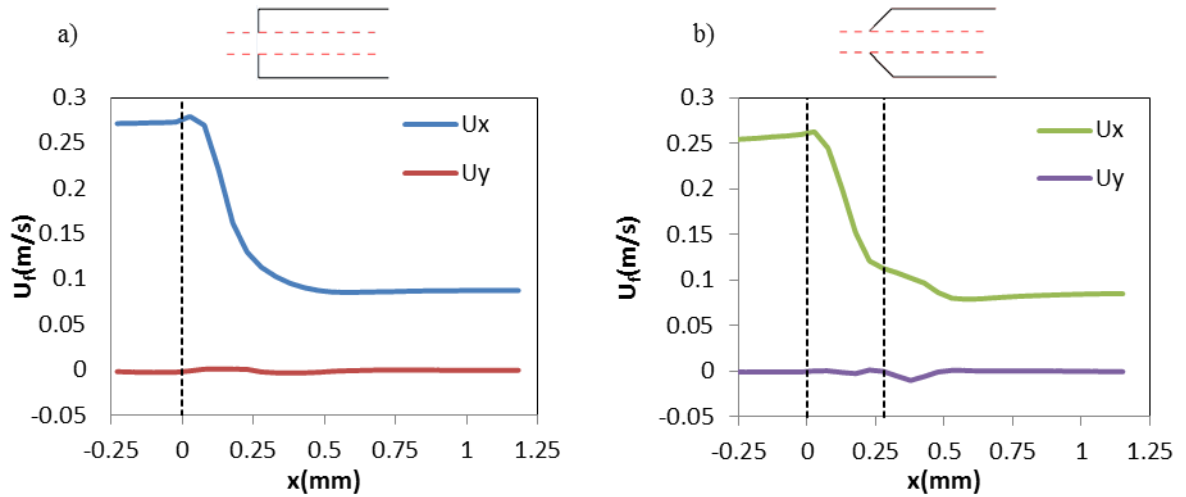
Figure 5.35 Velocity components along the central line (shown above the plots) in a) sudden expansion, b) gradual expansion. The dotted lines indicate the change in the width of the channel. There seems to be a velocity overshoot near the expanding point which is most likely a PIVlab overestimation due to large bubble deformations.

5.3.2.2.2 Elastic deformation

The texture tensor, as described by Aubouy *et al.* (2003), was used to evaluate elastic bubble deformation in the expanding channels. At first, the centres of each of the bubbles are extracted. Then using Delaunay triangulation, the centres are linked to their closest neighbour, and the data is recorded as the list of pairs of all the neighbours (s_1, s_2) and their connections (links) $\vec{l} = (l_x, l_y)$, which are in terms of their position vectors $\vec{l} = (\overrightarrow{r_{s2}} - \overrightarrow{r_{s1}})$. The size of the image can be thought of as the network of all the links. The network is then split into identical volumes $V(\vec{R})$ (Figure 5.36 (a)) at position $\vec{R}$ so that links can be evaluated in each of the volumes and then averaged over at least 500 frames. The texture tensor is then defined as

$$\bar{\bar{M}}(\vec{R}) = <\vec{l} \otimes \vec{l}> \tag{5.2}$$

where $(\vec{l} \otimes \vec{l})_{i,j} = l_i l_j$ is the tensor product. The texture tensor is, therefore, a symmetric tensor with positive eigenvalues by its definition. The tensor is represented by two orthogonal

185

lines which correspond to the two eigenvalues and are oriented along the corresponding values of the eigenvectors. The larger eigenvalue indicates the direction of the elastic stress of the bubble, i.e. compression or elongation. Such tensor is then represented by an ellipse fitted to the two orthogonal lines (Figure 5.36 (b)) which describes the elastic strain of the foam. It has to be noted that the texture tensor is entirely geometrical.
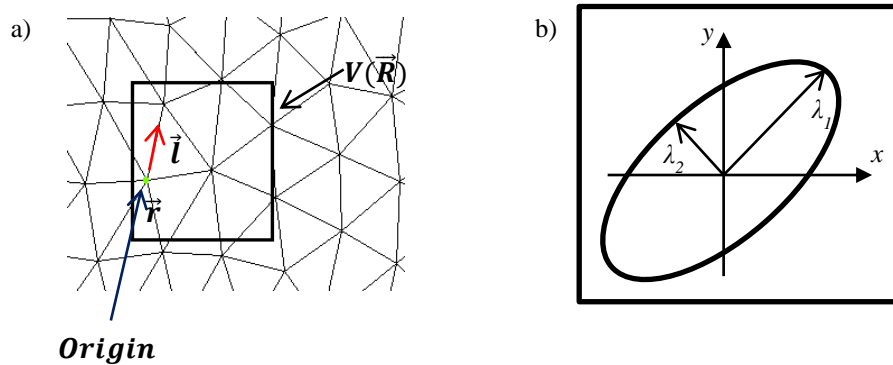
Figure 5.36 An illustration of a) the network based on Delaunay triangulation with a sample representative volume $V(\vec{R})$, b) elliptic representation of the tensor with two eigenvalues (λ_1, λ_2) corresponding to the direction and magnitude of the deformation. In (a) the volume has only three links since all the other vertices (centres of the bubbles in this case) fall outside of the box.

Two texture tensor maps were produced for both of the expansions (Figure 5.37). The maximum deformations and therefore stresses, in both of the cases, were found near the expanding section. The sudden expansion had bubbles getting compressed as soon as they reached the expansion zone. Some bubbles were forced to flow towards the corners, which reduced their deformation near the walls just before the corners since there was more space for them to relax. The bubbles in those corners that were overtaken by other bubbles were often squeezed by them which produced almost entirely horizontally elongated ellipses. In the next bubble column set, bubbles would reach their maximum compression before starting their elastic relaxation in order to reach their equilibrium state. It can be clearly seen that ellipses gradually change their shape as they flow towards the exit; however, their final

equilibrium state was reached outside of the field of view. The gradual expansion was found to have similar deformations as the sudden expansion; however, on average, the maximum stress obtained just outside the expanding zone was slightly greater. This is due to the fact that bubbles do not flow towards the 90° corners, but instead carry on gradually expanding while being compressed. Furthermore, because the straight channel section was reached later than in the case of the sudden expansion, the bubbles did not relax as much as in the former before leaving the field of view.
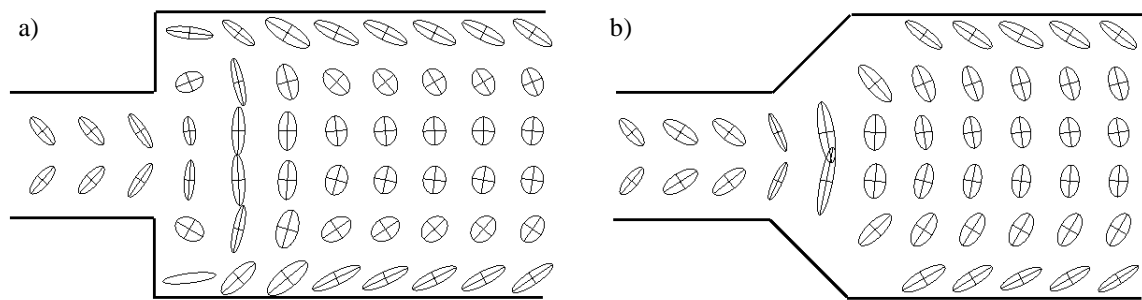
Figure 5.37 Maps of ellipses representing texture tensors: a) sudden expansion and b) gradual expansion.

5.3.2.2.3 Plastic deformation

Plastic deformation is shown as a map of the locations of occurrence of the T1 events. Since the foam was in the wet regime, the T1 events were identified once the two small plateau borders formed a larger one indicating the change of their neighbour. Two expansions can be compared by direct observation of the two fields (Figure 5.38). Both of the expansions have many similarities. At first, there are zones of almost no plasticity just at the expansion entrance zone. These are the zones where bubbles are starting to elongate, as shown in the previous elastic section. The bubbles simply attempt to maintain the 2-row structure, just like in the upstream channel. Furthermore, it can be noted that the gradual expansion has a longer "zero plasticity" zone which again corresponds to the fact that bubbles stretch gradually for longer, instead of going towards the far corners when compared to the sudden expansion.

187

Once the bubbles can no longer stretch, they start undergoing T1 events. Clearly, the maxima of T1 events are located at the centres of the channels where bubbles no longer can flow as the 2-row structure. The sudden expansion has a larger number of the T1 events due to the more drastic change of the channel width and bubbles trying to fill all the other locations across the channel. Moreover, both of the expansions have a second maximum at the expansion walls since many bubbles near those walls are too close together and are often forced to flow towards the central part of the channel rather than along the walls. Similar results have been reported by Dollet, (2010) in a Hele-Shaw cell for a dry foam ($0.2\ \% \leq \varepsilon_L \leq$ $0.4\ \%$) through a contraction wherein the downstream section the foam had secondary plasticity maxima near the expansion walls outside of the constriction. Further downstream of the expansion, in both cases, the foam experienced some small plastic deformations near the channel walls where bubbles are sheared more (due to the wall friction) than in the central part of the channel. Near the very final section in the central channel where bubbles are relaxed the most, the foam underwent almost no T1 events indicating the viscoelastic behaviour of the foam. Thus, it has been shown that foam flows like a viscoplastic fluid near the diverging channel where the change of channel dimensions occurs (i.e. the expansion imposes stress that forces bubbles to exhibit plasticity) and then starts behaving more like a viscoelastic fluid in the straight channel.

Calculating the frequency of the T1 events (f_{T1}) as follows

$$f_{T1} = \frac{N_{T1}}{(A_{box} * t_{movie})}$$
(5.3)

where N_{T1} is the number of T1 events found, A_{box} is the area investigated, and t_{movie} is the length of the video, more data could be compared. Surprisingly, along the central line of the channel, the gradual expansion has a higher frequency peak (Figure 5.39 (a)). Since the channel expands gradually, the bubbles divide themselves across the channel at the almost

exact location and therefore, generate higher frequency. However, the peak is slightly narrower compared to the sudden expansion. In the sudden expansion due to the wider channel width, the plastic deformations are spread across the channel and thus have a lower
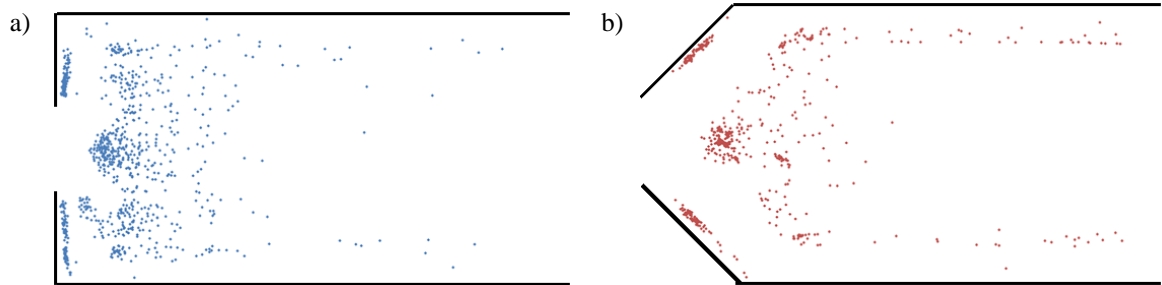
Figure 5.38 Locations of the T1 events across two expansions: a) sudden and b) gradual. Only expansion parts are shown since the upstream channel had a stable staircase structure.

frequency even though the total number is higher. This can again be noted in the same figure along the *y*-axis (Figure 5.39 (b)) where most of the T1 events occurred; the peak of the gradual expansion is larger; however, the total integral below the curve of the sudden expansion is greater which means the broader spread of the plasticity along the *y*-axis.
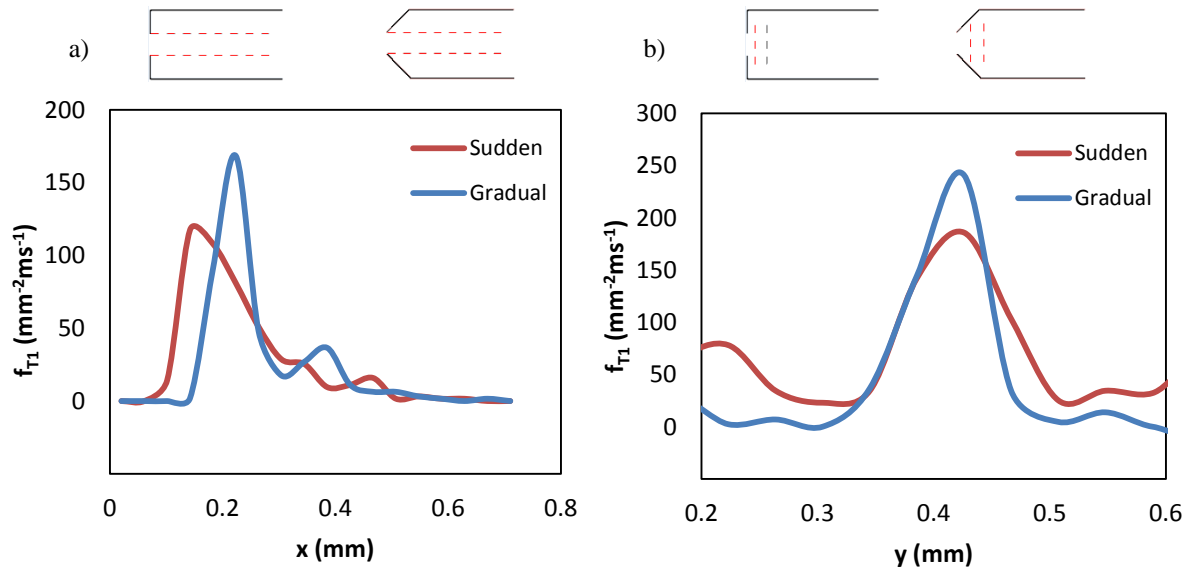
Figure 5.39 Plot of the frequency of the T1 events a) along the central axis b) along the *y*-axis where the maximum T1 events occurred. The locations of the axis that the frequencies are calculated along are shown above the plots.

5.3.2.3 Effect of velocity and bubble size on foam elasticity and plasticity

Elastic deformation in both of the channels can be explained best using the cases where bubbles do not undergo any plastic deformation so that they elongate most, like in the case of the 2-row to 2-row or bamboo to 1-row. Bamboo is chosen for simplicity since the films can be measured precisely along the channel width. It has already been shown that the width of the bamboo can elongate as much as three times since the channel walls in both of the expansions increase by a factor of three. However, at the corners of the expansions, the film stretches the most (Figure 5.41) (reaching widths larger than three times the initial width of the channel) due to its parabolic shape caused by the pressure differences across the film. In the staircase foam case study, it has been mentioned that on average bubbles elongated more in the gradual expansion due to a smaller total number of the T1 events. However, the maximum elongation caused by a higher pressure drop was observed in the sudden expansion. This can be seen on the plot of the bamboo width scaled with the initial width (w_b/w_i) along the x-axis (Figure 5.40). It can be seen that for the gradual expansion, the width increases gradually at a lower gradient reaching a maximum value at 3.20 and then decreasing to the value of 3. The sudden expansion, on the other hand, reaches its peak at a faster gradient since the distance from the expansion location that the film has to travel towards the very corners of the expansion is shorter than in the gradual expansion. Moreover, the maximum elongation reached in the sudden expansion (4.13) is caused by the faster sudden change of the channel width and, therefore, higher pressure drop. Increasing the velocity did not change the maximum film elongation but instead allowed smaller bamboo sizes to reach the same maximum value as mentioned earlier (Figure 5.32).
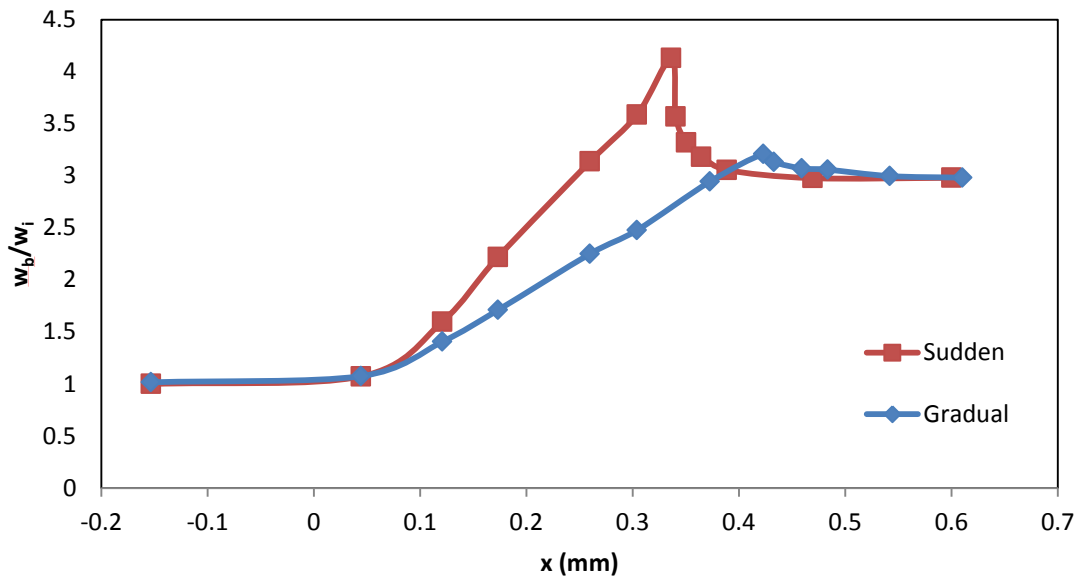
Figure 5.40 Bamboo width along the x-axis in the case of 1 to 1 flow. The zero value along the *x*-axis corresponds to the expansion point.
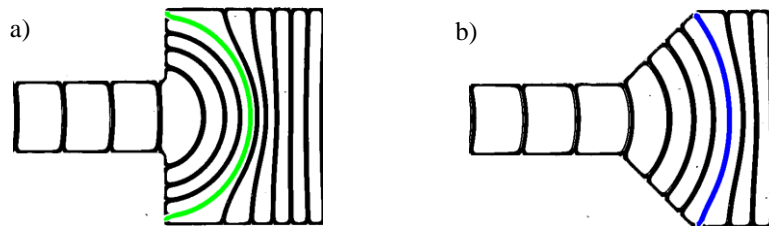
Figure 5.41 Illustration of the 1 to 1 flow in expansions highlighting the maximum stretch of the films: a) sudden and b) gradual.

The same foam structure as the reference case, i.e. staircase foam with very similar bubble size was investigated at different velocities. Data is shown only for the gradual expansion since the main differences between sudden and gradual expansion have been presented. The data are shown in terms of T1 frequencies along the central line (Figure 5.42). As expected, the frequency of plastic deformations increases with an increase in velocity i.e. a greater number of bubbles passes through the expansion at a faster velocity, which generates a higher frequency of bubbles in general, and therefore, a higher frequency of T1 events. Moreover, the location of the peak varies, moving further away from the expansion point with

the increase in the velocity. Faster velocity means a more substantial energy input into the system which allows the bubbles to travel further down the expanding channel before relaxing and starting to change their shape to hexagonal.

Similar results were observed for flows with different bubble sizes. Firstly, larger bubbles will take more space and, therefore, have fewer re-arrangements than smaller bubbles which naturally reduce the frequency of the T1 events. For instance, bubbles flowing from the 2 to the 2-row structure will undergo no T1 events at all. In addition, larger bubbles can expand for longer periods of time than smaller bubbles; simply because their size is sufficient enough to maintain the 2-row structure (they require smaller deformations in order to maintain it). This allows them to travel further downstream as the 2-row structure before restoring their shapes and in consequence, experience many T1 events, which again explains the different location of the maximum frequency along the *x*-axis (Figure 5.43).
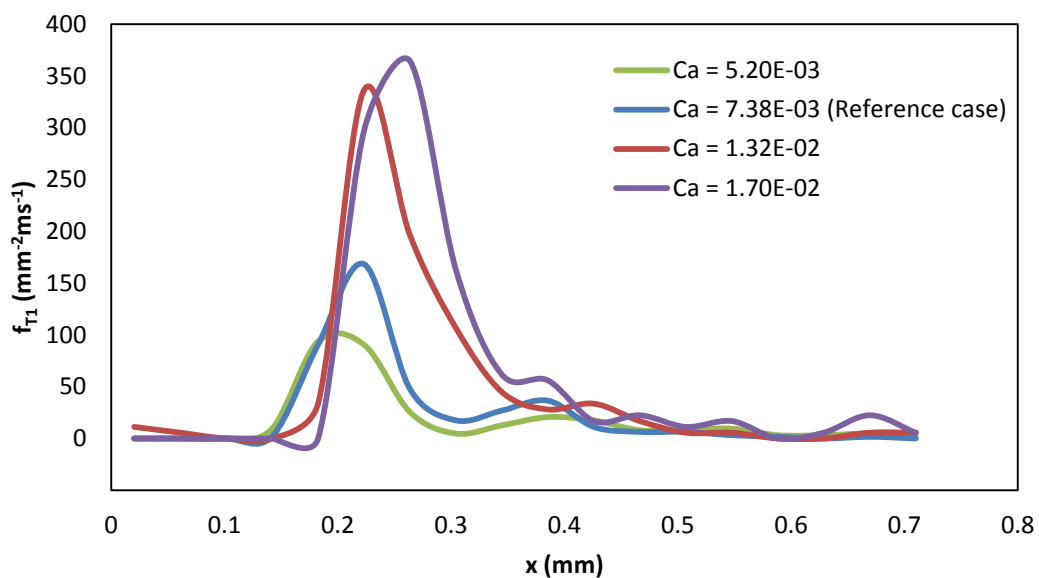
Figure 5.42 Plot of the frequency of the T1 events in the gradual expansion for four different velocities.
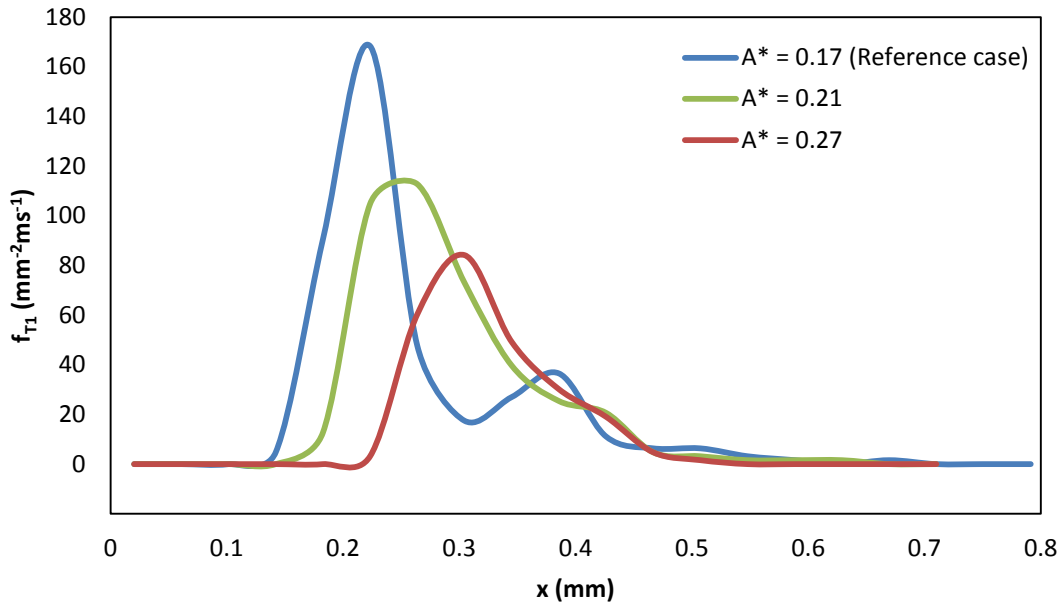
Figure 5.43 Plot of the frequency of the T1 events in the gradual expansion for three different bubble sizes.

5.4 CONCLUSIONS

Different foam regimes were investigated in the microfluidic channels generated using a flow-focusing junction. The bubbles were found to undergo different foam dynamics across different bubble sizes and capillary numbers. In the sudden constriction, three types of break-ups were identified, such as snap-off due to the capillary pressure difference, neighbour-wall pinch-off caused by the bubble and wall of the constriction and the neighbour-neighbour pinch-off caused solely by the bubble-bubble interaction. The later was generally occurring at higher capillary numbers where the shear stress was sufficient for soft bubbles to pinch another bubble. In addition, gradual walls of the constrictions introduced new dynamics such as bubble re-orientation whenever bubbles had the required size (usually with $0.3 < A^{*} < 0.6$) and often low velocity (depending on the constriction type).

The narrower constrictions were found to favour snap-off in wetter conditions and showed that it was caused by the radial flow of the liquid. The width of the constriction was found to be crucial in order to impose break-ups, requiring lower capillary numbers to cause most of the instabilities. The length, on the other hand, was not found to be a significant factor, causing a much lower impact on the bubble dynamics, especially when the width was not as narrow.

The neck collapse was found to decrease at different power-law exponents for each of the break-ups. The snap-off scaled with the power-law exponent of 0.33, which corresponds to the effect of liquid inertia and agrees with the results found for snap-off in single bubble flow. The neighbour-wall pinch-off scaled with the exponent of 0.5 which corresponds to the flow in the low viscosity external phase (<10 mPa.s) caused by the pinching bubble which flows freely at a velocity similar to the mean liquid velocity. The neighbour-neighbour pinch-off was found to have an exponent of 1 which corresponds to the external phase of highly viscous fluids (>100 mPa.s), caused, by the almost stationary movement of the two pinching bubbles.

Foam flow in suddenly and gradually diverging channels was studied. The velocity profiles obtained for both of the expansions were more similar than expected, mostly due to temporary recirculating zones in the corners of the sudden expansion. As such, "effective gradual corners" were generated; this resembled the profile of that in the gradual expansion.

Bubbles were found to stretch the most near the diverging walls, where they had to expand because of the sudden or gradual change in the width of the channel. Once the size or velocity was insufficient for the deformed bubbles to span the width of the channel, bubbles started undergoing T1 events. The staircase foam in the gradual expansion had, on average a higher elongation near the centre caused by the gradually increasing channel width.

Moreover, this produced a higher frequency of T1 events along the central line once the bubbles could no longer stretch and were forced by the surface tension to obtain a more hexagonal shape. The sudden expansion, on the other hand, caused bubbles to undergo a maximum elongation as indicated by the largest expansion of the bamboo foam. However, in the case of the initial 2-row foam, the bubbles were found on average to have smaller elongations near the central axis, caused by a wider spread of the T1 events in the vertical direction due to bubbles flowing towards the corners of the expansion.

Higher velocity increased the frequency of the T1 events as well as moved the location of the peak further in the downstream channel of the expansion due to higher energy input from the flow-rates and viscous forces allowing larger and therefore, longer elongations. Bubble size, on the other hand, reduced the frequency of the T1 events because of the smaller number of bubbles (i.e. lower number of films) required to span the width of the channel and pushed forward the location of the maximum frequency peak due to smaller deformations required to maintain a 2-row structure.

Based on the above results, it has been shown that foams can break and therefore, generate new bubbles in porous media through mechanisms such as neighbour-wall and neighbour-neighbour and not just snap-off, lamella division or leave-behind (2.6.1.1). Hence, these mechanisms should be incorporated more into the modelling of flowing foams which could help predict the bubble size distribution and hence, improve mobility control of foams flowing through a network of porous media for oil recovery companies.

Sudden constriction was shown to require a smaller capillary number to impose a break-up and reduce the possibility of re-orientation. Thus, for microfluidic applications where it is often important to reduce the bubble size distribution, a similar suddenly contracting constriction could be added to a channel. Moreover, the results from the expanding channels

suggest that the gradual expansion imposes smaller elastic and plastic deformations when compared to the sudden expansion. In addition, the bubbles are less likely to be stuck in the corners which also have a minor effect on the mean flow velocity. Thus, it might be worth to create a suddenly contracting constriction in order to impose break-ups and increase the total number of bubbles in the channel followed by a gradually expanding constriction so that the bubbles exiting the constriction are affected as little as possible.

6 FOAM FLOW AROUND OBSTACLES

In this chapter, the flow of *in situ* foam around obstacles in presented. As earlier, microfluidics is chosen as the experimental platform allowing good flow visualisation and fabrication of different obstacles. Foams composed of larger bubbles, especially bamboo foams, are studied as they flow around a single cylindrical obstacle located in the centre and off-centre, and multiple obstacles. The goal of this study is to improve a fundamental understanding of foams and how they behave around obstacles, including bubble division and topological changes. Moreover, a study is compared with numerical results by calculating the new number of bubbles generated around the obstacles. The results are found to be in good agreement.

6.1 INTRODUCTION

The well-known Stokes experiment for flow past a sphere has shown that the drag force exhorted on a sphere by a Newtonian fluid at low Reynolds number is $F = 6\pi\mu Ru$ where μ is the dynamics viscosity, R is the radius of the sphere, and u is the flow velocity relative to the object. This study served as a basis for viscometers with falling spheres. If the radius and the density of the sphere are known, the viscosity of the fluid can be measured once the sphere reaches the terminal velocity. In foams, measuring a drag force could, therefore, allow calculating the effective viscosity of the flowing foam which has been previously done by de Bruyn (2004). However, the first well-detailed work was carried out by Dollet, Elias, Quilliet, Huillier *et al.* (2005) in a two-dimensional flow of foam between two plates past a cylindrical obstacle. The drag force was measured using a glass fibre attached to a cylindrical obstacle that could move horizontally and then was balanced by the fibre. This allowed calculating a drag force exerted on the obstacle and studying the influence of the flow-rate, liquid viscosity, bubble area, obstacle size and its boundary condition. They showed that the

foam exhibited the solid-like properties by observing the drag not going to zero at a low flow-rate and fluid-like properties by the increase of the drag as the flow-rate was increased. The drag force (F) which was represented by the yield drag (F_0) and the viscosity coefficient ($m \propto \mu_{eff}Q$) had different dependencies on the control parameters. The yield drag, for example, was independent of the viscosity of the liquid since it depends on the yield characteristic of the foam which is dependent on the bubble size and the surface tension (Princen, 1983). Thus, it was shown to decrease with the increase in the bubble size and increase with the increase in the obstacle diameter. Moreover, for the yield drag, a cogwheel (obstacle with teeth like perimeter) was shown to behave like a large cylinder due to bubbles being trapped in the obstacle. However, the obstacle behaved like a smaller cylinder for the flow-rate dependent viscous coefficient. The explanation was that at low flow-rates the obstacle together with the trapped bubbles serves as the "effective obstacle", whereas, at higher flow-rates, the friction between the trapped bubbles and the flowing bubbles is lower than the friction between the solid obstacle and flowing bubbles. In addition, the viscous coefficient was found to increase (power-law) with the liquid viscosity, thus working in a similar way to the capillary number at a pore-scale. However, both the viscosity and liquid flow-rate (product should be proportional to the capillary number) had different power exponent ($F = F_0 + Q\mu_L^{0.77 \pm 0.05}$) meaning that capillary number is not sufficient enough to describe the dynamics of such a foam system, instead, more foam characteristics are required such as bubble shape, surface viscosity and elasticity. The viscous coefficient was also found to decrease with the increase in the bubble area. The proposed explanation was based on the dissipation model of Cantat, Kern and Delannay (2004) that reasons the dissipation occurs in the plateau borders between walls and bubbles which should increase with the number of

bubbles surrounding the obstacle and, therefore, decrease with the bubble size since fewer bubbles will surround the obstacle.

Furthermore, the same group (Dollet, Elias, Quilliet, Raufaste, *et al.*, 2005) has shown that the drag force does not vary much when exerted on a square obstacle at different orientations and that the simulations around the circular obstacle using Surface Evolver and Potts model agree well with the theoretical and experimental models for different liquid fractions (Raufaste *et al.*, 2007).

Using the same system as the above references, Dollet and Grander (2007) have performed local measurements of elasticity, plasticity and flow in a similar way that was described in the introduction of the constriction chapter (Chapter 5) carried out by Dollet (2010). In the reference case, they observed that velocity field far from the obstacle is a simple plug flow. Upstream and downstream of the obstacle, foam exhibits two symmetric stagnation points. Along the central axis of the flow, they observed a fore-aft asymmetry, showing that the velocity decreases gradually in the upstream part before the obstacle, whereas it has an overshoot downstream of the obstacle. The fore-aft asymmetry is not fully explained by the authors, they only suggest that it involves extensional stresses balanced by either shear or normal stress differences. The pressure was shown to be greatest in the upstream part, and lowest in the downstream. In addition, it was found to be almost flow-rate independent and have a dependence close to an elastic fluid, meaning it is most likely due to the elastic properties of the foam. Plastic deformation (T1 events) were traced and again found to have a fore-aft asymmetry. Although, all of them were found close to the obstacle, in the upstream part they were more distributed and spread over the sides whereas in the downstream they were mostly near the obstacle wake. They also studied control parameters

including, flow-rate, bubble size and foam liquid fraction, and did not observe any qualitative differences; most of the results fell on the same master curve.

In applications where foam flows through a porous medium (e.g. soil remediation, oil recovery), flow past an obstacle can cause a bubble split. This is known as bubble-lamella division (Chapter 3) and has been experimentally studied in a network of porous media (Géraud *et al.*, 2017) in a Hele-Shaw cell as well as numerically in a single obstacle problem (Cox, 2015). Géraud *et al.* (2017) showed that in a two-dimensional system full of obstacles/disks separated in such a way that lamella division is dominant over snap-off, bubble size distribution is reduced and characterised mostly by the geometry of the medium rather than foam properties. Cox (2015) simulated a repeated flow of bamboo past a circular obstacle and found that the polydispersity increased as the foam was repeating another cycle until the division stopped occurring so that the size distribution remained constant. The final average bubble size was slightly larger than the size of the obstacle. Furthermore, by moving the obstacle off the centre, he showed that the polydispersity of the average bubble size was largest. Thus, using an obstacle could be used for a controlled break-up in order to increase the number of bubbles in the channel.

A similar study was carried out by Link *et al.* (2004) in a microfluidic channel using droplets. The droplets were split into two daughter droplets by placing a square obstacle in the middle of the channel. Moreover, placing the obstacle off-centre allowed changing the relative size of the droplets produced and in some instances changed the droplet arrangement downstream of the obstacle. The droplets distribution was dense, and they flowed as neighbours. Protière *et al.* (2010) later investigated single droplets around a cylindrical obstacle and identified critical conditions above which the droplet will always break. The experimental observations and critical conditions were supported with a one-dimensional

model that suggests a surface-tension driven instability due to a variation in the permeability in the flow direction.

The objective of this chapter is to study the flow of foam around single cylindrical obstacles experimentally and observe the dynamics that bubbles exhibit during such flow, with the emphasis on lamella division. The diameter of the obstacle is varied, as well as the location. Calculating the sizes of the daughter bubbles at different flow conditions will help identify the parameters affecting the final bubble size distribution and therefore, improve the foam mobility control for microfluidics and porous media applications. Furthermore, a study of a bamboo foam through a four-obstacle is carried out in order to shed some light on bubble formation through break-ups in a more complex geometry. Identifying control parameters of the foam formation should improve understanding of foams used for oil recovery. The results are compared with a numerical model for wet foams, showing good agreement and future prospect of using the model for foam flow in porous media.

6.2 CHANNEL AND SOLUTIONS PROPERTIES

The dimensions of the channel used in this chapter are shown in (Figure 6.1). The flow-focusing dimensions and the depth of the channel are kept the same, only the size or location of the obstacle is varied. As in the previous chapters, the dimensions and the arrangement of the obstacle/s are shown in the relevant sections.
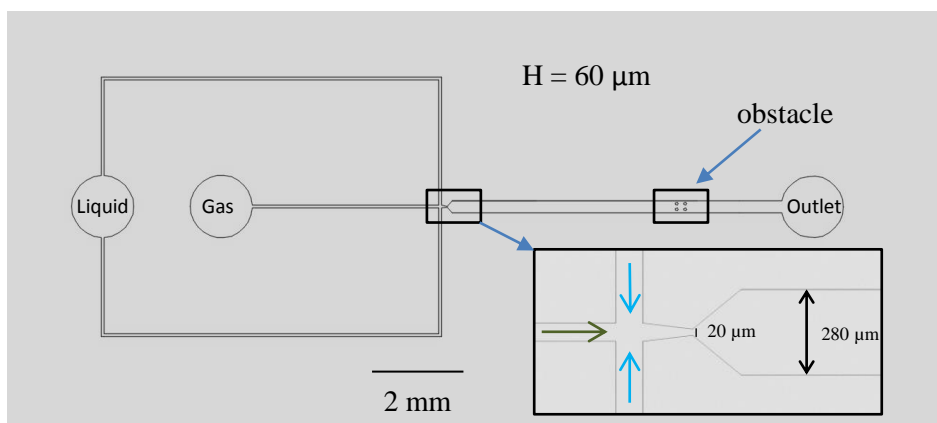
Figure 6.1 Schematic of the channel used in this chapter. The flow focusing (highlighted) junction was kept the same for all of the channels, only the downstream section, i.e. obstacle size/arrangement was changed (shown in the related results section). Green arrows indicate gas phase whereas blue arrows indicate the liquid phase.

The solution used was a distilled water with 3 cmc of NaDBS ($\sigma = 32.2$ mNm^{-1}, $\mu_L = 0.93$ mPa.s) for the majority of the foam experiments. Thus the capillary number was varied by changing the mean flow velocity using gas and liquid pressures. In the case of the bamboo and staircase foam around the single obstacles, the capillary number was also varied by changing the viscosity of the solution (Table 6.1).

Foam experiments	NaDBS(cmc)	Glycerol (w/w)%	Viscosity (μ) mPa.s	Surface tension (σ) mNm^{-1}
All	3	0	0.93	32.2
Bamboo/staircase near centre/off-centre obstacle	3	30	3.3	34.2
Bamboo/staircase near centre/off-centre obstacle	3	50	7.4	35.1

Table 6.1 Liquid parameters used in the experiments in this chapter.

6.3 Results and discussion

6.3.1 Flow of foam past a single obstacle in the centre

Three different diameters (d_o = 100 μm, 150 μm and 200 μm) of the obstacle located transversely in the middle of the channel were studied (Figure 6.2). The obstacles will be referred to as small, medium and large for the diameters of 100, 150 and 200 μm respectively.
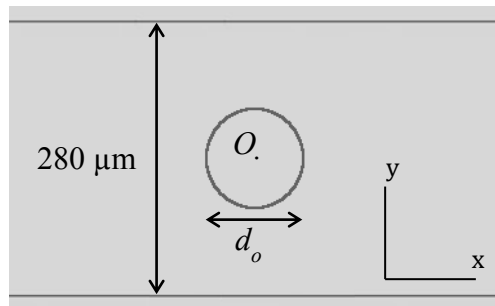
Figure 6.2 A schematic of the obstacle located in the middle of the channel. The diameters of the obstacle investigated in this chapter were 100, 150 and 200 μm. The origin is located in the centre of the obstacle (not to scale).

6.3.1.1 Phenomena observed

Similarly to Chapter 5, as different foam regimes passed around the obstacle located in the centre of the channel, they underwent different phenomena such as no effect, lamella division, and snap-off. They are now discussed in more details.

<u>No effect</u>

As the bubbles passed around the obstacle, the structure was unchanged exactly as in the no effect in Chapter 5. Bubbles simply flowed around the obstacle through the permeable gaps between the obstacle and the walls. Very similar to the constriction flow, bubbles of small sizes or under low shear rates were found in the "no-effect". Naturally, small bubbles can flow through the gaps more easily (Figure 6.3 (a)), whereas at low shear-rates and therefore, low velocities, the shear stress is insufficient to cause large deformations and hence, bubbles have enough time to flow around the obstacle (Figure 6.3 (c)). Exceptions were observed for

the staircase structure and a particular >3-row foam structure ($U_f = 0.870$ ms^{-1}), where bubbles at higher capillary numbers managed to flow without any topological deformation (Figure 6.3 (b & d)). Thus, the foam behaviour is strongly dependent on the initial foam arrangement. The bamboo foam was the only foam regime that was absent in the no effect due to the lamella of the bubbles that spanned the total width of the channel. Examples of foams undergoing no effect are shown in Figure 6.3.
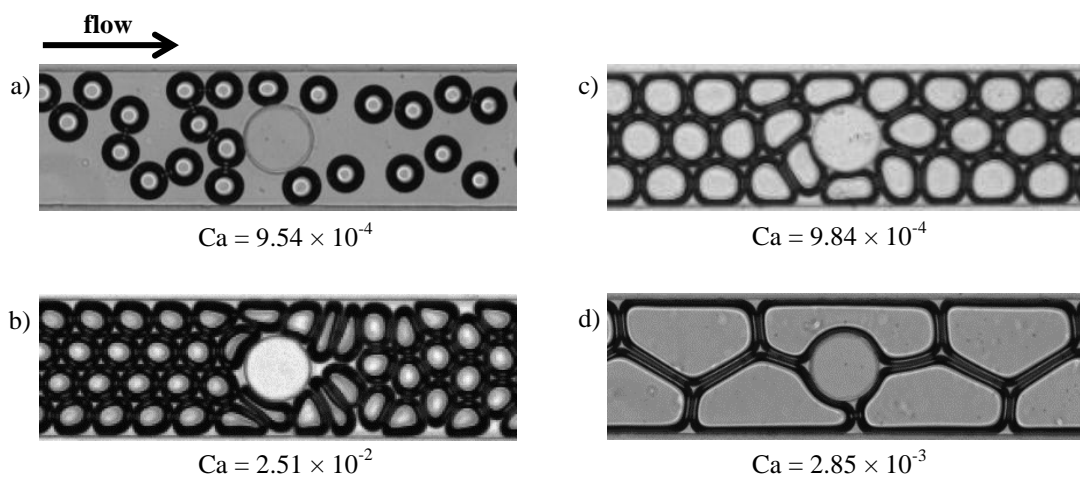
Figure 6.3 Examples of foams exhibiting no effect as they flow around the medium obstacle: a) >3-row foam at low velocity b) >3-row foam at high velocity, c) 3-row foam, d) 2-row foam.

Lamella division

As explained in the introduction chapter (2.6.1.1), lamella division occurs when the bubble is split into two smaller bubbles as a result of flowing directly into a branching point such as a rock or obstacle. This can occur in single slug bubbles (or droplets), once the bubble fills both of the gaps between the obstacle and the walls and two menisci propagate downstream of the obstacle until the lamella is split. However, in foam structures, a bubble is often confined between other adjacent bubbles and is forced to flow directly into the obstacle because of the upcoming bubble behind it. Thus, the lamella division here is somehow similar to the

neighbour-wall pinch-off since its lamella is split by the upcoming bubble. The two can be distinguished assuming that the neighbour-wall breaks near the permeable gaps (Figure 6.4 (a)) whereas lamella division occurs near the central *y*-axis (Figure 6.4 (b)). However, some bubbles were broken in between those two regions, which made it difficult to differentiate between the two phenomena (Figure 6.4 (c)). The main focus in this work is on the lamella division, and so most of the bubble division is assumed to be that. However, the actual neighbour-wall pinch-off (i.e. close to the obstacle/wall gaps) occurrence is briefly mentioned for the 3-row foam and >3-row foam.

$$Ca = 2.95 \times 10^{-2} \qquad Ca = 2.36 \times 10^{-2}$$
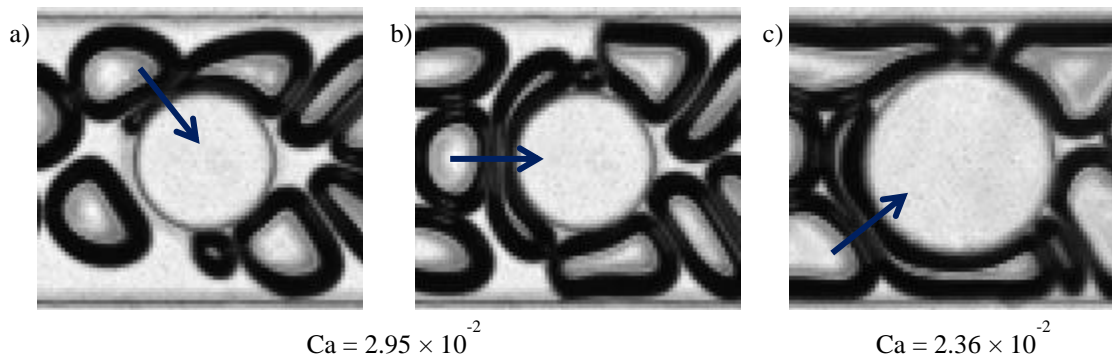
Figure 6.4 Examples of bubbles exhibiting a) neighbour-wall pinch-off, b) lamella division and c) ambiguous division. In (a) the division is relatively close to the wall/obstacle gap and clearly resembles the neighbour-wall pinch-off observed in Chapter 5. In (b) the lamella is about to be divided near the central line with both of the daughter bubbles propagating on the opposite sides of the obstacle, thus, it is clearly the lamella division mechanism. In (c) the division is more ambiguous, although it resembles the neighbour-wall pinch-off from (a), the daughter bubbles will flow on the opposite sides of the obstacles, thus possessing features of both of the mechanisms.

The major requirement for the lamella division was that the foam structure consisted of an odd number of bubbles per row, i.e. 1, 3 or 5. In the 3- and 5-row foam, many small bubbles managed to flow without being divided mainly at low flow-rates (often associated with wetter conditions) where surface tension dominated. However, quite often central bubbles still ended up flowing directly into the obstacle due to initial structure confinement

and were then split into two smaller bubbles. As expected, the bamboo foam was always divided into two smaller bubbles since its lamella spans the total width of the channel and simply cannot flow around it. Examples of bubbles exhibiting lamella are be shown later for each particular foam regime.

Snap-off

Snap-off, which was explained and presented to occur in single bubbles through constrictions in Chapter 4, as well as foams in Chapter 5, was observed very rarely. Snap-off is favoured in narrower and longer channels as well as in wetter conditions. Additionally, large bubble sizes are often required as it was shown in both of the above-mentioned chapters. Thus, it was only observed for the 2-row foam around the largest obstacle, at a relatively high capillary number and very wet conditions (Ca = 7.63×10^{-2}, ϕ_{or} = 36%). Snap-off is, therefore, not discussed in this chapter.

6.3.1.2 Dynamics of different foam regimes

Foam dynamics around the obstacles for particular foam regimes will now be presented. For the structures such as >3-row, 3-row and 2-row, only details of the observation are presented, whereas the primary focus is on the bubble division of the bamboo foam.

6.3.1.2.1 >3-row foam

Most of the >3-row foam conditions are relatively wet, meaning the bubbles are not confined. Thus, most of the time, bubbles have enough space to flow around the obstacle rather than undergo a division. Hence, this small bubble regime was dominated by the no effect for the three different diameters of the obstacle. Even when the foam velocity was very high (0.870 ms^{-1}) and caused the bubbles to obtain a 4-row compact structure, two of the rows were always above $y = 0$ axis whereas the other two were below. Hence, because the structure is almost y-axisymmetric, the bubbles follow their corresponding streamlines around the

206

obstacle dictated by the central axis, as shown in (Figure 6.5 (a)). Furthermore, the gap between the wall and the medium obstacle was large enough (65 μm) for two bubbles to squeeze through together, therefore, avoiding the neighbour-wall pinch-off. Around the largest obstacle, some bubbles underwent the neighbour-wall pinch-off in almost identical condition (Figure 6.5 (b) & (c)). Since the gap between the wall and the obstacle is now reduced to 40 μm, bubbles do not have enough space to flow together. In addition, the narrower gap is causing a more significant velocity gradient across the interface of the bubble which imposes greater bubble elongation. In consequence, lower shear stress is required for the adjacent bubbles to pinch their tails. Lamella division was observed at almost the extremity of the system used with a very high foam velocity ($U_f = 1.231$ ms^{-1}) where the foam had a 5-row compact structure (Figure 6.6). It has to be noted that at lower flow-rates (Q_L, $Q_G \leq 600$ μLm^{-1}) the foam did not have a close together 5-row structure which made it easier for the bubbles to flow around the obstacle without undergoing any division. Hence, the 5-row compact structure is almost a requirement for the small bubbles to undergo division, thus, suggesting that an odd number of rows (1, 3, 5-foam) with one bubble flowing directly into the obstacle is a necessary condition.
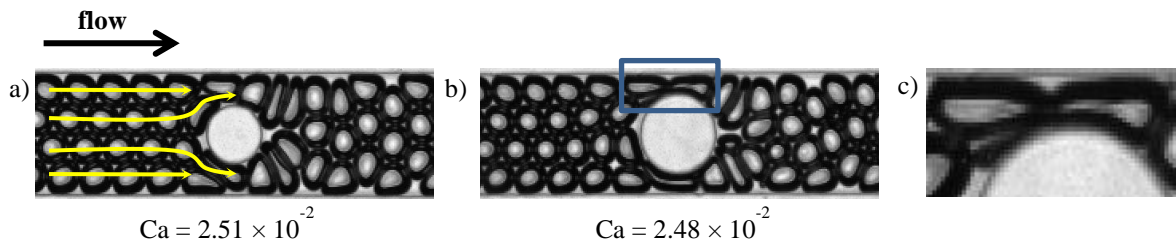
Figure 6.5 Examples of >3-row foams at high foam velocities that did not undergo lamella division a) >3-row foam around the medium obstacle, b) >3-row foam around the large obstacle, c) close up of (b) showing neighbour-wall pinch-off above the obstacle.

$$Ca = 3.56 \times 10^{-2}$$
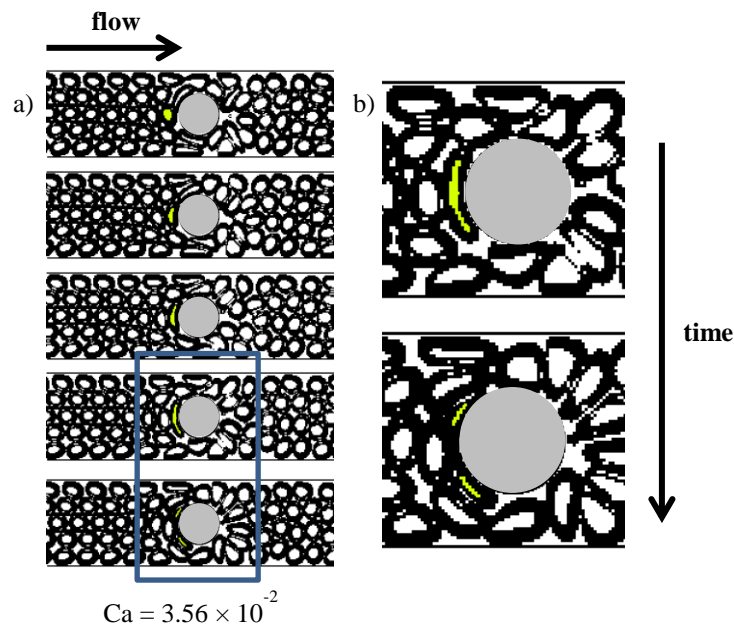
Figure 6.6 Consecutive sequence of images of a foam undergoing lamella division a) >3-row foam b) close up on the last two images of a) showing the final division.

6.3.1.2.2 3-row foam

The structure of the 3-row foam makes it a good system to observe lamella division since there is always a central bubble that flows directly into the obstacle. However, the central bubble may flow around the obstacle without any significant deformation at lower velocities, where the shear stress is not sufficient. Additionally, the division may be avoided in wetter conditions where bubbles have more space, and the surface tension can pull the extremities of the bubbles around the obstacles. Thus, there is a critical condition where bubbles start undergoing lamella division which was found to be independent of the obstacle size. The critical capillary number varies with the size, i.e. larger bubbles require smaller capillary number and vice versa, in a similar way to the 3-row and >3-row foam flows through constrictions in Chapter 5 (5.3.1.1.2.1). As earlier, smaller bubbles are associated with higher liquid fractions in microfluidic channels. In consequence, bubbles have more space to move around and therefore; they require more substantial shear stress to experience division (Figure 6.7). The critical conditions can be observed on the plot of Ca vs A^* in Figure 6.8.

Neighbour-wall pinch-off was also observed but only near the medium and large obstacle since the gap between the smallest obstacle and wall (90 μm) had a size close to the diameter of a 3-row bubble or larger. Thus, two elongated bubbles of almost the same size (or one smaller bubble that was generated via lamella division) could easily flow through it. The bubbles were observed to start pinching around Ca $= 9.13 \times 10^{-3}$ and Ca $= 6.62 \times 10^{-3}$ for the medium and large obstacle, respectively.

a) Ca $= 3.14 \times 10^{-3}$, $A^* = 0.085$
b) Ca $= 1.30 \times 10^{-2}$, $A^* = 0.035$
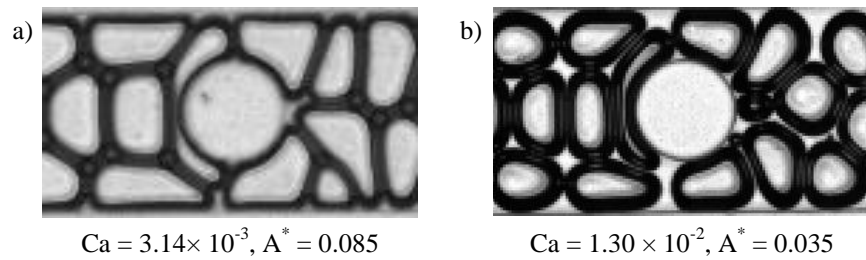
Figure 6.7 Examples of the 3-row foam that undergo lamella division at two different conditions: a) larger bubble size requiring lower capillary number, b) smaller bubble size requiring greater capillary number.
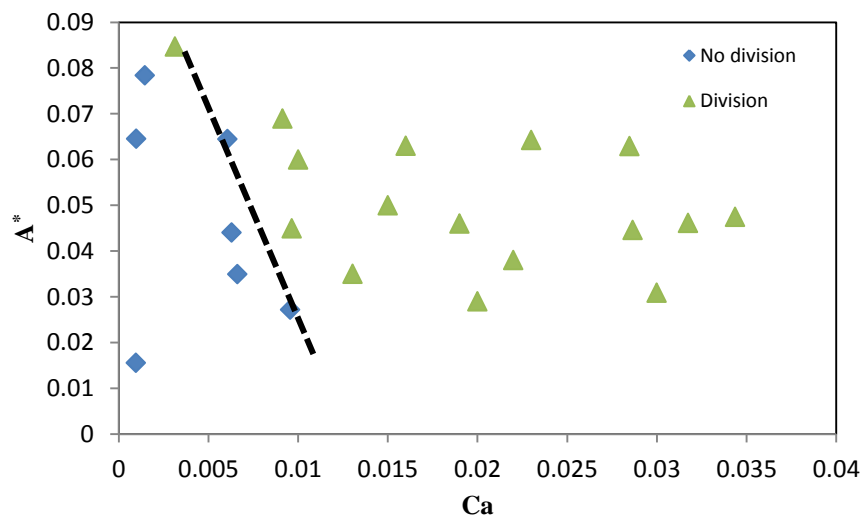
Figure 6.8 Plot of the capillary number against the dimensionless bubble area for the 3-row foam. The line indicating critical points for the bubble division is arbitrary.

6.3.1.2.3 2-row foam

In the case of the staircase foam, the dry foam did not undergo any split. The bubbles would always flow around it as in the plug flow without any change of the structure independently of the obstacle size. This study is relatively similar to the work carried out by Drenckhan *et al.* (2005) who used a Y-shape channel to split a two-dimensional staircase foam into two single lanes of bamboo foam and then showed that the process is reversible. The obstacle works in a similar way to the Y-shape channel where bubbles are temporarily split from each other and then reconnected. Such dynamics can be attributed to the minimisation of surface energy.

At the majority of the conditions, no lamella division was observed. In some instances when bubbles are relatively large and could flow as a bamboo foam ($A^* > 0.25$) but arrange themselves initially in the 2-row structure, a small division might occur. This was only observed around the large obstacle and whenever the foam was relatively wet ($\phi_{or} > 25$ %), with large areas of liquid in between the bubbles (Figure 6.9). In this example, the vertex of each of the bubble that is close to the centre of the channel axis is on the opposite side of $y = 0$ axis from the rest of the bubble (top of the green bubble in the first image of Figure 6.9). Moreover, because the liquid volume fraction is relatively high (i.e. there are large liquid areas between the bubbles) the vertex of the bubble fills the liquid void with the lower pressure and hence, follows the streamline on the opposite side of the $y = 0$ axis. In turn, the bubble interface exhibits a velocity gradient which wraps around the obstacle, causing a significant deformation. The surface tension forces than try to contract the interface by pulling it around the obstacle. However, the upcoming bubble is too close to the obstacle and splits the bubble into two smaller pieces. The example looks like the neighbour-wall pinch-off, but because the bubble is wrapped around the obstacle just before the division and the newly formed smallest bubble flows on the other side of the obstacle, it can be considered as the

lamella division. This example also highlights significant differences between bulk foams and single bubbles, as it is likely that the bubble could avoid the division if it was not flowing in the presence of other bubbles.

$$Ca = 8.78 \times 10^{-3}$$
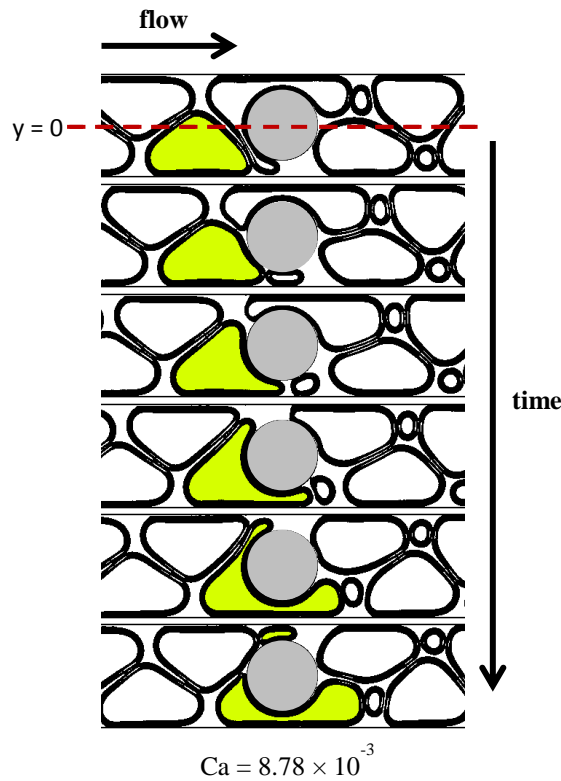
Figure 6.9 Consecutive sequence of images of a 2-row foam undergoing lamella division.

6.3.1.2.4 Bamboo

As mentioned earlier, the bamboo foam is always divided as it flows around any obstacle. Since the lamella of the bamboo spans the total width of the channel, it cannot naturally flow around the obstacle like other bubbles. Thus, bamboo always gets divided into two smaller bubbles, independent of the obstacle size or shape. The division, however, is not symmetrical. One of the bubbles generated is always smaller, and the rest of the bubble follows the trend of the very first one, generating a very ordered structure. Similar behaviour was observed in the staircase break-up through gradual constrictions (5.3.1.4.1) where the foam downstream of the constriction reached nearly a steady-state and the foam had an ordered structure. The

asymmetric daughter bubbles have been reported before in simulations of foams (Cox, 2015) and in droplet break-up (Link *et al.*, 2004). Hence, the behaviour seems to be universal and is driven by the velocity gradient of the interface as well as the surface tension.

It was also observed that the pressure fluctuations associated with the very low capillary number, could swap the bubble sizes, i.e. the top bubble will become the larger of the two (if it was, the smaller one before). However, this was observed (Figure 6.10) only at very small capillary numbers (from $Ca = 1.12 \times 10^{-4}$ to $Ca = 1.35 \times 10^{-4}$) when the obstacle caused the foam upstream to visually oscillate, rather than flow steadily i.e. the foam upstream of the obstacle was slowing down as the bubble was being divided and then accelerated as the two new bubbles passed the obstacle. Furthermore, even though there was a switch between the two newly formed bubbles and in between the switch the two bubbles had completely different sizes (green in Figure 6.10), they then ultimately went back to the two same sizes ($\bar{A}_1 = \bar{A}'_1, \bar{A}_2 = \bar{A}'_2$ in Figure 6.10, dispersity index < 5%). The same dynamics were observed on a few occasions and hence, it can be concluded that lamella division around a centred cylindrical obstacle is dependent on the parameters of the flow conditions. Thus, the size of the two newly formed bubbles can be predicted given capillary number, liquid hold-up and bubble size as it will now be presented.
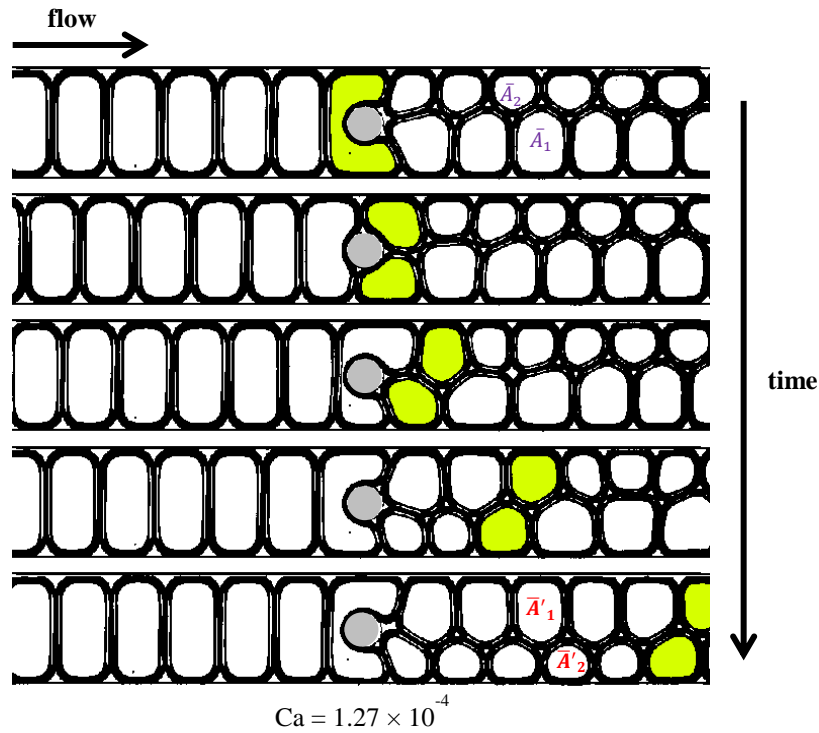
Figure 6.10 Consecutive sequence of images of a foam exhibiting a switch of the newly formed bubbles due to some pressure fluctuations caused by the obstacle. The green bubble is the one that begins the switch of the rows, and the two produced bubbles are of different sizes.

6.3.1.2.4.1 Size of the daughter bubbles

As the bamboo foam is divided into two smaller bubbles, the ratio of the areas of the two daughter bubbles given by $\Lambda_A = \frac{A_1}{A_2}$ (where $A_1 > A_2$) varies with the flow conditions.

At the lowest flow-rates, the ratio observed can be as large or even larger than 2 for three of the obstacles. Since the surface tension dominates, when bubble meets the obstacle, its front lamella wraps around it and loses its symmetry. One of the bubbles in front is entirely detached from the obstacle, and the closest film fills the gap through T1 event. The T1 event causes that interface to accelerate which result in the bubble having its front interface flowing at different velocities on the opposite sides of the obstacle. If the initial bubble is small, the division will occur before or just as the T1 event begins thus, not allowing one of the bubbles to accelerate much further and therefore, keep the daughter ratio small. Hence, there is clearly

size dependence i.e. the ratio decreases with the decrease in the initial bubble size. Increasing the velocity and therefore, the capillary number results in a faster division; hence, the ratio should also decrease. There seems to be a plateau around $\Lambda_A = 1.3$ as the capillary number increases. Since both of the parameters have opposite effects, dividing the capillary number by the initial size should describe the ratio of the daughter bubbles. However, the liquid volume fraction is approximately inversely proportional to the size (i.e. liquid volume fraction decreases with the bubble size) (Raven *et al.*, 2006) and since the viscosity of the solution was changed, the bubble size does not represent the same liquid fraction and thus, it must be taken into the account. Calculating the modified capillary number one (modCa$_1$) as follows $\frac{Ca\phi_{ch}}{A^*}$, the graph follows a good trend (Figure 6.11) which shows that the size of the daughter bubbles is an interplay between the initial bubble size, the volume liquid fraction and the capillary number. The volume liquid fraction of the channel (image-based) is used rather than the volume liquid fraction of the orifice (ϕ_{or} based on the flow-rates) because the liquid flow-rate necessary to produce bamboo was much smaller than the gas flow-rate, sometimes even lower than the smallest flow sensor value (< 1.07 μLm^{-1}) which could not always be measured.
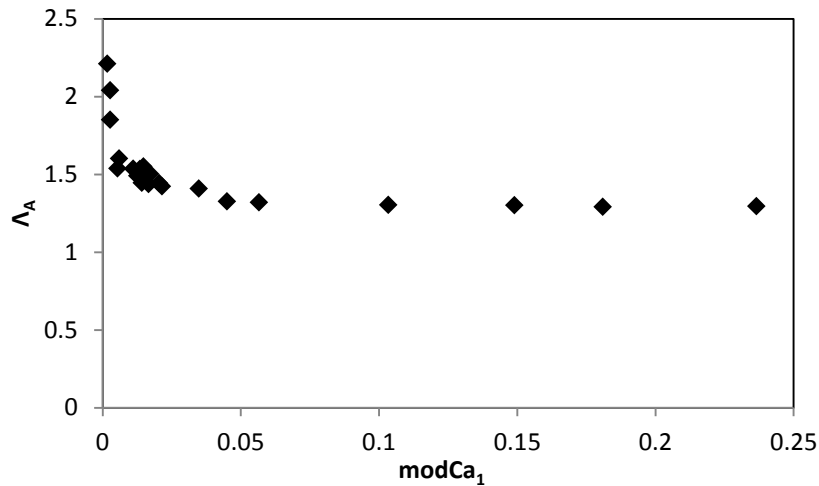
Figure 6.11 Plot of the first modified capillary number ($modCa_1$) against the ratio of the size of the daughter bubbles for the small obstacle.

For the medium and large obstacle, a similar behaviour was observed at the low flow-rates. However, as the flow-rates increased, the ratio did not reach a plateau but rather started increasing gradually. Moreover, the trend is better described by a different combination of the three flow variables compared to the smallest obstacle given by $modCa_2 = \frac{CaA^*}{\phi_{ch}}$. Since both of the obstacles are larger than the small one, the diameters are close (or greater) than the lengths of the bamboo bubbles studied (max bamboo length 155 μm). The bamboo is, therefore, divided when the daughter bubble fills approximately the gap between the obstacle and the wall. However, larger bubbles are more easily deformed and displaced since they experience lower drag viscous force per unit area (Cantat *et al.*, 2006) which causes the film of the bamboo behind the larger daughter to displace the larger daughter in front and hence, accelerate as it expands, resulting in the increased ratio. Thus, if the velocity is kept constant and the smaller daughter is roughly the same, the ratio will increase with the initial size of the bamboo foam. This explains the opposite effect of the bubble size to the flow around the small obstacle and the choice of using $modCa_2$. Furthermore, increasing the velocity causes a faster division which should result in more symmetrical daughters and therefore, a reduced

ratio. However, as the velocity is increased, the film on the opposite side accelerates further as it expands while the smaller daughters are more difficult to propagate further down the channel (Figure 6.12) which causes the ratio to increase. The smaller gap between the largest obstacle and wall caused greater velocity differences of the interface, which resulted in the highest ratio of the daughter bubbles (Figure 6.13).

$Ca = 1.25 \times 10^{-2}$
$modCa2 = 2.71 \times 10^{-3}$
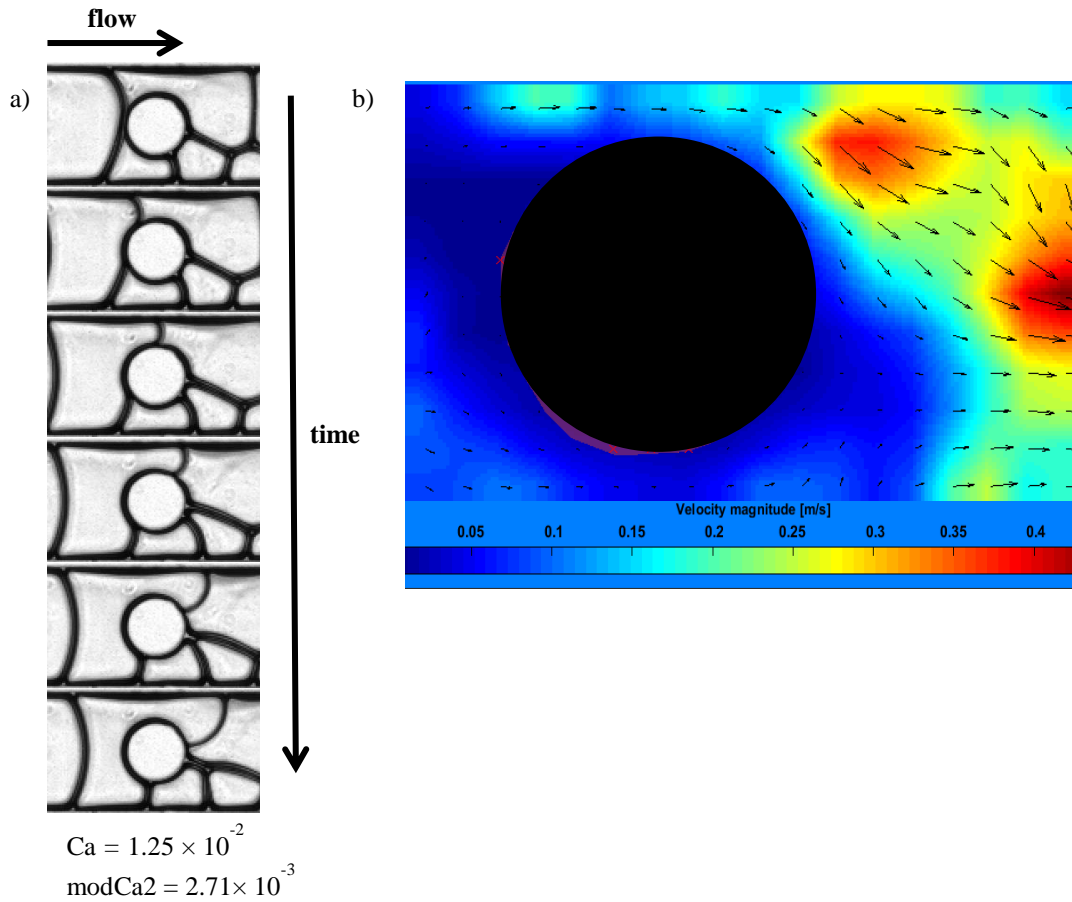
Figure 6.12 Illustration of a film flowing around the medium obstacle at different velocities: a) sequence of images showing the film above the obstacle to accelerate as it expands while the film below the obstacle has not propagated past the centre of the obstacle (also notice the length of the small daughter in the third image from top is roughly the diameter of the obstacle) b) velocity field of the bubble film in (a) showing higher velocities above the obstacle and right after the obstacle. The velocities above the obstacle are not very clear due to software deficiencies. The maximum velocity at the end of the image (far right) is caused by T1 event. The velocity profile was obtained as explained in 3.2.9.

Based on the above results, the polydispersity becomes higher with the increase in the obstacle and $modCa_2$, thus, the size distribution is dependent on the initial conditions and the obstacle size (or pore geometry). Since the sum of the area of the daughter bubbles is almost equal to the size of the initial bubble ($A_1 + A_2 = A_b$), knowing the ratio from above results can be used to approximate the bubble size distribution of bubble trains in different pore-like structures where the bubble fragmentation is dominated by lamella division. In addition, the obstacles can be used for a controlled break-up of the bamboo foam where a non-uniform structure is desired for analysis (e.g. Vitasari and Cox, 2017) or to study, for example, coarsening on a microscopic scale.
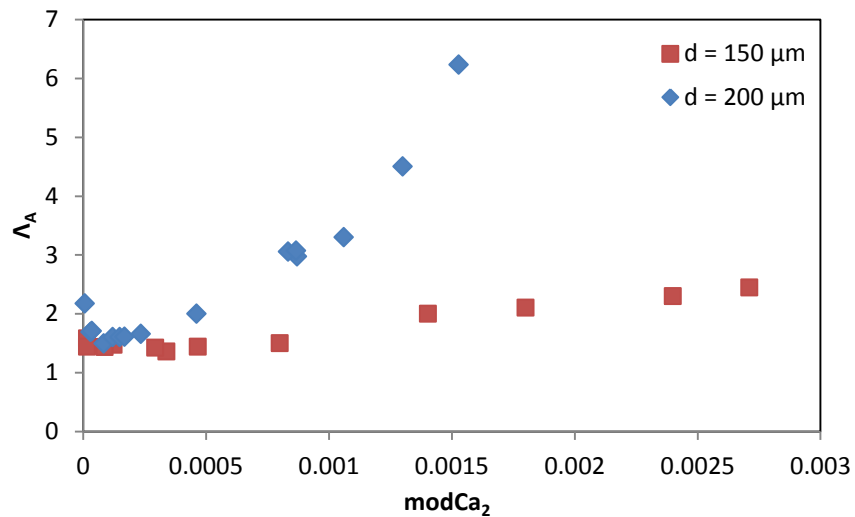
Figure 6.13 Plot of the second modified capillary number ($modCa_2$) against the ratio of the size of the daughter bubbles for the medium and large obstacle.

6.3.2 FLOW OF FOAM PAST A SINGLE OBSTACLE OFF-CENTRE

A study of foam around a single obstacle located off-centre has been carried out. The channel consisted of the smallest obstacle ($d_o = 100$ μm) that had its centre shifted vertically by 50 μm from the origin so that the gaps between the obstacle and the walls were 40 μm and 140 μm (Figure 6.14). The smallest obstacle was chosen since the medium and large obstacles were not possible to move significantly without creating a small gap between the obstacle and the

wall. The focus is on the two larger foam regimes (2-row, 1-row) due to possessing size features of foams used in porous media applications.

140 μm

100 μm

280 μm
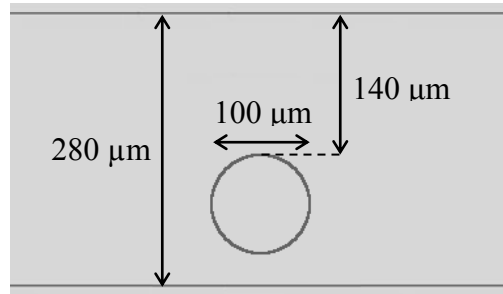
Figure 6.14 Schematic of the obstacle located off-centre (not to scale).

6.3.2.1 2-row foam

The 2-row foam underwent the most noticeable change of structure as it passed around the off-centre obstacle when compared to the centre-located. The smaller gap (40 μm) between the obstacle and the channel wall was much smaller than the typical projected diameter of the 2-row structure (>130 μm) which resulted in a very few instances of bubbles not exhibiting division. At low velocities and in wetter conditions where bubbles have spherical shapes and are separated by large areas of liquid, one of the bubbles was trapped in the gap (Figure 6.15). This shows that there is a minimum velocity for the bubbles to flow through the narrower gap. The stuck bubble works as an effective obstacle, blocking the narrow passage completely and diverging the rest of the foam through the more permeable gap. Application-wise, such as oil recovery or soil remediation, it is crucial that the foam is delivered or passes through all the possible pores, thus, this minimum pressure has to be surpassed so the foam can reach the narrowest pores. Increasing velocity and therefore, shear rates can naturally solve such a problem. However, larger bubbles have lower pressures and experience lower drag viscous force; thus, they are more easily deformed and displaced. Subsequently, larger bubbles were observed to pass through the narrow gap by the lamella division mechanism in similar flow conditions, including mean flow velocity and volume liquid fraction. A new small bubble

generated by division had a diameter slightly larger than the 40 μm gap between the obstacle and the wall, which could easily flow through it. Some other large bubbles were pulled around through the wider gap by the surface tension, thus having their motion reversed. This feature distinguishes bubbles (and droplets) from the continuous phase because although the average axial pressure drop is directed towards the downstream channel, the velocity of the interface is reversed. As such, some bubbles had their interfaces contracted and in turn, avoiding the division (Figure 6.15 (c)). However, at the same flow conditions, other bubbles were split by the upcoming bubbles before the surface tension forces could entirely contract the interface (Figure 6.15 (b)). The local liquid fraction in the wet conditions as the one presented in the mentioned figures varied around the obstacle because the bubbles were not well confined. Such variations caused bubbles to favour the streamlines with higher liquid fractions in front and in consequence, the front tip of the bubble could flow into the smaller gap far enough so that the upcoming bubble divided it against the obstacle (Figure 6.15 (b)).
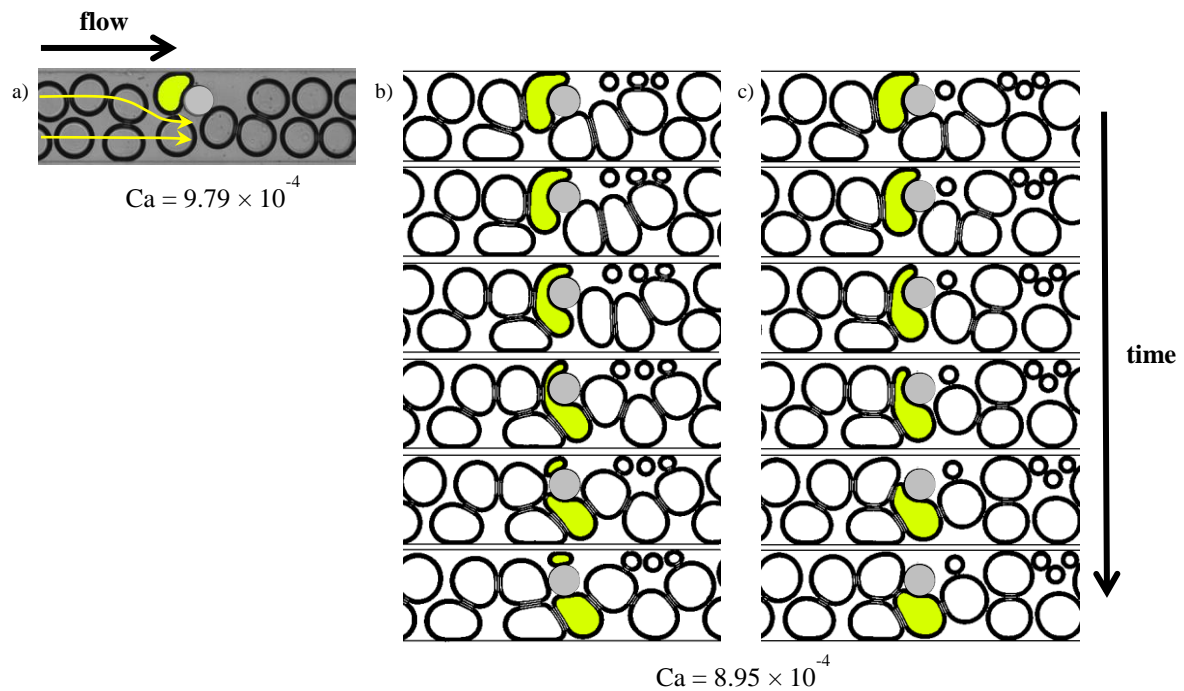
Figure 6.15 Flow of wet 2-row foam around the off-centre obstacle: a) example of a trapped bubble diverging the rest of the foam through the wider gap, b) example of a larger bubble being divided at the obstacle, c) example of a larger bubble being pulled around by surface tension and hence, avoiding the division.

For the usual 2-row, compact structure, one of the rows was flowing almost directly into the obstacle, making it difficult for the bubbles to avoid the division. Some bubbles did manage to flow without being fragmented into smaller bubbles, especially at lower capillary numbers. However, a small variation in the bubble size or pressure fluctuation could trigger the bubbles to experience lamella division. Thus, it was difficult to extract the critical flow conditions where bubbles supposedly start the division. Moreover, the deformed bubbles around the obstacle altered the upstream bubbles causing regular T1 events in the upstream section until the bubbles passed the obstacle. This resulted in the bubble row flowing through the wider gap to have its velocity increased as it was approaching the obstacle and therefore, ending up with different neighbours in the downstream section (Figure 6.16). Depending on how early in the upstream section the T1 events started, the number of them could be between

4 to 1 which resulted in one of the rows having their position shifted forward by the same number (from 4 to 1). The earlier the T1 event occurred, the higher the frequency of them (max 4). Clearly, the non-centre location of the obstacle is responsible for such dynamics, where bubbles at lower velocities struggle to flow through the gap, which can slow down or deform other bubbles. The bubble that flows in the top row and approaches the obstacle wraps around it, which forces the bubble to elongate vertically. Since the velocities are relatively slow, the interfaces of the bubbles in the bottom row are more deformable and so they are forced to elongate horizontally. This generates a more substantial liquid fraction which is filled by the next bubble, triggering the T1 event. Depending on the volume liquid fraction as well as the capillary number, bubbles in the upstream section might also deform which can cause more T1 events. The actual plug flow even near the obstacle was observed above $modCa_2 = 9.45 \times 10^{-5}$, where the T1 events started occurring only around the obstacle. This again shows the complex features of the foam as it flows through narrow passages; behaves as a viscoplastic fluid not just near the obstacle, but within some distance away from the obstacle (maximum distance observed around twelve obstacle diameters away i.e. ~1200 μm).

The location of the T1 events occurring upstream was observed to be furthest away from the obstacle for slowest and smallest bubbles. Thus, when the flow is most perturbed by the obstacle (low capillaries) and when the liquid fractions are relatively large and close to each other so that small fluctuations can impose merging (smallest bubbles). As the velocity was increased the surface tension became less of a factor, and thus, the bubbles were not getting deformed elastically (having less time to respond) but instead being regularly divided as they met the obstacle. Thus, the location of the earliest T1 event (scaled by the diameter of the obstacle) was found to decrease non-linearly as a function of $modCa_2$ (Figure 6.17).

flow

a)

$$\text{Ca} = 1.89 \times 10^{-3}$$
$$\text{modCa}_2 = 2.58 \times 10^{-5}$$

time

b)
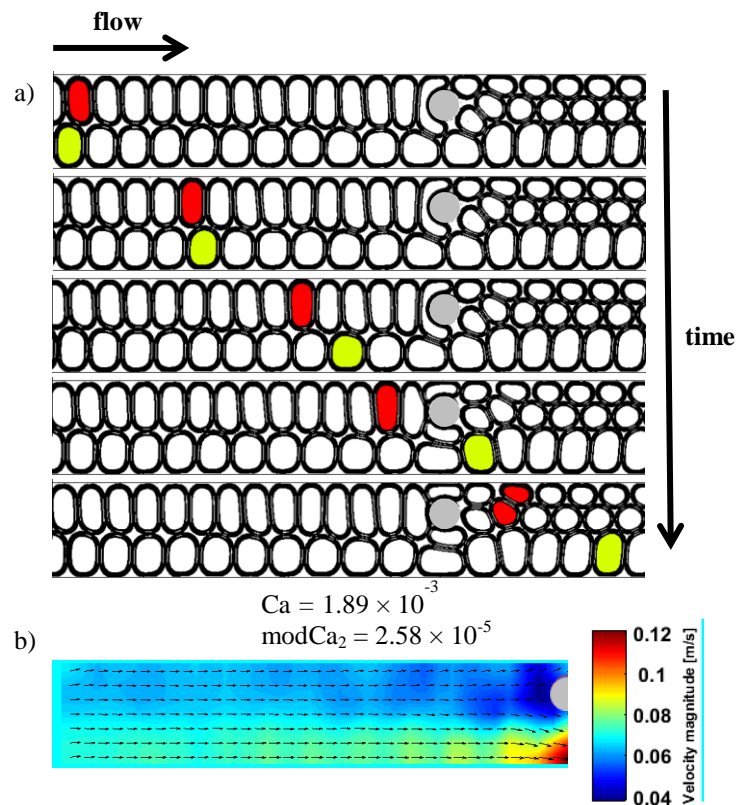
Figure 6.16 Flow of foam exhibiting T1 events upstream of the obstacle a) consecutive sequence of images showing the initial location of the two neighbours (top image red ahead of green) and their final location (bottom image, green bubble shifted forward by 4 positions), b) velocity field of a) of the upstream section just before the centre of the obstacle. The field shows two different magnitudes for the two rows of the bubbles caused by the deformation of the bubbles and T1 events; top row average $U_f = 0.062$ ms^{-1}, bottom row average $U_f = 0.084$ ms^{-1}.
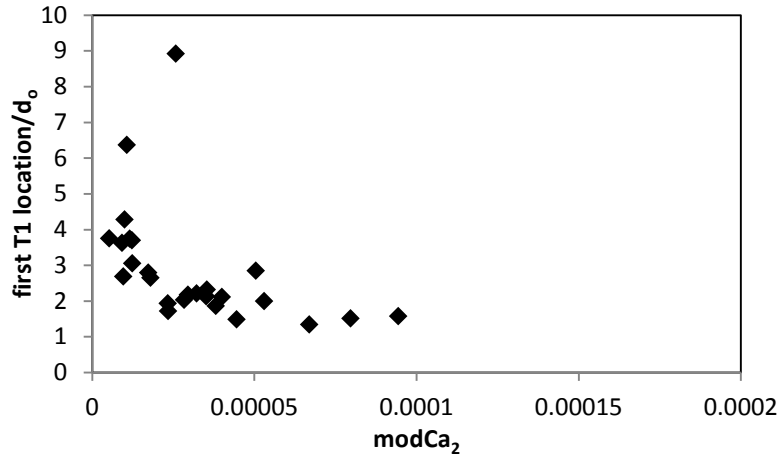
Figure 6.17 Plot of the location of the first T1 event upstream scaled by the diameter of the obstacle and plotted as a function of $modCa_2$.

6.3.2.1.1 Size of the daughter bubbles

The flow of the 2-row foam around the off-centre obstacle can be associated with the flow of bamboo foam around the centre obstacle. One of the rows almost always flows directly into the obstacle which is somewhat similar to the bamboo flow, but instead of being confined by the channel walls, the row of bubbles that gets divided is constrained between a wall and another row of bubbles. Naturally, films of the bubbles are soft and deformable when compared to walls, thus, producing slightly different results. As mentioned above, one of the results was a series of T1 events occurring upstream of the obstacle as well as around the obstacle which affected the structure of the foam near it. Thus, as a consequence, the bubbles were not always being divided uniformly. The liquid fractions near the obstacle were not always filled by the extremities of the same bubbles which produced a less uniform division and therefore, non-uniform sizes of the daughter bubbles. The ratio is calculated in a similar way as for the bamboo foam (as a function of $modCa_2$). However, the average of both of the daughter bubbles has a higher dispersity index (13% - 20%). Moreover, at the lowest $modCa_2$ values ($< 1.25 \times 10^{-5}$) and especially lower velocities where surface tension plays a role, some bubbles were divided just as their extremity was pulled by the surface tension and so one of

223

the produced daughters was relatively small, generating a ratio larger than 8 (Figure 6.18). The ratio then decreased very suddenly reaching the smallest value of 1.3. This was the lowest ratio observed for the bamboo foam around each of the centre-located obstacle. The ratio then almost reaches a constant value around 2.5 which slightly increases with the increase in $modCa_2$. This again shows a similarity to the bamboo flow, especially around the medium obstacle where the ratio reached a minimum value at low values of $modCa_2$ and then gradually started increasing. The average width of the bubble just before the division is 200 µm (because it elongates vertically) which is two times greater than the diameter of the obstacle. Thus the ratio of the bubble width to the obstacle diameter is approximately 2. The bamboo foam passing through the medium obstacle spans the total width of the channel and since the obstacle diameter is 150 µm, it produces a ratio of 1.87. Hence, the two ratios are relatively close which explains the similar trend of the daughter ratio. However, the actual values vary from each other due to more deformable interfaces of the bubbles in the case of the 2-row structure.
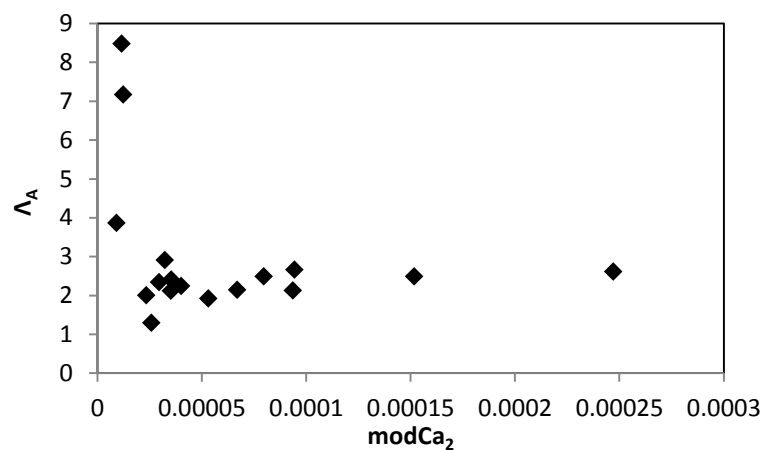
Figure 6.18 Plot of the ratio of the daughter bubbles as a function of $modCa_2$ for the 2-row foam around the off-centre obstacle.

6.3.2.2 Bamboo

As the bamboo flow past the off-centre obstacle, it was getting divided into two smaller daughter bubbles every single time it met the obstacle. The apparent reason (as in the case of the bamboo around any centre-located obstacle) is its film that spans the total width of the channel. Since the gaps between the obstacle and walls were not equal as in the case of the centre-located obstacle, the produced bubbles should be different from each other, with sizes similar to the distances between the walls and the obstacle.

6.3.2.2.1 Size of the daughter bubbles

The first difference observed between the centre, and an off-centre obstacle is a fact that the smaller daughter produced is always ahead of the larger daughter. In the former, the larger daughter had its film reaching the back of the obstacle first, which triggered a T1 event and structured the two bubbles in such a way that the larger daughter was always ahead. In the latter, the interface of the soon to be small daughter is much closer the back of the obstacle (because of the location of the obstacle close to the wall near the small obstacle) which triggers a T1 event that pulls the smaller daughter forward. It was shown before that pressure fluctuation caused by the centre obstacle could flip the relative sizes of the daughter bubbles. Thus, the smaller bubble did not always have to be produced in the same row (above or below $y = 0$). These results are entirely different from the off-centre obstacle, where the smaller daughter was always produced in the same row. Consequently, the off-centre produced a different outcome. The ratio was found to be dependent only on the initial bubble size and not the mean velocity of the flow. Smallest bamboo bubbles were divided before passing the obstacle, which resulted in daughter bubbles with sizes close to the area enclosed by the obstacle and the wall (Figure 6.19 (a)) and therefore, largest ratio. Increasing the size resulted in a smaller ratio. As mentioned earlier, the front film of the smaller daughter (before the

actual division) reaches a liquid area behind the obstacle that initiates T1 event (Figure 6.19 (b) top image). The film then grows (yellow line in Figure 6.19 (b)) which pulls the smaller soon to be daughter forward, thus, growing in size. This continues until the larger part of the mother bubble reaches the liquid area (behind the obstacle) so that another T1 is triggered (transition between image 4 and 5 in Figure 6.19 (b)). The new film is an edge shared between both of the daughters (blue line in Figure 6.19 (b)), which grows and therefore, pulls both of the bubbles forwards. Longer bubble means division occurs later, which gives more time for the smaller bubble to expand, reaching ratios as small as 1.38 (Figure 6.20). It has been shown by Durand and Stone (2006) that the relaxation time of the T1 event (time for the new edge to grow from zero to full length) depends on the interfacial viscoelasticity of the films but not on the shear viscosity of the bulk liquid. Thus, it can be understood that change in viscosity or velocity (i.e. the capillary number) is not one of the driving forces responsible for the bubble fragmentation of the bamboo foam around the off-centre obstacle. The size of the daughter bubbles is therefore, dependent on the location of the obstacle as well as the initial bubble size, which gives better control of the daughter bubbles.

flow →

a)

$Ca = 3.44 \times 10^{-4}, A^* = 0.18$

b)

time

$Ca = 5.26 \times 10^{-4}, A^* = 0.55$
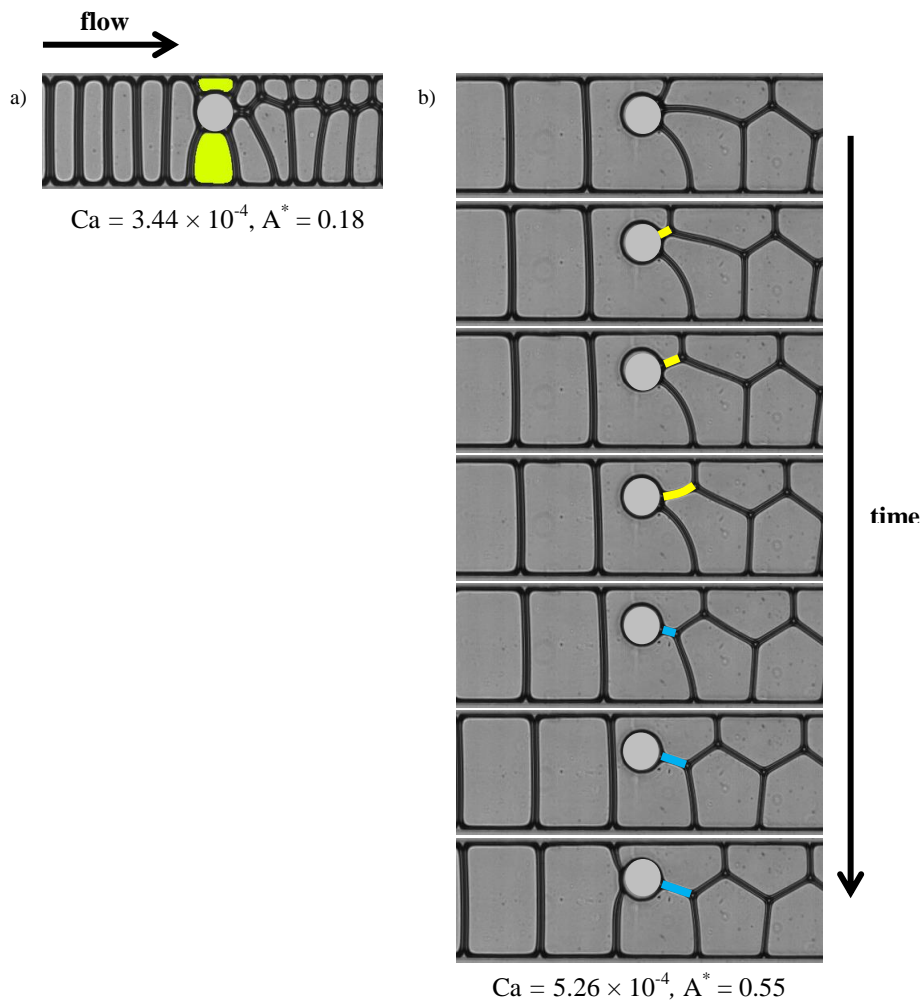
Figure 6.19 Flow of bamboo foam around the off-centre obstacle; a) smallest bamboo studied, the daughter bubbles have roughly sizes of the areas between the obstacle and the wall, b) consecutive sequence of images of a larger bamboo, the smaller part of the mother bubble undergoes a T1 event as indicated by the growth of the yellow film until the larger part reaches the rear of the obstacle and they both undergo a T1 event, sharing the same edge (blue line) and moving forward until the lamella is divided.
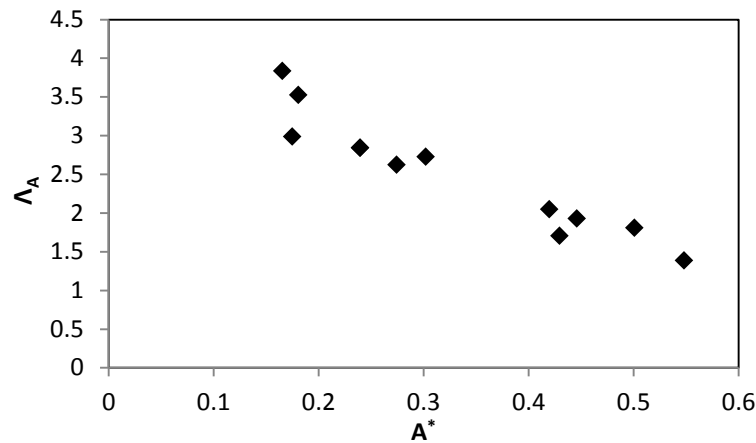
Figure 6.20 Plot of the initial bamboo size against the ratio of the size of the daughter bubbles around the off-centre obstacle.

6.3.3 FLOW OF FOAM PAST A FOUR-OBSTACLE

A study of bamboo foam flowing through a four-disk like structure was carried out. The arrangement of the four obstacles can be seen in Figure 6.21. Four of the obstacles are 100 μm in diameter, arranged in two pairs. Each obstacle is located 20 μm away from the wall, and each pair has two obstacles 40 μm away from each other. The second pair is located 100 μm after the first one.

As the bamboo foam passed through the four-disk like obstacles, it either underwent no effect at low velocities or division once the critical velocity was reached. The presence of the obstacles leads to foam generation through bubble break-up, providing both a robust validation of the simulation method and information about foam formation in porous media. The objective of this work is to determine how the bubbles break-up, and how the frequency of break-up events depends upon the liquid fraction, the foam velocity and the bubble size. The focus is on the number of new bubbles generated as the foam flows between the obstacles in order to allow straightforward comparison with the simulations. This has the advantage of being a scalar quantity that can be easily measurable on images. First, observations from the

experiments are explained, then the numerical model is presented and finally, the results are compared.
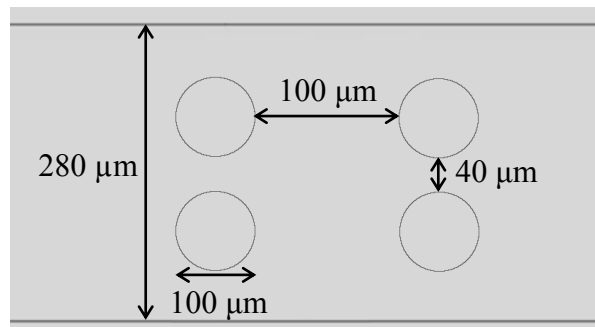
Figure 6.21 Schematic of the four obstacles (not to scale).

6.3.3.1 Experimental results

Examples of foam behaviours at different velocities are shown in Figure 6.22.

At very low velocities, on some occasions, a few small bubbles were generated as they flowed around the first pair of obstacles which then did not pass the second pair and, therefore, remained trapped between the obstacles (Figure 6.22 top). The trapped bubbles become the effective obstacles that reduce the permeability of the system and diverge the upcoming bubbles through the central, more permeable area. The outcome of such a flow was no break-up at all, and the bamboo foam was re-oriented into a staircase structure.

At intermediate velocity (Figure 6.22 middle), when each bubble meets the first pair of obstacles, two new bubbles may be generated. The second pair of obstacles can cause further break-up event so that each bubble is split into four bubbles. This occurs through the creation of asymmetry and hence, a slanted film between the four obstacles that impinges on one of the second pair of obstacles part-way along its length. The foam that is generated is polydisperse and disordered.

At the highest flow velocity, two bubbles are generated as the bubble meets the first pair of obstacles (Figure 6.22 bottom), one next to each wall. These then propagate downstream around the second pair of obstacles with no further break-up events. Hence, each bubble is

split into three parts, and the foam remains ordered. It should be noted that the largest (hence, driest and most compact) bubbles even at small velocities generated similar ordered structures downstream of the obstacles. This occurred because the bubbles did not have space to retract its interface before meeting the obstacles. Hence, it is expected that velocity and bubble size are the major factors responsible for the bubble generation through the obstacles.
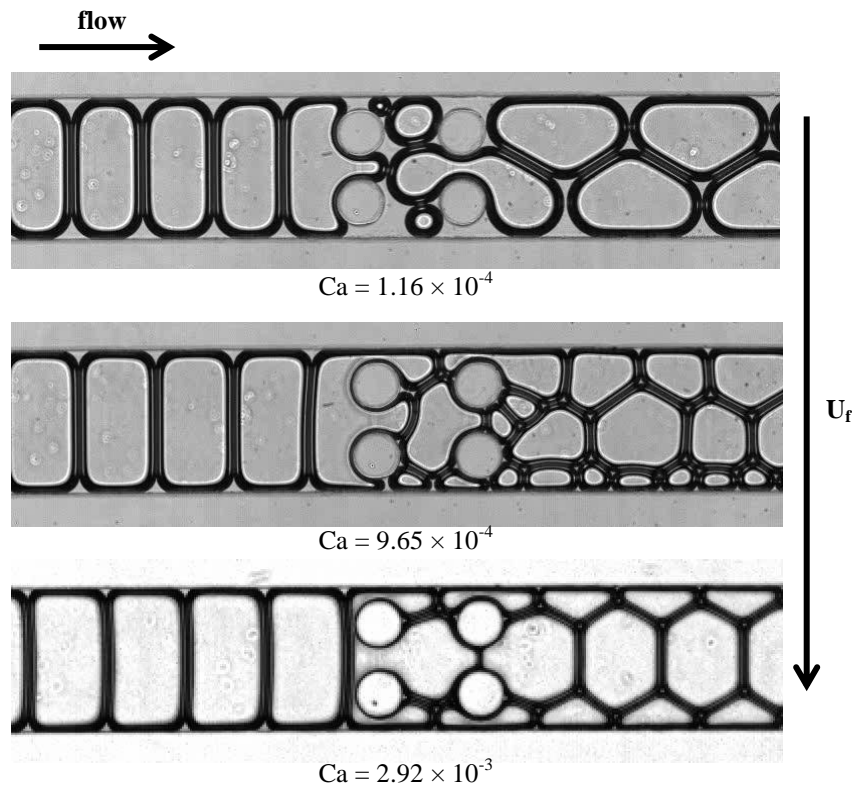
Figure 6.22 Images of the bamboo foam in experiments at increasing velocity (top to bottom).

Total number of bubbles downstream of the obstacles was extracted with time. This represents the number of new bubbles generated as the foam passes through the obstacles. The number of bubbles increases in time for different velocities and bubble sizes (Figure 6.23). The data is separated into three different initial bubble sizes: small ($0.3 < A^* < 0.5$), medium ($0.5 < A^* < 0.76$) and large ($0.9 < A^* < 1.4$). Naturally, faster velocity means more bubbles passing through the obstacles and hence, more bubbles generated. Therefore, the gradient becomes steeper with the velocity in each of the graphs.
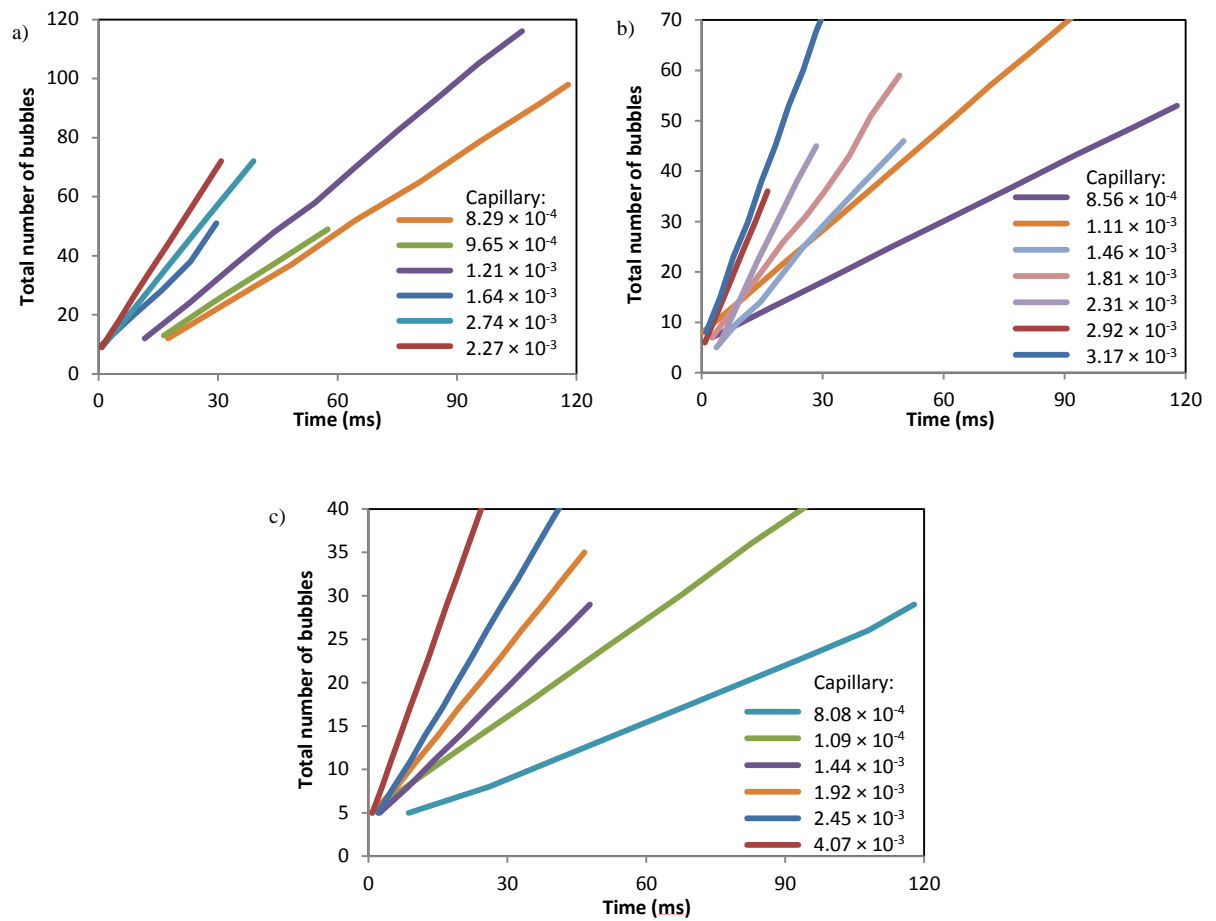
Figure 6.23 The number of bubbles generated by break-up events in the experiments for different capillary numbers. Graphs are sorted into three ranges of bubble size a) small, b) medium and c) large.

6.3.3.2 Simulations

Simulations have been run by collaborators from the Aberystwyth University of the bamboo foam through the four-obstacles. The results of the simulations were extracted in a similar way to the experimental results (number of bubbles generated in time) and compared. The model used including mathematical formulations, and numerical information will now be presented.

6.3.3.2.1 Mathematical model

The height (60 μm) of the experimental channel is relatively small compared to the width of the channel (280 μm), hence, in the case of a small aspect ratio, a two-dimensional model is

appropriate, and so the movement of bubbles is primarily opposed by friction with the top and bottom plates forming the channel. A key ingredient is, therefore, a friction force (with friction coefficient λ) that acts on each bubble interface, as in a viscous froth model (Kern *et al.*, 2004). To be able to accurately predict the break-up of one bubble into smaller ones further requires an accurate representation of the shape of each bubble, and hence (via the Laplace-Young Law) its pressure, which is chosen so as to keep its area A_b constant. Finally, to allow the modelling of foams of arbitrary liquid fraction, thin films separating two bubbles need to be distinguished from the larger liquid regions between three or more bubbles; this is done by introducing a disjoining force similar to the one presented by Kähärä, Tallinen and Timonen (2014) that depends on the distance between two bubble interfaces.
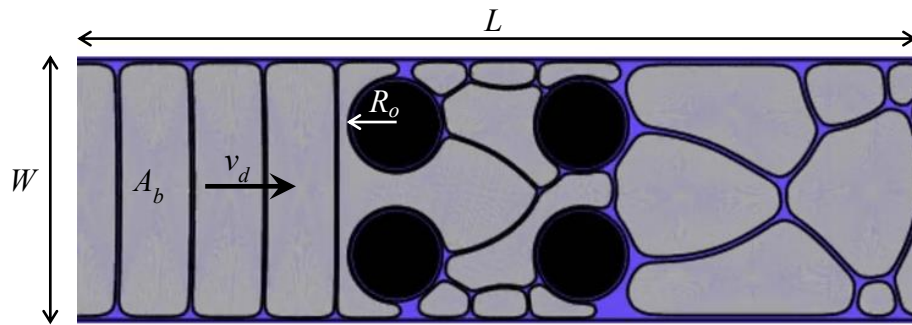
Figure 6.24 A simulated foam with liquid fraction 12 % and initial bubble area $A_b = 0.84$ that is being driven with velocity $v_d = 2.5$. Note that the liquid is not distributed uniformly around the bubbles, that some small bubbles are trapped against the walls, between the obstacles, and that there is a small amount of asymmetry that develops which leads to the formation of a different foam structure downstream. After some time, this becomes the staircase structure observed in the experiments.

The model is based on two-dimensional foam consisting of *N* bubbles contained within a rectangular channel of length *L* and width *W*, as shown in Figure 6.24. Each bubble consists of a single connected interface with interfacial tension (σ), forming a closed-loop of area A_b. For the numerical implementation of the model, this interface is discretised into short, straight, segments, with segment lengths in the range [l_{min}, l_{max}]. These segments meet in

232

points with time-dependent positions $\underline{x}(t)$, and it is at these points, that a force balance is performed to determine the dynamics of the foam. The curvature force $\underline{F}_\kappa$ is determined by the local interfacial tension and the angle θ between the neighbouring edges

$$\underline{F}_\kappa = \sigma \frac{\theta}{l} \underline{n},\tag{6.1}$$

where l is the average of the lengths and edges adjacent to the point (Figure 6.25).
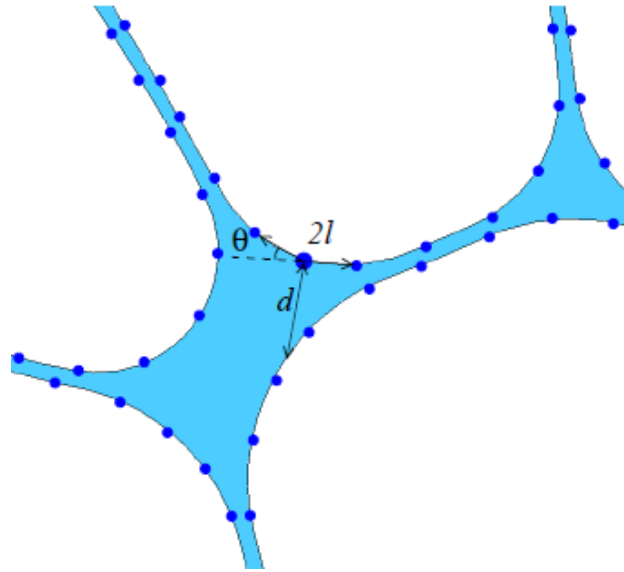
Figure 6.25 Sketch of the region where five bubbles meet in thin films and one three-sided and one four-sided Plateau border. The figure illustrates the discretisation of the foam into points and straight edges (for simplicity only a selection of points as large dots are highlighted, and so the edges appear curved). The curvature of the interface at each point, for example, the one marked with a larger dot, is measured by the angle θ between adjacent edges, and normalised by the total length $2l$ of the edges adjacent to the point. The disjoining force between interfaces is determined by d, the distance, in the direction of the outward normal to the point, of the nearest interface.

The pressure force $\underline{F}_p$ arises from the pressures in the bubbles. The force per unit length of the interface is the difference in pressure between the bubble and the fluid outside the bubble. The latter is taken to be zero, without loss of generality. Then,

$$\underline{F}_p = -p_b \underline{n},\tag{6.2}$$

where p_b is calculated from the equation of motion, as described below.

The friction force $\underline{F}_\lambda$ acting on the point depends on the velocity of the point in the direction normal to the interface (Cantat *et al.*, 2004; Kern *et al.*, 2004):

$$\underline{F}_\lambda = -\lambda \underline{v}_n. \tag{6.3}$$

Finally, the disjoining force $\underline{F}_d$ depends upon the distance d between two nearby interfaces. Whenever interfaces from two different bubbles come with some small distance d_{crit} of each other, they are repelled with a force that varies exponentially with distance (Bergeron, 1997). Thus, for each point, the nearest edge in the outward direction must be found, and the distance d from the point of intersection to the given point (see Figure 6.25) is recorded. Then

$$\underline{F}_d = \begin{cases} -\eta e^{-d/d_{crit}}\underline{n}, & d < d_{crit} \\ 0, & d \geq d_{crit}, \end{cases} \tag{6.4}$$

where η plays the role of a disjoining pressure. Any hydrodynamic forces are neglected, presuming they are small in comparison to the viscous friction with the bounding glass plates. Overdamped dynamics are assumed, and a balance of these four forces is considered at each point of the interface, resolved in the direction of the outward unit normal n to that interface, to give the point velocity in terms of the forces per unit length acting on it. A force balance then gives the equation of motion for each point:

$$\lambda \underline{v}_n = \left(\sigma \frac{\theta}{l} - p_b + \eta e^{-d/d_{crit}}\right)\underline{n} \tag{6.5}$$

(assuming that the interface is sufficiently close to another that the disjoining force is acting). Bubbles are assumed to be incompressible with a fixed area (i.e. there is no diffusion-driven coarsening of the foam over the duration of an experiment). The pressure of each of the bubble is determined by integrating equation 6.5 around the bubble's perimeter (Kern *et al.*, 2004) as a point-wise sum. The friction term on the left-hand side gives the change in the area of the bubble, ΔA_b. Thus

$$p_b = \frac{1}{\Sigma l}\left[\Sigma\left(\sigma\theta + \eta l e^{-d/d_{crit}}\right) - \lambda\Delta A_b\right], \qquad (6.6)$$

where the sums are over all of the bubbles' edges, using the previously calculated values of θ and d. Retaining the ΔA_b term allows for correcting any variation in bubble areas and keeping them at their target values.

6.3.3.2.2 Numerical details

The numerical solution of equations 6.5 and 6.6 is performed in dimensionless units relative to a length scale determined by the bubble size, $\mathcal{L} = \sqrt{A_b}$. Then pressures are normalised by $\sigma/\mathcal{L}$, the disjoining pressure is $\hat{\eta} = \eta\mathcal{L}/\sigma$, and the time-scale is set by the balance between frictional drag and surface tension forces, $T_\lambda = \lambda\mathcal{L}^2/\sigma$. Simulations are performed in the Surface Evolver (Brakke, 1992), which has inbuilt energy methods to calculate point-wise curvature for equation 6.1, allows easy control of the surface discretisation, and provides a graphical interface to view the motion of the foam (it should be noted that the usual use of Surface Evolver, i.e. minimisation of the energy is not performed here). $\mathcal{L}$ is chosen to be of order 1 and $\sigma = \kappa = 1$. The remaining material parameters are associated with the disjoining force, $\hat{\eta}$ and d_{crit}. These affect the shape of the bubbles around the transition region between thin films and plateau borders but have little effect on the overall dynamics. Then, $\hat{\eta} = 30$ and $d_{crit} = 0.02$ (one-fiftieth of $\mathcal{L}$) are chosen. The motion of each point is found by writing the velocity in equation 6.5 as the rate of change of position, and then each interface is evolved using Euler's method with a timestep $dt = 5 \times 10^{-5}$. The liquid fraction of the foam is determined by the fraction of the domain filled by bubbles when the simulation starts:

$$\phi_L = 1 - \frac{\Sigma_b A}{(LW - 4A_{obstacle})}. \qquad (6.7)$$

It can be set by adjusting the initial bubble area, and remains fixed throughout each simulation, even when bubbles break-up into two or more components.

The break-up process itself is initiated whenever two points on the same bubble (but not on the same edge) approach to within $2d_{crit}$ of each other. Then, a process of reconnection of the four edges adjacent to these two vertices is performed so that the bubble is split into two parts. The bubble area is partitioned in proportion to the actual area of the two new components of the bubble. The objective of the simulations is to determine how the bubbles break-up, and how the frequency of break-up events depends upon the liquid fraction ϕ_L , the driving velocity v_d and the bubble size A_b. Hence, for all the simulations, the channel width is fixed to $W = 1.8$ and radii of the four obstacles are fixed at $R_o = 0.32$. In the experiments, a continuous stream of bamboo foam is produced which is too computationally expensive, and so a periodic boundary condition is used in the direction of the channel so that bubbles can re-appear at the inflow after leaving the channel to the right. Therefore, in the simulations, every bubble passes the discs in the centre of the channel exactly once. As in the experiments, each simulation is started with bamboo foam consisting of ten bubbles. For bubbles of area $A_b = 0.83$, a channel length of $L = 6$ is chosen and reduced or extended for bubbles of different size.

6.3.3.2.3 Simulation results

Much the same range of responses as in the experiments was observed in the simulations. There is a critical driving velocity, close to $v_d \approx 1$, below which the foam does not flow at all. That is, small driving velocities are not sufficient to overcome the foam's yield stress and induce sustained motion. Liquid collects downstream of the second pair of discs, and the bubbles are squeezed together upstream. At higher velocities, bubbles often break into three parts when they meet the first pair of obstacles, and any asymmetry is magnified when a slanting film touches one of the second pair of obstacles (this is about to happen in Figure 6.24). This induces a rearrangement of the downstream structure of the foam into a staircase

structure. Bubble division is more likely as the velocity increases or as the liquid fraction decreases since in fast-moving or dry foam the bubble has less time or space (respectively) to rearrange before its edges are forced to self-intersect.

The number of new bubbles generated is again recorded as a function of time. An example is shown in Figure 6.26 (a) at a fixed driving velocity and fixed liquid fraction. For the larger bubbles, there are more new bubbles generated, as it is more difficult for the bubbles to flow around the obstacles. If the liquid fraction is varied, as in Figure 6.26 (b), then more bubbles are generated at a low liquid fraction, while if the liquid fraction is high enough the foam flows past the obstacles without breaking up. Increasing the driving velocity (Figure 6.26 (c)) leads to more foam being generated, as the bubbles have less time to adjust their shape to flow around the obstacles.
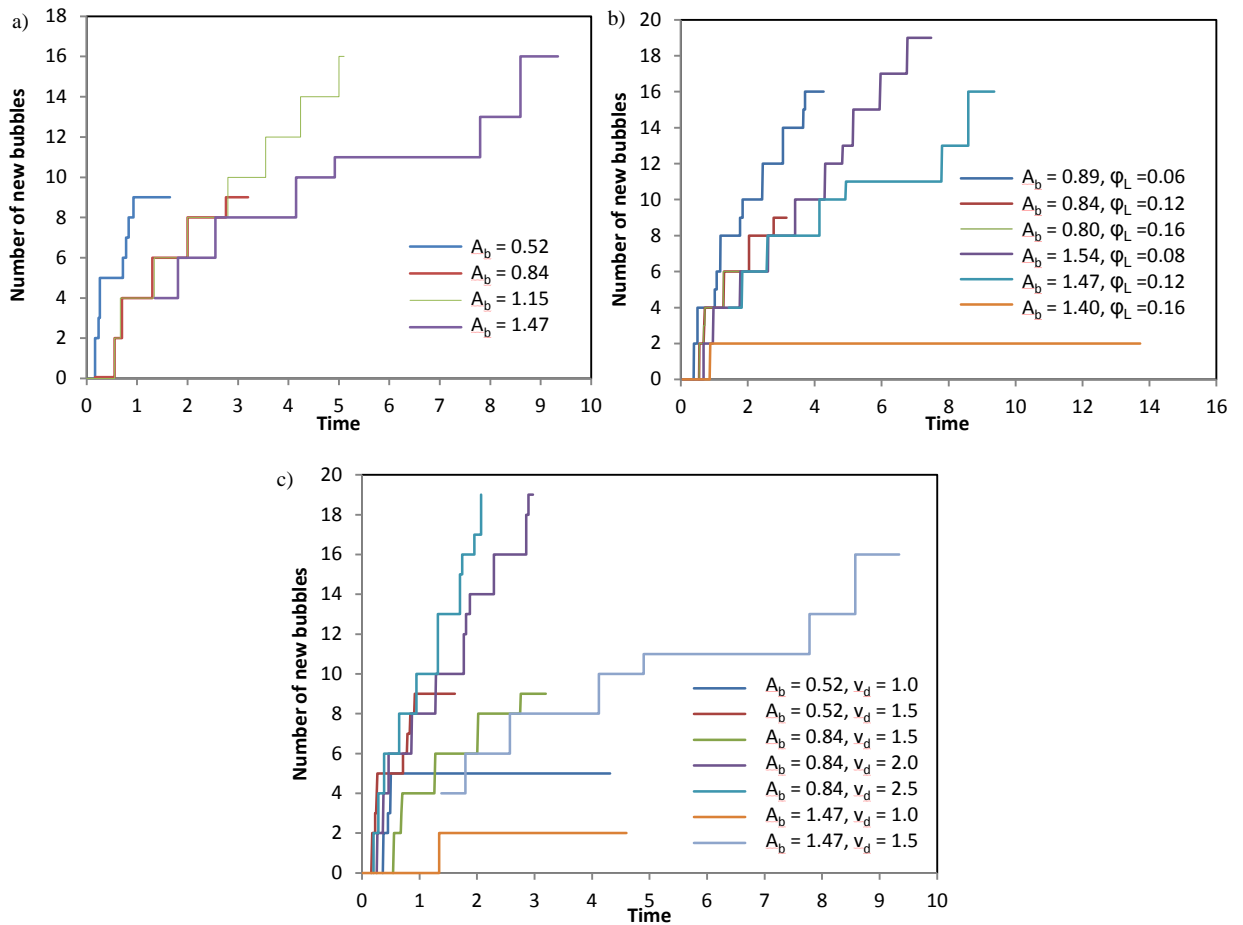
Figure 6.26 The number of bubbles generated by break-up events in simulations, a) liquid fraction 12% and driving velocity 1.5 for different initial bubble areas, b) liquid fraction between 6% and 16% for two narrow ranges of bubble size and driving velocity 1.5, c) liquid fraction 12% and various driving velocities and bubble sizes.

6.3.3.3 Comparison

The rate at which the foam is generated has been shown in Figure 6.23 and Figure 6.26. The objective is to reconcile the data. Clearly, the number of new bubbles generated when the bamboo foam passes between the obstacles is higher when the foam moves more quickly. Therefore, the time axis is scaled by the driving velocity (foam velocity for experiments). Furthermore, the length of a bubble in the flow direction is roughly A_b/W, and so the time scale

$$\tau_o = \frac{A_b}{W v_d} \qquad (6.8)$$

should be an appropriate measure of the rate of bubble break-up events.

Figure 6.27 shows the re-scaled data by the time scale τ_o. The data falls between the lines $2t/\tau_o$ and $4t/\tau_o$, which corresponds to two and four new bubbles being generated each time a bamboo bubble passes the four obstacles. Deviations occur only when no break-up events occur, for example, at a high liquid fraction or very low driving velocity, in which case the number of new bubbles generated becomes constant. The simulations agree well with the experiments, although they cover much shorter times.
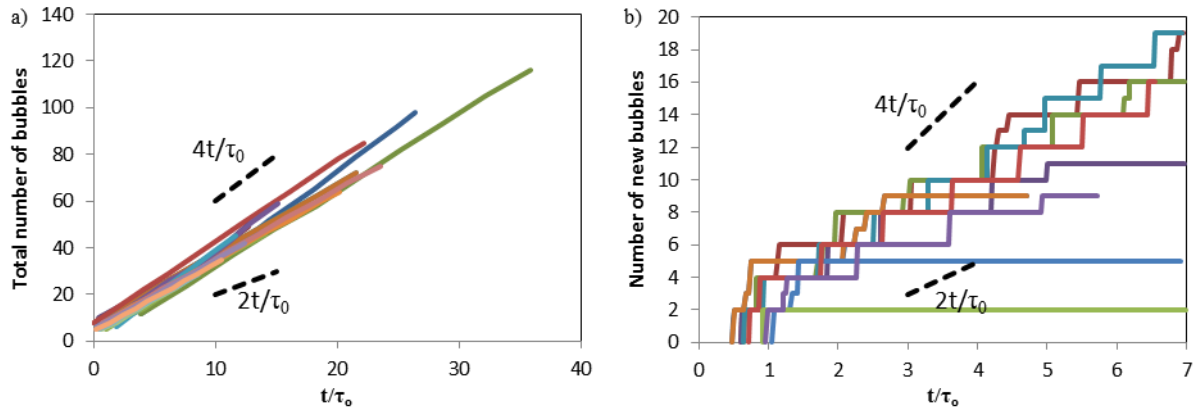
Figure 6.27 Data rescaled using the time scale: a) all of the experimental data from Figure 6.23, b) all of the simulations data from Figure 6.26. The short dotted lines indicate a gradient of 2 (below the data) and gradient of 4 (above the data).

6.4 CONCLUSIONS

Various foam regimes were studied in microfluidic channels with the cylindrical centre-located obstacle of three different diameters. Bubbles were observed to exhibit lamella division depending on both, initial foam arrangement including size and number of bubbles per row and the flow velocity. Majority of bubbles with an even number of bubbles in a row managed to flow around the obstacle by following the streamlines on the opposite sides of the $y = 0$ axis. Most of the foams composed of an odd number of bubbles per row were found to

undergo bubble division, primarily because of the centre bubble following the central streamline and thus, flowing directly into the obstacle. Deviations occurred for the slowest and smallest foams which had enough time and space to adjust their shape before their lamella was split. Larger bubbles i.e. foam with a lower number of bubbles required smaller capillary numbers in order to exhibit lamella division.

The bamboo foam was divided into two smaller asymmetric daughter bubbles across different conditions due to each bubble being confined by the channel walls and therefore, spanning the total width of the channel. The ratio of the daughter bubbles (associated with the size of the bubbles downstream) was found to be correlated by different variables including the capillary number, bubble size and liquid volume fraction. The smallest obstacle was best described by $\text{modCa}_1 = \text{Ca}\phi_{ch}/A^*$ whereas the two larger obstacles by $\text{modCa}_2 = \text{Ca}A^*/\phi_{ch}$. Smallest obstacle had different size dependence due to largest permeability on both sides of the obstacle which generated the lowest velocity gradient across the gas-liquid interface. All three obstacles produced similar results at lowest values of their corresponding modified capillary numbers i.e. the ratio decreased suggesting that bubbles were getting more symmetrical. The ratio then reached almost a plateau, increased very gradually and increased rapidly for the small, medium and large obstacle respectively. Hence, the polydispersity increased with the increase in the obstacle size. Thus, the above modified capillary numbers can be used as the control parameters for calculating and predicting bubble size distribution of foams in simple porous media for both oil recovery and soil remediation applications. In addition, the single obstacle can also be added to a microfluidic system in order to split a bamboo foam (or emulsion) into two smaller bubbles. This allows obtaining a staircase structure at a smaller liquid volume fraction (since initial bamboos are often much drier see

Figure 3.10 and Figure 5.5) which can be difficult using the usual flow-focusing device. The results suggest the use of the smallest obstacle due to the smallest polydispersity.

Staircase foam around the off-centre foam was found to exhibit many T1 events due to bubble elastic deformation which produced a velocity gradient of the two bubble rows in the upstream section. Such results highlight the viscoelastic and viscoplastic behaviour of the foams. Moreover, the daughter ratio trend was found to be similar to that of the bamboo foam around the medium obstacle due to a similar ratio of the bubble width just before the division to the diameter of the obstacle.

Bamboo foam around the off-centre obstacle was found to be dependent only on the initial bubble size due to the close location of the obstacle to one of the channel walls. Thus, the daughter bubbles were dependent on the obstacle location. Therefore, the off-centre obstacle gives better control of the daughter sizes when compared to the centre located obstacle since it requires fewer parameters.

Bamboo foam through a four-obstacle structure was found to exhibit no effect (or re-orientation) at very low velocities or high liquid fractions. This occurred primarily because of small bubbles becoming trapped in the less permeable areas. At higher velocities and larger sizes, bubbles were getting divided into three or four bubbles, thus generating three or four times more bubbles in the downstream channel. The number of new bubbles with time was found to increase with the velocity and size. In addition, simulations based on a two-dimensional model were found to produce a similar response with regards to the foam dynamics observed. The time scale given by A_b/WU_f allowed reconciling the experimental and numerical data together and showed a good agreement between the two. Thus, the model used in this study can be successfully used to predict the foam dynamics in foams far from the usual dry limit, which is more applicable for example to the growth of bubbles due to

diffusion-driven coarsening. Moreover, the number of bubbles generated at the obstacles gives a robust method of comparing the experimental and numerical results of flowing foams in porous media.

7 CONCLUSIONS AND FUTURE WORK

7.1 CONCLUSIONS

Flows of bubbles and foams through various microfluidic geometries have been investigated experimentally. Rectangular channels have been used in all of the problems which are far more popular and useful in many applications including microfluidics (e.g. lab on a chip, organ on a chip) when compared to cylindrical or square channels. However, the rectangular axisymmetric cross-section of the channel is more complex than in the cylindrical or square capillary and requires a better understanding of the system especially in the presence of a bubble or foams.

Effect of the capillary number on single bubbles in a sudden constriction was studied. Bubbles were observed to increase their curvature upon approaching the reduction of the channel in the form of a sudden contraction. Bubbles propagating through a channel with constrictions exhibited a velocity gradient which caused elastic deformation. The bubble elongated to its maximum size when the front tip and the rear tail were on the opposite sides of the constriction (front tip sometimes located inside the actual constriction). Upon exiting the constriction, the bubble contracts and changes its elastic strain from elongation to compression, which produces a croissant-like shape. The maximum deformations were presented to vary with the capillary number. At low capillary numbers, surface tension forces dominated and so large deformations were prevented. Increasing the capillary number caused stronger viscous shear forces which in consequence generated larger deformations. Moreover, the bubble inside the constriction was confined by the constriction walls which enforced dependence on the bubble size for the maximum elongations. Hence, the deformation was dependent on the local mean flow i.e. the capillary number, geometry of the constriction as well as the bubble size. The compression upon exiting was only found to be dependent on the

capillary number since the bubble was not constrained in the transversal direction. The maximum velocities observed for the front tip and the rear tail were shown to be relatively different from each other. Surface tension forces which contributed to the bubble contraction in the downstream section of the channel caused a greater velocity of the rear tail when compared to the front tip. This behaviour allows understanding the bubble dynamics near contractions and expansions which are often faced in microfluidics flows and is applicable to foams.

Single bubbles of various sizes were studied in rectangular channels with narrow constrictions. The bubbles were shown to undergo snap-off instability that caused bubble fragmentation, one of the main mechanisms of foam generation/regeneration in porous media. Capillary pressure and, therefore, the surface tension, as well as the curvature of the bubble, were presented to be the main cause of the break-up. Narrow constrictions exhibited a fast break-up time, caused by the liquid contribution from the thin films near the bubble front. The 20 μm wide constrictions satisfied the "Roof criterion" (>50% change in the smallest side of the cross-section) which caused a quick merge of the liquid in the corners inside the constriction. The wider constrictions ($w_c = 40$ μm) required larger capillary numbers to undergo snap-off since the curvature of the bubble was smaller. In addition, the liquid close to the bubble front was not sufficient to cause a neck collapse. Thus, a longer time was required for the liquid to invade the constriction, which also experienced larger flow resistance, especially for longer bubbles. Hence, the break-up time was shown to be size-dependent, strongly for the sharp constrictions and weakly for the long constrictions. The gradual constrictions were found to have a similar dependence. The narrow constrictions had almost identical break-up time which confirmed the contribution of liquid close to the bubble front. The wider constrictions, on the other hand, were found to exhibit slightly shorter break-up

times when compared to the sudden constrictions. This is most likely due to a smaller axial radius of curvature which normally stabilises against snap-off.

The analysis of the neck collapse for different constrictions, velocities and viscosities used in this chapter showed a universal neck collapse once the neck was smaller than all of the constriction walls. The non-linear collapse had a power exponent very close to 1/3 which exhibited similar behaviour to flow-focusing channels but varied from the vertical bubble pinch-off experiments that were found to be viscosity dependent. The analysis of the dimensionless numbers that relate main forces acting on the collapsing neck showed that the final neck reduction was caused by inertial forces, more specifically liquid inertia. Hence, it was presented here, that the inertial forces which are very often omitted in the micro-flows (gravitational forces are negligible when compared to the surface tension forces see 2.6.2) are the main driving forces in the very last stage of snap-off. Furthermore, employing the analysis of the two radii of curvatures showed that the axial radius of curvature decreased with a different power exponent than the circumferential and so the neck became less slender as it was approaching the final decrease.

The number of new daughters generated was correlated with the bubble size and the remaining size of the bubble after the first break-up. It was shown that the break-up time of the very first bubble might be dependent on the initial size of the bubble (mainly in the wider throats). However, once the first bubble was snapped, the size of the remaining bubble was reduced significantly and surrounded by thick liquid films which snapped bubbles more easily. Hence, the new number of bubbles generated was found to be dependent on the product of the remaining bubble size and the capillary number for all of the constrictions. Moreover, the two times wider constrictions produced twice as fewer bubbles which allowed scaling the number of bubbles generated with the ratio of narrow width to the wide width and

plotting all the data on the same line. Thus, for the porous media applications where snap-off is the dominant foam generation method, the remaining bubble size and therefore, the break-up time is one of the control parameters of the number of bubbles generated. Therefore, the break-up time should be considered in any of the future models for predicting bubble size distribution.

In Chapter 5 the system was changed from single bubbles to the more complicated flow of foams through constrictions. Foam regimes were identified based on the number of bubbles spanning the width of the channel. In the sudden constriction, bubbles were observed to undergo topological changes such as snap-off and two other instabilities due to bubble interaction, namely neighbour-wall and neighbour-neighbour pinch-off. Critical conditions were identified for the mentioned instabilities for different flow regimes. Snap-off was favoured by larger bubbles and wetter conditions, confirming the results of single bubbles in Chapter 4. The two pinch-off mechanisms required larger shear stresses which were applied by increasing the flow-rates and, therefore, the capillary number. Neighbour-wall pinch-off required moderate stress so that two bubbles approached the constriction together, whereas the neighbour-neighbour required large stress so that the bubbles were well confined and three of them approached the constriction together. The critical capillary number for most of the break-ups was also found to vary with the bubble size. Smaller bubbles were observed to squeeze through the throat of the constriction more easily, thus requiring larger stress for the pinch-offs.

Gradual constriction introduced another form of topological changes such as re-orientation and re-orientation with pinch-off. The bubbles were found to change their shape upon sliding along the constriction walls from horizontal to vertical. Bubble size was found to be critical for this phenomenon since there was a minimum size that was required for bubbles

to fill vertically the width of the channel. Furthermore, re-orientation with pinch-off allowed identifying transition regime from no-effect/re-orientation to pinch-off for the 3-row foam.

Staircase structure was studied in four constrictions of two different widths and lengths. The width of the constriction was found to have profound effects on foam behaviour since bubble deformation depended on it. Narrower constrictions were found to have lower critical capillary numbers for pinch-offs and favoured snap-off since the curvature of bubbles was greater inside the constriction, whereas the wider constrictions required larger critical capillary numbers and snap-off was rarely observed. The length, on the other hand, was found to have a smaller effect on the critical conditions for the instabilities in the narrow constrictions and was almost negligible for wider throats.

The analysis of the neck collapse for the snap-off and two pinch-off mechanisms produced different power exponents. Snap-off was found to thin with an exponent of 1/3 which confirms and extends the results found in Chapter 4 from single bubbles to foams. Thus, it may be concluded that bubbles final collapse during snap-off is universal, driven by liquid inertia and independent of viscosity. In the neighbour-wall pinch-off, the neck is reduced by one of the adjacent bubbles which move at a velocity similar to the mean flow velocity. The neck collapsed with a power exponent of 0.5 which corresponds to the bubble collapse in a low viscosity fluid. Since the bubble moves at a mean flow velocity, it behaves like the carrier fluid and its viscosity. The neighbour-neighbour pinch-off on the other hand, was found to decrease with a power exponent of 1. Such exponent corresponds to the neck collapse in a highly viscous fluid (>100 mPa.s). The neck of the pinched bubble is reduced by the two adjacent bubbles which are confined and move relatively slowly when approaching the pinch-off. Hence, the behaviour mimics that of a very viscous fluid with a large flow resistance.

Foams flowing through diverging channels (aspect ratio of 3) were forced to expand which yet again caused bubbles to deform elastically. Moreover, due to expanding channel the bubbles had to find a different equilibrium arrangement when compared to the upstream channel (1 or 2-row) which resulted in bubbles undergoing many plastic deformation more specifically T1 events. Thus, the flow was dominated by the elasticity and plasticity. Both of the gradual and sudden expansions possessed many similarities. The conditions investigated were relatively wet, thus much lower velocities were found in the very corners of the sudden expansion which caused temporary dead zones, a behaviour not observed in the dry foams in Hele-Shaw cells or simulations. Hence, the corners became effective walls which allowed other bubbles to bypass them. Consequently, the velocity field was very similar to the gradual expansion.

The map of elastic stress showed that maximum deformation was observed near the expansion zone where bubbles were sheared the most. Moreover, in the gradual expansion, the bubbles were observed to maintain the elongated shape for longer, due to gradually expanding walls. However, in the sudden constriction the bubbles could not maintain the large elongation because of the more drastic change of the channel width. The initial size was not large enough to fill immediately the total width of the expansion. The map of plastic stress was drawn showing the frequency of the T1 events. It was found to have the major maxima near the central line after the expansion and the minor maxima along the walls of the expansion. Right after the bubbles could not maintain the deformed shape; they restored their initial (or new) hexagonal shape and underwent many T1 events before relaxing and restoring equilibrium. The frequency of the main peak was larger in the gradual expansion since the bubble size was insufficient at the exact same location along the axial axes. However, the number of the T1 events was greater in the sudden expansion because as soon as the width of

the channel was changed, the bubbles could not maintain the elongation (insufficient size) and they flowed towards other parts of the channel such as the sudden corners. Thus, the number of T1 events was greater along the transversal axis. Changing both bubble size and velocity, did not have any qualitative differences. Larger bubbles were observed to undergo a smaller number of T1 events and also larger elongations. Bubbles flowing at higher velocities reached larger frequencies of the T1 events and also greater elongations caused by the larger input of energy.

Chapter 6 investigated a closer look at the dynamics of bubbles in channels with spherical obstacles. Bubbles composed of an even number of bubbles per row were found to exhibit the smallest deformations around the centrally located obstacle, especially the 2-row foam. Bubbles composed of an odd number (but more than 1-row) of bubbles had a middle bubble flowing towards the obstacle, which was often broken through a lamella division. Hence, lamella division was identified as the main mechanism causing bubble split, although, neighbour-wall was also observed in some instances.

The bamboo foam was investigated as it flowed around the obstacles. Since it spans the total width of the channel, it was divided regularly, breaking-up into two smaller daughter sizes. The break-up was not symmetric and the ratio of the size of the daughter bubbles was found to depend on the capillary number, liquid volume fraction and initial bubble size for three obstacles of different diameters. However, the ratio for the smallest obstacle was described using a different arrangement of the parameters ($modCa_1 = Ca\phi_{ch}/A^*$ for small, $modCa_2 = Ca\,A^*/\phi_{ch}$ for medium and large) due to different dependence on the initial bubble size. In general, at the smallest values of the modified capillary numbers the ratio of the two daughter bubble sizes was becoming smaller (bubbles becoming more monodisperse) with the increase and then either reaching a plateau (small obstacle) or increase to larger values

249

(medium and large obstacle) producing more polydisperse bubbles. The off-centre obstacle had a significant effect on the two-row structure. One of the bubble rows was regularly split into two bubbles. Moreover, the elastic deformation of bubbles near the obstacle affected the upstream section of the channel, causing T1 events, especially for the wetter and slower bubbles. Thus, the velocity gradient was observed between the two rows of bubbles flowing in the upstream channel with no obstacle, a phenomenon not observed in single-phase flows. The bamboo foam was yet again split into two bubbles; however, the ratio of the daughter bubbles was dependent only on the initial size of the bubble caused by a much closer distance of the obstacle to one of the channel walls.

The bamboo foam was also investigated through a four-obstacle structure, in order to shed some light on the foam formation in the porous media. At very small velocities, small bubbles that were broken up were trapped between the obstacles and the walls. Consequently, the upcoming bubbles flowed through the largest pores which resulted in the re-orientation to the staircase structure and therefore, no division. Increasing the flow velocity forced a division that was irregular, thus generating either 3 or 4 new bubbles. At highest velocities (or largest bubbles) the foam was always divided in a regular manner, producing ordered foam with two small bubbles near the walls and one central bubble. The number of bubbles generated was plotted as a function of time and varied linearly for all of the conditions. Numerical results showed much the same response, although the number of bubbles studied was much lower since it was too computationally expensive. The time scale that involved the initial velocity and bubble length was proposed and allowed plotting the data on the same line. All of the data was found to be in agreement, thus, showing a robust way of comparing the experimental and numerical results.

7.2 FUTURE WORK

The studies carried out in this thesis open up many new scientifically challenging problems.

- For the small bubbles in localised constrictions, it would be interesting to investigate more viscous fluids (>100 mPa.s) and compare the dynamic response to low viscous fluids or perhaps even more complex fluids such as a polymeric liquid that have a very high viscosity (≥1000 Pa.s).

- Slug bubbles and snap-off
  - o It would be interesting to study the dynamics of the bubbles in constrictions numerically. The flow of bubbles and slugs in straight channels was already given much attention. The dynamics of thin films, corner flow and pressure drop were investigated for channels of different cross-sections, different aspect ratios of width to length and in the presence of one or more bubbles in the channel (Hazel and Heil, 2002; De Lózar *et al.*, 2008). However, little work has been done showing the liquid velocity field as well as the bubble pressure drop during snap-off in channels of various cross-sections. Visualising the dynamics of thin films during snap-off could significantly improve understanding of this break-up which has been previously identified as one of the main mechanisms in enhanced oil recovery when using foam flooding (Almajid and Kovscek, 2016). Moreover, the results could also be applicable to soil remediation where the foam can also be generated through snap-off. The numerical results could also help predicting the bubble size distribution in the downstream section of the constriction which improves the mobility control of foams in porous media and is desirable by the oil recovery industries.

o Experiments using μPIV and, therefore, particle tracers could also improve understanding of this mechanism in channels of different cross-sections.

o It would be interesting to study snap-off in solutions with surfactants that have a large surface viscoelasticity and, therefore, fully rigid interfaces. Such a change in the characteristic of the interface could produce a different effect on the break-up time and scaling exponent during the final collapse. If the results become more prominent, such surfactants could reduce the average mean bubble size of the foam inside a porous medium which could, in turn, give a better mobility control for applications such as oil recovery and soil remediation.

o It would be interesting to study snap-off in rectangular channels with more complicated structures such as a double or even a triple constriction, or through three-dimensional structures which mimic better the geometries of actual porous media. Understanding the pressure that is necessary to push the bubble through the constriction and the resulting bubble size distribution could allow obtaining a mathematical model which is again desirable by oil companies.

o It would be interesting to study slugs in glass microfluidic channels with constrictions at much higher temperature. Glass channels would reduce the hydrophobicity of the studied material, a challenge that was faced in the work here. Moreover, high temperatures are the typical conditions in enhanced oil recovery. Hence, studying snap-off at those conditions could confirm if the results found here as well as the existing models for snap-off in porous media would be applicable at those conditions.

- Foams

  o It would be interesting to study foams and their dynamics through constrictions using different surfactants with e.g. high surface viscoelasticity or particle-stabilised foams. The rigid interfaces and high wall friction could have a profound effect on the stress required for bubbles to exhibit different instabilities such as pinch-offs. Moreover, it would be interesting to see if the bubble neck collapsed with the same power exponent. Additionally, the rate of bubble break-up could also be investigated for high and low surface viscoelastic surfactants by for example measuring the size distribution downstream of the constriction with time.

  o It would be interesting to study foams in similar geometries using non-Newtonian solutions such as Boger fluid (which is an elastic fluid with a constant viscosity) so that by comparing results with the Newtonian fluid the effects of elasticity could be investigated. Such experiments would improve fundamental understanding of foams made out of complex fluids.

  o It would be interesting to study foams and their dynamics in more complicated structures composed of double constrictions, double obstacles, multiple constrictions and obstacles, a mixture of constrictions and obstacles. Those studies could be later extended to three-dimensional structures for enhanced oil recovery applications. In addition, by employing glass microchannels the study could also focus on:

    ▪ High temperatures/high pressures that are typically used in EOR and, therefore:

- Study of very stable foams using mixtures of surfactants and/or particles in order to identify the most efficient surfactant for EOR.

- Use of steam or CO_2 as a dispersed phase that is typically used in EOR.

- Investigate oil displacement using foams and other methods such as gas, water flooding or nano-agents.

o It would be also interesting to use microfluidics for applications such as sclerotherapy (varicose vein treatment). Soft-lithography can be used to fabricate microchannels with elastic valves that mimic the actual veins. Thus, foams behaviour around flexible valves could be investigated which could improve understanding of the treatment mentioned above and help identify and understand any side effects that this treatment might cause.

REFERENCES

Alargova, R. G., Warhadpande, D. S., Paunov, V. N. and Velev, O. D. (2004) 'Foam superstabilization by polymer microrods', *Langmuir*, 20(24), pp. 10371–10374.

Almajid, M. M. and Kovscek, A. R. (2016) 'Pore-level mechanics of foam generation and coalescence in the presence of oil', *Advances in Colloid and Interface Science*. Elsevier B.V., 233, pp. 65–82.

Aubert, J. H., Kraynik, A. M. and Rand, P. B. (1986) 'Aqueous Foams', *Scientific American*. Springer Nature, 254(5), pp. 74–82.

Aubouy, M., Jiang, Y., Glazier, J. A. and Graner, F. (2003) 'A texture tensor to quantify deformations', *Granular Matter*, 5(2), pp. 67–70.

Bai, T., Jiang, W. and Fan, Y. (2018) 'Influence of Syringe Volume on Foam Stability in Sclerotherapy for Varicose Vein Treatment', *Dermatologic surgery : official publication for American Society for Dermatologic Surgery [et al.]*, 44(5), pp. 689–696.

Barigou, M. and Davidson, J. F. (1993) 'The fluid mechanics of the soap film meter', *Chemical Engineering Science*, 48(14), pp. 2587–2597.

Bergeron, V. (1997) 'Disjoining pressures and film stability of alkyltrimethylammonium bromide foam films', *Langmuir*, 13(13), pp. 3474–3482.

Bikerman, J. J. (1973) *Foams*. Berlin, Heidelberg: Springer Berlin Heidelberg.

Binks, B. P. (2002) 'Particles as surfactants - Similarities and differences', *Current Opinion in Colloid and Interface Science*, 7(1–2), pp. 21–41.

Blauer, R. E., Mitchell, B. J. and Kohlhaas, C. A. (1974) 'Determination of laminar, turbulent, and transitional foam flow losses in pipes', in *Society of Petroleum Engineers - SPE California Regional Meeting, CRM 1974*

Brakke, K. A. (1992) 'The surface evolver', *Experimental Mathematics*, 1(2), pp. 141–165.

Bretherton, F. P. (1961) 'The motion of long bubbles in tubes', *Journal of Fluid Mechanics*, 10(02), p. 166.

de Bruyn, J. R. (2004) 'Transient and steady-state drag in foam', *Rheologica Acta*, 44, pp. 150–159.

Burley, R. W., Nutt, C. W. and Bayat, M. G. (1984) 'Studies of Fluid Displacement By Foam in Porous Media.', *Chemical Engineering Research and Design*, 62(2), pp. 92–100.

Burton, J. C., Waldrep, R. and Taborek, P. (2005) 'Scaling and instabilities in bubble pinch-off', *Physical Review Letters*, 94(18).

Calvert, J. R. (1988) 'The flow of foam through constrictions', *International Journal of Heat and Fluid Flow*, 9(1), pp. 69–73.

Calvert, J. R. (1990) 'Pressure drop for foam flow through pipes', *International Journal of Heat and Fluid Flow*, 11(3), pp. 236–241.

Cantat, I., Kern, N. and Delannay, R. (2004) 'Dissipation in foam flowing through narrow channels', *Europhysics Letters*, 65(5), pp. 726–732.

Cantat, I., Poloni, C. and Delannay, R. (2006) 'Experimental evidence of flow destabilization in a two-dimensional bidisperse foam', *Physical Review E - Statistical, Nonlinear, and Soft Matter Physics*, 73(1).

Ceulen, R. P. M., Jagtman, E. A., Sommer, A., Teule, G. J. J., Schurink, G. W. H. and Kemerink, G. J. (2010) 'Blocking the saphenofemoral junction during ultrasound-guided foam sclerotherapy - Assessment of a presumed safety-measure procedure', *European Journal of Vascular and Endovascular Surgery*, 40(6), pp. 772–776.

Chen, H., Meng, Q. and Li, J. (2015) 'Thin lubrication film around moving bubbles measured in square microchannels', *Applied Physics Letters*, 107(14).

Chen, Q., Gerritsen, M. G. and Kovscek, A. R. (2008) 'Effects of reservoir heterogeneities on the steam-assisted gravity-drainage process', *SPE Reservoir Evaluation and Engineering*, 11(5), pp. 921–932.

Chowdiah, P., Misra, B. R., Kilbane, J. J., Srivastava, V. J. and Hayes, T. D. (1998) 'Foam propagation through soils for enhanced in-situ remediation', *Journal of Hazardous Materials*, 62(3), pp. 265–280.

Cohen, D., Patzek, T. W. and Radke, C. J. (1996) 'Two-dimensional network simulation of diffusion-driven coarsening of foam inside a porous medium', *Journal of Colloid and Interface Science*, 179(2), pp. 357–373.

Conn, C. A., Ma, K., Hirasaki, G. J. and Biswal, S. L. (2014) 'Visualizing oil displacement with foam in a microfluidic device with permeability contrast', *Lab on a Chip*. Royal Society of Chemistry, 14(20), pp. 3968–3977.

Cooke, T. F. and Hirt, D. E. (2017) 'Foam wet processing in the textile industry', in *Foams: Theory, Measurements, and Applications*.

Cox, S. J. (2015) 'Simulations of bubble division in the flow of a foam past an obstacle in a narrow channel', *Colloids and Surfaces A: Physicochemical and Engineering Aspects*. Elsevier B.V., 473, pp. 104–108.

Dawson, G., Häner, E. and Juel, A. (2015) 'Extreme deformation of capsules and bubbles flowing through a localised constriction', *Procedia IUTAM*, 16, pp. 22–32.

Denkov, N. D., Tcholakova, S., Golemanov, K., Ananthpadmanabhan, K. P. and Lips, A. (2009) 'The role of surfactant type and bubble surface mobility in foam rheology', *Soft Matter*, 5(18), pp. 3389–3408.

Deshpande, N. S. and Barigou, M. (2000) 'The flow of gas-liquid foams in vertical pipes', *Chemical Engineering Science*, 55(19), pp. 4297–4309.

Deshpande, N. S. and Barigou, M. (2001a) 'Flow of gas-liquid foams through pipe fittings', *International Journal of Heat and Fluid Flow*, 22(1), pp. 94–101.

Deshpande, N. S. and Barigou, M. (2001b) 'Foam flow phenomena in sudden expansions and contractions', *International Journal of Multiphase Flow*, 27(8), pp. 1463–1477.

Dollet, B. (2010) 'Local description of the two-dimensional flow of foam through a contraction', *Journal of Rheology*, 54(4), pp. 741–760.

Dollet, B. and Bocher, C. (2015) 'Flow of foam through a convergent channel', *European Physical Journal E*, 38(11), pp. 1–11.

Dollet, B., Elias, F., Quilliet, C., Huillier, A., Aubouy, M. and Graner, F. (2005) 'Two-dimensional flows of foam: Drag exerted on circular obstacles and dissipation', *Colloids and Surfaces A: Physicochemical and Engineering Aspects*, 263(1–3 SPEC. ISS.), pp. 101–110.

Dollet, B., Elias, F., Quilliet, C., Raufaste, C., Aubouy, M. and Graner, F. (2005) 'Two-dimensional flow of foam around an obstacle: Force measurements', *Physical Review E - Statistical, Nonlinear, and Soft Matter Physics*, 71(3).

Dollet, B. and Grander, F. (2007) 'Two-dimensional flow of foam around a circular obstacle: Local measurements of elasticity, plasticity and flow', *Journal of Fluid Mechanics*, 585, pp. 181–211.

Dollet, B., Van Hoeve, W., Raven, J. P., Marmottant, P. and Versluis, M. (2008) 'Role of the channel geometry on the bubble pinch-off in flow-focusing devices', *Physical Review Letters*, 100(3), pp. 1–4.

Dollet, B. and Raufaste, C. (2014) 'Rheology of aqueous foams', *Comptes Rendus Physique*. Elsevier Masson, 15(8–9), pp. 731–747.

Drenckhan, W., Cox, S. J., Delaney, G., Holste, H., Weaire, D. and Kern, N. (2005)

'Rheology of ordered foams - On the way to Discrete Microfluidics', *Colloids and Surfaces A: Physicochemical and Engineering Aspects*, 263(1–3 SPEC. ISS.), pp. 52–64.

Duffy, D. C., McDonald, J. C., Schueller, O. J. A. and Whitesides, G. M. (1998) 'Rapid prototyping of microfluidic systems in poly(dimethylsiloxane)', *Analytical Chemistry*, 70(23), pp. 4974–4984.

Durand, M. and Stone, H. A. (2006) 'Relaxation time of the topological T1 process in a two-dimensional foam', *Physical Review Letters*, 97(22).

Eggers, J., Fontelos, M. A., Leppinen, D. and Snoeijer, J. H. (2007) 'Theory of the collapsing axisymmetric cavity', *Physical Review Letters*, 98(9).

Ettinger, R. A. and Radke, C. J. (1992) 'Influence of texture on steady foam flow in Berea sandstone', *SPE Reservoir Engineering (Society of Petroleum Engineers)*, 7(1), pp. 83–90.

Falls, A. H., Hirasaki, G. J., Patzek, T. W., Gauglitz, D. A., Miller, D. D. and Ratulowski, T. (1988) 'Development of a mechanistic foam simulator: The population balance and generation by snap-off', *SPE Reservoir Engineering (Society of Petroleum Engineers)*. Society of Petroleum Engineers (SPE), 3(3), pp. 884–892.

Farajzadeh, R., Andrianov, A., Krastev, R., Hirasaki, G. J. and Rossen, W. R. (2012) 'Foam-oil interaction in porous media: Implications for foam assisted enhanced oil recovery', *Advances in Colloid and Interface Science*. Elsevier B.V., 183–184, pp. 1–13.

Fu, T., Funfschilling, D., Ma, Y. and Li, H. Z. (2010) 'Scaling the formation of slug bubbles in microfluidic flow-focusing devices', *Microfluidics and Nanofluidics*, 8(4), pp. 467–475.

Fuerstman, M. J., Lai, A., Thurlow, M. E., Shevkoplyas, S. S., Stone, H. A. and Whitesides,

G. M. (2007) 'The pressure drop along rectangular microchannels containing bubbles', *Lab on a Chip*, 7(11), pp. 1479–1489.

Gardiner, B. S., Dlugogorski, B. Z. and Jameson, G. J. (1998) 'Rheology of fire-fighting foams', *Fire Safety Journal*, 31(1), pp. 61–75.

Garstecki, P., Fuerstman, M. J., Stone, H. A. and Whitesides, G. M. (2006) 'Formation of droplets and bubbles in a microfluidic T-junction - Scaling and mechanism of break-up', *Lab on a Chip*, 6(3), pp. 437–446.

Garstecki, P., Gitlin, I., Diluzio, W., Whitesides, G. M., Kumacheva, E. and Stone, H. A. (2004) 'Formation of monodisperse bubbles in a microfluidic flow-focusing device', *Applied Physics Letters*, 85(13), pp. 2649–2651.

Gauglitz, P. A., Laurent, C. M. S., Radke, C. J., Gauglitz, P. A. and Laurent, C. M. S. (1988) 'Experimental Determination of Gas-Bubble Breakup in a Constricted Cylindrical Capillary', *Industrial and Engineering Chemistry Research*, 27(7), pp. 1282–1291.

Gauglitz, P. A., St. Laurent, C. M. and Radke, C. J. (1987) 'An Experimental Investigation of Gas-Bubble Breakup in Constricted Square Capillaries', *Journal of Petroleum Technology*, 39(09), pp. 1137–1146.

Gauglitz, P. A. and Radke, C. J. (1990) 'The dynamics of liquid film breakup in constricted cylindrical capillaries', *Journal of Colloid And Interface Science*, 134(1), pp. 14–40.

Géraud, B., Jones, S. A., Cantat, I., Dollet, B. and Méheust, Y. (2016) 'The flow of a foam in a two-dimensional porous medium', *Water Resources Research*. John Wiley & Sons, Ltd, 52(2), pp. 773–790.

Géraud, B., Méheust, Y., Cantat, I. and Dollet, B. (2017) 'Lamella Division in a Foam Flowing through a Two-Dimensional Porous Medium: A Model Fragmentation Process', *Physical Review Letters*. American Physical Society, 118(9), p. 098003.

Van Ginkel, C. G. (2007) 'Ultimate Biodegradation of Ingredients Used in Cleaning Agents', in *Handbook for Cleaning/Decontamination of Surfaces*. Elsevier Science B.V., pp. 655–694.

Golemanov, K., Tcholakova, S., Denkov, N. D., Ananthapadmanabhan, K. P. and Lips, A. (2008) 'Breakup of bubbles and drops in steadily sheared foams and concentrated emulsions', *Physical Review E - Statistical, Nonlinear, and Soft Matter Physics*, 78(5), pp. 26–33.

Gordillo, J. M., Sevilla, A., Rodríguez-Rodríguez, J. and Martínez-Bazán, C. (2005) 'Axisymmetric bubble pinch-Off at high reynolds numbers', *Physical Review Letters*, 95(19), pp. 1–4.

Günther, A. and Jensen, K. F. (2006) 'Multiphase microfluidics: From flow characteristics to chemical and materials synthesis', *Lab on a Chip*. Royal Society of Chemistry, pp. 1487–1503.

Hammond, P. S. (1983) 'Nonlinear adjustment of a thin annular film of viscous fluid surrounding a thread of another within a circular cylindrical pipe', *Journal of Fluid Mechanics*, 137, pp. 363–384.

Hazel, A. L. and Heil, M. (2002) 'The steady propagation of a semi-infinite bubble into a tube of elliptical or rectangular cross-section', *Journal of Fluid Mechanics*, 470, pp. 91–114.

van Hoeve, W., Dollet, B., Versluis, M. and Lohse, D. (2011) 'Microbubble formation and pinch-off scaling exponent in flow-focusing devices', *Physics of Fluids*, 23(9), pp. 1–18.

Hubbard, A. (2004) 'Colloidal Science of Flotation', *Journal of Colloid and Interface Science*

Huisman, F. M., Friedman, S. R. and Taborek, P. (2012) 'Pinch-off dynamics in foams, emulsions and suspensions', *Soft Matter*, 8(25), pp. 6767–6774.

Hunter, T. N., Pugh, R. J., Franks, G. V. and Jameson, G. J. (2008) 'The role of particles in stabilising foams and emulsions', *Advances in Colloid and Interface Science*, 137(2), pp. 57–81.

Jay, P., Magnin, A. and Piau, J. M. (2002) 'Numerical simulation of viscoplastic fluid flows through an axisymmetric contraction', *Journal of Fluids Engineering, Transactions of the ASME*, 124(3).

Jones, S. A. and Cox, S. J. (2012) 'On the effectiveness of a quasistatic bubble-scale simulation in predicting the constriction flow of a two-dimensional foam', *Journal of Rheology*, 56(3), pp. 457–471.

Jones, S. A., Dollet, B., Méheust, Y., Cox, S. J. and Cantat, I. (2013) 'Structure-dependent mobility of a dry aqueous foam flowing along two parallel channels', *Physics of Fluids*, 25(6).

Jones, S. A., Dollet, B., Slosse, N., Jiang, Y., Cox, S. J. and Graner, F. (2011) 'Two-dimensional constriction flows of foams', *Colloids and Surfaces A: Physicochemical and Engineering Aspects*, 382(1–3), pp. 18–23.

Kähärä, T., Tallinen, T. and Timonen, J. (2014) 'Numerical model for the shear rheology of two-dimensional wet foams with deformable bubbles', *Physical Review E - Statistical, Nonlinear, and Soft Matter Physics*, 90(3), p. 32307.

Kern, N., Weaire, D., Martin, A., Hutzler, S. and Cox, S. J. (2004) 'Two-dimensional viscous froth model for foam dynamics', *Physical Review E - Statistical Physics, Plasmas, Fluids, and Related Interdisciplinary Topics*, 70(4), p. 13.

Khatib, Z. I., Hirasaki, G. J. and Falls, A. H. (1988) 'Effects of capillary pressure on coalescence and phase mobilities in foams flowing through porous media', *SPE Reservoir Engineering (Society of Petroleum Engineers)*, 3(3), pp. 919–926.

Kilbane, J. J., Chowdiah, P., Kayser, K. J., Misra, B., Jackowski, K. A., Srivastava, V. J., Sethu, G. N., Nikolov, A. D., Wasan, D. T. and Hayes, T. D. (1997) 'Remediation of Contaminated Soils Using Foams', *Land Contamination and Reclamation*, 5(1), pp. 41–54.

Kovscek, A. R. and Radke, C. J. (1994) 'Fundamentals of Foam Transport in Porous Media', in, pp. 115–163.

Kraynik, A. M. and Reinelt, D. a (1999) 'Foam microrheology : from honeycombs to random foams', *Plateau*, 37(12), pp. 1619–23.

Langevin, D. (2000) 'Influence of interfacial rheology on foam and emulsion properties', *Advances in Colloid and Interface Science*, 88(1–2), pp. 209–222.

Legait, B. (1983) 'Laminar flow of two phases through a capillary tube with variable square cross-section', *Journal of Colloid And Interface Science*, 96(1), p. 28.

Link, D. R., Anna, S. L., Weitz, D. A. and Stone, H. A. (2004) 'Geometrically Mediated Breakup of Drops in Microfluidic Devices', *Physical Review Letters*, 92(054503).

Liontas, R., Ma, K., Hirasaki, G. J. and Biswal, S. L. (2013) 'Neighbor-induced bubble pinch-off: Novel mechanisms of in situ foam generation in microfluidic channels', *Soft Matter*, 9(46), pp. 10971–10984.

De Lózar, A., Juel, A. and Hazel, A. L. (2008) 'The steady propagation of an air finger into a rectangular tube', *Journal of Fluid Mechanics*, 614, pp. 173–195.

Lu, Y., Fu, T., Zhu, C., Ma, Y. and Li, H. Z. (2014) 'Pinch-off mechanism for Taylor bubble formation in a microfluidic flow-focusing device', *Microfluidics and Nanofluidics*, 16(6), pp. 1047–1055.

Ma, K., Liontas, R., Conn, C. A., Hirasaki, G. J. and Biswal, S. L. (2012) 'Visualization of improved sweep with foam in heterogeneous porous media using microfluidics', *Soft

Matter, 8(41), pp. 10669–10675.

Morrison, N., Neuhardt, D. L., Rogers, C. R., McEown, J., Morrison, T., Johnson, E. and Salles-Cunha, S. X. (2010) 'Incidence of side effects using carbon dioxideeoxygen foam for chemical ablation of superficial veins of the lower extremity', *European Journal of Vascular and Endovascular Surgery*, 40(3), pp. 407–413.

Ohta, M., Kikuchi, D., Yoshida, Y. and Sussman, M. (2011) 'Robust numerical analysis of the dynamic bubble formation process in a viscous liquid', *International Journal of Multiphase Flow*, 37(9), pp. 1059–1071.

Okpobiri, G. A. and Ikoku, C. U. (1983) 'Experimental determination of friction factors for mist and foam drilling and well cleanout operations', *Journal of Energy Resources Technology, Transactions of the ASME*, 105(4), pp. 542–553.

Plateau, J. A. F. (1873) *Statique expérimentale et théorique des liquides soumis aux seules forces moléculaires*, *Gauthier-Villars.*

Princen, H. M. (1983) 'Rheology of foams and highly concentrated emulsions. I. Elastic properties and yield stress of a cylindrical model system', *Journal of Colloid And Interface Science*, 91(1), pp. 160–175.

Protière, S., Bazant, M. Z., Weitz, D. A. and Stone, H. A. (2010) 'Droplet breakup in flow past an obstacle: A capillary instability due to permeability variations', *Europhysics Letters*, 92(5).

Prud'homme, R. K. and Khan, S. A. (1996) *Foams : theory, measurements, and applications*. New York: Marcel Dekker, Inc.

Pugh, R. J. (1996) 'Foaming, foam films, antifoaming and defoaming', *Advances in Colloid and Interface Science*, 64(95), pp. 67–142.

Pugh, R. J. (2005) 'Experimental techniques for studying the structure of foams and froths',

Advances in Colloid and Interface Science.

Pugh, R. J. (2016) *Bubble and Foam Chemistry*, *Bubble and Foam Chemistry*. Cambridge University Press .

Ransohoff, T. . and Radke, C. . (1986) 'Laminar flow of a wetting liquid along the corners of a predominantly gas-occupied noncircular pore', *Journal of Colloid and Interface Science*, 121(2), pp. 392–401.

Ransohoff, T. C., Gauglitz, P. A. and Radke, C. J. (1987) 'Snap-off of gas bubbles in smoothly constricted noncircular capillaries', *AIChE Journal*, 33(5), pp. 753–765.

Ransohoff, T. C. and Radke, C. J. (1988) 'Mechanisms of Foam Generation in Glass-Bead Packs.', *SPE Reservoir Engineering (Society of Petroleum Engineers)*, 3(2), pp. 573–585.

Raufaste, C., Dollet, B., Cox, S., Jiang, Y. and Graner, F. (2007) 'Yield drag in a two-dimensional foam flow around a circular obstacle: Effect of liquid fraction', *European Physical Journal E*, 23(2), pp. 217–228.

Raven, J. P., Marmottant, P. and Graner, F. (2006) 'Dry microfoams: Formation and flow in a confined channel', *European Physical Journal B*, 51(1), pp. 137–143.

Raven, J. P. and P. Marmottant (2007) 'Foams in microfluidics', *Univ-Ubs.Fr*, pp. 27–31.

Raza, S. H. and Marsden, S. S. (2007) 'The Streaming Potential and the Rheology of Foam', *Society of Petroleum Engineers Journal*, 7(04), pp. 359–368.

Reynolds, O. (1883) 'XXIX. An experimental investigation of the circumstances which determine whether the motion of water shall be direct or sinuous, and of the law of resistance in parallel channels', *Philosophical Transactions of the Royal Society of London*. The Royal Society, 174, pp. 935–982.

Rhein, L. (2007) 'Surfactant Action on Skin and Hair. Cleansing and Skin Reactivity

Mechanisms', *Handbook for Cleaning/Decontamination of Surfaces*. Elsevier Science B.V., 1, pp. 305–369.

Roman, S., Abu-Al-Saud, M. O., Tokunaga, T., Wan, J., Kovscek, A. R. and Tchelepi, H. A. (2017) 'Measurements and simulation of liquid films during drainage displacements and snap-off in constricted capillary tubes', *Journal of Colloid and Interface Science*. Elsevier Inc., 507, pp. 279–289.

Roof, J. G. (1970) 'Snap-Off of Oil Droplets in Water-Wet Pores', *Society of Petroleum Engineers Journal*, 10(01), pp. 85–90.

Rossen, W. R. (2000) 'Snap-off in constricted tubes and porous media', *Colloids and Surfaces A: Physicochemical and Engineering Aspects*, 166(1–3), pp. 101–107.

Sadhal, S. S. and Johnson, R. E. (1983) 'Stokes flow past bubbles and drops partially coated with thin films. Part 1. Stagnant cap of surfactant film - exact solution', *Journal of Fluid Mechanics*, 126, pp. 237–250.

Schneider, C. A., Rasband, W. S. and Eliceiri, K. W. (2012) 'NIH Image to ImageJ: 25 years of image analysis', *Nature Methods*, pp. 671–675.

Shi, Z., Zhang, Y., Liu, M., Hanaor, D. A. H. and Gan, Y. (2018) 'Dynamic contact angle hysteresis in liquid bridges', *Colloids and Surfaces A: Physicochemical and Engineering Aspects*. Elsevier B.V., 555, pp. 365–371.

Singh, G., Hirasaki, G. and Miller, C. (1997) 'Dynamics of foam films in constricted pores', *AIChE Journal-American*, 43(23), pp. 3241–3252.

Stevenson, P. (2012) *Foam Engineering: Fundamentals and Applications*, *Foam Engineering: Fundamentals and Applications*. Edited by P. Stevenson. Chichester, UK: John Wiley & Sons, Ltd.

Surenjav, E., Priest, C., Herminghaus, S. and Seemann, R. (2009) 'Manipulation of gel

emulsions by variable microchannel geometry', *Lab on a Chip*, 9(2), pp. 325–330.

Taylor, G. I. (1961) 'Deposition of a viscous fluid on the wall of a tube', *Journal of Fluid Mechanics*, 10(2), pp. 161–165.

Tessari, L., Cavezzi, A. and Frullini, A. (2001) 'Preliminary experience with a new sclerosing foam in the treatment of varicose veins', *Dermatologic Surgery*, 27(1), pp. 58–60.

Thondavadi, N. and Lemlich, R. (1985) 'Flow Properties of Foam with and without Solid Particles', *Industrial and Engineering Chemistry Process Design and Development*, 24(3), pp. 748–753.

Tsai, T. M. and Miksis, M. J. (1994) 'Dynamics of a Drop in a Constricted Capillary Tube', *Journal of Fluid Mechanics*, 274, pp. 197–217.

Valkó, P. and Economides, M. J. (1992) 'Volume equalized constitutive equations for foamed polymer solutions', *Journal of Rheology*, 36(6), pp. 1033–1055.

Vitasari, D. and Cox, S. (2017) 'A viscous froth model adapted to wet foams', *Colloids and Surfaces A: Physicochemical and Engineering Aspects*, 534, pp. 8–15.

Vuong, S. M. and Anna, S. L. (2012) 'Tuning bubbly structures in microchannels', *Biomicrofluidics*, 6(2), pp. 1–18.

Wang, S. and Mulligan, C. N. (2004) 'An evaluation of surfactant foam technology in remediation of contaminated soil', *Chemosphere*, 57(9), pp. 1079–1089.

Weaire, D. and Hutzler, S. (1999) 'The physics of foams'. Clarendon Press, Oxford.

Williams, J. J. (2007) 'Formulation of Carpet Cleaners', in *Handbook for Cleaning/Decontamination of Surfaces*. Elsevier Science B.V., pp. 103–123.

Wong, H., Radke, C. J. and Morris, S. (1995a) 'The Motion of Long Bubbles in Polygonal Capillaries. Part 1. Thin Films', *Journal of Fluid Mechanics*, 292, pp. 71–94.

Wong, H., Radke, C. J. and Morris, S. (1995b) 'The Motion of Long Bubbles in Polygonal

Capillaries. Part 2. Drag, Fluid Pressure and Fluid Flow', *Journal of Fluid Mechanics*, 292, pp. 95–110.

Wu, Y., Fang, S., Dai, C., Sun, Y., Fang, J., Liu, Y. and He, L. (2017) 'Investigation on bubble snap-off in 3-D pore-throat micro-structures', *Journal of Industrial and Engineering Chemistry*. The Korean Society of Industrial and Engineering Chemistry, 54, pp. 69–74.

Yuan, C. L., Xu, Z. Z., Fan, M. X., Liu, H. Y., Xie, Y. H. and Zhu, T. (2014) 'Study on characteristics and harm of surfactants', *Journal of Chemical and Pharmaceutical Research*, 6(7), pp. 2233–2237.

Zhang, R., Xu, Y., Wen, B., Sheng, N. and Fang, H. (2014) 'Enhanced permeation of a hydrophobic fluid through particles with hydrophobic and hydrophilic patterned surfaces', *Scientific Reports*, 4, pp. 1–5.